

THE UNIVERSITY OF SHEFFIELD



DIRECT AND INDIRECT TORQUE CONTROL OF UNBALANCED PERMANENT MAGNET SYNCHRONOUS MACHINES

By

Atheer Habash Abosh

A thesis submitted for the degree of Doctor of Philosophy

Department of Electronic and Electrical Engineering

The University of Sheffield

Mappin Street, Sheffield, S1 3JD, UK

June 2016

ABSTRACT

Electrical machines may exhibit various types of imbalances and undesirable harmonic distortions. These may increase the torque and flux ripples, acoustic noise, unbalanced three-phase currents, while also reducing efficiency. These types of imbalances and undesirable harmonic distortions cannot be controlled by using the conventional indirect torque control (ITC) and direct torque control (DTC) strategies. For some high-performance motion control, such as precision machine tools, robotics, and servo drives, low torque ripples are, however, obligatory. Nowadays, more studies have been conducted on the ITC strategy to control undesired current harmonics, such as double synchronic reference frames (DSRF), resonant controller, second order generalized integration, and reference current generation. Such strategies, however, can rarely be applied to DTC strategy.

In this research, the influence of asymmetric winding impedances, unbalanced back-EMF, and inverter nonlinearity in three-phase surface-mounted PMSMs has been systematically investigated by employing space vector modulations (SVM) based ITC and DTC strategies. This thesis firstly presents a modified ITC strategy by extracting the positive and negative sequence components in the stationary abc frame, and then a coordination transformation is used to control the machine in DSRF. This strategy provides faster dynamic response when compared with the conventional DSRF strategy, since the filters and the decoupling network are not required.

Due to the lack of research regarding the DTC strategy under unbalanced conditions, this research investigates and proposes modified cascaded and parallel DTC-SVM strategies. The conventional cascaded DTC strategy is investigated under balanced and unbalanced conditions. Then, a modified control strategy is introduced by adding two compensators (the conventional PI-controller with a resonant controller, and the use of the negative- and positive-sequence voltage vectors) to suppress the 2nd harmonic components in the torque and stator flux linkage.

Furthermore, for parallel DTC-SVM, the compensation of the 2nd and 6th harmonic components is investigated by means of either a resonant controller or an adaptive filter. In addition to the simplicity of the proposed strategies, these may also be able to significantly reduce the torque and flux ripples, while maintaining the merit of the fast dynamic response of the conventional DTC strategy even under variable fundamental frequency. Moreover, it has been proven that the compensation from using a resonant controller or an adaptive filter is parameter independent. Thus, regardless of unbalanced conditions, an effective torque ripple minimisation can still be achieved by properly selecting the dominant harmonic compensation.

ACKNOWLEDGEMENTS

Firstly, I would like to express the sincerest thanks to my supervisor, Professor Zi Qiang Zhu, who gave me an opportunity to study a PhD in one of the best Electrical Machines and Drives (EMD) groups around the world. Under his supervision, continued support, and encouragement, I have developed myself in many fields, which will eventually push me towards my goals in life. I consider myself extremely lucky to have such an enthusiastic and competent supervisor.

I also would like to gratefully acknowledge Dr. Kan Liu and Dr. Yuan Ren for their patience and help during all these years. They were ready to offer any help whenever I requested. My huge thanks to all my colleagues in the EMD group and the staff members in the Department of Electronic and Electrical Engineering at the University of Sheffield, who were very kind and helpful to me during all of these years. I will never forget the happy moments we have shared together.

Unlimited thanks to my family and friends back home. Despite your harsh circumstances, you never stop your moral support and look after me, a big thank to you all.

Finally, I would like to thank my wife, Ann, and our little baby, Chris, you have been amazing since the moment you became part of my life. To you and to the memory of my mother Teerez Zaya (1955-2000), I dedicate this thesis.

*“Great minds discuss ideas, average minds discuss events,
and small minds discuss people”*

Richard Gere

CONTENTS

ABSTRACT	I
ACKNOWLEDGEMENTS	II
LIST OF ABBREVIATIONS AND SYMBOLS	VII
LIST OF FIGURES	XII
LIST OF TABLES	XVI
1. CHAPTER 1	1
GENERAL INTRODUCTION	1
1.1. Background	1
1.2. Control Strategies of Balanced PMSM Drives	5
1.2.1. Indirect torque control	5
1.2.2. Direct torque control (DTC)	10
1.3. Control Strategies of Unbalanced PMSM Drives	15
1.3.1. Hysteresis control	15
1.3.2. Repetitive control	16
1.3.3. Deadbeat control	16
1.3.4. Double synchronous reference frame controller (DSRFs)	19
1.3.5. Double second-order generalized integrator (SOGI)	23
1.3.6. Resonant controller	26
1.4. Thesis Outline and Major Contributions	30
1.4.1. Thesis outline	30
1.4.2. Major contributions	32
2. CHAPTER 2	34
SYSTEM HARDWARE AND SOFTWARE IMPLEMENTATION	34
2.1. Introduction	34
2.2. dSPACE Control System	34
2.2.1. CPU board-DS1006	34
2.2.2. PWM board-DS5101	35
2.2.3. A/C board-DS2004	35
2.2.4. Encoder board-DS3001	36
2.3. Voltage Source Inverter (VSI)	37
2.3.1. Hardware configuration	37
2.3.2. Software implementation	40
2.4. Software Environment	51
2.5. Test Rig	52

2.6. Summary	54
3. CHAPTER 3	55
CURRENT CONTROL OF UNBALANCED THREE-PHASE PMSM BASED ON DOUBLE SYNCHRONOUS REFERENCE FRAME CONTROLLER	55
3.1. Introduction	55
3.2. Mathematical Model of PMSM under Balanced and Unbalanced Conditions	57
3.2.1. Representation of PMSM in stationary abc reference frame	57
3.2.2. Representation of PMSM in stationary $\alpha\beta$ -reference frame	61
3.2.3. Representation of PMSM in synchronous dq -reference frame	66
3.3. System Behavior under Unbalanced Conditions	69
3.3.1. Symmetrical components	69
3.3.2. Quadrature-signal generation (QSG) techniques	73
3.4. Proposed Current Control Method	76
3.5. Experimental Validations	79
3.5.1. Steady-state performance	82
3.5.2. Dynamic performance	85
3.5.3. Influence of adding extra resistance	88
3.5.4. Inverter dead-time effects	88
3.6. Summary	89
4. CHAPTER 4	90
CASCADED DIRECT TORQUE CONTROL OF UNBALANCED PMSM WITH LOW TORQUE AND FLUX RIPPLES	90
4.1. Introduction	90
4.2. Conventional Cascaded DTC-SVM Strategy for Balanced PMSM	92
4.2.1. Machine model represented in stator flux reference frame	92
4.2.2. Torque and flux control	96
4.3. Proposed Cascaded DTC-SVM Strategy for Unbalanced PMSM	104
4.3.1. Machine behavior under unbalanced conditions	104
4.3.2. Sequential components extraction	106
4.3.3. Positive and negative RVVs generation	108
4.3.4. Torque ripple minimization	109
4.4. Experimental Verification	111
4.4.1. Compensation under steady-state conditions	111
4.4.2. Compensation under dynamic conditions	115
4.4.3. Speed control	118

4.5. Summary	119
5. CHAPTER 5	120
REDUCTION OF TORQUE AND FLUX RIPPLES IN DIRECT TORQUE CONTROL OF ASYMMETRIC PERMANENT MAGNET SYNCHRONOUS MACHINE	120
5.1. Introduction	120
5.2. Conventional Parallel DTC-SVM Strategy for Balanced PMSM	122
5.2.1. Mathematical model represented in stator flux reference frame	122
5.2.2. Torque and flux control	124
5.3. Influence of Unbalanced and Inverter nonlinearity	127
5.3.1. Inverter nonlinearity	127
5.3.2. Impact of unbalanced Back-EMF and Inverter nonlinearity	129
5.4. Proposed Parallel DTC-SVM Strategy for Unbalanced and Distorted PMSM	132
5.4.1. Resonance controller	132
5.4.2. Dynamic behavior of PIR controller	133
5.5. Experimental Verification	136
5.5.1. Compensation under steady-state conditions	137
5.5.2. Compensation under dynamic condition	144
5.5.3. Machine start-up	148
5.6. Summary	149
6. CHAPTER 6	150
REDUCTION OF TORQUE AND FLUX RIPPLES OF UNBALANCED PERMANENT MAGNET SYNCHRONOUS MACHINES BY DIRECT TORQUE CONTROL WITH ADAPTIVE FILTER	150
6.1. Introduction	150
6.2. Conventional Parallel DTC-SVM Strategy	152
6.3. Proposed Control Strategy	153
6.3.1. Compensation of torque and flux ripples by means of adaptive filters	154
6.3.2. Robustness and system response analysis	156
6.4. Experimental Verification	158
6.4.1. Investigation under steady state conditions	159
6.4.2. Investigation under dynamic conditions	163
6.4.3. System start-up	165
6.5. Summary	166
7. CHAPTER 7	168
CONCLUSIONS AND FUTURE RESEARCH	168

7.1. Introduction	168
7.2. Current Control of Unbalanced Three-phase PMSMs Based on Double Synchronous Reference Frame Controller	168
7.3. Cascaded Direct Torque Control of Unbalanced PMSMs with Low Torque and Flux Ripples	169
7.4. Reduction of Torque and Flux Ripples in Direct Torque Control of Unbalanced PMSMs by Means of Resonant Controllers	170
7.5. Reduction of Torque and Flux Ripples in Direct Torque Control of Unbalanced PMSMs by Means of Adaptive Filter	171
7.6. Future Research	172
7.7. Publications	172
REFERENCES	174
APPENDIX A. MACHINE BASIC TRANSFORMATION	191
APPENDIX B. DERIVATIVE OF THE DYNAMIC MODEL OF SYMMETRICAL AND ASYMMETRIC PMSMS	195
APPENDIX C SCHEMATIC DIAGRAM OF THE INVERTER BOARD	207

LIST OF ABBREVIATIONS AND SYMBOLS

Abbreviations And Symbols	Explanation of Symbols	Units
AC	Alternating current	
A/D	Analogue to digital converter	
AF	Adaptive filter	
ANF	Adaptive notch filter	
ABPF	Adaptive band pass filter	
BLAC	Brushless alternating current	
BLDC	Brushless direct current	
CM	Current model	
CPU	Central processing unit	
DAC	Digital to analogue converter	
DC	Direct current	
DTC	Direct torque control	
DSRF	Double synchronous reference frame	
DFIG	Double fed induction generator	
DTC-SVM	Direct torque control based on space vector modulation	
EMF	Electromagnetic force	
GI	Generalized integration	
I/O	Input/ Output	
IPM	Interior PM	
IGBTs	Insulated-gate bipolar transistors	
ILC	Iterative learning control	
LPF	Low pass filter	
LUT	Lookup table	

LMS	Least mean square
MMF	Magnetomotive force
MOSFETs	Metal-oxide-semiconductor field-effect transistors
NSC	Negative sequence component
NSRF	Negative synchronous reference frame
PSC	Positive sequence component
PSRF	Positive synchronous reference frame
PM	Permanent magnet
PMSM	Permanent magnet synchronous machine
PI	Proportional-integral
PIR	Proportional-integral-resonant
PR	Proportional-resonant controller
PWM	Pulse width modulation
R	Resonant controller
RVV	Reference voltage vector
QSG	Quarter signal generation
SCE	Sequential components extractor
SOGI	Second order generalized integration
SRF	Synchronous reference frame
SPM	Surface-mounted PM
SVM	Space vector modulation
SVPWM	Space vector pulse width modulation
THD	Total harmonic distortion
TRF	Torque ripple factor
TF	Transfer function
UPS	Universal power source

VM	Voltage model	
VSI	Voltage source inverter	
ZSC	Zero sequence components	
abc	Stationary a - b - c reference frame	
$\alpha\beta 0$	Stationary alpha-beta-zero reference frame	
dqs	Stator flux oriented reference frame	
$dq0$	Rotational d - q - 0 reference frame	
B	Viscosity friction	Nm. sec
\vec{e}	Phase back-EMF vector	-
I_m	Stator phase current magnitude	Ampere [A]
I_R	Rated stator phase current	A
\bar{i}_{abc}	Stator phase current matrix	-
i_a, i_b, i_c	Stator phase currents in abc frame	A
i_{abc+}, i_{abc-}	Positive and negative sequence current components in abc frame	A
i_α, i_β	Stator phase currents in the stationary $\alpha\beta$ frame	A
$i_{\alpha\beta+}, i_{\alpha\beta-}$	Positive and negative sequence current components in $\alpha\beta$ frame	A
i_d, i_q	Phase current in the rotational dq frame	A
i_{dq+}, i_{dq-}	Positive and negative sequence current components in the dq frame	A
J	Inertia	kg.m ²
\bar{L}_{abc}	Stator inductance matrix	Henry [H]
L_s	Stator self-inductance	H
$L_{aa,bb,cc}$	Stator phases a, b, c self-inductance	H
$L_{a,b,c}$	Average value of phases a, b, c self-inductances	H
$L_{aa2,bb2,cc2}$	Sinusoidal components of phases a, b, c self-inductances	H
L_d, L_q	dq -axis inductance	H
$M_{ab,bc,ba,bc,ca,cb}$	Average value of mutual inductance	H

$M_{ab2,bc2,ba2,bc2,ca2,cb2}$	Sinusoidal componets of mutual inductacnces	H
MMF	Stator phase magneto-motive force	Volt [V]
N_s	Number of effective turn in one phase winding	-
p_n	Number of pole pairs	-
R_s	Stator phase resistance	Ohm [Ω]
S_a, S_b, S_c	Inverter switching state	-
T_e	Electromagnetic torque	Newton. meter [Nm]
T_l	Load torque	Nm
T_s	Sampling time	Second [s]
T_{sw}	Switching time	s
T_{DT}	Dead-time	s
v_{abc}	Stator phase to neutral voltage	V
$v_{ab,bc,ca}$	Stator phase to phase voltage	V
$v_{\alpha\beta+}, v_{\alpha\beta-}$	Positive and negative sequence voltage components in $\alpha\beta$ frame	V
v_d, v_q	Voltages in the rotational dq reference frame	V
ρ	Derivative factor	-
ψ_{PM}	Permanent magnet flux	Webber [Wb]
ψ_d, ψ_q	Flux linkages in rotational dq - reference frame	Wb
ω_r	Electrical angular velocity	rad/sec
θ_r^+, θ_r^-	Electrical angles in forward and backward rotation directions	Electrical degree
f_c	Cut-off frequency of the low pass filter	Hertz [Hz]
f_s	Fundamental frequency (Hz)	Hz
P	Active Power	Watt [W]
Q	Reactive power	Volt-ampere reactive [Var]

S	Apparent Power	Volt-ampere [VA]
Subscript “ A_{\pm} ”	Positive and negative sequence components	
Superscript “ A^{\pm} ”	Positive and negative synchronous reference frame	

LIST OF FIGURES

Fig. 1.1 Classification of different types of PM machines.	2
Fig. 1.2 Cross section of PMSM shows the rotor shaft and PM bars placement.	4
Fig. 1.3 General classification of PMSM control strategies [9].	4
Fig. 1.4 Spatial relationships among machine coordinate.	7
Fig. 1.5 Schematic diagram of field oriental control strategy [17].	7
Fig. 1.6 Vector diagram of constant torque per ampere control under steady state.	8
Fig. 1.7 Current and PM flux vectors under maximum torque per ampere operation.	9
Fig. 1.8 Current and PM flux vectors under unity power factor (UPFC).	9
Fig. 1.9 Current and PM flux vectors under constant stator flux control strategy.	10
Fig. 1.10 Possible voltage space vector in voltage source inverter.	11
Fig. 1.11 Block diagram of hysteresis DTC.	11
Fig. 1.12 Circular trajectory of stator flux linkage in stationary $\alpha\beta$ -reference frame.	12
Fig. 1.13 Direct torque control using SVM.	14
Fig. 1.14 Electrical machine fault classification.	14
Fig. 1.15 Control method classification.	17
Fig. 1.16 Principle of deadbeat control.	17
Fig. 1.17 Double synchronous reference frame controllers.	20
Fig. 1.18 Oscillation cancellations in DSRFs controller using ANF [73].	21
Fig. 1.19 Decoupled DSRF controller [74].	23
Fig. 1.20 A quadrature signal delay generator.	24
Fig. 1.21 SOGI structure for sequential component extractor.	26
Fig. 1.22 Equivalent of DSRF controller represented in the stationary frame.	29
Fig. 1.23 Flow chart of thesis organization.	32
Fig. 2.1 Experimental system setup.	34
Fig. 2.2 Inverter box with function type (top view).	37
Fig. 2.3 Top view of the inverter board.	38
Fig. 2.4 Top view of interface board.	38
Fig. 2.5 Schematic diagram of power supply.	39
Fig. 2.6 Schematic diagram of optocoupler.	40
Fig. 2.7 Function parts of control and connection panel.	40
Fig. 2.8 Three-phase six switch VSI.	42

Fig. 2.9 Equivalent power circuit topology of a three-phase six switch VSI	43
Fig. 2.10 Inverter output voltage from load side.	44
Fig. 2.11 PWM technique with additional ZSS.....	47
Fig. 2.12 PWM waves with ZSS	47
Fig. 2.13 Inverter space voltage vectors.	48
Fig. 2.14 Calculation of voltage vector duration time.....	50
Fig. 2.15 Experimental system setup.....	53
Fig. 2.16 Implementations of unbalanced conditions.....	54
Fig. 3.1 Equivalent of three-phase winding in rotational reference frame.	62
Fig. 3.2 Definition of sequential components [142].....	69
Fig. 3.3 Sequential components extraction in the stationary <i>abc</i> reference frame.....	72
Fig. 3.4 PLL based on the Hilbert transform.....	74
Fig. 3.5 Proposed quarter signal generation based on the integer sample delay.....	75
Fig. 3.6 Current behavior in the DSRF.....	76
Fig. 3.7 Spatial relations between different reference frames.....	77
Fig. 3.8 Current behavior in the DSRF.....	78
Fig. 3.9 Schematic diagram of the conventional and proposed DSRF strategies.....	80
Fig. 3.10 Currents behavior in the conventional DSRF control strategy.	81
Fig. 3.11 Currents behavior in the proposed DSRF control.	82
Fig. 3.12 Comparison of current responses at steady-state between the conventional and proposed DSRFs strategies.	84
Fig. 3.13 Electromagnetic torques.....	85
Fig. 3.14 Dynamic performances of different strategies.	86
Fig. 3.15 Dynamic response comparison.	87
Fig. 3.16 Speed step response of the three control strategies.....	87
Fig. 3.17 Influence of unbalanced condition on TRF for different control strategies.....	88
Fig. 3.18 Influence of dead-time on TRF.....	89
Fig. 4.1 Spatial relationship of PMSM variables represented in different frames.	92
Fig. 4.2 Adaptive stator flux estimator.....	95
Fig. 4.3 Relationship between different quantities in different reference frames.	96
Fig. 4.4 Block diagram of the conventional cascaded DTC-SVM strategy.	97
Fig. 4.5 Block diagram of the RVV calculation.....	97

Fig. 4.6 Flux model of PMSM in stator coordinate.....	99
Fig. 4.7 Flux control loop in stationary $\alpha\beta$ reference frame.....	99
Fig. 4.8 Simplified flux control loop in stationary $\alpha\beta$ reference frame.....	100
Fig. 4.9 Block diagram of the dynamic flux controller.....	100
Fig. 4.10 Torque control loop with PI regulator.....	101
Fig. 4.11 Block diagram of the torque control loop represented in s-domain.....	102
Fig. 4.12 Relationship between different quantities in different reference frames under unbalanced conditions.....	105
Fig. 4.13 Proposed cascaded DTC-SVM strategy.....	106
Fig. 4.14 Performance of SCE without/with adding extra resistance.....	108
Fig. 4.15 Simulation model of the resonant controller.....	110
Fig. 4.16 Additional winding placement.....	112
Fig. 4.17 Steady-state performance with/without compensation.....	113
Fig. 4.18 Current behaviours with/without compensation.....	114
Fig. 4.19 Voltage behaviours with/without compensation.....	115
Fig. 4.20 Torque and flux dynamic responses with/without compensation.....	116
Fig. 4.21 Start-up response under symmetrical conditions using Mode [1].....	116
Fig. 4.22 Start-up response under asymmetric conditions using Mode [1].....	117
Fig. 4.23 Start-up response under asymmetric conditions using Mode [3].....	117
Fig. 4.24 Comparative of torque step responses under different modes.....	118
Fig. 4.25 Speed reversal response with/without compensation.....	119
Fig. 5.1 Spatial relationship between different reference frames.....	123
Fig. 5.2 Block diagram of the parallel DTC-SVM structure.....	124
Fig. 5.3 Block diagram of the flux control loop.....	125
Fig. 5.4 Block diagram of the torque control loop in s-domain.....	126
Fig. 5.5 Output voltage with the influence of voltage drop across power devices.....	127
Fig. 5.6 Gate drive signal control on one inverter lag.....	128
Fig. 5.7 Dead time effect on the inverter output voltage.....	128
Fig. 5.8 Asymmetric condition (unbalanced back-EMF and inverter nonlinearity).....	130
Fig. 5.9 Frequency response of non-ideal resonant controller.....	133
Fig. 5.10 Frequency response of the proposed compensation.....	134
Fig. 5.11 Schematic diagram of the proposed strategy.....	136
Fig. 5.12 Stator winding configuration with measured back-EMF at 1500 rpm.....	138

Fig. 5.13	Steady-state performance without/with compensation for case A.	140
Fig. 5.14	Steady-state performance without/with compensation for case B.	142
Fig. 5.15	Compensation of 6 th and 2 nd harmonic under steady-state conditions.	143
Fig. 5.16	Compensation of 6 th and 2 nd harmonic in the dqs reference frame.	144
Fig. 5.17	Experimental results under dynamic condition without/with compensation. ...	145
Fig. 5.18	Speed and corresponding torque responses without/with compensation.	146
Fig. 5.19	Speed-reversing test.	147
Fig. 5.20	Machine start-up.	148
Fig. 5.21	Torque step responses without/with compensation.	149
Fig. 6.1	Block diagram of the torque and flux control loops.	152
Fig. 6.2	Second order adaptive filter.	155
Fig. 6.3	System open-loop response with/without ABPF.	158
Fig. 6.4	Block diagram of the proposed control strategy.	159
Fig. 6.5	Steady state performance.	160
Fig. 6.6	Phase current without/with compensation, channels: i_{abc} (0.5 A/div), horizontal: time (50 ms/div).	161
Fig. 6.7	Voltage command without/with compensation.	161
Fig. 6.8	Compensation under steady state conditions, channel 1: ψ_s (5 mWb/div), channel 2: T_e (0.1 Nm/div), channel 3: i_a (1 A/div), horizontal: time (1 s/div).	162
Fig. 6.9	Influence of added extra resistance on TRF.	162
Fig. 6.10	Dynamic responses with/without compensation.	163
Fig. 6.11	Speed control, channels 1&2: reference and estimated torques, T_e (0.2 Nm/div), channels 3&4: reference and estimated speeds, ω_r (1000 rpm/div), horizontal: time (5 s/div).	164
Fig. 6.12	Speed control with/without compensation, channels 1&2: reference and estimated torques, T_e (0.2 Nm/div), channel 3&4: reference and estimated speeds, ω_r (1000 rpm/div), horizontal: time (5 s/div).	165
Fig. 6.13	Motor start up from a standstill.	166

LIST OF TABLES

TABLE 1.1	DIFFERENCES BETWEEN PMSM AND BLDC MACHINES.....	2
TABLE 2.1	DEFINITION OF PWM AND TRANSDUCER CONNECTOR.....	41
TABLE 2.2	SWITCHING PATTERNS AND OUTPUT VOLTAGES OF SIX SWITCH THREE PHASE INVERTER.....	45
TABLE 2.3	SECTOR SELECTION.....	49
TABLE 2.4	PROTOTYPE PARAMETERS.....	54
TABLE 3.1	PI-REGULATOR PARAMETERS.....	83
TABLE 4.1	CONTROLLER PARAMETERS.....	111
TABLE 4.2	PHASE BACK-EMF HARMONICS (V) AT 1500 RPM.....	112
TABLE 5.1	EXPERIMENTAL SYSTEM PARAMETERS.....	137
TABLE 6.1	EXPERIMENTAL SYSTEM PARAMETERS.....	159
TABLE 7.1	COMPARISON BETWEEN CONVENTIONAL DSRFs AND PROPOSED DSRF.....	169
TABLE 7.2	COMPARISON BETWEEN CONVENTIONAL CASCADED DTC AND PROPOSED CASCADED DTC-SVM.....	170
TABLE 7.3	COMPARISON BETWEEN THE CONVENTIONAL PARALLEL DTC- SVM AND PROPOSED PARALLEL DTC-SVM STRATEGIES.....	171
TABLE 7.4	COMPARISON BETWEEN PR AND AF.....	172

CHAPTER 1

GENERAL INTRODUCTION

1.1. Background

Since the introduction of modern permanent magnet (PM) materials, i.e. ferrite magnets in 1950s, SmCo magnets in 1960s, and NdFeB magnets in 1980s, as well as semiconductor devices and power electronic switching circuits, enormous development has been carried out on various PM machines. By replacing the rotor electromagnetic poles which employ winding excitations and require an electrical supply source with the PM poles, the slip rings/commutators and brushes are eliminated in brushless PM machines. Many innovative PM machines have also been developed. Several outstanding features have been acquired by using brushless PM machines, for example [1], [2]:

- Since the magnets are placed on the rotor, the copper losses are reduced and high efficiency and better thermal characteristics can be obtained.
- The lack of mechanical components such as slip rings/commutators and brushes make the machine lighter with high power/weight ratio, large torque/inertia ratio, and good reliability.
- The structural rigidity allows the PM machines to operate at very high speed without special method.

PM machines are now used for many applications, which include, but are not limited to, domestic use, aerospace use, industrial use, and wind power generators, amongst others. PM machines, on the other hand, also have some drawbacks, such as high cost of rare earth PM materials, low reliability at high temperature and electric loading due to the irreversible demagnetisation of PM materials, as well as difficulties in handling during the manufacturing [3], [4].

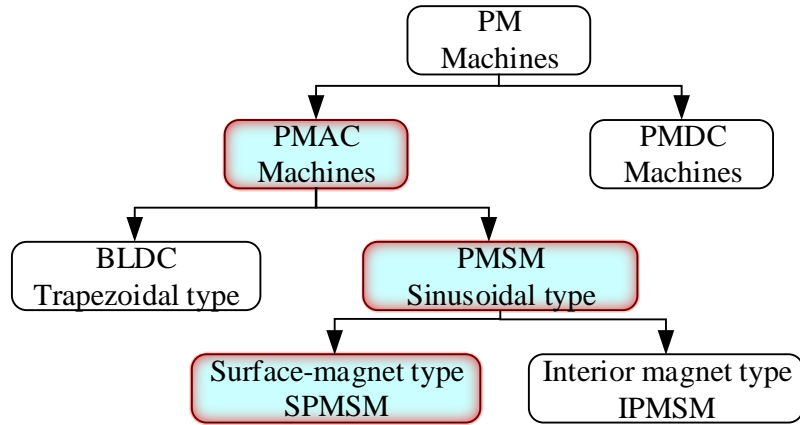


Fig. 1.1 Classification of different types of PM machines.

TABLE 1.1 DIFFERENCES BETWEEN PMSM AND BLDC MACHINES

	PMSMs	BLDCs
Flux density (in space)	Sinusoidal distribution	Square distribution
Back EMF	Sinusoidal waveform	Trapezoidal waveform
Stator current	Sinusoidal waveform	Square waveform
Electromagnetic Torque	Constant	Almost constant
Energized phases	3-phases on at any time	2-phases on at any time

PM machines can be classified into two groups: PMDC machines and PMAC machines as shown in Fig. 1.1 [3]. The construction of PMDC machines is similar to that of DC machines with commutators. The only difference is that the PM replaces the field winding. For PMAC machines, the field is generated by the PMs located on the rotor while the brushes and the commutators are no longer required. Therefore, the machine structure is simpler and more attractive when compared to PMDC machines. Depending on the shape of the back electromotive force (EMF) waveform, PM machines can be further classified into two types: a trapezoidal type called ‘brushless DC machines’ (BLDCs), and a sinusoidal type called ‘PM synchronous machines’ (PMSMs) or brushless AC machines (BLACs), as shown in Fig. 1.1.

Essentially, PM brushless DC and AC machines are similar, with laminated stators housing the phase windings and multi-pole PM rotors. The main difference lies in the shape of the back-EMF and the control technique. BLDC machines induce trapezoidal back-EMF voltage waveform in each stator phase winding during rotation, while brushless PMAC have sinusoidal back-EMF [3]. Table 1.1 summarises the main differences between PMAC and BLDC machines.

Depending on the stator and rotor configurations, PMSMs can be divided into two main groups with respect to how the magnets are mounted on the rotor [5], [6]:

- Surface-mounted PMSMs (SPMSM): In this type of machine, the PMs are mounted on the surface of the rotor, as shown in Fig. 1.2 (a). The magnets can be regarded as air space to the armature field because the permeability of the magnets is close to unity ($\mu_r=1$). Thus, this kind of rotor can be considered as a non-saliency machine, and therefore, the inductances in the quadrature coordinates, i.e., dq -axis, are approximately equal ($L_d=L_q$). The electromagnetic torque in a SPMSM is not produced by rotor saliency and can be considered only as the interaction between the stator phase currents and their relevant stator flux linkages [7].
- Interior magnet PMSMs (IPMSM): For this type of machines, the PMs are buried inside the rotor lamination, as shown in Fig. 1.2 (b). IPMSMs can be considered as a salient pole machine with different dq -axis inductances ($L_d < L_q$), since the permeability of the PM materials is lower than that of the rotor's iron core. These machines have some drawbacks such as less structural integrity and mechanical robustness. The electromagnetic torque produced in IPMSMs is similar to that of SPMSM with the addition of the reluctance torque component associated with rotor saliency features.

Theoretically, to achieve smooth torque and flux linkage with low ripples, both waveforms of the EMFs and the phase currents regulated by the drive system need to be purely sinusoidal and symmetrical [5], [8]. Regardless of the rotor configuration, the fundamental principle of motor drive is the same, and the differences are only in some particularities. In practice, for driving a three-phase PMSM, a three-phase six switch voltage source inverter, as well as a suitable control strategy, are required. Recently, various control strategies were proposed for induction machine drives. These can be extended for PMSMs and can be categorised into two broad groups: scalar and vector controls, Fig. 1.3.

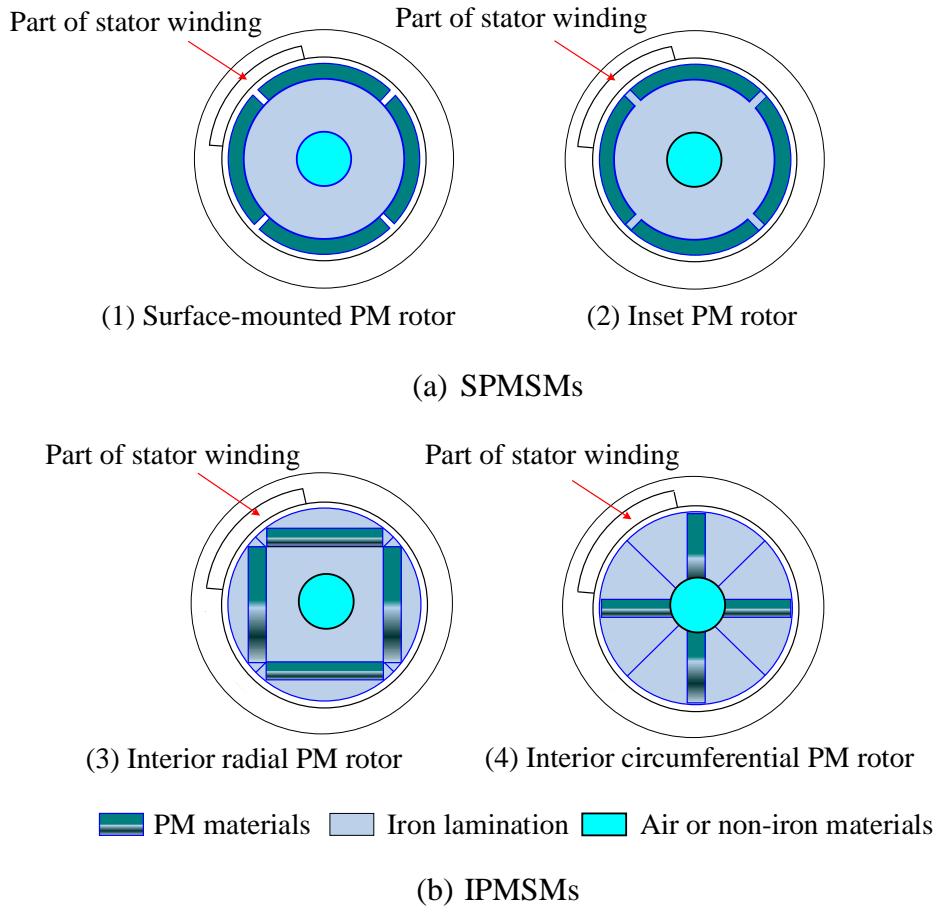


Fig. 1.2 Cross section of PMSM shows the rotor shaft and PM placement.

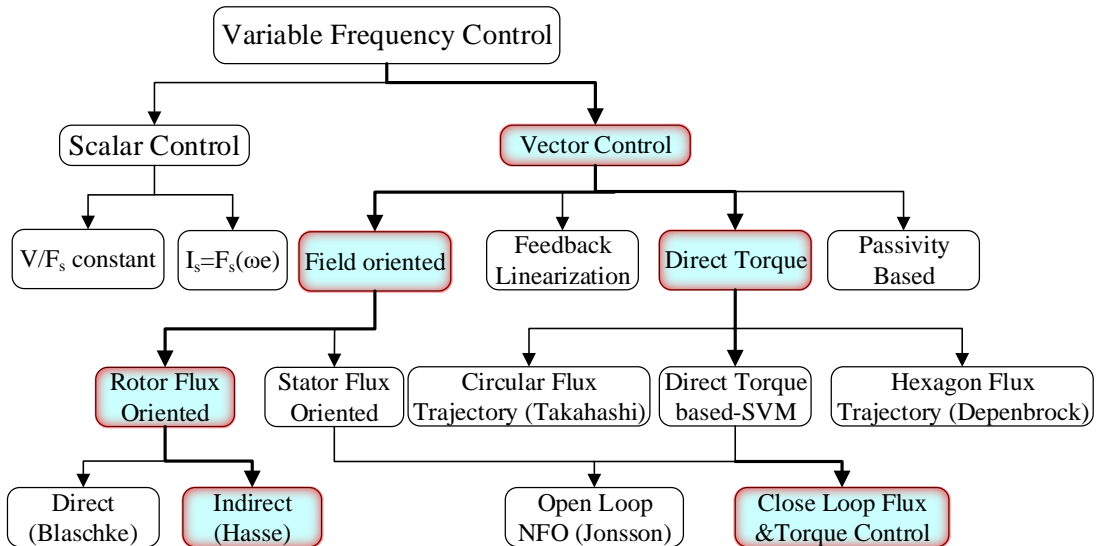


Fig. 1.3 General classification of PMSM control strategies [9].

For scalar control strategies, the magnitude and frequency (angular speed) of voltage, current, and flux linkage space vectors are controlled. While this is simple to implement, there is a restriction for use in high-performance applications. These

strategies, however, are still commonly employed in many industrial applications, for instance, in the constant voltage/frequency ($V/Hz=const.$) strategy. On the other hand, in vector control strategies, not only are the magnitude and frequency of the space vectors of voltage, current, and flux linkage controlled, as in scalar strategies but instantaneous vector positions are also controlled. These techniques and their subdivisions can be summarised in the general flow chart shown in Fig. 1.3 [9], [10].

1.2. Control Strategies of Balanced PMSM Drives

Vector control strategies for PMSM drives are used extensively for industry applications, in particular in servo motor drives, in which constant torque operation is desired. In traction and spindle drives, constant power (field weakening) operation is also desired. The vector control of PMSMs is very similar to that of induction machine drives. It is based on the relationships and expressions of space vectors in a dynamic state. In this manner, the vector control gives the exact orientation of the vectors at each moment (steady and transient states). This control strategy provides better performance than the scalar control method, but it is more complicated and expensive. It is, also, still the most common control strategy. There are different criteria to classify the vector control strategies as shown in Fig. 1.3 [9].

Amongst these strategies, the most popular methods are indirect torque control (also known as field oriented control (FOC)) [11], [12], and direct torque control (DTC) [13], [14], which will be discussed below.

1.2.1. Indirect torque control

Indirect torque control strategy (or FOC) is one of the most popular linear control strategies for induction machines. It was firstly presented more than 45 years ago in the early 1970s in Germany by F. Blaschke [11]. It was further developed in the 1980s to meet the challenges of oscillating flux and torque responses in the inverter-fed synchronous and induction motor drives [2].

In FOC, the stator flux linkage and electromagnetic torque are indirectly and independently controlled as those of separately excited DC machines. It is usually implemented in a single rotational (dq) synchronous reference frame (single-SRF), with two closed-loop current controllers required. Hence, the control of d -axis current component is contributed to the magnetising component only, while the regulation of

the q -axis current is solely associated with torque production [11]. Usually, these controllers are the conventional proportional integrator (PI) regulators, due to their low steady-state error and fast dynamic response. The current reference, however, should be constant or slowly varying. Nevertheless, applying the conventional PI-regulators to control the AC components associated with the constant value is not straightforward (as will be discussed later in this thesis). For a three-phase system, with i_a , i_b , and i_c being the currents in each of the phases, the Clark-Park transformation is necessary to meet the main concept of FOC (see Appendix A) [15], then the current in the stationary frame can be expressed as

$$\begin{bmatrix} i_\alpha \\ i_\beta \end{bmatrix} = \frac{2}{3} \underbrace{\begin{bmatrix} 1 & -\frac{1}{2} & -\frac{1}{2} \\ 0 & \frac{\sqrt{3}}{2} & -\frac{\sqrt{3}}{2} \end{bmatrix}}_{CLARK} \cdot \begin{bmatrix} i_a \\ i_b \\ i_c \end{bmatrix} \quad (1.1)$$

where i_α and i_β are current in the stationary $\alpha\beta$ reference frame, Fig. 1.4 [15]. These two variables (and also $i_{\alpha\beta} = i_\alpha + ji_\beta$) include all the information about the positive- and negative-sequence components of the three-phase currents i_{abc} . These currents still have alternating values so can be used to control the three-phase current i_{abc} using only two controllers. Furthermore, the Park transformation is often employed to obtain direct values from the alternating three-phase currents [16]

$$\begin{bmatrix} i_d \\ i_q \end{bmatrix} = \frac{2}{3} \underbrace{\begin{bmatrix} \cos(\theta_r) & \cos\left(\theta_r - \frac{2\pi}{3}\right) & \cos\left(\theta_r + \frac{2\pi}{3}\right) \\ \cos(\theta_r) & \sin\left(\theta_r - \frac{2\pi}{3}\right) & \sin\left(\theta_r + \frac{2\pi}{3}\right) \end{bmatrix}}_{PARK} \begin{bmatrix} i_a \\ i_b \\ i_c \end{bmatrix} \quad (1.2)$$

where $\theta_r = \omega_r t$ is the instantaneous phase angle at the instant of t and ω_r is the fundamental synchronous frequency [16].

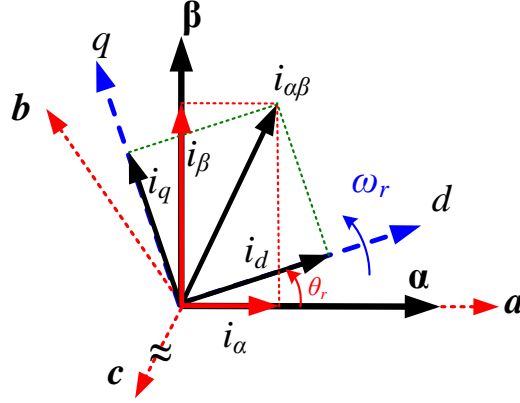


Fig. 1.4 Spatial relationships among machine coordinate.

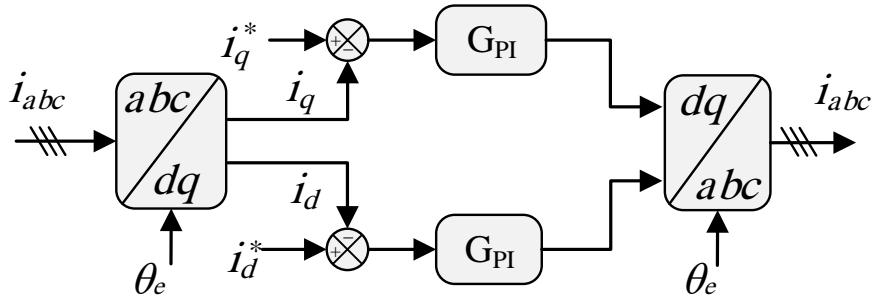


Fig. 1.5 Schematic diagram of field orientated control strategy [17].

The currents i_d and i_q are the projection of i_{abc} represented onto two perpendicular axes rotating with an angular speed of ω_r . This rotating frame is associated with the Park transformation and synchronised with the rotor phase angle is known as the synchronous reference frame (SRF). These currents have a DC value in the SRF and can be expressed as $i_{dq} = i_d + j i_q$ while they are alternating at the frequency of ω_r in the stationary $\alpha\beta$ reference frame. Fig. 1.4 illustrates the relationship between the stationary and synchronous reference frames.

Moreover, by using transformations (see Appendix A) the current in the stationary and synchronous frames can be represented by the following expressions:

$$i_{\alpha\beta} = i_{dq} e^{j\omega_r t} = i_{dq} [\cos(\omega_r t) + j \sin(\omega_r t)] \quad (1.3)$$

$$i_{dq} = i_{\alpha\beta} e^{-j\omega_r t} = i_{\alpha\beta} [\cos(\omega_r t) - j \sin(\omega_r t)]. \quad (1.4)$$

Fig. 1.5 shows a schematic diagram of the FOC based on the single-SRF. Furthermore, several operating modes for both SPMSM and IPMSM can be achieved by accordingly controlling both d - and q -axis current components. These are:

1.2.1.1. Constant torque angle (CTA)

For a simple control strategy, some implication has to be taken into consideration regarding the produced torque. The load torque can be controlled by maintaining the torque angle δ (which is the angle between the stator current vector and the rotor permanent magnet flux) at a constant value of 90° , Fig. 1.6.

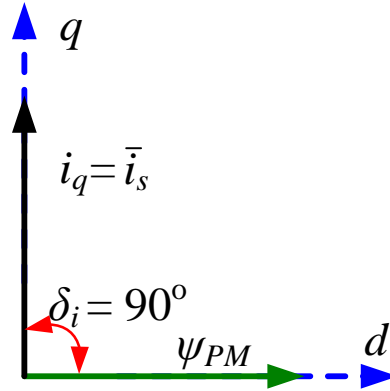


Fig. 1.6 Vector diagram of constant torque per ampere control under steady state.

This control strategy can be implemented by controlling the d -axis current component to be zero, while the current vector is aligned with the q -axis to maintain the torque angle equal to 90° . This strategy is hence also known as $i_d=0$ control, which is one of the most commonly used strategies due to its simplicity. The rotor PM flux vector amplitude and the torque angle are constant. This method is commonly used especially for SPMSM, while not preferred for IPMSM due to the existence of the rotor saliency. The change in the produced torque thus only depends on the stator's current amplitude.

1.2.1.2. Maximum torque per ampere (MTPA)

The main target of this strategy is to keep the stator current as small as possible for a given electromagnetic torque. In this manner, the maximum torque per ampere (MTPA) can be achieved. The i_d component, however, is not equal to zero and may cancel some reluctance torque produced by high saliency ratios, Fig. 1.7. It is therefore recommended for IPMSMs, since both the electromagnetic and the reluctance torques are taken into consideration. For SPMSMs, this strategy is similar to CTA control strategy, [18], [19].

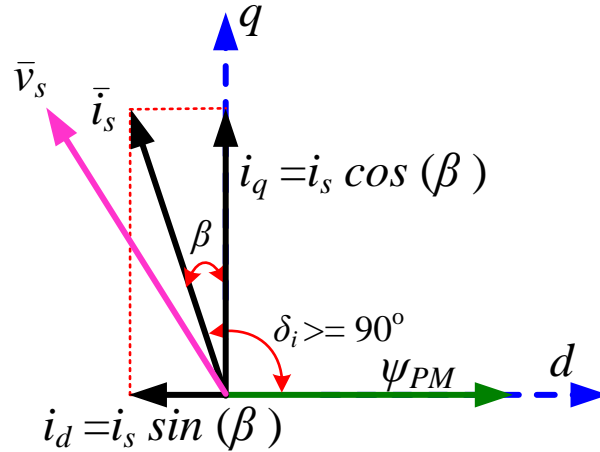


Fig. 1.7 Current and PM flux vectors under maximum torque per ampere operation.

1.2.1.3. Unity power factor (UPF)

The advantage of this control strategy is that the phase shift between the current and voltage vectors is zero, which reduces the power consumed by the machine as shown in Fig. 1.8. When the power factor angle becomes zero under this control strategy, only active power is therefore supplied to the machine under this strategy [19], [20].

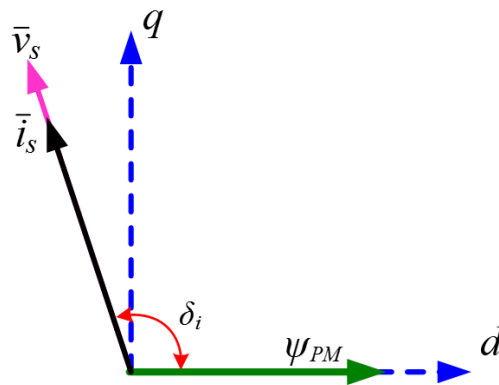


Fig. 1.8 Current and PM flux vectors under unity power factor (UPFC).

1.2.1.4. Constant stator flux (CSF)

In this case, the stator flux linkage magnitude is kept constant with an amplitude of the PM flux $|\psi_s| = \psi_{PM}$ as shown in Fig. 1.9. To achieve this mode, the d -axis current must be less than zero, $i_d < 0$. The power factor in this control scheme is close to unity and the current required for achieving torque up to 1.1 per unit is the lowest compared with other control modes [19], [21].

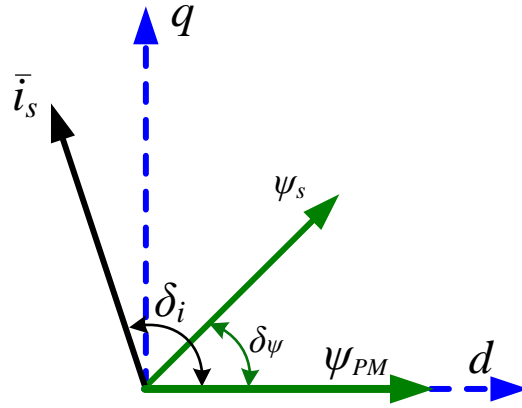


Fig. 1.9 Current and PM flux vectors under constant stator flux control strategy.

1.2.2. Direct torque control (DTC)

Nearly 20 years after introducing FOC, direct self-control (DSC) and direct torque control (DTC) strategies were first presented for induction machines in Japan by Takahashi [13] and in Germany by Depenbrock [22], [23], [24]. These methods rely on ‘bang-bang control’ instead of decoupling control, which is the idea of FOC. They are capable of faster torque responses and better dynamic performance than the conventional FOC [13]. Despite the difference between IMs and PMSMs in magnetisation, the application of DTC strategy was extended to PMSMs. In the late 1990s, the conventional DTC technique for IPMSM was introduced in [14], [25], [26]. Recently, investigation of DTC strategy was further extended for BLDC drives as reported in [27], [28].

The main operating principle of DTC strategy is based on controlling the electromagnetic torque and the stator flux linkage directly and independently in the stationary reference frame by appropriately selecting one of the eight voltage vectors and then controlling the flux and torque of the selected vector. Fig. 1.10 shows the eight voltage vectors of the power source inverter output [13]. These vectors express the output of the three-phase voltage source inverter. Depending on the inverters’ six switching states (On or OFF), six of these eight vectors can be active with the maximum magnitude of $2/3V_{dc}$, and the other two vectors have zero magnitudes [29]. The switching states applied to the inverter are selected from a predefined optimum switching look-up table (LUT) to minimise the instantaneous torque and stator flux magnitude error [13].

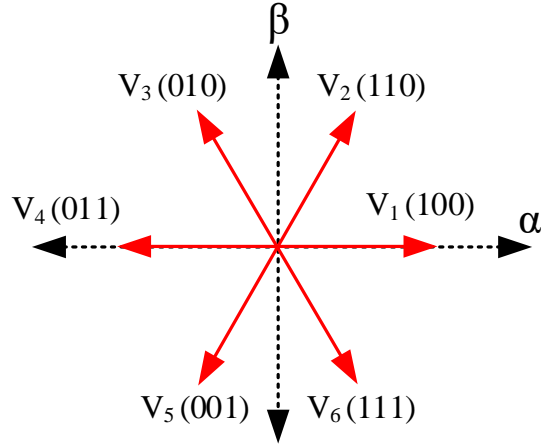


Fig. 1.10 Possible voltage space vector in voltage source inverter.

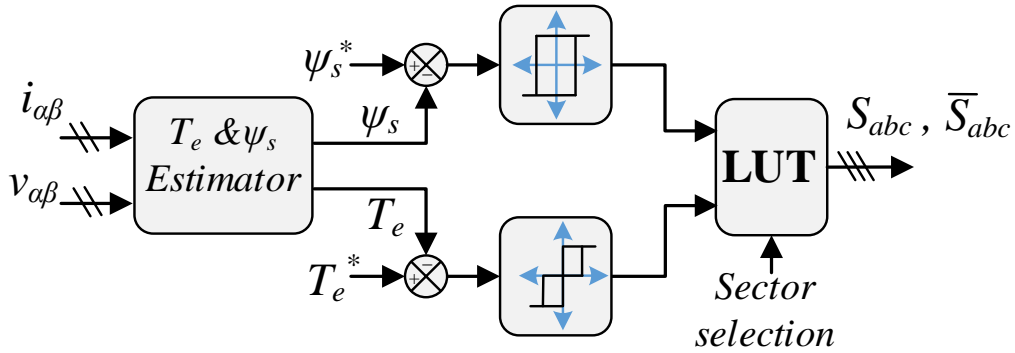


Fig. 1.11 Block diagram of hysteresis DTC.

Typical hysteresis DTC employs two hysteresis comparators, which are used for comparing the reference torque and flux with their actual values calculated by the machines' model, Fig. 1.11. One of them is a three-level-hysteresis comparator for torque error correction, and the other is a two-level-hysteresis comparator for flux-linkage error correction. Fig. 1.11 shows the block diagram of the hysteresis based DTC of PMSM [26]. In [13], the application of DTC for IM was introduced, both zero and non-zero voltage vectors were employed for the optimum switching LUT. An optimum switching LUT, however, without the zero voltage vector, was proposed in [14], [30]. This scheme is based on the idea that the zero voltage vectors cannot keep the stator flux linkage vector at its original position as the PMs placed in a rotating rotor [14], [31].

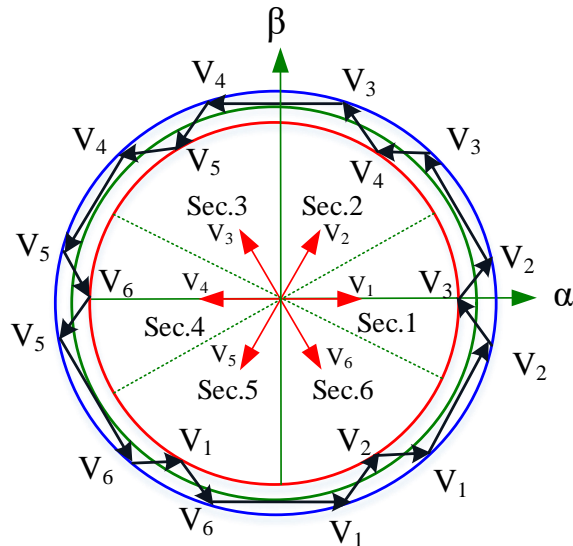


Fig. 1.12 Circular trajectory of stator flux linkage in stationary $\alpha\beta$ -reference frame.

Zero voltage vectors can be presented in the optimum LUT without causing any problems, because these vectors are only employed when the electromagnetic torque is inside its hysteresis band [32], [33]. By using hysteresis comparators, the magnitude of the stator flux is usually kept constant by making the stator flux rotate in a circular trajectory along the reference path for sinusoidal AC machines as shown in Fig. 1.12. While the hysteresis torque controller tries to keep the motor torque within a pre-defined hysteresis band [34]. Hysteresis DTC strategy has a lot of advantages and disadvantages, which can be summarised as follows [9], [35], [36]:

Advantages:

- Simple, and independence of machine parameters except the stator resistance, which is involved in stator flux estimation.
- The processing time is less than other methods like PWM modulator used in FOC.
- Direct control of the torque and stator flux linkage in the stator frame. Therefore, it does not require the vector coordinate transformation and the inner current loop, which provides a better dynamic response.

Disadvantages:

- A three-phase inverter is modulated directly, thus the switching state of the power devices remains constant until the output state of each hysteresis controller changes, which leads to serious torque and stator flux ripples in the

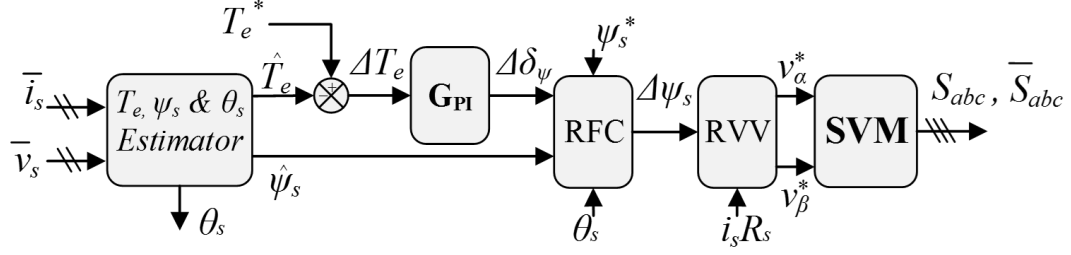
conduction region due to the small conductance. Although increasing the modulation frequency can reduce degradation in performance, it is still limited by the processor speed.

- The switching frequency changes with motor speed, load torque, and the bandwidth setting of the two hysteresis comparators.

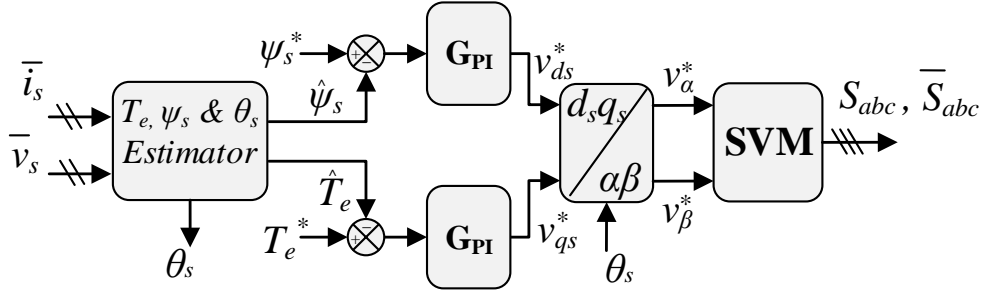
To mitigate the inherent drawback of hysteresis DTC, numerous control strategies have been proposed in literature [14], [37], [38], [39], [40]. The most common way is direct torque control, based on space vector modulation (DTC-SVM) strategies, which are usually implemented by replacing the hysteresis comparators and switching table with PI-regulators and SVM. Several benefits can be realised through using DTC-SVM strategies compared with the conventional hysteresis DTC strategy, such as constant switching frequency and low torque and stator flux ripples. Essentially, the DTC-SVM can be implemented by utilising either one PI-regulator (cascaded) DTC-SVM [37], [38], [39], [40], [41], or two PI-regulators (parallel) DTC-SVM [42], [43], [44], [45]. Both schemes aim to generate the reference voltage vector (RVV) from the torque and stator flux linkage errors, followed by using calculations to operate the voltage source inverter (VSI) via SVM algorithm [46].

Different SVM algorithms have been presented, such as right aligned sequence, symmetrical sequence, alternating zero vector sequence, and highest current non-switched sequence [47], [48]. Symmetrical sequence SVM has been employed in this thesis since it produces a lower total harmonic distortion (THD) [48]. Further discussions about SVM will be presented in Chapter 2.

In the cascaded DTC-SVM, the PI-regulator is placed in the closed-loop torque controller. The outputs of the PI-regulator represent the variation of the torque angle ($\Delta\delta_\psi$). According to this variation, the error in the stator flux vector $\Delta\psi_s$ can be predicted by comparing the current with the previous values. Afterwards, the final RVV can be calculated [37], [49] as shown in Fig. 1.13 (a) [37], [38], [39], [40], [41].



(a) Cascaded structure DTC-SVM



(b) Parallel DTC-SVM

Fig. 1.13 Direct torque control using SVM.

For parallel DTC-SVM on the other hand, the outputs of the PI-controllers in the torque and flux loops are interpreted as a reference stator voltage component in the stator flux ($d_s q_s$) reference frame. These voltages are then transformed into the stationary reference frame using stator flux position angle θ_s to generate the final RVV as shown in Fig. 1.13 (b) [50]. Besides, the PI-regulators in torque and flux loops can be further eliminated if model predictive/dead-beat control strategies are used. These types of DTC-SVM strategies, however, suffer from excessive calculations, they are time-consuming and dependent on machine parameters [51], [52].

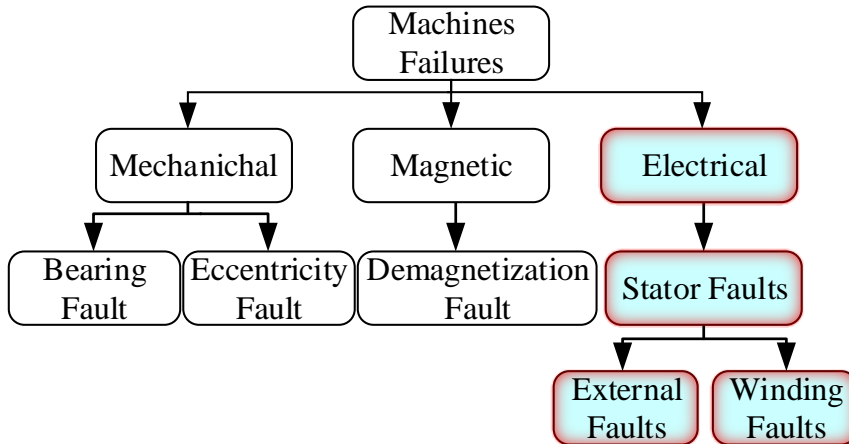


Fig. 1.14 Electrical machine fault classification.

1.3. Control Strategies of Unbalanced PMSM Drives

In reality, systems being unbalanced and distorted are quite common in electric drives and wind power generators. Imbalance and distortion can occur due to failures or some variances, which cause many abnormal operation conditions. These failures and/or variances can be classified into three broad groups: mechanical, electrical, and magnetic problems, Fig. 1.14, which can be further summarised as follows [4], [8]:

- Stator winding open or short circuit fault;
- Static or/and dynamic air-gap irregularities (rotor eccentricity);
- Gearbox and bearing failures;
- Defects of the permanent magnets of PM motors;
- Unbalanced load conditions.

The above conditions have a direct influence on the machine's normal operation and produces several symptoms, such as torque ripple, unbalanced phase current, acoustic noise, vibration, speed pulsations, decreased efficiency and average torque, excessive heating, and increased iron and copper losses. To mitigate the torque and flux ripples, two major groups of techniques have therefore been proposed. In the first group, torque ripple was minimised using machine design optimisation features, such as magnet sizing, distributed windings, and/or stator/rotor skewing, to reduce the cogging torque and harmonics in the induced electromotive force (EMF) [53], [54].

Despite these design techniques providing a valuable solution in terms of reducing torque ripples, they are unable to achieve the same performance under different operating conditions. Moreover, they impose additional manufacturing costs and reduce their efficiency. The second group, on the other hand, which is within the scope of this thesis, involves using techniques that are concentrated on control strategies, which will be discussed and categorised in the following sections.

1.3.1. Hysteresis control

As mentioned previously, hysteresis controllers are often employed for both indirect (current control) [55] and direct torque control under both symmetrical [13], [14] and asymmetric conditions [56]. They can be used effectively for tracking both DC and AC reference values. A simple hysteresis comparator is a two-level fixed-band hysteresis controller (as in stator flux control loop), or a three-level fixed-band

hysteresis controller (as in torque control loop) (see section §1.2.2). The modified band hysteresis controller is more advanced. This controller can minimise torque/current ripples and either limit the switching frequency or fix it, which makes the machine performance very similar to that of a PWM [57], [58]. Hysteresis controllers are also used for direct power control under unbalanced conditions.

1.3.2. Repetitive control

Repetitive current control is often employed to compensate for torque ripple in the synchronous reference frame [59]. It is based on the internal compensation model to achieve perfect tracking and for rejecting arbitrary periodic signals in a fixed period and provide zero steady-state errors for the given reference signal [60].

It has some similarities with iterative learning control [61]. It can be implemented via adapting a digital model, as it is able to generate the required periodic signals. These generated signals could be either based on discrete Fourier transformation or feedback included in the closed-loop controller [62].

1.3.3. Deadbeat control

The deadbeat control is a linear control strategy originating from the family of predictive controllers [10] as shown in Fig. 1.15. It is currently widely used in many applications [63], [64]. It is based on the common principle of discrete-time implementation to predict the required input signal (current, for example) to obtain the desired output signals. Using this prediction, it can select the switching state of the converter (ON/OFF) [65], or the output voltage vector produced by the converter (predictive control with pulse width modulator) [66]. The design of the dead-beat is assumed to minimise the number of possible computations (and thus delay) at all frequencies. It can provide zero steady-state errors after two cycles. The first cycle is consumed in the computation process, while the next cycle is for modulation and other delays such as filters and inverter dead time [67], [68]. When the deadbeat controller is well tuned, it can thus achieve the fastest transient response of all digital current control systems [59], [69], [70]. Fig. 1.16 (a) shows an equivalent diagram of a three-phase system represented in single-phase.

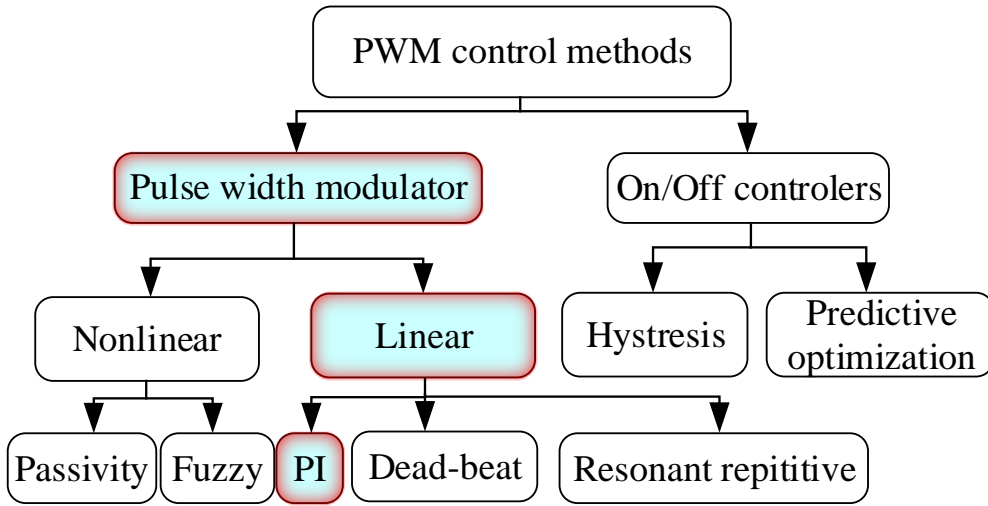


Fig. 1.15 Control method classification.

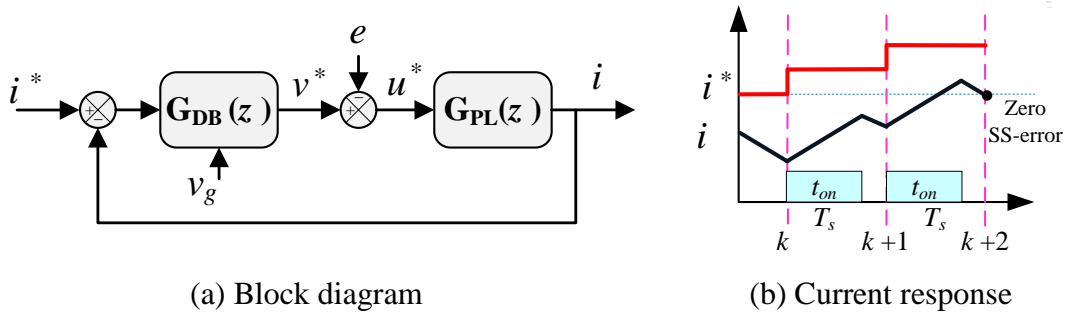


Fig. 1.16 Principle of deadbeat control.

The plant transfer function (TF) is simply an RL circuit. Then, the input voltage to the plant $u(t)$ can be represented in time-domain as:

$$u(t) = L \frac{di(t)}{dt} + Ri(t) \quad (1.5)$$

$$L \frac{di(t)}{dt} = -Ri(t) + u(t) \quad (1.6)$$

$$\frac{di(t)}{dt} = \frac{R}{L}i(t) - \frac{1}{L}u(t) \quad (1.7)$$

where $u(t)=[v(t)-e(t)]$ is the input voltage to the plant, $v(t)$ is the inverter voltage, $e(t)$ the disturbance voltage, $i(t)$ is the current, and R, L are the plant resistance and inductance, respectively. Assuming the delay due to computation is $e^{-\frac{R}{L}T_s}$, which can be substituted by z^{-1} and the PWM replaced by zero-order hold (ZOH), then expression (1.5) can be written as:

$$i(k+1) = e^{-(R/L)T_s} i(t) - \frac{1}{R} (e^{-(R/L)T_s} - 1) u(t) \quad (1.8)$$

$$i(k+1) = ai(t) - bu(t) \quad (1.9)$$

where $a = e^{-\frac{R}{L}T_s}$, $b = -\frac{1}{R}(e^{-\frac{R}{L}T_s} + 1)$, and T_s is the sampling time. Then, using the z -transformation, the following expression can be derived as:

$$I(z)z = aI(z) + bU(z) \quad (1.10)$$

and

$$I(z) = \frac{b}{z-a} U(z) = \frac{bz^{-1}}{1-az^{-1}} U(z) \quad (1.11)$$

Then, the plant TF in discrete time domain is:

$$G_{PL}(z) = \frac{I(z)}{U(z)} = \frac{bz^{-1}}{1-az^{-1}} \quad (1.12)$$

The system closed-loop TF can be driven as:

$$G_{sys,CL}(z) = \frac{G_{DB}(z)G_{PL}(z)}{1-G_{DB}(z)G_{PL}(z)} \quad (1.13)$$

In the deadbeat control, it is assumed that the closed-loop system TF has the lowest possible delay, which is $G_{sys,OL}(z) = z^{-k}$, where k is the lowest possible delay in the closed-loop control system. As mentioned previously, in deadbeat control, Fig. 1.16, the actual current can track the reference current and provide zero steady state errors at the end of two sampling periods, hence $k=2$. Then, the closed-loop system TF can be written as:

$$G_{sys,OL}(z) = \frac{z^{-2}}{1-z^{-2}} \quad (1.14)$$

Then, the resulting TF of the deadbeat controller is:

$$G_{DB}(z) = \frac{1}{G_{PL}(z)} \frac{z^{-2}}{1-z^{-2}} = \frac{1}{b} \frac{1-az^{-1}}{z-z^{-1}} \quad (1.15)$$

The main drawbacks of deadbeat control technique can be summarised by:

- High sensitivity to parameter variation from their estimated values, which generate tracking errors and stability problems.

- Very sensitive to measurement errors caused by transducers or scaling.
- Unable to achieve zero steady-state errors at non-zero frequencies (it is not preferable to use for AC components, although it is possible).
- Dead-time compensation is required.
- Two samples delay is always present.

To overcome these disadvantages, several improvements have been proposed in literature [67], [69]. Most of them are based on adding observers to compensate for the delay caused by computation and plant nonlinearity to reduce the controller's sensitivity to parameter variation and mismatches. These schemes usually increase the drive's complexity, which may not be necessary for applications in which a fast dynamic response is not required [67], [69], [71].

1.3.4. Double synchronous reference frame controller (DSRFs)

As discussed in section §1.2.1, the current can be easily controlled in single SRF, since the measured AC components and/or voltages of the proper sequence are transformed into their relevant DC quantities in the SRF using Park's transformation [16]. As long as the DC quantities are involved, the classical control technique using a PI controller can be implemented to achieve the desired performance. On the other hand, under unbalanced conditions, the electrical variables of voltage and current can be deconstructed into their positive, negative, and zero sequence components. They may thus require a unique control strategy. In general, the most common way to control current/voltage vectors is by using two synchronous reference frames, or so-called 'double synchronous reference frame' (DSRF) controllers [72], [73], [74]. Both SRFs rotate at the fundamental frequency in both positive and negative sequence directions. They therefore provide the perfect solution to control the positive- and negative-sequence current components, both individually and simultaneously.

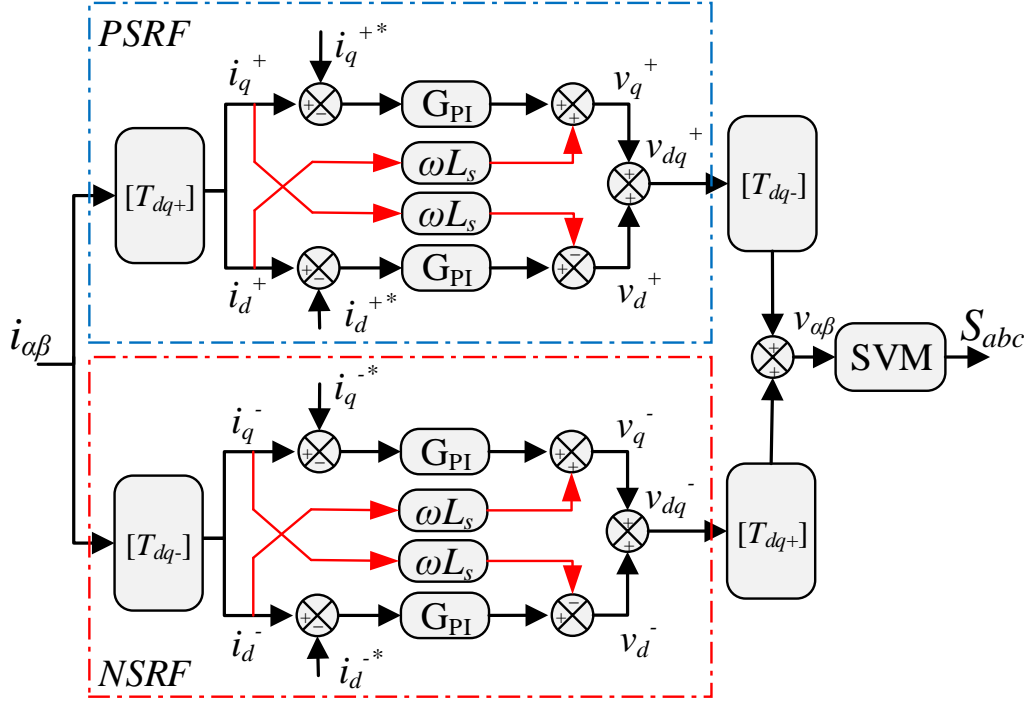


Fig. 1.17 Double synchronous reference frame controllers.

In practice, DSRF strategy is widely employed for phase-locked-loop and grid voltage synchronisation under unbalanced conditions [75], [76]. It uses a pair of PI-controllers in each of the positive and negative SRFs, as shown in Fig. 1.17. For most standard DSRF control strategies, the measured unbalanced three-phase currents are transformed into both positive and negative rotating SRFs using Park's transformation:

$$i_{dq}^+ = i_{dq+}^+ + i_{dq-}^- e^{-j2\omega_r t}, \quad \begin{bmatrix} i_d^+ \\ i_q^+ \end{bmatrix} = \underbrace{\begin{bmatrix} i_{d+}^+ \\ i_{q+}^+ \end{bmatrix}}_{DC \text{ terms}} + \underbrace{\begin{bmatrix} i_{d-}^- \cos(2\theta_r^+) + i_{q-}^- \sin(2\theta_r^+) \\ -i_{d-}^- \sin(2\theta_r^+) + i_{q-}^- \cos(2\theta_r^+) \end{bmatrix}}_{AC \text{ terms}} \quad (1.16a)$$

$$i_{dq}^- = i_{dq-}^- + i_{dq+}^+ e^{j2\omega_r t}, \quad \begin{bmatrix} i_d^- \\ i_q^- \end{bmatrix} = \underbrace{\begin{bmatrix} i_{d-}^- \\ i_{q-}^- \end{bmatrix}}_{DC \text{ terms}} + \underbrace{\begin{bmatrix} i_{d+}^+ \cos(2\theta_r^-) + i_{q+}^+ \sin(2\theta_r^-) \\ -i_{d+}^+ \sin(2\theta_r^-) + i_{q+}^+ \cos(2\theta_r^-) \end{bmatrix}}_{AC \text{ terms}} \quad (1.16b)$$

where $\theta_r^+ = \omega_r t$ and $\theta_r^- = -\omega_r t$, in (1.16). The currents in the positive and negative SRFs are not pure DC due to the cross-coupling effect between both SRFs, which appears as oscillation at twice the fundamental frequency $2\omega_r$ overlapped with the DC quantities in both SRFs [72], [76]. The amplitude of the oscillations in one of the SRFs matches the DC amplitude of the other and vice versa. Moreover, when the tracking references have DC values, these oscillations will appear in the resulting error signals at the input

of the PI controllers, which cannot be avoided by using a conventional PI controller due to its limited bandwidth [77]. They hence give rise to steady-state errors and increase the torque ripple. To achieve full control of the injected currents under unbalanced conditions, these $2\omega_r$ oscillations in both SRFs must be cancelled out. Many solutions oriented to overcome this issue have hence been presented, which will briefly be discussed in the following section, for example filtering the measured feedback currents to obtain a pure DC value by employing the low pass filter (LPF) or notch filter [72], [78], [79].

1.3.4.1. DSRF controller based on adaptive filter (AF)

The most straightforward solution to attenuate the effects of the $2\omega_r$ oscillations consists of filtering the measured currents by using the adaptive notch filter (ANF), tuned at twice the fundamental frequency $2\omega_r$, as shown in Fig. 1.18 [72]. The output of the ANF is the measured currents without $2\omega_r$ frequency. The error signal at the input of the PI controller will therefore be free from oscillation. The main drawbacks of the ANF, however, include unavoidable dynamic response delays, which reduce the phase margin of the system. These obstacles can be solved by increasing the damping factor of the ANF, but at the expense of the system's stability.

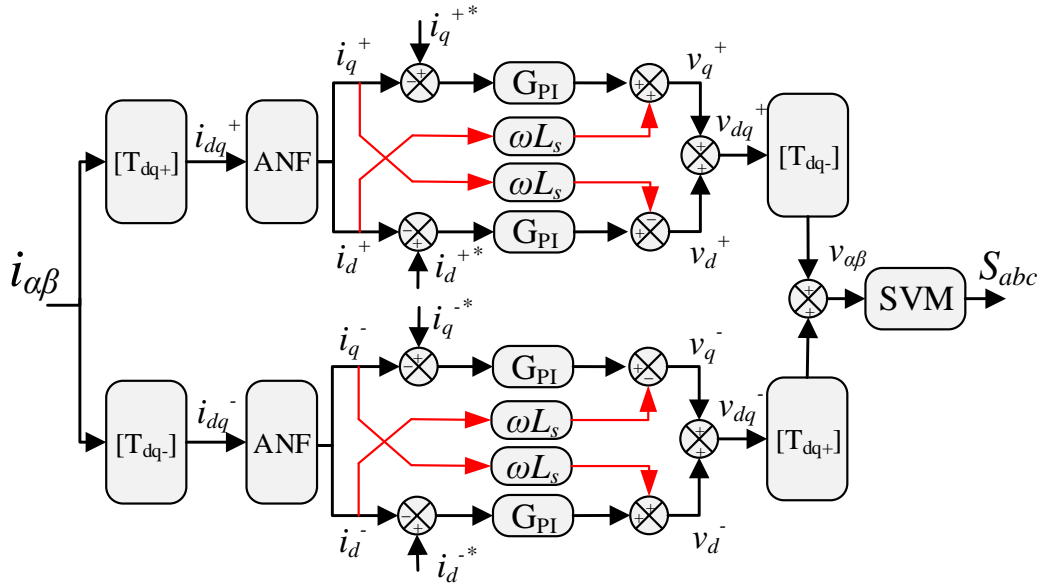


Fig. 1.18 Oscillation cancellations in DSRFs controller using ANF [72].

Moreover, a very low damping factor will increase the filter selectivity of the particular frequency, which may cause a problem when the system frequency deviates.

Using an adaptive notch filter may thus reduce these issues and cancel out the $2\omega_r$ oscillations under variable frequency [78].

1.3.4.2. Decoupled DSRF controller (DDSRF)

In the previous techniques, the effect of the $2\omega_r$ oscillation resulting from the cross-coupling between the reference frames and the current vectors with different sequences has been overcome by using filters or by modifying the controller. Nevertheless, the amplitude of the AC oscillations in the positive SRF is matched to the DC amplitude in the negative SRF and vice versa. Researchers have developed techniques which can compensate for these oscillations by adding a decoupling network between both SRFs [73], [76], [80]. This structure is also known as a ‘decoupled DSRF controller’ (DDSRF). It can be implemented by estimating the decoupling terms (DC terms) of each SRF by using a low-pass filter [73], [76], and then using a cross-coupling network to re-inject them into the opposite sequence frame after converting them to AC at the frequency of $2\omega_r$. The AC oscillation in the measured currents of both positive and negative SRFs is hence cancelled out. An excellent DC-reference current tracking can thus be achieved, which results in error signals free of oscillations at the input of the PI controllers, as proposed in [73], [80], [81], [82].

Conversely, when there is a mismatch between the DC reference currents and the DC measured currents in the synchronous reference frames, the instantaneous errors generated between the reference and the measured currents at the input of the PI controllers will have oscillations. It would therefore not be possible to achieve full control of the oscillations in the measured currents.

A modified DDSRF is proposed in [76], in which the values of the cross-coupling terms indicated in (1.16) are obtained from the reference currents and the resulting error signals by using a first-order low-pass filter as shown in Fig. 1.19. The output signal of these filters can thus be used to compensate for the errors generated by the feed-forward loops in the cancellation of the 2ω oscillations. This scheme provides a better dynamic response in comparison to the one based on ANF technology as demonstrated in [79].

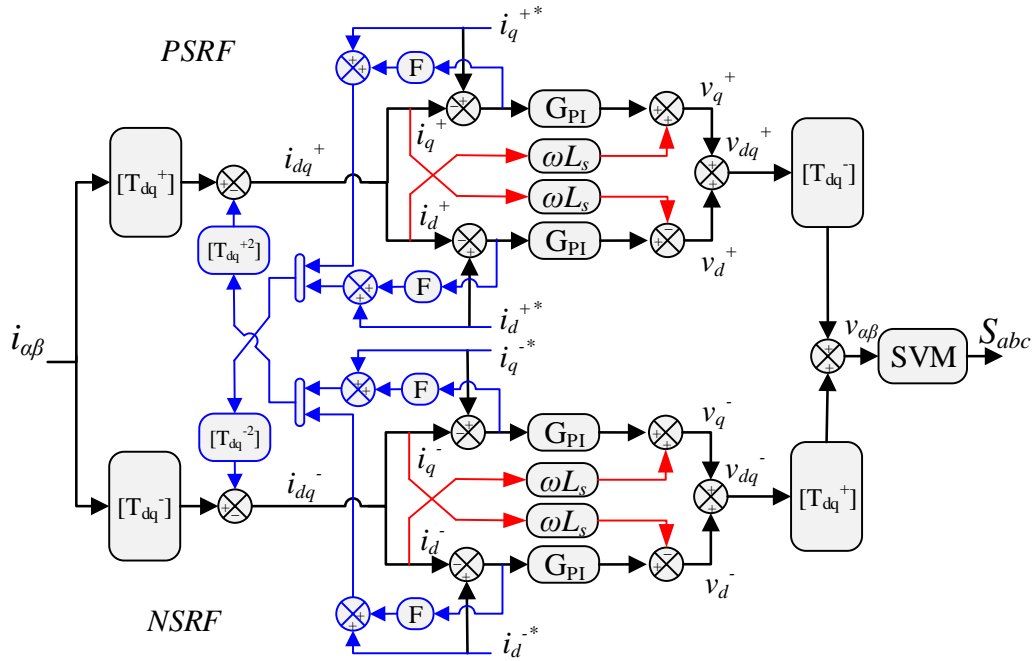


Fig. 1.19 Decoupled DSRF controller [73].

Apart from the above techniques to compensate for the $2\omega_r$ oscillations in the measured currents, it is also possible to achieve zero steady-state error at the input of the PI regulator by adding the oscillation terms obtained from the measured feedback currents into the tracking reference currents. This technique does not need ANF or an additional decoupling network, unlike the DDSRF strategy. The estimation of the oscillation terms is still required, however. This technique is widely employed for direct power control (DPC) under unbalanced grid connections. It does not matter if the controller schemes utilise a PI-controller [75] or hysteresis comparators [55], [56], [83], since the reference and measured values are always matched [55], [56], [75], [79], [83], [84], [85]. Furthermore, a resonant controller (as will be discussed in section §1.3.6) can be implemented to avoid any mismatches in canceling these oscillations and achieve good dynamic and steady-state performance.

1.3.5. Double second-order generalized integrator (SOGI)

Unlike the DSRF, in which the positive and negative sequence components of the unbalanced three-phase system are extracted in both SRFs. It is possible to extract them from their original unbalanced input signals in the stationary $\alpha\beta$ frame using the principle of signal delay. It is based on adding or subtracting the real-time signals and the signals delayed by a quarter of the period, which can be mathematically described as:

$$F_{\alpha+}(\omega_s) = \frac{1}{2} \left[F_{\alpha}(\omega_s) - F_{\beta}(\omega_s - \frac{\pi}{2} \omega_s) \right]$$

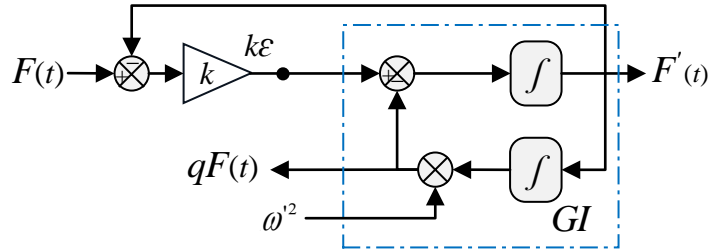
$$F_{\beta+}(\omega_s) = \frac{1}{2} \left[F_{\beta}(\omega_s) + F_{\alpha}(\omega_s - \frac{\pi}{2} \omega_s) \right].$$
(1.17a)

$$F_{\alpha-}(\omega_s) = \frac{1}{2} \left[F_{\alpha}(\omega_s) + F_{\beta}(\omega_s - \frac{\pi}{2} \omega_s) \right]$$

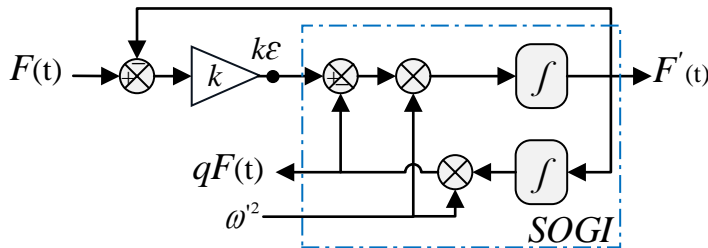
$$F_{\beta-}(\omega_s) = \frac{1}{2} \left[F_{\beta}(\omega_s) - F_{\alpha}(\omega_s - \frac{\pi}{2} \omega_s) \right].$$
(1.17b)

where the factor F could be any variables, i.e., voltage, current, and stator flux linkage, in the stationary $\alpha\beta$ frame. In (1.17), attaining a phase shift delay of 90° is an interesting target. Researchers have therefore attempted to explore the easiest and most efficient way to achieve such a delay under variable frequency, for example, adaptive filters [86] [87], generalised integrators (GI), and second order generalised integrators (SOGI) [88] [89], [90].

Fig. 1.20 (a) shows the second order adaptive filter (AF) based on the implementation of the generalised integrator (GI). This structure uses two integrators, one in the forward direction and the other in the backward direction. The transfer functions (TF) of the adaptive filter taken from different nodes can be expressed as [91]:



(a) Adaptive filter based on a GI



(b) Second-order AF based on SOGI

Fig. 1.20 A quadrature signal delay generator [91].

$$GI(s) = \frac{F'}{k\varepsilon}(s) = \frac{s}{s^2 + \omega_r'^2} \quad (1.18)$$

$$D(s) = \frac{F'}{F}(s) = \frac{ks}{s^2 + ks + \omega_r'^2} \quad (1.19)$$

$$Q(s) = \frac{qF'}{F}(s) = \frac{k\omega'^2}{s^2 + ks + \omega_r'^2} \quad (1.20)$$

The TF of GI provides an infinite gain at the resonant frequency, which cancels out any steady-state error when controlling sinusoidal signals at a particular resonant frequency. Moreover, another interesting feature of GI (also known as a resonant controller in many applications, as will be discussed in section §1.3.6), is that it generates a signal output $qF'(t)$ shifted by 90° as shown in Fig. 1.20 (a). These TFs also indicate that the bandwidth of the band-pass filter given by (1.19) and the static gain of the low-pass filter of (1.20) are not only a function of the gain k , but also depend on the fundamental frequency, ω_r' . Under variable fundamental frequency, such as variable speed, however, this issue becomes inconvenient since the controller would not be able to control the bandwidth of the filter.

To overcome this problem, a modified GI structure has been proposed, which is known as a second-order generalised integrator (SOGI) to distinguish it from the conventional GI [91]. The AF structure based on the SOGI is shown in Fig. 1.20 (b), where its TF are given as:

$$SOGI(s) = \frac{F'}{k\varepsilon}(s) = \frac{\omega' s}{s^2 + \omega_r'^2} \quad (1.21)$$

$$D(s) = \frac{F'}{F}(s) = \frac{k\omega' s}{s^2 + k\omega' s + \omega_r'^2} \quad (1.22)$$

$$Q(s) = \frac{qF'}{F}(s) = \frac{k\omega'^2}{s^2 + k\omega' s + \omega_r'^2} \quad (1.23)$$

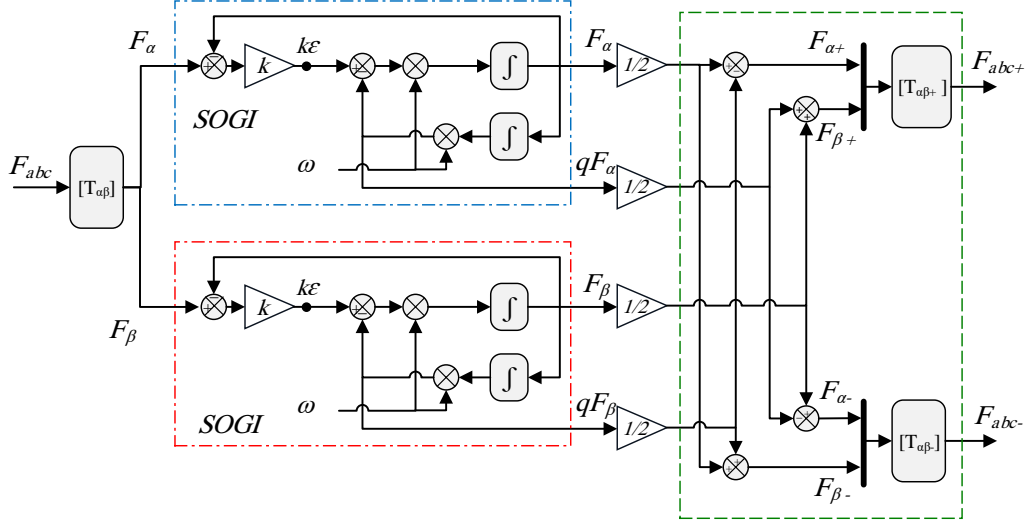


Fig. 1.21 SOGI structure for sequential component extractor.

The above TFs show that the bandwidth of the AF based SOGI is not a function of the fundamental frequency ω_r' . It only depends on the gain k , and thus it is suitable for variable frequency applications. Furthermore, the magnitude of the in-quadrature signals, F' and qF' are similar to the magnitude of the input signal F when the estimated frequency (ω_r') of the filter is the same as the input frequency (ω_r), i.e., $\omega_r' = \omega_r$. In this manner, the filter structure of SOGI shown in Fig. 1.20 (b) will be highly suitable for quadrature signal generation (QSG). Once a QSG is obtained, the sequential component extraction can be easily calculated in the stationary $\alpha\beta$ frame based on the expressions (1.17), as shown in Fig. 1.21 [92].

1.3.6. Resonant controller

Recently, resonant controllers have started to be widely used in many applications, partially under unbalanced and distorted conditions. The implementation of resonant controllers is equivalent to the conventional PI controller represented in two SRFs simultaneously, of which the first one is in the positive-sequence SRF and the other in the negative-sequence SRF [77], [93], [94]. It is thus capable of tracking sinusoidal reference signals at any frequency with zero steady-state errors, and can be used very effectively in both stationary and synchronous reference frames. Nevertheless, conventional PI controllers are unable to eliminate low-order harmonic components and achieve zero steady-state errors due to their bandwidth limitation. To increase the bandwidth, increasing the proportional gain is an option. It may result in system stability problems, however [94], [95]. The best solution is hence to replace the conventional PI-controllers with resonant controllers (R) or combine them (PI and R)

to work together as a proportional resonant controller (PIR). Nowadays, resonant controllers are used directly in the stationary reference frame. It provides many advantages such as simplicity and important savings of computational burden because of the elimination of Park's transformation, decreasing sensitivity to noise and synchronisation errors, and reducing the number of controllers required to drive the machine, since the controllers can simultaneously track both sequences. It has thus been employed in many fields, for example, wind power application, active power filters [96], [97], [98], photovoltaic converters, uninterruptible rectifiers, PMSMs [99], [100], [101], [102], boost converters [103], [104], and micro-grids.

1.3.6.1. Principle of resonant controllers

As mentioned in the DSRF control strategy, Fig. 1.17, the conventional PI controller TF (G_{PI}) can be expressed as:

$$G_{PI}(s) = K_p + \frac{K_i}{s} \quad (1.24)$$

where G_{PI} provides an infinite DC gain controller at ω frequency in the synchronous reference frame. The equivalent TF of the PI controller of the positive SRF represented in the stationary reference frame can be obtained via application of a frequency shift of $(-j\omega_r)$ at all frequency ranges by substituting $s \rightarrow (s - j\omega_r)$, which results in:

$$G_{PI}^+(s) = G_{PI}(s - j\omega_r) = K_p + \frac{K_i}{s - j\omega_r} \quad (1.25)$$

In a similar way, the TF of the PI controller in the negative SRF can be represented in the stationary frame by substituting $s \rightarrow (s + j\omega_r)$ as:

$$G_{PI}^-(s) = G_{PI}(s + j\omega_r) = K_p + \frac{K_i}{s + j\omega_r} \quad (1.26)$$

Combining (1.25) and (1.26) yields:

$$G_{PR}(s) = G_{PI}^+(s) + G_{PI}^-(s) = 2K_p + 2K_i \frac{s}{s^2 + j\omega_r^2} = K_{pr} + K_r \frac{s}{s^2 + j\omega_r^2} \quad (1.27)$$

Equation (1.27) is the TF of the proportional resonant controller (PR) [77], which provides an infinite open-loop gain at the frequency of $\pm\omega_r$ (also known as resonant frequency). Infinite open-loop gain means unity gain and zero steady-state errors (zero

phase deviation) in a closed-loop response at this frequency. Furthermore, it can be deduced that the TF of G_{PR} is the same as the TF of the GI, as discussed in section §1.3.5, which can be implemented by using two integrator methods as will be discussed in Chapter 4.

1.3.6.2. Resonant controller in stationary reference frame

In the unbalanced three-phase systems, the most dominant harmonics are the negative sequence at $6k-1$ and the positive-sequence harmonics at $6k+1$, where k is an integer number. It can therefore be deduced that odd harmonics will appear in the spectrum analysis of the current/voltage in the stationary abc or $\alpha\beta$ reference frames. Generally, for control in abc frame, an individual controller in each phase is required, where the reference currents are compared with the actual measured currents. The abc frame structure can be implemented by employing a hysteresis or deadbeat controller in the current loop for nonlinear control schemes, or a PR controller for a linear control system. Moreover, for controlling in the stationary $\alpha\beta$ reference frame, the DSRF controller system in Fig. 1.17 can be represented by its equivalent in the stationary $\alpha\beta$ reference frame as:

$$v_{dq+}(s) = [G_{PI}(s)] * \Delta i_{dq+} \quad (1.28)$$

$$v_{dq-}(s) = [G_{PI}(s)] * \Delta i_{dq-} \quad (1.29)$$

$$v_{\alpha\beta+}(s) = \underbrace{[T_{dq-}][G_{PI}(s)][T_{dq+}]}_{G_{PR}} * \Delta i_{\alpha\beta+}(s) \quad (1.30)$$

$$v_{\alpha\beta-}(s) = \underbrace{[T_{dq+}][G_{PI}(s)][T_{dq-}]}_{G_{PR}} * \Delta i_{\alpha\beta-}(s) \quad (1.31)$$

where the transformation matrices $[T_{dq+}]$ and $[T_{dq-}]$ in (1.30) and (1.31) correspond to the Park's transformation (see Appendix A). Then, the voltage and current in the stationary $\alpha\beta$ reference frame are represented in terms of their positive and negative sequence components, which can be obtained by adding the two portions of (1.30) and (1.31), giving:

$$v_{\alpha\beta}(s) = v_{\alpha\beta+}(s) + v_{\alpha\beta-}(s) \quad (1.32)$$

$$\Delta i_{\alpha\beta}(s) = \Delta i_{\alpha\beta+}(s) + \Delta i_{\alpha\beta-}(s) \quad (1.33)$$

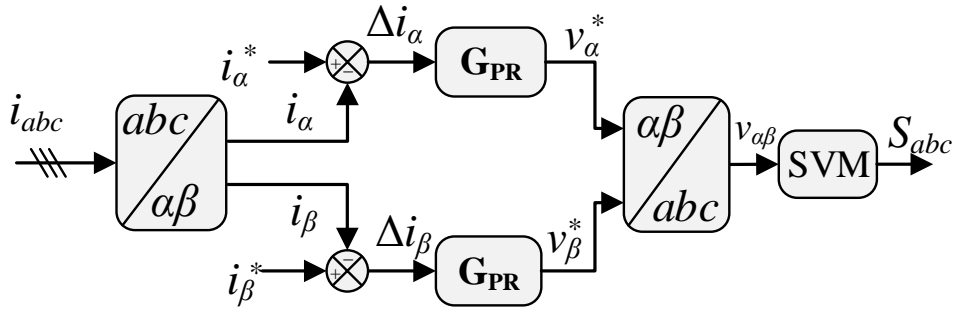


Fig. 1.22 Equivalent of DSRF controller represented in the stationary frame.

Fig. 1.22 shows an equivalent circuit diagram of a DSRF controller represented in stationary $\alpha\beta$ reference frame.

1.3.6.3. Resonant controller in synchronous reference frame

Under symmetrical conditions, the electrical variables in the SRF have pure DC components. Using a PI controller, therefore, only provides satisfactory performance. On the other hand, under asymmetric conditions, various harmonic components may exist in the SRF. The resonant controller can thus be combined with the conventional PI controller (PI+R) to compensate for the undesired harmonic components. Moreover, if more than one frequency compensation is required, the multi-resonant controller can be employed, since each resonant controller is responsible for compensating for one frequency. This technique is widely applied in many applications, for example unbalanced grid connections, [105], [106], [107], inverter dead time compensation [95], and multi-harmonics compensation [108]. Moreover, the positive $6k+1$ and negative $6k-1$ harmonic components in the stationary reference frame will be combined in a single harmonic of order $6k$ when they are expressed in the fundamental SRF. The even harmonic will therefore dominate in the fundamental SRF, so just one resonant controller tuned at $h=6k$ will be enough to track both stationary harmonics [93], [109], [110], [111], [112]. It is worth mentioning that all the previous strategies discussed have been focused on current or direct power control. However, information about direct torque control under unbalanced conditions has rarely been explored. Some special techniques and modification schemes are used, which will be highlighted in the following chapters of this thesis.

1.4. Thesis Outline and Major Contributions

1.4.1. Thesis outline

The main objective of this thesis is to present a study of the possible indirect and direct torque control strategies for three-phase SPMSMs that have asymmetric phase winding impedances. This thesis includes an extensive review of the existing control strategies for balanced and unbalanced machine drives, mathematical models for balanced and unbalanced PMSMs, and discussions about symmetrical components. Both indirect and direct torque control strategies have been studied, with modified schemes then being proposed to mitigate the drawbacks of operation under unbalanced conditions. In addition, the influences of inverter nonlinearities, unbalanced back-EMF, and variable winding resistances and inductances are also included in this study. This thesis consists of seven chapters, which are organised as follows:

CHAPTER 1: In this chapter, the fundamentals of PMSMs, their types, differences, construction, and applications are presented, followed by a general review of existing indirect and direct torque control strategies for balanced and unbalanced PMSMs. In addition, the main causes of machine imbalances are also briefly discussed.

CHAPTER 2: In this chapter, the details of the hardware configurations and software implementation used in this thesis are presented. The different control strategies are modelled in MATLAB/Simulink- V.2010b, and then constructed on a dSPACE-DS1006 control box for the real-time applications. The test rig details, including the machine model modification to make it suitable for operations in both balanced and unbalanced conditions, are also introduced. Furthermore, the six-switch inverter topology based on space vector modulation (SVM) is reviewed.

CHAPTER 3: In this chapter, mathematical models for symmetrical and asymmetric PMSMs are derived and the abnormal behaviours associated with unbalanced structures are highlighted. Based on this analysis, a modified current control strategy based on DSRFs is then presented. The proposed scheme is based on extracting the positive and negative sequence components in the stationary abc reference frame, then employing the Clark-Park transformation on the resulting components instead of using them

directly on the unbalanced current. Decoupling networks, reference current generations or adaptive filters are therefore not required, which increases simplicity and enhances dynamic performance.

CHAPTER 4: Since the information regarding the use of DTC-SVMs under unbalanced machine conditions can scarcely be found in literature, a modified cascaded structure DTC-SVM for an unbalanced PMSM, in which the torque and flux ripples are low, is presented in this chapter. This scheme is implemented by utilising a PIR controller instead of a conventional PI-regulator for closed-loop torque control. Moreover, the reference voltage vector is modified by including the information of both positive and negative sequence voltage vectors. Furthermore, a comparison between the existing and proposed strategies is presented, demonstrating that significant improvement in the machine performance can be achieved with the proposed strategy through the minimisation of torque and stator flux ripples.

CHAPTER 5: In this chapter, a compensation method in the parallel structure direct torque control-based space vector modulation (DTC-SVM) is proposed for unbalanced PMSMs, including consideration of the influence of inverter nonlinearity by means of resonant controllers. Low torque and flux ripples are achieved using this strategy for unbalanced PMSMs, considering only the second and sixth harmonic components.

CHAPTER 6: In this chapter, a control method of torque and flux linkage loops is developed by coupling the conventional PI-controller with two adaptive filters based on noise cancelation algorithm for suppression of the second and sixth torque and flux harmonics. The developed method is mathematically analyzed and experientially verified under steady and dynamic states under different asymmetric scenarios. Compared with the conventional DTC-SVM scheme based on the PI controller, the proposed compensation scheme can significantly reduce both torque and flux ripples as well as the three-phase current harmonics under asymmetric and distorted conditions.

CHAPTER 7: A summary of this research work is presented in detail, in addition to some valuable ideas that may be investigated in future work.

Fig. 1.23 shows the flow chart of the thesis organization.

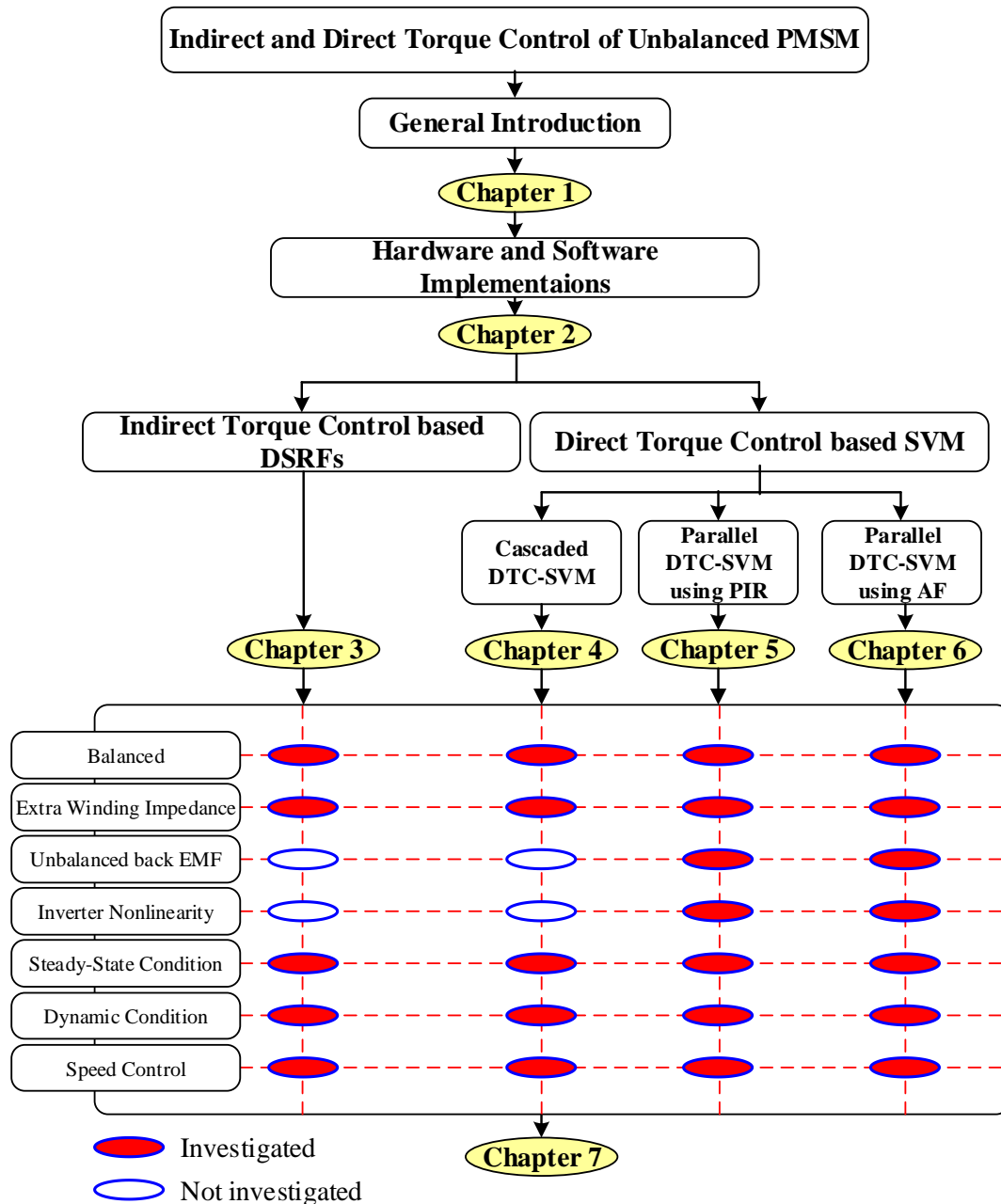


Fig. 1.23 Flow chart of thesis organization.

1.4.2. Major contributions

The main contributions of this thesis are summarised as follows:

- Derivation of the mathematical model for balanced and unbalanced (salient/non-salient pole) PMSMs.
- Modification of the DSRF control strategy, which eliminates the need for AF, reference current generation, and decoupling networks. In addition to the

simplicity of the proposed method, it provides better dynamic performance than the conventional DSRF strategy.

- Development a new method of implementation of a 90^0 phase shift delay algorithm for sequential component extraction.
- Proposal of a cascaded structure DTC-SVM strategy for PMSMs with unbalanced back-EMF in order to minimise the torque and flux ripples regardless of machine imbalance.
- Proposal of a parallel structure DTC-SVM control strategy, which can be used to compensate for multiple harmonics by means of resonant controllers and to compensate for the second and sixth harmonics in the torque and flux signals.
- Implementation of a parallel structure DTC-SVM control strategy for unbalanced PMSMs by means of the adaptive filter, to compensate for the second and sixth harmonics in the torque and flux signals.

CHAPTER 2

SYSTEM HARDWARE AND SOFTWARE IMPLEMENTATION

2.1. Introduction

This chapter provides an overview of the system hardware configurations and software implementations, of which the experimental tests through the whole thesis are conducted based on the dSPACE control system for the real-time operation. Fig. 2.1 shows the block diagram of the system hardware setup. The information regarding the dSPACE control system, inverter board, software environment, and the test rig will be extensively discussed in the following sections.

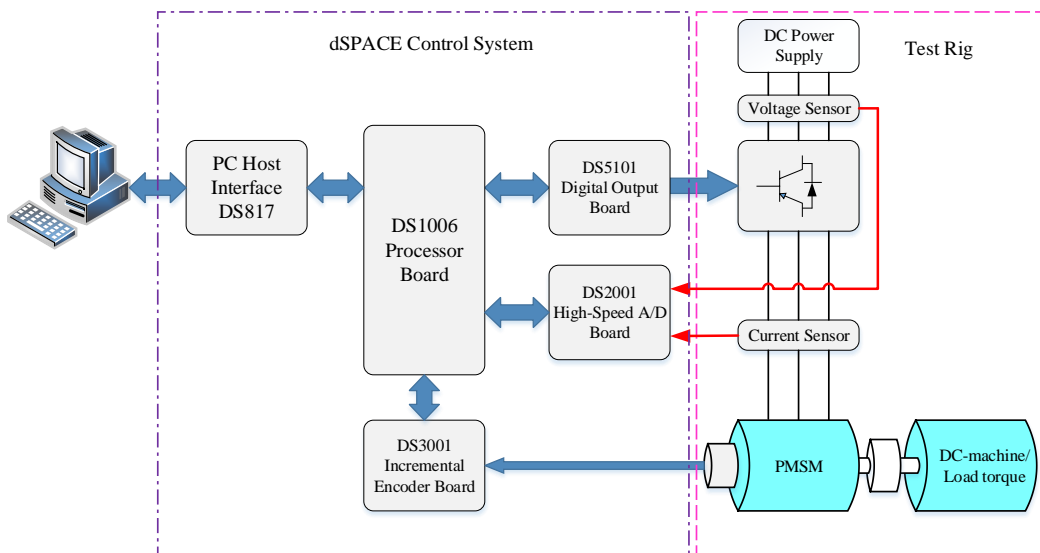


Fig. 2.1 Experimental system setup.

2.2. dSPACE Control System

2.2.1. CPU board-DS1006

The dSPACE control system used in this thesis is based on the DS-1006 processor board with a central processing unit (CPU) based on a 2.4 GHz-core AMD Opteron. The main processing unit can access modular input/output (I/O) boards via its PHS-bus, and multiprocessing is capable via the DS911 Giga-Link Module. Hence, the real-time application can be running on two or more processor cores of a multi-core DS-

1006 board, on two or more multi-core DS-1006 boards, or a combination of all these. Each multi-core CPU contains 512KB L2 on-chip cache per core, 6 MB L3 cache, 128MB DDR2-267 global memory per core for hosting the data exchange, and 1GB DDR2-800 local memory for the dynamic application data. The operation frequency of the CPU 2.4 GHz per core. Hence, even for the extremely complex control strategies for standard DSP, they can be easily implemented on the dSPACE control system. Moreover, the dSPACE control system is not only applied to motor drive development, but also for automotive engineering, aerospace, and industrial control.

2.2.2. PWM board-DS5101

The DS5101 digital waveform output board is designed to generate complex, high-speed digital signal at high resolution. The board can produce multi signals at various frequencies such as encoder signals and pulse-width modulation waveforms. It is able to vary signal pulse widths on the fly, by using different trigger and interrupt mechanisms, which provides a high degree of flexibility.

The DS5101 board can generate up to 16 channels of PWM output. This output can be used as single-phase PWM signals (PWM1), three-phase PWM signal (PWM3), or three-phase with both inverted and non-inverted PWM signal (PWM6).

Regarding PWM1, the I/O timing unit of the DS5101 generates a single-phase PWM signal with run-time adjustable PWM period and duty cycle on up to 16 channels. While for PWM3, the I/O timing unit generates three-phase PWM signals with run-time adjustable PWM period, duty cycle, and interrupt shift. For PWM6, the I/O timing unit generates three-phase/six-channel PWM signals with three inverted and three non-inverted outputs.

2.2.3. A/C board-DS2004

Analog to digital (A/D) conversion is an element of most application in rapid control systems due to use of sensors, for example, the phase current and DC-link voltage provide analog signals by current and voltage transducers, which have to be processed as digital signals. The control system in this thesis uses a DS2004 high-speed A/D board in the dSPACE systems, which is based on the processor board DS1006 for digitizing the analog input signals. It can digitize any analog input signal at high sampling rates.

The DS2004 high-speed A/D board contains 16 A/D conversion channels, which provides a differential input to a sample/hold unit and an A/D converter, and swinging buffers for decoupling the conversion process from the read process. The A/D channel applies the successive approximation conversion technique to achieve 16-bit resolution and maximum conversion time of 800ns. The input voltage range is selectable which is $\pm 5V$ or $\pm 10V$. Meanwhile, the sources for triggering A/D conversions are also selectable, for example, external trigger inputs, channel timers, and software trigger. For the external trigger inputs, four independent hardware interrupts are associated with each A/D conversion state.

DS2004 A/D board can realize two different models, i.e. burst model for digitizing a data set of up to 16384 analog values per burst including triggered sampling with selectable trigger source for starting the bursts and continuous sampling with automatically started successive bursts, and single A/D converter without utilizing its burst capability. If the conversion settings are set to burst conversion mode, the output comprises the A/D conversion result of the last burst of A/D conversions on the selected channel, which is a vector of 1~16384 results depending on the buffer settings. If the conversion settings are set to single conversion mode, the output is the outcome of the last A/D conversion on the current channel. Then based on the selected input signal range, the output signal in the simulation will be in the double range from -1 to +1 [113].

2.2.4. Encoder board-DS3001

The encoder board DS3001 is specially designed for the implementation of high-speed multivariable digital controllers whose essential features are

- Regulated 5V encoder power supply with sense line.
- Compatible with the dSPACE PHS-bus.
- Five parallel 24-bit encoder interface channels.
- Fourfold pulse multiplication.
- Differential (RS422) or single ended (TTL) encoder inputs.
- Digital noise pulse filters for the phase lines.

When the encoder input lines are from -2^{21} to $+2^{21}$, the output to Simulink should be scaled within -1 to +1. Therefore, to receive the radial angle from the scaled output value of the DS3001 Simulink block, the following conversion must be applied.

$$\theta_r = 2^{21} \cdot \frac{2\pi}{\text{encoder_resolution}} \cdot \text{scaled_output} \quad (2.1)$$

For the incremental encoders with the resolution of 2048 PPR, which are implemented in this thesis, the derived rotor position should be calculated by:

$$\theta_r = 2^{21} \cdot \frac{2\pi}{2048} \cdot \text{scaled_output} \quad (2.2)$$

2.3. Voltage Source Inverter (VSI)

2.3.1. Hardware configuration

The inverter board consists of six switching devices together with six freewheeling power diodes to form six-switch three-phase inverter as depicted in Fig. 2.2. The inverter is designed to drive a dual three-phase motor, and its kits information are discussed below.



Fig. 2.2 Inverter box with function type (top view).

2.3.1.1. Inverter board

The heart of the inverter is based on STEVAL-IHM027V1 power board with MC connector as shown in Fig. 2.3. The STEVAL-IHM027V1 demonstration board is designed to be compatible with single-phase AC supply from 90 to 220 V, or DC supply from 125 to 350 V. The system is a DC to AC three-phase inverter for IMs or PMSMs driving at rated power up to 1000 W. The STEVAL-IHM027V1 is a three-phase motor control demonstration board featuring the STGIPS10K60A 600 V, 10 A, IGBT intelligent power module from STMicroelectronics. Further information and details can be found in inverter datasheet (the schematic diagram is given in Appendix C).

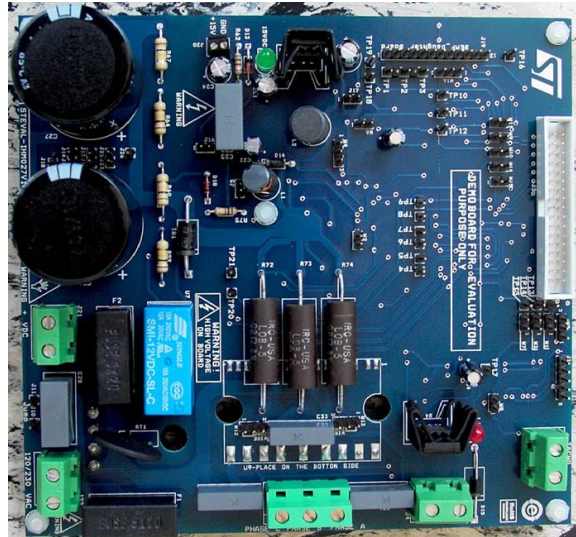


Fig. 2.3 Top view of the inverter board.

2.3.1.2. Interface board

A top view of the interface board with the name of its functional parts is shown in Fig. 2.4, and a brief details regarding these parts are given below:

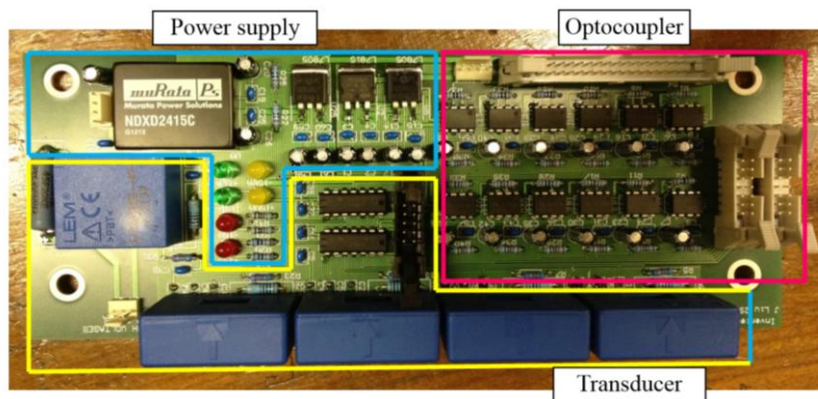


Fig. 2.4 Top view of interface board.

- **Power supply**

The power supply unit is defined in the BLUE frame in Fig. 2.4, while its schematic diagram is depicted in Fig. 2.5. This unit consists two ground terminals, i.e., “GD” and “GND”. The “GND” is connected with the dSPACE and all the other control and sensing system. Whereas, the “GD” is connected to the inverter and the other drive system. These two grounds are completely isolated. When the power supply is ON, all the six LEDs in Fig. 2.4 should lighten.

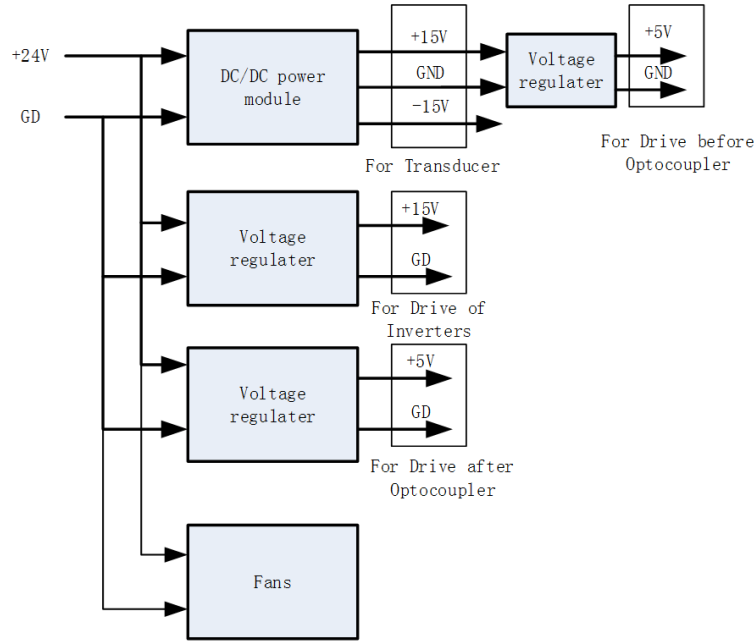


Fig. 2.5 Schematic diagram of power supply.

- **Transducers**

The transducer unit is shown in the YELLOW frame in Fig. 2.4. There are one voltage transducer and four current transducers. The output voltage of the current transducer to the A/C-board of the dSPACE has the following relationship.

$$V_o = \frac{4 \times i_{in}}{1000} \times 100 = 0.4i_{in} \quad (2.3)$$

For voltage transducer, the relationship is

$$V_o = \frac{V_{in}}{20000} \times 2.5 \times 100 = \frac{V_{in}}{80} \quad (2.4)$$

where V_o , V_{in} , and i_{in} are the output, input voltages and input current, respectively.

- **Optocoupler**

The optocoupler unit is shown in the RED frame in Fig. 2.4. The schematic diagram of the optocoupler is shown in Fig. 2.6. The input and output signals are in the same phase.

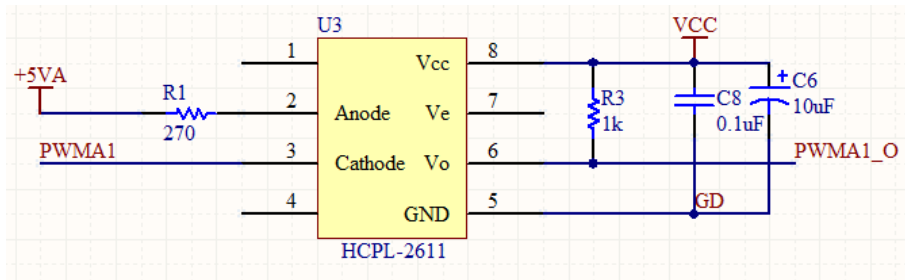


Fig. 2.6 Schematic diagram of optocoupler.

2.3.1.3. Control and connection panel

The control and connector panel has five parts as shown in Fig. 2.7:

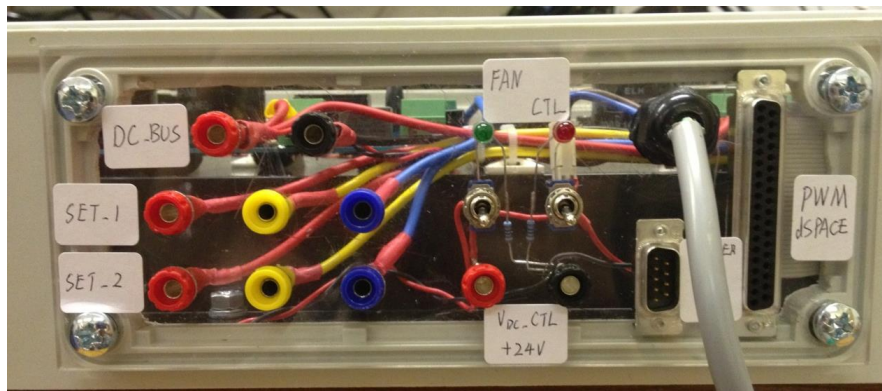


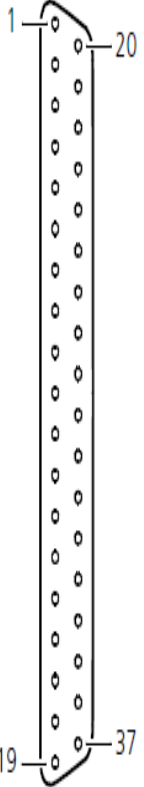
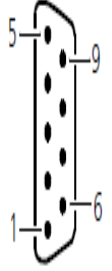
Fig. 2.7 Function parts of control and connection panel.

- Power connector part is for the input DC-link voltage;
- Power supply is for inverter control elements and switches, and should be +24V;
- Right switch is for the power supply of turning on/off the inverter;
- Left switch is for controlling the inverter cooling fans;
- Emergency (EM) stop connector is connected to the NC stop switch;
- The sensors and PWM connectors of the inverter, which are connected to the dSPACE and their pin connection description are defined in Table 2.1.

2.3.2. Software implementation

A three-phase VSI is widely employed for DC to AC power conversion, which is illustrated in Fig. 2.8. It consists of three-phase bridges with six ($S_1, S_2 \sim S_6$) power transistor switches. In practice, the most traditional power devices employed for the machine drive applications are power MOSFETs and IGBTs.

TABLE 2.1 DEFINITION OF PWM AND TRANSDUCER CONNECTOR

Connector	Pins	Signal	Pins	Signal	Connector	Pins	Signal
	1	GND	20	PWM_AT_SET1		1	V _{DC}
	2	GND	21	PWM_AB_SET1		2	I _B SET2
	3	GND	22	PWM_BT_SET1		3	I _A SET2
	4	GND	23	PWM_BB_SET1		4	I _B SET1
	5	GND	24	PWM_CT_SET1		5	I _A SET1
	6	GND	25	PWM_CB_SET1		6	GND
	7	GND	26	N/A		7	GND
	8	GND	27	N/A		8	GND
	9	GND	28	PWM_AT_SET2		9	GND
	10	GND	29	PWM_AB_SET2			
	11	GND	30	PWM_BT_SET2			
	12	GND	31	PWM_BB_SET2			
	13	GND	32	PWM_CT_SET2			
	14	GND	33	PWM_CB_SET2			
	15	GND	34	N/A			
	16	GND	35	N/A			
	17	GND	36	N/A			
	18	GND	37	N/A			
	19	GND					

The output AC voltage of the inverter is computed from the supply DC-link voltage, V_{DC} , and the switching on/off states of the power transistors, which are controlled by adjusting the a , a' , b , b' , and c , c' gate signals. When the upper leg transistors are switched “on”, i.e., the S_1 , S_3 , or S_5 is “1”, the corresponding lower leg transistors are switched “off”, i.e., the S_4 , S_6 , or S_2 is “0”. That implies, tuning the upper line switches “on” requires turning “off” the lower line switches and vice versa. The on/off switching states of the upper transistors or equivalent are sufficient to evaluate the output voltage, v_a , v_b , and v_c , and supplies the three-phase load.

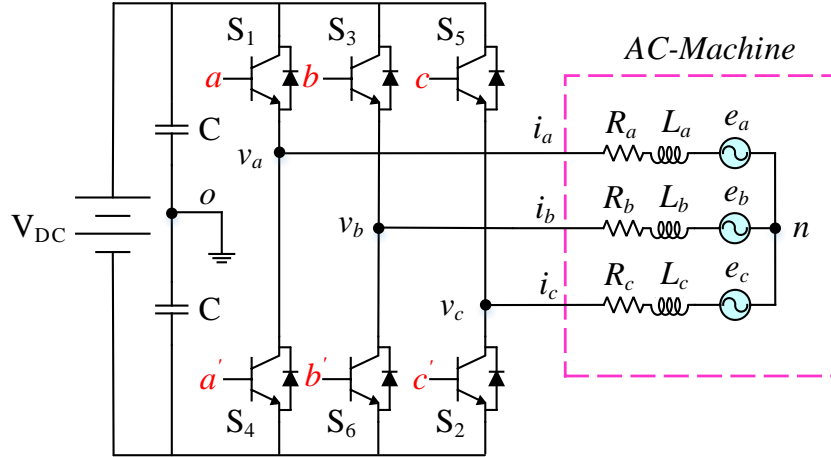


Fig. 2.8 Three-phase six switch VSI.

2.3.2.1. Switching patterns and output voltages

Three-phase VSI has three legs with two transistor switches in one leg. Each transistor switch consists of a feedback diode (freewheeling diode) connected in anti-parallel with a transistor. The feedback diode conducts current when the load current direction is opposite to the voltage direction. Suppose that the power switch devices are ideal (inverter nonlinearity will be discussed in Chapter 5). It gives the possibility to connect each of the three motor phase coils to a positive or negative terminal of the DC-link voltage. Thus, the equivalent scheme of the three-phase inverter is shown in Fig. 2.9. There are eight possible combinations of the on/off patterns for the three upper power transistors, which feed the three-phase power inverter.

The six positions of switches ($V_1 \sim V_6$) produce a phase output voltage equal $\pm 1/3$ or $\pm 2/3$ of the DC-link voltage. The last two vectors (V_0, V_7) give zero output voltage. The relationship of the output stator (phase-to-neutral) voltage components and the output stator (phase-to-zero) voltage components can be calculated as,

$$\begin{bmatrix} v_{an} \\ v_{bn} \\ v_{cn} \end{bmatrix} = \begin{bmatrix} v_{ao} \\ v_{bo} \\ v_{co} \end{bmatrix} - \begin{bmatrix} v_{no} \\ v_{no} \\ v_{no} \end{bmatrix} \quad (2.5)$$

where v_{ao} , v_{bo} , and v_{co} are the stator phase-to-zero voltages of phases a , b , and c respectively, and v_{no} refers to the neutral-to-zero voltage. The value of the phase-to-zero voltages is equal to the DC-link voltage, V_{DC} . Because in balance operation

conditions, the sums of all three line-to-neutral voltages must be zero, then the stator phase-to-neutral voltage components can be given by,

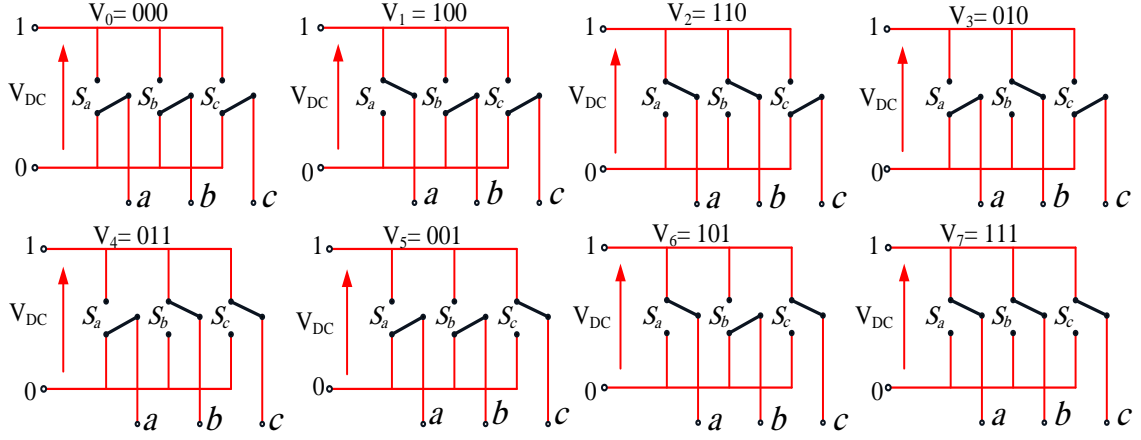


Fig. 2.9 Equivalent power circuit topology of a three-phase six switch VSI.

$$v_{an} + v_{bn} + v_{cn} = 0 \quad (2.6)$$

Moreover, the neutral-to-zero voltages can be expressed in terms of the stator phase-to-zero voltage by substituting (2.5) into (2.6), yielding:

$$v_{no} = \frac{1}{3}(v_{ao} + v_{bo} + v_{co}) \quad (2.7)$$

Substituting (2.7) into (2.5) will give

$$\begin{bmatrix} v_{an} \\ v_{bn} \\ v_{cn} \end{bmatrix} = \begin{bmatrix} \frac{2}{3} & -\frac{1}{3} & -\frac{1}{3} \\ -\frac{1}{3} & \frac{2}{3} & -\frac{1}{3} \\ -\frac{1}{3} & -\frac{1}{3} & \frac{2}{3} \end{bmatrix} \begin{bmatrix} v_{ao} \\ v_{bo} \\ v_{co} \end{bmatrix} = \begin{bmatrix} \frac{2}{3} & -\frac{1}{3} & -\frac{1}{3} \\ -\frac{1}{3} & \frac{2}{3} & -\frac{1}{3} \\ -\frac{1}{3} & -\frac{1}{3} & \frac{2}{3} \end{bmatrix} \begin{bmatrix} S_a \\ S_b \\ S_c \end{bmatrix} \cdot V_{DC} \quad (2.8)$$

where S_a , S_b , and S_c are the switching states on the inverter legs, Fig. 2.9. Moreover, the phase-to-neutral voltages can be expressed by the Fourier series formula given below [114]:

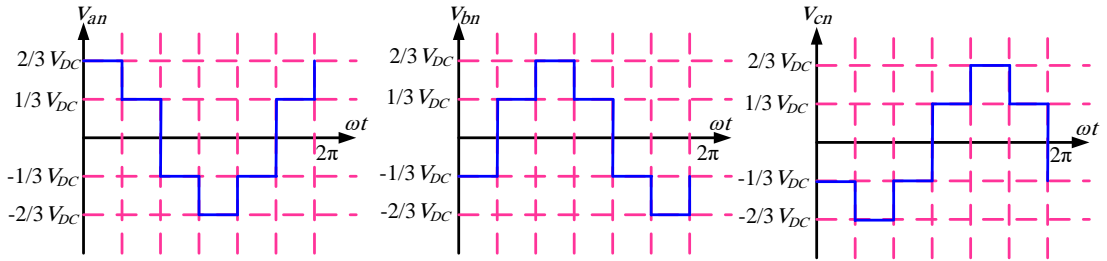
$$v_{an} = \frac{2}{3}V_{DC} \sum_{n=1}^{\infty} \frac{1}{n} \sin(n\omega t) = V_{m(n)} \sum_{n=1}^{\infty} \frac{1}{n} \sin(n\omega t) \quad (2.9)$$

where $V_{m(n)}$ is the peak value of the n -th harmonic. On the other hand, the phase-to-phase voltages can be calculated as:

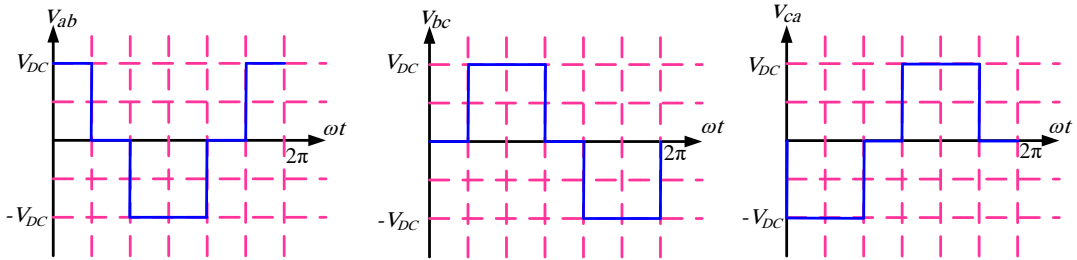
$$\begin{bmatrix} v_{ab} \\ v_{bc} \\ v_{ca} \end{bmatrix} = \begin{bmatrix} v_{an} - v_{bn} \\ v_{bn} - v_{cn} \\ v_{cn} - v_{an} \end{bmatrix} = \begin{bmatrix} S_a & -S_b \\ S_b & -S_c \\ S_c & -S_a \end{bmatrix} \cdot V_{DC} \quad (2.10)$$

Fig. 2.10 presents the phase-to-neutral and phase-to-phase voltages as they appear from the load side based on (2.8) and (2.10). On the other hand, the relation between V_{DC} and the $\alpha\beta$ voltage can be obtained by applying Clark's transformation on equation (2.10) (refer to Appendix A), which gives:

$$\begin{bmatrix} v_\alpha \\ v_\beta \end{bmatrix} = \begin{bmatrix} \frac{2}{3} & -\frac{1}{3} & -\frac{1}{3} \\ 0 & \frac{1}{\sqrt{3}} & -\frac{1}{\sqrt{3}} \end{bmatrix} \begin{bmatrix} S_a \\ S_b \\ S_c \end{bmatrix} \cdot V_{DC} \quad (2.11)$$



(a) Phase-to-neutral voltages



(b) Phase-to-phase voltages

Fig. 2.10 Inverter output voltage from load side.

TABLE 2.2 SWITCHING PATTERNS AND OUTPUT VOLTAGES OF SIX SWITCH THREE PHASE INVERTER

Vectors No. $V_{i=0-7}$	Switching state ($S_{a,b,c}$)	Phase-to-zero voltage			Phase-to-neutral voltage			$\alpha\beta$ -voltage		
		V_{ao}	V_{bo}	V_{co}	V_{an}	V_{bn}	V_{cn}	V_{α}	V_{β}	
V0	000	$-\frac{1}{2}$	$-\frac{1}{2}$	$-\frac{1}{2}$	0	0	0	0	0	Zero vector
V1	100	$\frac{1}{2}$	$-\frac{1}{2}$	$-\frac{1}{2}$	$\frac{2}{3}V_{DC}$	$-\frac{1}{3}V_{DC}$	$-\frac{1}{3}V_{DC}$	$\frac{2}{3}V_{DC}$	0	Non-Zero Vectors
V2	110	$\frac{1}{2}$	$\frac{1}{2}$	$-\frac{1}{2}$	$\frac{1}{3}V_{DC}$	$\frac{1}{3}V_{DC}$	$-\frac{2}{3}V_{DC}$	$\frac{1}{3}V_{DC}$	$\frac{1}{\sqrt{3}}V_{DC}$	
V3	010	$-\frac{1}{2}$	$\frac{1}{2}$	$-\frac{1}{2}$	$-\frac{1}{3}V_{DC}$	$\frac{2}{3}V_{DC}$	$-\frac{1}{3}V_{DC}$	$-\frac{1}{3}V_{DC}$	$\frac{1}{\sqrt{3}}V_{DC}$	
V4	011	$-\frac{1}{2}$	$\frac{1}{2}$	$\frac{1}{2}$	$-\frac{2}{3}V_{DC}$	$\frac{1}{3}V_{DC}$	$\frac{1}{3}V_{DC}$	$-\frac{2}{3}V_{DC}$	0	
V5	001	$-\frac{1}{2}$	$-\frac{1}{2}$	$\frac{1}{2}$	$-\frac{1}{3}V_{DC}$	$-\frac{1}{3}V_{DC}$	$\frac{2}{3}V_{DC}$	$-\frac{1}{3}V_{DC}$	$-\frac{1}{\sqrt{3}}V_{DC}$	
V6	101	$\frac{1}{2}$	$-\frac{1}{2}$	$\frac{1}{2}$	$\frac{1}{3}V_{DC}$	$-\frac{2}{3}V_{DC}$	$\frac{1}{3}V_{DC}$	$\frac{1}{3}V_{DC}$	$-\frac{1}{\sqrt{3}}V_{DC}$	
V7	111	$\frac{1}{2}$	$\frac{1}{2}$	$\frac{1}{2}$	0	0	0	0	0	Zero vector

Moreover, the relationship between the switching state and the amplitude of the 8th voltage vectors of the three-phase VSI are summarized in Table 2.3.

2.3.2.2. Pulse width modulation based SVM

Pulse width modulation (PWM) techniques are widely employed to obtain the suitable duty cycle for each switch in the VSI. Therefore, many different modulation methods were proposed in literature [114], [115], [116]. Most of them aim to provide some general features such as

- Increased range of linear operation region;
- Reduced high order voltage and current harmonics;
- Operated in over-modulation;
- Minimal number of switching to reduce the switching power losses;
- Low common mode voltage.

Each PWM technique has specific feature, which may be different from the others, and cannot meet all requirements in the full operating region. Thus, the content of the higher harmonics voltage (current) and electromagnetic interference generated in the inverter fed drive depend on the modulation technique. Hence, the development of modulation methods may improve converter parameters. In the carrier based PWM techniques, the zero sequence signals (ZSS) are added to extend the linear operation range. The most commonly used PWM techniques are carrier based, which is also

known as the sinusoidal (SPWM), triangulation, sub-harmonic, or sub-oscillation techniques [114], [116]. SPWM is based on a triangular carrier signal of which three reference signals v_a, v_b, v_c are compared with triangular carrier signal V_C . In this manner, the switching signals $S_a, S_b,$ and S_c are generated. The modulation index (M) of SPWM is defined as

$$M = \frac{\hat{V}_{m(n)}}{\hat{V}_C} \quad (2.12)$$

$$V_{phase} = \frac{1}{2\sqrt{2}} M \cdot V_{DC} \quad (2.13)$$

$$V_{line} = \frac{\sqrt{3}}{2\sqrt{2}} M \cdot V_{DC} \quad (2.14)$$

where $V_{m(n)}$ and V_C are the modulating and carrier signal voltages, respectively. The modulation index in this technique can be varied between 0 and 1 to give a linear relation between the reference and output waves. At $M=1$, the maximum peak value of the fundamental phase voltage is $V_{DC}/2$, the maximum phase-to-phase (line) output voltage with SPWM is approaching to 61.2% of the DC-link voltage in the linear modulation range.

When the neutral point **N** on the AC side is not connected to the DC side midpoint 0, (see Fig. 2.8), the phase currents will depend only on the voltage difference between phases. Therefore, it is possible to inject an additional Zero Sequence Signal (ZSS). A schematic diagram of the modulator based on the additional ZSS is shown in Fig. 2.11 [117]. Moreover, many modulation techniques are depending on the ZSS waveform. The most popular PWM methods are shown in Fig. 2.12. These techniques are divided into two groups: continuous and discontinuous. In the continuous PWM (CPWM) techniques, the modulation waveform is always within the triangular peak boundaries and in every carrier cycle triangle and modulation waveform intersections. Hence, on and off switchings occur.

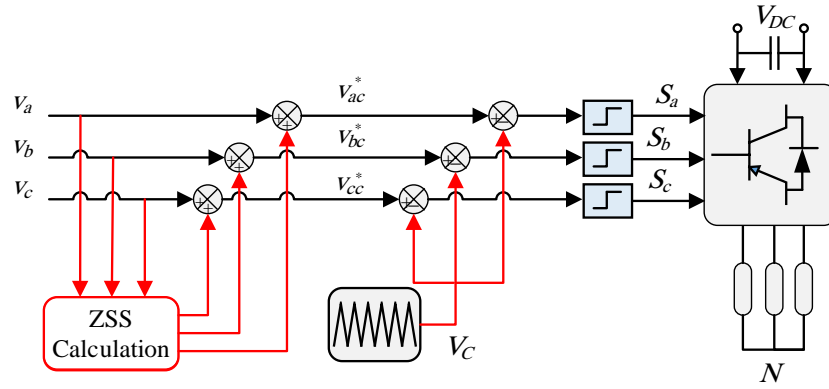


Fig. 2.11 PWM technique with additional ZSS.

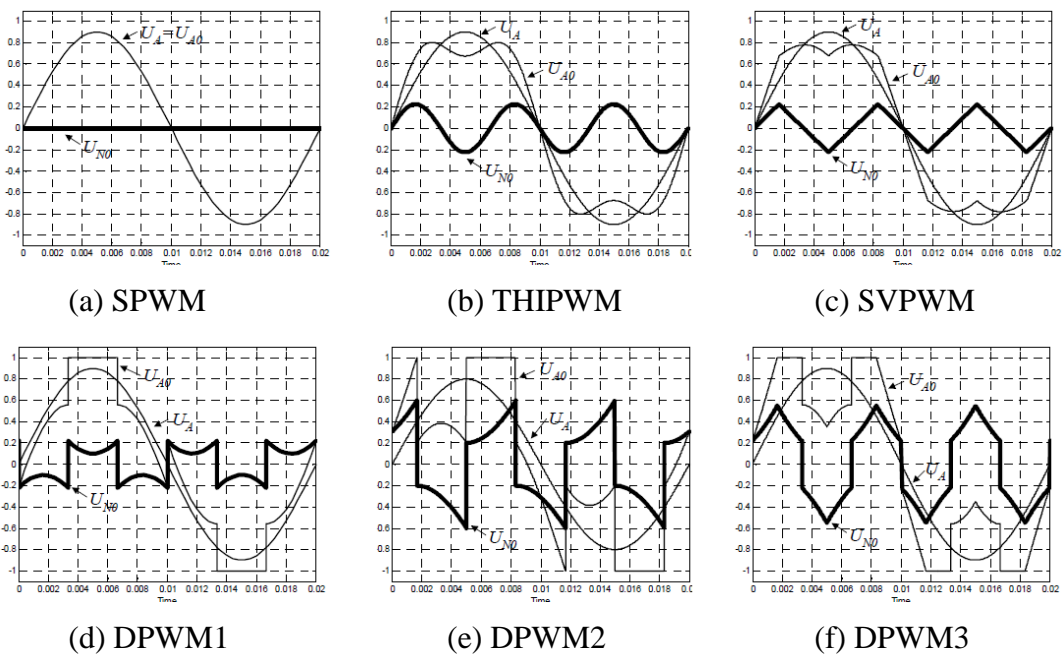


Fig. 2.12 PWM waves with ZSS

Fig. 2.12 also shows sinusoidal PWM (SPWM), third harmonic PWM (THIPWM), and space vector PWM (SVPWM) with ZSS equal to 0.25 of the peak value corresponding to a minimum of output current harmonics. In the discontinuous PWM (DPWM) techniques, a modulation waveform of a phase has a segment, which is clamped to the positive or negative DC-link voltage. In these segments, some power converter switches do not switch. Therefore, less switching losses (average 33%) can be ensured. The modulation method with triangular shape of ZSS with 0.25 of peak value corresponds to space vector modulation (SVPWM) with a symmetrical placement of the zero vectors in a sampling period will be discussed in the next section.

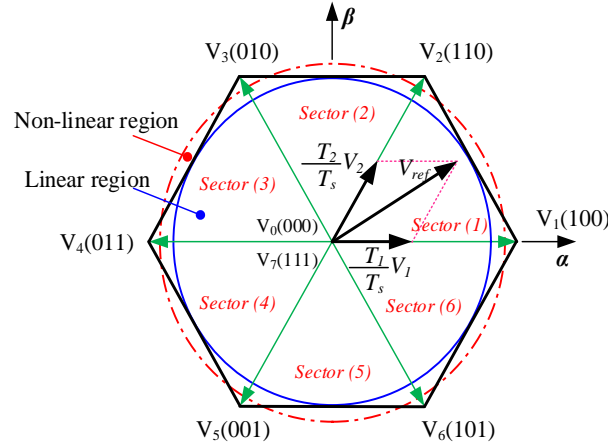


Fig. 2.13 Inverter space voltage vectors.

2.3.2.3. Space vector pulse width modulation (SVM)

Space vector PWM technique (also called space vector modulation (SVM) as will be used in this thesis) is used to generate the required voltage or current to feed the motor or phase signals. It is widely employed for AC drives with the condition that the harmonic current is as small as possible, and the maximum output voltage is as large as possible. Recently, SVM becomes the most common PWM technique that is used in a three-phase VSI for the control of induction, switched reluctance, and PMSM machines. Comparing with the conventional SPWM, the SVM is more suitable for digital implementation and can increase the maximum output voltage with maximum line voltage approaching to 70.7% of the DC-link voltage (compared to SPWM's 61.2%) in the linear modulation range. Moreover, it can obtain a higher efficiency, a better voltage total harmonic distortion (THD), and a higher torque at a higher speed range [118], [119].

The zeros, non-zero, and reference voltage vectors are shown in Fig. 2.13. The 8th vectors are corresponding to the operation state of the inverter. The active six vectors ($V_1, V_2 \sim V_6$) divide the space plan into six equal area (six sectors) displaced by 60° , which can be represented by a complex vector expression as:

$$V_i = \begin{cases} \frac{2}{3}V_{DC} \exp^{j(i-1)\pi/3} & ; \quad i = 1, 2, \dots, 6 \\ 0 & ; \quad i = 0, 7 \end{cases} \quad (2.15)$$

In the SVM, to define of which active voltage space vector is responsible for generating the synthesized output voltage vector. The values of the instantaneous

voltage v_α and v_β in the $\alpha\beta$ reference frames are used to predict the sector of the operating active vector. Assume three variable values of V_{ref1} , V_{ref2} , and V_{ref3} that can be defined as:

$$V_{ref1} = v_\beta \quad (2.16)$$

$$V_{ref2} = \sqrt{3}v_\alpha - v_\beta \quad (2.17)$$

$$V_{ref3} = -\sqrt{3}v_\alpha - v_\beta \quad (2.18)$$

Then calculate the operating transistors as:

$$N = 4 \times C + 2 \times B + A \quad (2.19)$$

where the values of the variables A, B, and C can be defined as follows:

$$\begin{aligned} A &= 1, \text{ if } V_{ref1} > 0; & \text{Otherwise, } A &= 0; \\ B &= 1, \text{ if } V_{ref2} > 0; & \text{Otherwise, } B &= 0; \\ C &= 1, \text{ if } V_{ref3} > 0; & \text{Otherwise, } C &= 0. \end{aligned}$$

The final relationship between N and the operating sectors is given in Table 2.3.

TABLE 2.3 SECTOR SELECTION

N	3	1	5	4	6	2
Sectors	Sector(1)	Sector(2)	Sector(3)	Sector(4)	Sector(5)	Sector(6)

Furthermore, in Fig. 2.13 there are two operation regions (linear and non-linear). For linear operation region, V_{ref} remains within the hexagon, which means that the maximum amplitude voltage is equal $V_{DC}/\sqrt{3}$ and the modulation index (M) is equal to

$$M = \frac{V_{DC} / \sqrt{3}}{2V_{DC} / \pi} = \frac{\pi}{2\sqrt{3}} = 0.9068 \quad (2.20)$$

The reference voltage vector is sampled with the fixed clock frequency $2f_s$. Assuming that V_{ref} is located in the sector (1) of Fig. 2.13 [120], [121], [122], it can be realized by employing the two nearest active voltage vectors V_1 and V_2 along with the zero vector as shown in Fig. 2.14. The integral of V_{ref} over single space vector modulation cycle gives

$$\int_0^{T_s} V_{ref} dt = \int_0^{T_1} V_1 dt + \int_{T_1}^{T_1+T_2} V_2 dt + \int_{T_1+T_2}^{T_s} V_0 dt \quad (2.21)$$

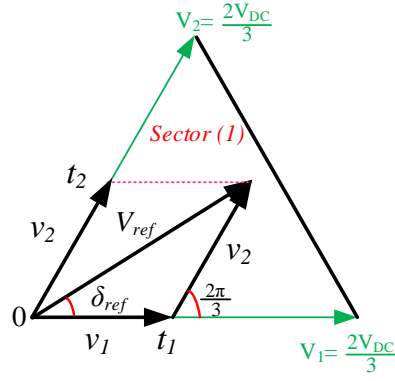


Fig. 2.14 Calculation of voltage vector duration time.

where t_1 and t_2 are the switching time durations spent on the output voltage vectors V_1 and V_2 , respectively, t_0 and t_7 are the time durations spent on the zero vectors V_0 and V_7 , and $T_s = 1/f_s$ is the sampling time. For sufficiently high switching frequency, V_{ref} is assumed constant during one switching cycle. Therefore, within the switching cycle, the variation of the stator voltage vector is $T_s V_{ref}$ and the status of vectors V_1 and V_2 should be controlled as [123]

$$T_s V_{ref} = t_1 V_1 + t_2 V_2 + t_0 (V_0 \text{ or } V_7) \quad (2.22)$$

where

$$t_1 + t_2 + t_0 = T_s \quad (2.23)$$

$$v_1 = \frac{t_1}{T_s} V_1 \quad (2.24)$$

$$v_2 = \frac{t_2}{T_s} V_2 \quad (2.25)$$

From Fig. 2.14, and according to *sine* law, the relationship between the three vectors can be written as

$$\frac{|V_{ref}|}{\sin(120^\circ)} = \frac{|v_1|}{\sin(60^\circ - \delta_{ref})} = \frac{|v_2|}{\sin(\delta_{ref})} \quad (2.26)$$

For this formula, the vectors v_1 and v_2 can be presented as

$$v_1 = \frac{|V_{ref}| \sin(60^\circ - \delta_{ref})}{\sin(120^\circ)} = \frac{2}{\sqrt{3}} |V_{ref}| \sin(60^\circ - \delta_{ref}) \quad (2.27)$$

$$v_2 = \frac{|V_{ref}| \sin(\delta_{ref})}{\sin(120^\circ)} = \frac{2}{\sqrt{3}} |V_{ref}| \sin(\delta_{ref}) \quad (2.28)$$

If the space vectors in the equation are described in dq coordinates, then it follows:

$$t_1 = \frac{v_1 T_s}{V_1} = \frac{\sqrt{3}|V_{ref}|T_s}{V_{DC}} \sin(60^\circ - \delta_{ref}) \quad (2.29)$$

$$t_2 = \frac{v_2 T_s}{V_2} = \frac{\sqrt{3}|V_{ref}|T_s}{V_{DC}} \sin(\delta_{ref}) \quad (2.30)$$

$$t_{0,7} = T_s - (t_1 + t_2) = T_s \left(1 - \sqrt{3} \frac{|V_{ref}|}{V_{DC}} \cos(30^\circ - \delta_{ref})\right) \quad (2.31)$$

Afterward, the time interval of the active and zero vectors, i.e., t_1 , t_2 , and $t_{0,7}$ are identical for all space vector of SVM technique. Hence, the duty time cycle for upper (S_1, S_3, S_5) and lower (S_4, S_6, S_2) transistor for all sectors obtained by (2.29) ~ (2.31) can be represented as

$$\begin{bmatrix} S_1 \\ S_3 \\ S_5 \end{bmatrix} = \begin{bmatrix} \underbrace{1 \ 1 \ k}_{Sector(1)} & \underbrace{1 \ 0 \ k}_{Sector(2)} & \underbrace{0 \ 0 \ k}_{Sector(3)} & \underbrace{0 \ 0 \ k}_{Sector(4)} & \underbrace{0 \ 1 \ k}_{Sector(5)} & \underbrace{1 \ 1 \ k}_{Sector(6)} \end{bmatrix} = \begin{bmatrix} t_1 \\ t_2 \\ t_{0,7} \end{bmatrix} \quad (2.32)$$

$$\begin{bmatrix} S_4 \\ S_6 \\ S_2 \end{bmatrix} = \begin{bmatrix} \underbrace{0 \ 0 \ k}_{Sector(1)} & \underbrace{0 \ 1 \ k}_{Sector(2)} & \underbrace{1 \ 1 \ k}_{Sector(3)} & \underbrace{1 \ 1 \ k}_{Sector(4)} & \underbrace{1 \ 0 \ k}_{Sector(5)} & \underbrace{0 \ 0 \ k}_{Sector(6)} \end{bmatrix} = \begin{bmatrix} t_1 \\ t_2 \\ t_{0,7} \end{bmatrix} \quad (2.33)$$

where $k=0.5$, which depends on the space vector location, the basic vectors must be selected to minimize the number of switching changes in the converter. On the other hand, operating in the nonlinear region (also called over-modulation region) is used to increase the range of maximum output voltage up to 100% at $M=1$. This technique has been widely discussed in literature [114], [122], [124], [125].

2.4. Software Environment

The mathematical model of the PM machine and the implementation of different control strategies have been conducted on the MATLAB/SIMULINK (V. R2009a) software. It can be easily adapted with the dSPACE, V. DS1006 platform for real-time applications. The MATLAB/SIMULINK provide a wide range of algorithm development, data analysis, data visualization, signal processing, and numerical computation. Then m-file, s-functions, and embedded functions are utilized to achieve

some mathematical expression such as fast Fourier transformation (FFT) for spectrum analysis, figure plotting and writing some expressions and the necessary functions. For figures plotting, the data obtained from the dSPACE are analyzed and Microsoft excel program is used.

2.5. Test Rig

The experimental tests are conducted on the balanced three-phase surface-mounted PM synchronous. It was designed and manufactured in the Electrical Machine and Drives Group (EMD), the University of Sheffield [126]. The machine stator has three-teeth of which one tooth for each phase. It was designed as two concentrated coils (non-overlapping winding coil) in series connection with the same phase, with a sinusoidal back-EMF. For investigation under different load torque conditions, the motor is mechanically coupled to the DC-generator, which acts as a loaded machine by adjusting a variable power resistor connected into the armature winding, and keeping excitation voltage applied to the field winding as shown in Fig. 2.15. It should be emphasized that the saturation effect of investigated motor can be neglected [126]. The machine is Y-connected and supplied by a three-phase VSI (the neutral point is not connected). It was designed for high-speed applications of which the rated speed is up to 9000 rpm at 200V of the DC-link voltage. However, the rated speed of the DC-load generator is 3000 rpm. Therefore, the maximum speed of the tested motor has to be limited within the speed range of the DC-load generator as well as the DC-link voltage should be reduced from 200V to 70V.

On the other hand, the unbalanced conditions of the tested machine have been generated by either adding extra impedance to the machine phases as shown in Fig. 2.16 or adding additional winding inside the machine as illustrated the terminal connection in Fig. 2.16 (b). These conditions will be separately explained through thesis chapters depending on the implementation method. Moreover, the parameters of the tested motor are given in Table 2.4.

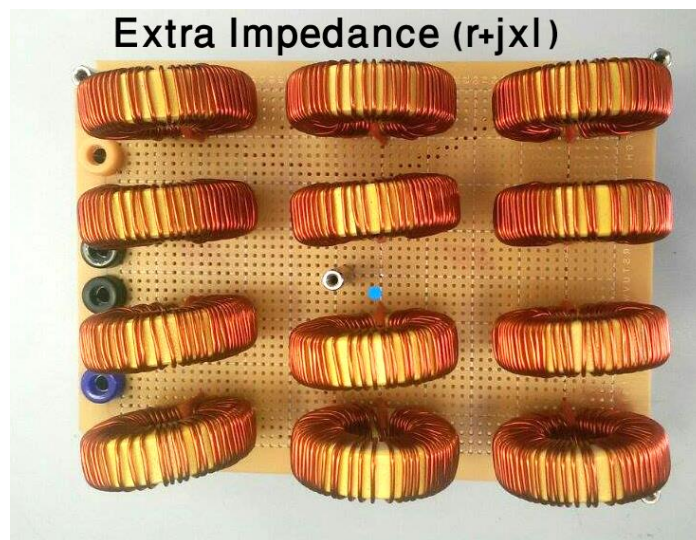


(a) Test rig.



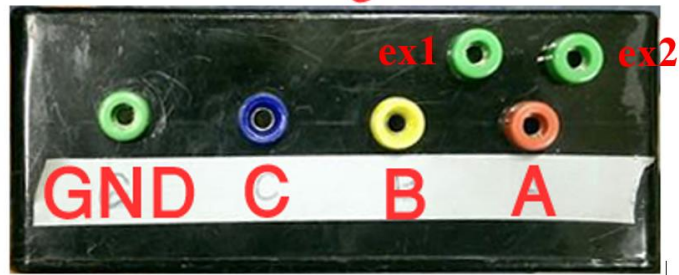
(b) System setup.

Fig. 2.15 Experimental system setup.



(a) Variable values impedance to create unbalanced behaviors

Extra windings terminal



(b) Front view of extra winding connections

Fig. 2.16 Implementations of unbalanced conditions.

TABLE 2.4 PROTOTYPE PARAMETERS

Parameters	Values	Units
Phase resistance	0.64	Ω
Winding inductance	3.19	mH
No. of pole pairs	1	-
No. of turns/phase	60	turn
Permanent magnet flux	0.0928	Wb
DC-link voltage	48	V
Rated DC-link voltage	70	V
Rated torque	0.3	Nm
Rated current	2.2	A
Rated speed	3000	r/min
Mechanical inertia	0.00363	kg.m ²

2.6. Summary

This chapter introduces the hardware and software system implementations. It presents a detail description of the dSPACE, inverter configuration, software environments, and the test rig of which all the experimental results in this thesis are carried out. On the other hand, the implementation of asymmetric PMSM situation will be discussed separately through thesis chapters. Moreover, a brief introduction to PWM techniques while an extensive discussion about SVM is also provided.

CHAPTER 3

CURRENT CONTROL OF UNBALANCED THREE-PHASE PMSM BASED ON DOUBLE SYNCHRONOUS REFERENCE FRAME CONTROLLER

Abstract— A simple and effective current control strategy for an asymmetric three-phase permanent magnet synchronous machine (PMSM) fed by a voltage source inverter (VSI). It is based on extraction of the positive and negative sequence components in phase frame, and then utilizes the double synchronous reference frame (DSRF) controller for the current ripple suppression caused by the machine asymmetry. Compared to the existing DSRF methods, the proposed strategy has advantages of no requirement of filters, decoupling network and specific current reference to obtain smooth positive and negative-sequence current components in both synchronous reference frames, which also bring the merit of better dynamic performance compared to the conventional DSRF methods. The feasibility of the proposed strategy has been verified by various experimental results under steady state and dynamic conditions.

3.1. Introduction

This chapter presents a mathematical model of the PMSM derived in stationary (abc -axis and $\alpha\beta$ -axis) and synchronous (dq) reference frames for both balanced and unbalanced cases. When these machines operate under balanced condition, the conventional field oriented control strategy, which is usually performed by proportional-integral (PI) regulators in a single synchronous reference frame (single-SRF) [4], [127], [128], can achieve very good dynamic and steady-state performance. On the other hand, under unbalanced conditions, the machine performance will deteriorate, which results in the rise of torque ripple, extensive heating, acoustic noise, increase losses and reduce the efficiency due to existing of positive, negative-, and zero sequence components. Hence, the conventional current control implemented on single-SRF does not achieve satisfactory performance. Thus, a DSRF control strategy was introduced to enhance the machine performance under such conditions [72], [75], [129], [130]. It is well developed and for most common DSRF strategies, the measured three-phase currents directly transformed into both positive and negative SRFs, which causes

AC oscillation at twice of the fundamental frequency $2\omega_e$ combined with the DC signal in both SRFs [130], [131].

Over the past few years, many approaches, including hysteresis current control, proportional-resonant (PR) control [132], direct power control [83], model-based predictive direct power control, and double synchronous reference frame (DSRF) control [72], [75], [129], [130], have been developed and extensively investigated to achieve decent performance of currents when the electrical machines are asymmetric. Particularly, in DSRF strategy, the current control can be obtained by using a pair of PI current regulators in each of the positive and negative SRFs. For most common DSRF control strategy, the measured unbalanced three-phase currents are directly transformed into both positive and negative rotating SRFs, resulting in AC oscillation at twice of the fundamental frequency $2\omega_e$ combined with the DC signal in both SRFs [130]. To overcome this problem, many methods have been proposed to eliminate the $2\omega_e$ oscillations in the positive and negative SRFs, such as, filtering the measured feedback currents to obtain a pure DC values by employing a low pass filter (LPF) or notch filter [72], [73].

Other research has suggested for compensating the cross-coupling effect by implementing a decoupling network between positive and negative SRFs [130], [73]. This structure is also known as a decoupled DSRF controller (DDSRF). It eliminates the $2\omega_e$ cross-coupled oscillations by using a decoupling network based on the current reference, and then re-injected into the positive and negative SRFs. Thus, the AC oscillations will be eliminated in the DSRF and only pure DC currents are fed back to the PI-regulators [130].

In addition, a DSRF controller without filters in the feedback currents is presented in [75], where the reference currents match the oscillation in the measured feedback currents for both SRFs. Thus, the reference currents will have AC and DC components. To reduce the steady-state error, a resonant-gain path is employed in the current regulator, i.e. state-feedback path in each SRF [75]. However, it has proven that the state-feedback technique (also called resonant-gain [75]) for decoupling the cross-coupling between the orthogonal axes of each SRF in the DSRF controller does not provide noticeable improvement, because the terms added to one SRF interfere with those added to the other SRF [133].

The main focus of this paper is to investigate the asymmetric phenomenon caused by the winding impedance asymmetry and its remedy. A modified DSRF controller is based on the extraction of positive and negative-sequence components in phase reference frame. The modified DSRF controller ensures pure DC feedback currents in both positive and negative SRFs. The major benefits of the proposed strategy are not only parameter independent but also simple structure due to (a) no employment of filters as used in [72], (b) no requirement of a decoupling network as addressed in [130], (c) no need of specific current reference generation [134]. The feasibility of the proposed method will be verified by various experimental results.

3.2. Mathematical Model of PMSM under Balanced and Unbalanced Conditions

3.2.1. Representation of PMSM in stationary abc reference frame

Comparing a primitive version of a PMSM with wound-rotor synchronous motor, the stator of a PMSM has windings similar to those of wound-rotor synchronous motor, which is three-phase, Y-connected, and sinusoidally distributed. However, on the rotor side, instead of using the electrical circuit in the wound-rotor synchronous motor, constant rotor flux ψ_{rabc} provided by the rotor PMs should be considered in the dq -model of a PMSM. Since the PMSM has a winding in the stator and a PM on the rotor, the three-phase stator voltage equations in the stationary abc reference frame of PMSM can be expressed in the matrix form as [4]:

$$\begin{bmatrix} v_{an} \\ v_{bn} \\ v_{cn} \end{bmatrix} = \begin{bmatrix} R_a & 0 & 0 \\ 0 & R_b & 0 \\ 0 & 0 & R_c \end{bmatrix} \begin{bmatrix} i_a \\ i_b \\ i_c \end{bmatrix} + \frac{d}{dt} \begin{bmatrix} \psi_{sa} \\ \psi_{sb} \\ \psi_{sc} \end{bmatrix}, \quad \vec{v}_{abc} = R_{abc} \vec{i}_{abc} + \frac{d\vec{\psi}_{abc}}{dt} \quad (3.1)$$

where v_{an} , v_{bn} , and v_{cn} represent the stator phase-to-neutral voltage of phases a , b and c , respectively; i_a , i_b , and i_c are respectively the stator phase currents of phases a , b and c ; R_a , R_b , and R_c are the stator resistances of phases a , b and c , respectively; ψ_{sa} , ψ_{sb} , and ψ_{sc} are respectively the stator flux linkages of phases a , b and c .

Moreover, the complex space vectors of the three-phase stator voltages, current, and flux linkages, all can be expressed in stationary reference frame as:

$$\vec{F}_s = \frac{2}{3} [F_a(t) + a F_b(t) + a^2 F_c(t)] \quad (3.2)$$

where the factors F can be any variables, i.e., voltage, current and stator flux linkage, and “ a ” and “ a ” are spatial operators for orientation of the stator windings $a=e^{j2\pi/3}$ and $a^2=e^{j4\pi/3}$. The resultant voltage, current, and stator flux linkage space vectors are given in (3.2). Then, the stator flux linkage can be calculated by multiplying instantaneous phase values by the stator winding orientations in which the stator reference axis for the a -phase is chosen to the direction of maximum MMF. Reference axes for the b - and c - stator frames are selected to be 120° (electrical degrees) ahead of the a -axis, respectively. Then, the three-phase stator flux linkage $\vec{\psi}_{sabc}$ can be expressed in the matrix form as [135]:

$$\begin{bmatrix} \psi_{sa} \\ \psi_{sb} \\ \psi_{sc} \end{bmatrix} = \begin{bmatrix} L_{aa} & M_{ab} & M_{ac} \\ M_{ba} & L_{bb} & M_{bc} \\ M_{ca} & M_{cb} & L_{cc} \end{bmatrix} \begin{bmatrix} i_a \\ i_b \\ i_c \end{bmatrix} + \begin{bmatrix} \psi_{ra} \\ \psi_{rb} \\ \psi_{rc} \end{bmatrix}, \quad \vec{\psi}_{sabc} = L_{abc} \vec{i}_{abc} + \vec{\psi}_{rabc} \quad (3.3)$$

where L_{aa} , L_{bb} , and L_{cc} are the self-inductances of the stator phases a , b and c windings, respectively, M_{ab} , M_{ac} , M_{ba} , M_{bc} , M_{ca} , and M_{cb} are the stator phase mutual inductances between the phase windings, and ψ_{ra} , ψ_{rb} , and ψ_{rc} are the rotor PM fluxes, which are a function of electrical rotor flux position (θ_r), and the peak value of the rotor PM flux (ψ_{PM}) can be written as:

$$\vec{\psi}_{rabc} = \psi_{PM} \begin{bmatrix} \cos(\theta_r) \\ \cos(\theta_r - \frac{2\pi}{3}) \\ \cos(\theta_r - \frac{4\pi}{3}) \end{bmatrix} \quad (3.4)$$

The PM rotor flux is changed according to the variation of θ_r at constant ψ_{PM} . Equation (3.4) is often known as the back-EMF constant. Due to the saturation effect and a mechanical structure of PMSM the inductance will be a function of θ_r , the relationship between the mechanical rotor position (θ_m) and the electrical rotor position θ_r is given by:

$$\theta_r = p_n \theta_m \quad (3.5)$$

where p_n is the number of pole pairs. The inductance matrix L_{abc} given in (3.3) can be expressed by Fourier series [136], [137]. Therefore, it will consist of a constant component and a sum of even harmonics when the rotor changes its position. Moreover, the inductance of any phase is at a minimum value when the rotor flux direction is

aligned with the phase. Thus, the self and mutual inductances of PMSM can be written in matrix form as [4]:

$$\vec{L}_{abc}(\theta_r) = \begin{bmatrix} L_{aa} & M_{ab} & M_{ac} \\ M_{ba} & L_{bb} & M_{bc} \\ M_{ca} & M_{cb} & L_{cc} \end{bmatrix} = \begin{bmatrix} L_a & M_{ab,ba} & M_{ac,ca} \\ M_{ab,ba} & L_b & M_{bc,cb} \\ M_{ac,ca} & M_{bc,cb} & L_c \end{bmatrix} + \begin{bmatrix} L_{a2} \cos(2\theta_r) & M_{ab,ba2} \cos\left(2\theta_r - \frac{2\pi}{3}\right) & M_{ac,ca2} \cos\left(2\theta_r - \frac{4\pi}{3}\right) \\ M_{ab,ba2} \cos\left(2\theta_r - \frac{2\pi}{3}\right) & L_{b2} \cos\left(2\theta_r - \frac{4\pi}{3}\right) & M_{bc,cb2} \cos(2\theta_r) \\ M_{ac,ca2} \cos\left(2\theta_r - \frac{4\pi}{3}\right) & M_{bc,cb2} \cos(2\theta_r) & L_{c2} \cos\left(2\theta_r - \frac{2\pi}{3}\right) \end{bmatrix} \quad (3.6)$$

where L_a , L_b , and L_c are the average self-inductances of the stator phases a , b and c windings, respectively, L_{a2} , L_{b2} , and L_{c2} are the position dependant (sinusoidal componets or saliency components) self-inductacnces, $M_{ab,ba} = M_{ab} = M_{ba}$, $M_{ac,ca} = M_{ac} = M_{ca}$, $M_{bc,cb} = M_{bc} = M_{cb}$ and $M_{ab,ba2} = M_{ab2} = M_{ba2}$, $M_{ac,ca2} = M_{ac2} = M_{ca2}$, $M_{bc,cb2} = M_{bc2} = M_{cb2}$ are the average and position dependant stator phase mutual inductances [138]. The stator flux linkage produced by the PM consists of a fixed and sinusoidal components and the sum of odd harmonics when it is represented in stationary abc reference frame. If this assumption is valid, the three-phase flux linkage produced by the PM has only a fundamental component as indicated in (3.5). On the other hand, the electromagnetic torque generated by PMSM can be obtained by using the co-energy of the electromagnetic system derivations [139]. The co-energy is defined as:

$$W_c(i_a, i_b, i_c, \theta_r) = \int_0^{i_{a0}} \psi_a i_a (i_b = 0, i_c = 0, \theta_r) di_a + \int_0^{i_{b0}} \psi_b i_b (i_a = 0, i_c = 0, \theta_r) di_b + \int_0^{i_{c0}} \psi_c i_c (i_a = 0, i_b = 0, \theta_r) di_c \quad (3.7)$$

and the electromagnetic torque can be determined from the co-energy expression (3.7) as:

$$T_e(i_a, i_b, i_c, \theta_r) = \frac{dW_c}{d\theta_m} = p \frac{dW_c}{d\theta_r} \quad (3.8)$$

Solving (3.8), the expression of co-energy for PMSM in stationary abc reference frame is found to be

$$\begin{aligned}
W_c = & \frac{1}{2}(L_{aa}i_a^2 + L_{bb}i_b^2 + L_{cc}i_c^2) + (L_{aa}i_a i_b + L_{bb}i_a i_c + L_{cc}i_b i_c) \\
& + \psi_{PM} [\cos(\theta_r)i_a + \cos(\theta_r - \frac{2\pi}{3})i_b + \cos(\theta_r - \frac{4\pi}{3})i_c]
\end{aligned} \tag{3.9}$$

Thus, according to (3.9) the electromagnetic torque of the PMSM can be written as:

$$T_e = \vec{i}_{abc}^T \frac{d\psi_{rabc}(\theta_r)}{d\theta_m} + \frac{1}{2} \vec{i}_{abc}^T \left[\frac{dL_{abc}(\theta_r)}{d\theta_m} \right] \vec{i}_{abc} \tag{3.10}$$

where $\vec{i}_{abc}^T = [i_a \ i_b \ i_c]$ represent the transport form of the stator phase current i_{abc} . For a balanced and symmetrical PMSM with Y-connection, the sum of the three-phase stator currents is zero and given by:

$$i_a + i_b + i_c = 0 \tag{3.11}$$

The derivation of inductance matrix (3.6) is given by:

$$\frac{d\vec{L}_{abc}(\theta_r)}{d\theta_m} = 2p_n \begin{bmatrix} -L_{a2} \sin(2\theta_r) & -M_{ab,ba2} \sin\left(2\theta_r - \frac{2\pi}{3}\right) & -M_{ac,ca2} \sin\left(2\theta_r - \frac{4\pi}{3}\right) \\ -M_{ab,ba2} \sin\left(2\theta_r - \frac{2\pi}{3}\right) & -L_{b2} \sin\left(2\theta_r - \frac{4\pi}{3}\right) & -M_{bc,cb2} \sin(2\theta_r) \\ -M_{ac,ca2} \sin\left(2\theta_r - \frac{2\pi}{3}\right) & -M_{bc,cb2} \sin(2\theta_r) & -L_{c2} \sin\left(2\theta_r - \frac{2\pi}{3}\right) \end{bmatrix} \tag{3.12}$$

By substituting (3.12) into (3.10), the electromagnetic torque can be derived as:

$$T_e = -p_n \left\{ \begin{aligned} & \psi_{PM} \left[\sin(\theta_r)i_a + \sin\left(\theta_r - \frac{2\pi}{3}\right)i_b + \sin\left(\theta_r - \frac{4\pi}{3}\right)i_c \right] \\ & + \left[L_{a2} \sin(2\theta_r)i_a^2 + L_{b2} \sin\left(2\theta_r - \frac{4\pi}{3}\right)i_b^2 + L_{c2} \sin\left(2\theta_r - \frac{2\pi}{3}\right)i_c^2 \right] \\ & + 2 \left[M_{ab,ba2} \sin\left(2\theta_r - \frac{2\pi}{3}\right)i_a i_b + M_{ac,ca2} \sin\left(2\theta_r - \frac{4\pi}{3}\right)i_b i_c + M_{bc,cb2} \sin(2\theta_r)i_b i_c \right] \end{aligned} \right\} \tag{3.13}$$

Equation (3.13) represents a general form of the electromagnetic torque of PMSM with asymmetric windings described in a three-phase reference frame. However, when the machine windings are symmetrical, i.e., $L_{a2}=L_{b2}=L_{c2}=L_2$ and $M_{ab,ba2}=M_{ac,ca2}=M_{bc,cb2}=M_2$, (3.13) can be simplified as:

$$T_e = -p \left\{ \begin{array}{l} \psi_{PM} \left[\sin(\theta_r) i_a + \sin(\theta_r - \frac{2\pi}{3}) i_b + \sin(\theta_r - \frac{4\pi}{3}) i_c \right] \\ + L_2 \left[\sin(2\theta_r) i_a^2 + \sin(2\theta_r - \frac{4\pi}{3}) i_b^2 + \sin(2\theta_r - \frac{2\pi}{3}) i_c^2 \right] \\ + 2M_2 \left[\sin(2\theta_r - \frac{2\pi}{3}) i_a i_b + \sin(2\theta_r - \frac{4\pi}{3}) i_b i_c + \sin(2\theta_r) i_b i_c \right] \end{array} \right\} \quad (3.14)$$

In (3.14), the second and third components represent the reluctance torque components associated with a salient pole PM rotor. Generally, regarding the sinusoidal back-EMF PMSMs, all high order back-EMF harmonic components can be neglected. For a non-salient pole, symmetrical PMSM with a sinusoidal back-EMF both self and mutual inductance are zero, i.e., $L_2=M_2=0$, and then (3.14) can be written as:

$$T_e = -p \psi_{PM} \left[\sin(\theta_r) i_a + \sin(\theta_r - \frac{2\pi}{3}) i_b + \sin(\theta_r - \frac{4\pi}{3}) i_c \right] \quad (3.15)$$

As the electromagnetic torque produced by the machine is balanced with the mechanical load applied to its rotor shaft, the acceleration equation can be given by:

$$\frac{d\omega_m}{dt} = \frac{1}{J} (T_e - T_L - B\omega_m) \quad (3.16)$$

where ω_m is the mechanical angular speed, T_L is the applied load torque, J is the inertia constant, and B denotes the viscosity constant.

3.2.2. Representation of PMSM in stationary $\alpha\beta\theta$ -reference frame

3.2.2.1. Electromagnetic torque and stator flux linkage of salient PMSM

In this special case, the PMSM mathematical modeling assumes that:

- The machine is Y-connected (no zero sequence) and symmetrical with 90° electrical degrees between α - and β -axes;
- The inductance versus rotor position is sinusoidal;
- The phase a winding impedance is slightly increased by $\Delta Z_a = (1+\Delta)R_a + (1+\Delta)L_{aa}$;
- The flux produced by the PM in the stator is sinusoidal.

Then, the current, voltage and stator flux will consist of positive and negative sequence components due to different phase impedance as:

$$F_{abc} = F_{abc_sym} + F_{abc_asy} \quad (3.17)$$

where F could be voltage, current, and stator flux linkage, whereas the impedance (R_{abc} and L_{abc}) matrix in the stationary abc reference frame can be written as [140]:

$$R_{abc} = \begin{bmatrix} (1+\Delta)R_a & 0 & 0 \\ 0 & R_b & 0 \\ 0 & 0 & R_c \end{bmatrix} = \underbrace{\begin{bmatrix} R_a & 0 & 0 \\ 0 & R_b & 0 \\ 0 & 0 & R_c \end{bmatrix}}_{R_{abc_sym}} + \underbrace{\begin{bmatrix} \Delta R_a & 0 & 0 \\ 0 & 0 & 0 \\ 0 & 0 & 0 \end{bmatrix}}_{R_{abc_asy}} \quad (3.18)$$

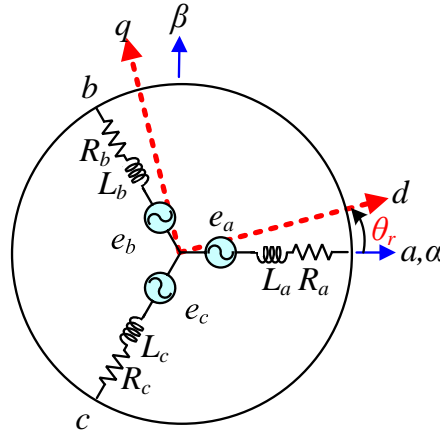


Fig. 3.1 Equivalent of three-phase winding in rotational reference frame.

$$L_{abc} = \begin{bmatrix} (1+\Delta)^2 L_{aa} & \Delta M_{ab} & \Delta M_{ac} \\ \Delta M_{ba} & L_{bb} & M_{bc} \\ \Delta M_{ca} & M_{cb} & L_{cc} \end{bmatrix} = \underbrace{\begin{bmatrix} L_{aa} & M_{ab} & M_{ac} \\ M_{ba} & L_{bb} & M_{bc} \\ M_{ca} & M_{cb} & L_{cc} \end{bmatrix}}_{L_{abc_sym}} + \underbrace{\begin{bmatrix} (\Delta^2 + 2\Delta)L_{aa} & \Delta M_{ab} & \Delta M_{ac} \\ \Delta M_{ba} & 0 & 0 \\ \Delta M_{ca} & 0 & 0 \end{bmatrix}}_{L_{abc_asy}} \quad (3.19)$$

According to [4] and from Fig. 3.1, the mathematical model in stationary $\alpha\beta 0$ reference frame is derived by using Clarke-transformation from stationary abc to stationary $\alpha\beta 0$ reference frames (refer to Appendix A). Thus, the parameter matrices in the stationary $\alpha\beta 0$ reference frame can be derived as:

$$R_{\alpha\beta 0} = [T_{\alpha\beta \leftarrow abc}] [R_{abc}] [T_{abc \leftarrow \alpha\beta}], \quad R_{\alpha\beta 0} = R_{\alpha\beta 0_sym} + R_{\alpha\beta 0_asy} \quad (3.20)$$

$$L_{\alpha\beta 0} = [T_{\alpha\beta \leftarrow abc}] [L_{abc}] [T_{abc \leftarrow \alpha\beta}], \quad L_{\alpha\beta 0} = L_{\alpha\beta 0_sym} + L_{\alpha\beta 0_asy} \quad (3.21)$$

where the healthy machine parameter (resistance and inductance) matrices under the assumption of $R_a=R_b=R_c=R_s$, $L_{aa}=L_{bb}=L_{cc}=L$, and $M_{ab}=M_{ba}=M_{ca}=M_{ac}=M_{bc}=M_{cb}=M$. Then, the symmetrical and asymmetric impedance matrices in the stationary $\alpha\beta 0$ reference frame can be derived as (mathematical derivation is given in Appendix B):

$$R_{\alpha\beta 0_sym} = \begin{bmatrix} \left(\frac{4}{6}R_a + \frac{1}{6}R_b + \frac{1}{6}R_c\right) & \left(\frac{1}{2\sqrt{3}}R_c - \frac{1}{2\sqrt{3}}R_b\right) & \left(\frac{2}{3}R_a - \frac{1}{3}R_b - \frac{1}{3}R_c\right) \\ \left(\frac{1}{2\sqrt{3}}R_c - \frac{1}{2\sqrt{3}}R_b\right) & R_b & \left(\frac{1}{2\sqrt{3}}R_b - \frac{1}{2\sqrt{3}}R_c\right) \\ \left(\frac{1}{3}R_a - \frac{1}{6}R_b - \frac{1}{6}R_c\right) & \left(\frac{1}{2\sqrt{3}}R_b - \frac{1}{2\sqrt{3}}R_c\right) & \left(\frac{1}{3}R_a + \frac{1}{3}R_b + \frac{1}{3}R_c\right) \end{bmatrix} \quad (3.22a)$$

$$= \begin{bmatrix} R_s & 0 & 0 \\ 0 & R_s & 0 \\ 0 & 0 & R_s \end{bmatrix}$$

$$R_{\alpha\beta 0_asy} = \begin{bmatrix} \frac{2}{3}\Delta R_a & 0 & \frac{2}{3}\Delta R_a \\ 0 & 0 & 0 \\ \frac{1}{3}\Delta R_a & 0 & 0 \end{bmatrix}. \quad (3.22b)$$

$$L_{\alpha\beta 0_sym} = \begin{bmatrix} (L-M) & 0 & - \\ 0 & (L-M) & - \\ - & - & - \end{bmatrix} + \begin{bmatrix} \left(\frac{1}{2}L_2 + M_2\right)\cos(2\theta_r) & \left(\frac{1}{2}L_2 + M_2\right)\sin(2\theta_r) & - \\ \left(\frac{1}{2}L_2 + M_2\right)\sin(2\theta_r) & -\left(\frac{1}{2}L_2 + M_2\right)\cos(2\theta_r) & - \\ - & - & - \end{bmatrix} \quad (3.23a)$$

$$L_{\alpha\beta 0_asy} = \begin{bmatrix} \left[\left(\frac{2}{3}\Delta^2 + \frac{4}{3}\Delta\right)L - \frac{4}{3}\Delta M\right] & 0 & \left[\left(\frac{2}{3}\Delta^2 + \frac{4}{3}\Delta\right)L + \frac{2}{3}\Delta M\right] \\ 0 & 0 & 0 \\ \left[\left(\frac{1}{3}\Delta^2 + \frac{4}{3}\Delta\right)L + \frac{1}{3}\Delta M\right] & 0 & \left[\left(\frac{1}{3}\Delta^2 + \frac{4}{3}\Delta\right)L + \frac{4}{3}\Delta M\right] \end{bmatrix} \quad (3.23b)$$

$$+ \begin{bmatrix} \left[\left(\frac{2}{3}\Delta^2 + \frac{4}{3}\Delta\right)L_2 + \left(\frac{2}{3}\Delta\right)M_2\right]\cos(2\theta_r) & (\Delta M_2)\sin(2\theta_r) & - \\ (\Delta M_2)\sin(2\theta_r) & 0 & - \\ - & - & - \end{bmatrix}.$$

The positive- and negative-sequence stator flux linkages of a salient PMSM can be derived as below:

$$\psi_{\alpha\beta\pm} = [L_{\alpha\beta_sym,asy}] [i_{\alpha\beta\pm}] + \psi_{r\alpha\beta\pm} \quad (3.24)$$

$$\psi_{\alpha+} = (L - M) i_{\alpha+} + \left(\frac{1}{2} L_2 + M_2 \right) \cos(2\theta_r) i_{\alpha+} + \left(\frac{1}{2} L_2 + M_2 \right) \sin(2\theta_r) i_{\beta+} + \psi_{r\alpha+} \quad (3.25)$$

$$\psi_{\beta+} = (L - M) i_{\beta+} + \left(\frac{1}{2} L_2 + M_2 \right) \sin(2\theta_r) i_{\alpha+} - \left(\frac{1}{2} L_2 + M_2 \right) \cos(2\theta_r) i_{\beta+} + \psi_{r\beta+}$$

$$\begin{aligned} \psi_{\alpha-} = & \left[\left(\frac{2}{3} \Delta^2 + \frac{4}{3} \Delta \right) L - \frac{4}{3} \Delta M \right] i_{\alpha-} + \left(\left(\frac{2}{3} \Delta^2 + \frac{4}{3} \Delta \right) L_2 + \frac{2}{3} \Delta M_2 \right) \cos(2\theta_r) i_{\alpha-} \\ & + \left(\frac{1}{2} L_2 + \Delta M_2 \right) \sin(2\theta_r) i_{\beta-} + \psi_{r\alpha-} \end{aligned} \quad (3.26)$$

$$\psi_{\beta-} = \left(\frac{1}{2} L_2 + \Delta M_2 \right) \sin(2\theta_r) i_{\alpha-} - \left(\frac{1}{2} L_2 + \Delta M_2 \right) \cos(2\theta_r) i_{\beta-} + \psi_{r\beta-}$$

while the positive- and negative- rotor PM fluxes can be expressed as:

$$\begin{aligned} \psi_{r\alpha+} &= \psi_{PM} \cos(\theta_r) \\ \psi_{r\beta+} &= \psi_{PM} \sin(\theta_r) \end{aligned} \quad (3.27)$$

$$\begin{aligned} \psi_{r\alpha-} &= \frac{2}{3} \Delta \psi_{PM} \cos(\theta_r) \\ \psi_{r\beta-} &= 0 \end{aligned} \quad (3.28)$$

Then, the final positive- and negative-sequence voltage equations in the stationary $\alpha\beta$ reference frame can be derived as:

$$v_{\alpha\beta} = v_{\alpha\beta+} + v_{\alpha\beta-} = \{ R_{\alpha\beta+} i_{\alpha\beta+} + \frac{d\psi_{\alpha\beta+}}{dt} \} + \{ R_{\alpha\beta-} i_{\alpha\beta-} + \frac{d\psi_{\alpha\beta-}}{dt} \} \quad (3.29)$$

and the electromagnetic torque can be expressed in the general form as

$$T_e = \vec{i}_{\alpha\beta 0}^T \frac{d\psi_{\alpha\beta 0}(\theta_r)}{d\theta_m} + \frac{1}{2} \vec{i}_{\alpha\beta 0}^T \left[\frac{dL_{\alpha\beta 0}(\theta_r)}{d\theta_m} \right] \vec{i}_{\alpha\beta 0} = T_{e+} + T_{e-} \quad (3.30)$$

$$T_{e+} = \frac{3}{2} P_n \left\{ \begin{aligned} & i_{\alpha+} \frac{d\psi_{\alpha+}}{d\theta_r} + i_{\beta+} \frac{d\psi_{\beta+}}{d\theta_r} - \left(\frac{1}{2} L_2 + M_2 \right) \sin(2\theta_r) i_{\alpha+}^2 \\ & + \left(\frac{1}{2} L_2 + M_2 \right) \sin(2\theta_r) i_{\beta+}^2 + (L_2 + 2M_2) \cos(2\theta_r) i_{\alpha+} i_{\beta+} \end{aligned} \right\} \quad (3.30a)$$

$$T_{e-} = \frac{3}{2} P_n \left\{ \begin{aligned} & i_{\alpha-} \frac{d\psi_{\alpha-}}{d\theta_r} + i_{\beta-} \frac{d\psi_{\beta-}}{d\theta_r} - \left[\left(\frac{2}{3} \Delta^2 + \frac{4}{3} \Delta \right) L_2 + \left(\frac{2}{3} \Delta \right) M_2 \right] \sin(2\theta_r) i_{\alpha-}^2 \\ & + (\Delta M_2) \sin(2\theta_r) i_{\beta-}^2 + (L_2 + 2\Delta M_2) \cos(2\theta_r) i_{\alpha-} i_{\beta-} \end{aligned} \right\} \quad (3.30b)$$

On the other hand, for a machine with Y-connected winding and sinusoidal back EMF all the high order harmonic components are neglected. Thus, the torque equation can be represented in terms of the positive- and negative-sequence flux and current components as:

$$\begin{aligned}
T_e &= 1.5p_n \operatorname{Im} \left\{ (\vec{\psi}'_{\alpha\beta\pm} \cdot \vec{i}_{\alpha\beta\pm}) \right\} \\
&= 1.5p_n \operatorname{Im} \left\{ (\vec{\psi}'_{\alpha\beta+} \cdot \vec{i}_{\alpha\beta+}) + (\vec{\psi}'_{\alpha\beta-} \cdot \vec{i}_{\alpha\beta-}) + (\vec{\psi}'_{\alpha\beta+} \cdot \vec{i}_{\alpha\beta-}) + (\vec{\psi}'_{\alpha\beta-} \cdot \vec{i}_{\alpha\beta+}) \right\} \\
&= 1.5p_n \left[\begin{aligned} &(\psi_{\alpha+} i_{\beta+} - \psi_{\beta+} i_{\alpha+}) + (\psi_{\alpha-} i_{\beta-} - \psi_{\beta-} i_{\alpha-}) \\ &+ (\psi_{\alpha+} i_{\beta-} - \psi_{\beta+} i_{\alpha-}) + (\psi_{\alpha-} i_{\beta+} - \psi_{\beta-} i_{\alpha+}) \end{aligned} \right]. \tag{3.31}
\end{aligned}$$

If the machine is balanced, i.e., $i_{\alpha\beta}=0$ and $\psi_{\alpha\beta}=0$, then, the electromagnetic torque can be simplified as:

$$T_e = 1.5p_n (\psi_{\alpha} i_{\beta} - \psi_{\beta} i_{\alpha}) \tag{3.32}$$

3.2.2.2. Electromagnetic torque and stator flux linkage equation of non-salient PMSM

For a non-salient PMSM, $L_2=M_2=0$. Whereas the positive and negative sequence flux linkage components, and the electromagnetic torque in the stationary $\alpha\beta$ reference frame are simpler than those in a salient PMSM, which can be presented as:

$$\begin{aligned}
\psi_{\alpha+} &= (L - M) i_{\alpha+} + \psi_{PM} \cos(\theta_r) \\
\psi_{\beta+} &= (L - M) i_{\beta+} + \psi_{PM} \sin(\theta_r). \tag{3.33}
\end{aligned}$$

$$\begin{aligned}
\psi_{\alpha-} &= \left[\left(\frac{2}{3} \Delta^2 + \frac{4}{3} \Delta \right) L - \frac{4}{3} \Delta M \right] i_{\alpha-} + \frac{2}{3} \Delta \psi_{PM} \cos(\theta_r) \\
\psi_{\beta-} &= 0. \tag{3.34}
\end{aligned}$$

and for the Y-connected winding PMSM, the electromagnetic torque is given by:

$$T_{e+} = \frac{3}{2} P_n \left\{ \frac{d\psi_{\alpha+}}{d\theta_r} i_{\alpha+} + \frac{d\psi_{\beta+}}{d\theta_r} i_{\beta+} \right\} \tag{3.35a}$$

$$T_{e-} = \frac{3}{2} P_n \left\{ \frac{d\psi_{\alpha-}}{d\theta_r} i_{\alpha-} \right\} \tag{3.35b}$$

Moreover, the electromagnetic torque for a Y-connected winding, non-salient sinusoidal back-EMF PMSM can be described as:

$$\begin{aligned}
T_e &= 1.5p_n \operatorname{Im}\left\{\left(\vec{\psi}'_{\alpha\beta\pm} \cdot \vec{i}_{\alpha\beta\pm}\right)\right\} = 1.5p_n \operatorname{Im}\left\{\left(\vec{\psi}'_{\alpha\beta+} \cdot \vec{i}_{\alpha\beta+}\right) + \left(\vec{\psi}'_{\alpha\beta-} \cdot \vec{i}_{\alpha\beta-}\right) + \left(\vec{\psi}'_{\alpha\beta+} \cdot \vec{i}_{\alpha\beta-}\right) + \left(\vec{\psi}'_{\alpha\beta-} \cdot \vec{i}_{\alpha\beta+}\right)\right\} \\
&= 1.5p_n \left[\left(\psi_{\alpha+} i_{\beta+} - \psi_{\beta+} i_{\alpha+}\right) + \left(\psi_{\alpha-} i_{\beta-} - \psi_{\beta-} i_{\alpha-}\right) + \left(\psi_{\alpha+} i_{\beta-} - \psi_{\beta+} i_{\alpha-}\right) + \left(\psi_{\alpha-} i_{\beta+} - \psi_{\beta-} i_{\alpha+}\right) \right]
\end{aligned} \tag{3.36}$$

For a balanced PMSM, the electromagnetic torque can be simplified as:

$$T_e = 1.5p_n (\psi_{\alpha} i_{\beta} - \psi_{\beta} i_{\alpha}) \tag{3.37}$$

3.2.3. Representation of PMSM in synchronous dq -reference frame

According to the reference frame transformation theory (refer to Appendix A and Appendix B), the symmetrical and asymmetric impedance matrices in the rotational $dq0$ reference frame can be derived as:

$$R_{dq0_sym} = \begin{bmatrix} R_d & 0 & 0 \\ 0 & R_q & 0 \\ 0 & 0 & R_0 \end{bmatrix} = \begin{bmatrix} R_s & 0 & 0 \\ 0 & R_s & 0 \\ 0 & 0 & R_s \end{bmatrix} \tag{3.38a}$$

$$R_{dq0_asy} = \frac{2}{3} \Delta R_a \underbrace{\begin{bmatrix} \cos^2(\theta_r) & \cos(\theta_r) \sin(\theta_r) & \frac{1}{2} \cos(\theta_r) \\ \sin(\theta_r) \cos(\theta_r) & \sin^2(\theta_r) & \frac{1}{2} \sin(\theta_r) \\ \frac{1}{2} \cos(\theta_r) & \frac{1}{2} \sin(\theta_r) & 0 \end{bmatrix}}_{R_{dq0-}} \tag{3.38b}$$

$$L_{dq0_sym} = \begin{bmatrix} (L-M) & 0 & - \\ 0 & (L-M) & - \\ - & - & - \end{bmatrix} + \begin{bmatrix} -\left(\frac{1}{2}L_2 + M_2\right) & 0 & - \\ 0 & \left(\frac{1}{2}L_2 + M_2\right) & - \\ - & - & - \end{bmatrix} \tag{3.39a}$$

$$L_{dq0_asy} = \begin{bmatrix} \left[\left(\frac{2}{3} \Delta^2 + \frac{4}{3} \Delta \right) L - \frac{4}{3} \Delta M \right] \cos^2(\theta_r) & \left[\left(\frac{2}{3} \Delta^2 + \frac{4}{3} \Delta \right) L - \frac{4}{3} \Delta M \right] \cos(\theta_r) \sin(\theta_r) & - \\ \left[\left(\frac{2}{3} \Delta^2 + \frac{4}{3} \Delta \right) L - \frac{4}{3} \Delta M \right] \cos(\theta_r) \sin(\theta_r) & \left[\left(\frac{2}{3} \Delta^2 + \frac{4}{3} \Delta \right) L - \frac{4}{3} \Delta M \right] \sin^2(\theta_r) & - \\ - & - & - \end{bmatrix} + \begin{bmatrix} \Delta L_{d2-}(\theta_r) & \Delta M_{dq2-}(\theta_r) & - \\ \Delta M_{qd2-}(\theta_r) & \Delta L_{q2-}(\theta_r) & - \\ - & - & - \end{bmatrix} \quad (3.39b)$$

The positive and negative voltage components represented in the positive and negative SRF can be presented as:

$$\begin{aligned} v_{d+}^+ &= R_{d_sym} i_{d+}^+ + \frac{d\psi_{d+}^+}{dt} - \omega_r \psi_{q+}^+ \\ v_{q+}^+ &= R_{q_sym} i_{q+}^+ + \frac{d\psi_{q+}^+}{dt} + \omega_r \psi_{d+}^+ \end{aligned} \quad (3.40)$$

$$\begin{aligned} v_{d-}^- &= R_{d_asy} i_{d-}^- + \frac{d\psi_{d-}^-}{dt} - \omega_r \psi_{q-}^- \\ v_{q-}^- &= R_{q_asy} i_{q-}^- + \frac{d\psi_{q-}^-}{dt} + \omega_r \psi_{d-}^- \end{aligned} \quad (3.41)$$

where v_{dq+}^+ , i_{dq+}^+ , ψ_{dq+}^+ are the positive sequence components of voltage, current, flux in the positive SRF, respectively, v_{dq-}^- , i_{dq-}^- , ψ_{dq-}^- are the negative sequence components of voltage, current, flux in the negative SRF, R_{dq_sym} , R_{dq_asy} are the symmetrical and asymmetric resistances, and ω_r is the electrical speed rad/sec. The next section presents the stator linkage flux and electromagnetic torque of salient and non-salient PMSMs in positive and negative $dq0^\pm$ synchronous reference frames.

3.2.3.1. Electromagnetic torque and stator flux linkage equation of salient PMSM

The flux positive and negative sequence components can be represented as

$$\begin{aligned} \psi_{d+} &= L_{d_sym} i_{d+} + \psi_{rd+} \\ \psi_{q+} &= L_{q_sym} i_{q+} + \psi_{rq+}. \end{aligned} \quad (3.42a)$$

$$\begin{aligned} \psi_{d-} &= L_{d_asy} i_{d-} + \psi_{rd-} \\ \psi_{q-} &= L_{q_asy} i_{q-} + \psi_{rq-}. \end{aligned} \quad (3.42b)$$

$$L_{d_sym} = [(L - M) - (\frac{1}{2}L_2 + M_2)] \quad (3.43a)$$

$$L_{q_sym} = [(L - M) + (\frac{1}{2}L_2 + M_2)]$$

$$L_{d_asy} = [[(\frac{2}{3}\Delta^2 + \frac{4}{3}\Delta)L - \frac{4}{3}\Delta M] \cos^2(\theta_r) + L_{d2-}] \quad (3.43b)$$

$$L_{q_asy} = [[(\frac{2}{3}\Delta^2 + \frac{4}{3}\Delta)L - \frac{4}{3}\Delta M] \sin^2(\theta_r) + L_{q2-}]$$

Then, the electromagnetic torque can be calculated by:

$$T_e = \vec{i}_{sq0}^T \frac{d\psi_{dq0}(\theta_r)}{d\theta_m} + \frac{1}{2} \vec{i}_{dq0}^T \left[\frac{dL_{dq0}(\theta_r)}{d\theta_m} \right] \vec{i}_{dq0} = T_{e+} + T_{e-} \quad (3.44)$$

$$T_{e+} = \frac{3}{2} P_n \left\{ \left(\frac{d\psi_{d+}}{d\theta_r} - \psi_{rq+} \right) i_{d+} + \left(\frac{d\psi_{q+}}{d\theta_r} + \psi_{rd+} \right) i_{q+} + (L_2 + 2M_2) i_{d+} i_{q+} \right\} \quad (3.44a)$$

$$T_{e-} = \frac{3}{2} P_n \left\{ \frac{d\psi_{d-}}{d\theta_r} i_{d-} + \frac{d\psi_{q-}}{d\theta_r} i_{q-} \right\} \quad (3.44b)$$

where $d\psi_{d+}/d\theta_r \neq 0$ and $d\psi_{q+}/d\theta_r \neq 0$ for non-sinusoidal back EMF PMSM. On the other hand, for sinusoidal back-EMF PMSM, the high order harmonic components are neglected, and the rotor flux can be simplified as:

$$\begin{aligned} \psi_{rd+} &= \psi_{PM} \\ \psi_{rq+} &= 0. \end{aligned} \quad (3.45a)$$

$$\begin{aligned} \psi_{rd-} &= \Delta \psi_{PM} \\ \psi_{rq-} &= 0. \end{aligned} \quad (3.45b)$$

The stator flux linkage and electromagnetic torque of the salient PMSM with sinusoidal back-EMF and Y-connection winding can be written as:

$$\begin{aligned} \psi_{d+} &= L_{d_sym} i_{d+} + \psi_{PM} \\ \psi_{q+} &= L_{q_sym} i_{q+}. \end{aligned} \quad (3.46a)$$

$$\begin{aligned} \psi_{d-} &= L_{d_asy} i_{d-} + \Delta \psi_{PM} \\ \psi_{q-} &= L_{q_asy} i_{q-}. \end{aligned} \quad (3.46b)$$

$$T_{e+} = \frac{3}{2} P_n (\psi_{d+} i_{q+} - \psi_{q+} i_{d+}) = \frac{3}{2} P_n [\psi_{PM} i_{q+} + (L_{d+} - L_{q+}) i_{d+} i_{q+}] \quad (3.47a)$$

$$T_{e-} = \frac{3}{2} P_n (\psi_{d-} i_{q-} - \psi_{q-} i_{d-}) = \frac{3}{2} P_n [\Delta \psi_{PM} i_{q-} + (L_{d-} - L_{q-}) i_{d-} i_{q-}] \quad (3.47b)$$

3.2.3.2. Electromagnetic torque and stator flux linkage equation of non-salient PMSM

For Y-connection winding, non-salient PMSM, i.e., $L_2=M_2=0$ and $i_0=0$, the electromagnetic torque equation in the positive SRF can be simplified as:

$$T_e^+ = 1.5p_n \text{Im}\left\{\langle \bar{\psi}_{dq^+}^+, \bar{i}_{dq^+}^+ \rangle\right\} = 1.5p_n \left[\begin{aligned} &(\psi_{d+}^+ i_{q+}^+ - \psi_{q+}^+ i_{d+}^+) + (\psi_{d-}^- i_{q-}^- - \psi_{q-}^- i_{d-}^-) \\ &+ (\psi_{d+}^+ i_{q-}^- - \psi_{q+}^+ i_{d-}^-) + (\psi_{d-}^- i_{q+}^+ - \psi_{q-}^- i_{d+}^+) \end{aligned} \right] \quad (3.48)$$

3.3. System Behavior under Unbalanced Conditions

3.3.1. Symmetrical components

As discussed earlier, when there is a slightly change between the three-phase winding impedances, the electrical variables of voltage, current, and stator flux linkage can be decomposed into their positive-, negative-, and zero sequence components. For Y-connected winding, the zero sequence components are neglected. Generally, the symmetrical components (also known as sequential components) have interesting features of which any unbalanced three-phase system can be represented into three sets of balanced components as shown in Fig. 3.2 [141].

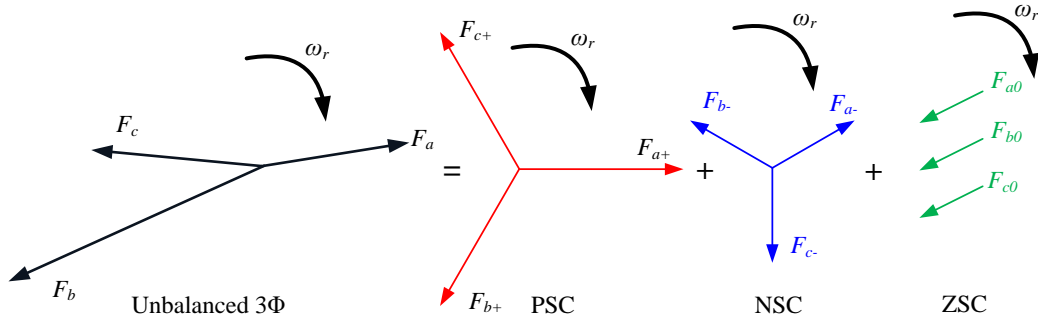


Fig. 3.2 Definition of sequential components [141]

In Fig. 3.2, the factor F can be any variables, i.e., voltage, current or flux-linkage, and the subscript of “+”, “-”, and “0” denote positive-, negative-, and zero-sequence components, respectively. Hence, the unbalanced vectors can be represented as the sum of three sequence vectors as shown below [141], [142]:

$$F_a = F_{a0} + F_{a+} + F_{a-} \quad (3.49a)$$

$$F_b = F_{b0} + F_{b+} + F_{b-} \quad (3.49b)$$

$$F_c = F_{c0} + F_{c+} + F_{c-} \quad (3.49c)$$

The mathematical expression (3.49) contain nine variable vectors, i.e., F_{a0} , F_{b0} , F_{c0} , F_{a+} , F_{b+} , F_{c+} , F_{a-} , F_{b-} , F_{c-} , in a system of three equations. From the definition of symmetrical components, each set has only one shared vector in system equations. For simplicity, let the operated “ a ” defined as:

$$a = 1\angle 120^\circ; \quad a^2 = 1\angle 240^\circ; \quad a^3 = 1\angle 0^\circ \quad (3.50)$$

Then, the relationship of symmetrical component refers to vector F_a can be derived as:

$$F_{b0} = F_{a0}; \quad F_{c0} = F_{a0} \quad (3.51a)$$

$$F_{b+} = a^2 F_{a+}; \quad F_{c+} = a F_{a+} \quad (3.51b)$$

$$F_{b-} = a F_{a-}; \quad F_{c-} = a^2 F_{a-} \quad (3.51c)$$

Substituting equation (3.61) into (3.49), the system equations can be represented in terms of operator ‘ a ’ in the matrix form is shown in below:

$$\begin{bmatrix} F_a \\ F_b \\ F_c \end{bmatrix} = \begin{bmatrix} 1 & 1 & 1 \\ 1 & a^2 & a \\ 1 & a & a^2 \end{bmatrix} \begin{bmatrix} F_{a0} \\ F_{a+} \\ F_{a-} \end{bmatrix}; \quad \begin{bmatrix} F_a \\ F_b \\ F_c \end{bmatrix} = A \begin{bmatrix} F_{a0} \\ F_{a+} \\ F_{a-} \end{bmatrix} \quad (3.52)$$

where A is the “ a ” operator matrix. Then, the positive, negative, and zero-sequence components can be obtained by taking the inverse of (3.52) as:

$$\begin{bmatrix} F_{a0} \\ F_{a+} \\ F_{a-} \end{bmatrix} = A^{-1} \begin{bmatrix} F_a \\ F_b \\ F_c \end{bmatrix}; \quad \begin{bmatrix} F_{a0} \\ F_{a+} \\ F_{a-} \end{bmatrix} = \frac{1}{3} \begin{bmatrix} 1 & 1 & 1 \\ 1 & a & a^2 \\ 1 & a^2 & a \end{bmatrix} \begin{bmatrix} F_a \\ F_b \\ F_c \end{bmatrix} \quad (3.53)$$

In the same manner of getting (3.51), it is possible to solve for phase b and c to obtain the instantaneous three-phase positive and negative sequence components of these phases. The final sequential component equations can be expressed as [143]:

$$\begin{bmatrix} F_{a+} \\ F_{b+} \\ F_{c+} \end{bmatrix} = \frac{1}{3} \underbrace{\begin{bmatrix} 1 & a & a^2 \\ a^2 & 1 & a \\ a & a^2 & 1 \end{bmatrix}}_{[T_{abc+}]} \begin{bmatrix} F_a \\ F_b \\ F_c \end{bmatrix} \quad (3.54a)$$

$[F_{abc+}]$ $[T_{abc+}]$ $[F_{abc}]$

$$\begin{bmatrix} F_{a-} \\ F_{b-} \\ F_{c-} \end{bmatrix} = \frac{1}{3} \underbrace{\begin{bmatrix} 1 & a^2 & a \\ a & 1 & a^2 \\ a^2 & a & 1 \end{bmatrix}}_{[T_{abc-}]} \begin{bmatrix} F_a \\ F_b \\ F_c \end{bmatrix} \quad (3.54b)$$

where $[T_{abc+}]$ and $[T_{abc-}]$ are the positive and negative sequence extracting matrixes. Moreover, the complex form of the operator “ a ” and “ a^2 ” is

$$a^2 = -\frac{1}{2} + j\frac{\sqrt{3}}{2} \quad \text{and} \quad a = -\frac{1}{2} - j\frac{\sqrt{3}}{2} \quad (3.55)$$

Substituting the complex form of “ a ” into (3.54), the positive and negative sequence components in phase frame can be calculated as:

$$\begin{bmatrix} F_{a+} \\ F_{b+} \\ F_{c+} \end{bmatrix} = \begin{bmatrix} \frac{1}{3} & -\frac{1}{6} & -\frac{1}{6} \\ -\frac{1}{2} & \frac{1}{3} & -\frac{1}{2} \\ -\frac{1}{2} & -\frac{1}{2} & \frac{1}{3} \end{bmatrix} \begin{bmatrix} F_a \\ F_b \\ F_c \end{bmatrix} - \frac{1}{j2\sqrt{3}} \begin{bmatrix} 0 & 1 & -1 \\ -1 & 0 & 1 \\ 1 & -1 & 0 \end{bmatrix} \begin{bmatrix} F_a \\ F_b \\ F_c \end{bmatrix} \quad (3.56a)$$

$$\begin{bmatrix} F_{a-} \\ F_{b-} \\ F_{c-} \end{bmatrix} = \begin{bmatrix} \frac{1}{3} & -\frac{1}{6} & -\frac{1}{6} \\ -\frac{1}{2} & \frac{1}{3} & -\frac{1}{2} \\ -\frac{1}{2} & -\frac{1}{2} & \frac{1}{3} \end{bmatrix} \begin{bmatrix} F_a \\ F_b \\ F_c \end{bmatrix} + \frac{1}{j2\sqrt{3}} \begin{bmatrix} 0 & 1 & -1 \\ -1 & 0 & 1 \\ 1 & -1 & 0 \end{bmatrix} \begin{bmatrix} F_a \\ F_b \\ F_c \end{bmatrix} \quad (3.56b)$$

The operator “ j ” refers to the imaginary part of the complex number, which can be represented in the real time-domain by a 90° phase shift delay. These two sets of equations can be used to extract the positive and negative sequence components in stationary abc reference frame as shown in Fig. 3.3 [144].

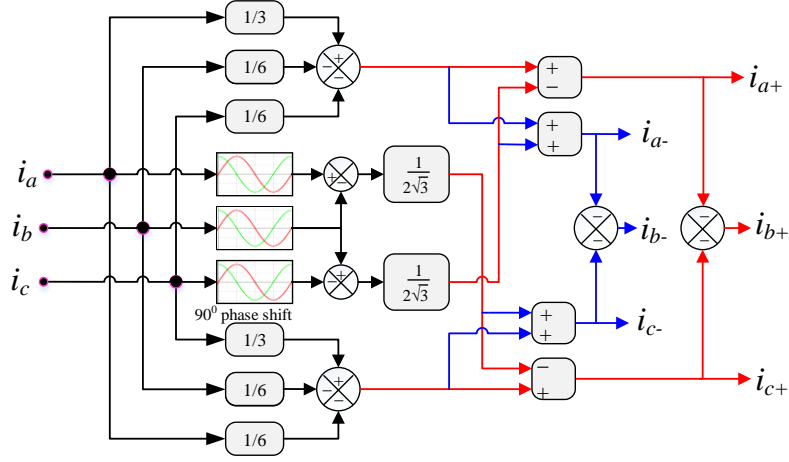


Fig. 3.3 Sequential components extraction in the stationary abc reference frame.

Furthermore, from the coordination transformations theory, the variables in the stationary abc can be presented in the stationary $\alpha\beta$ reference frame using *Clark* transformation matrix as:

$$\begin{bmatrix} F_{\alpha+} \\ F_{\beta+} \\ F_{\alpha\beta+} \end{bmatrix} = [T_{\alpha\beta \leftarrow abc}] [F_{abc+}] \quad (3.57a)$$

$$\begin{bmatrix} F_{\alpha-} \\ F_{\beta-} \\ F_{\alpha\beta-} \end{bmatrix} = [T_{\alpha\beta \leftarrow abc}] [F_{abc-}] \quad (3.57b)$$

Substituting (3.57) into (3.54) yields:

$$[F_{\alpha\beta+}] = [T_{\alpha\beta \leftarrow abc}] [T_{abc+}] [F_{abc}] \quad (3.58a)$$

$$[F_{\alpha\beta-}] = [T_{\alpha\beta \leftarrow abc}] [T_{abc-}] [F_{abc}] \quad (3.58b)$$

Taking the inverse of $[T_{\alpha\beta \leftarrow abc}]^{-1} = [T_{abc \leftarrow \alpha\beta}]$, then the positive- and negative-sequence components in the stationary $\alpha\beta$ reference frame can be calculated by:

$$[F_{\alpha\beta+}] = [T_{\alpha\beta \leftarrow abc}] [T_{abc+}] [T_{abc \leftarrow \alpha\beta}] [F_{\alpha\beta}], \quad [F_{\alpha\beta+}] = [T_{\alpha\beta+}] [F_{\alpha\beta}] \quad (3.59a)$$

$$[F_{\alpha\beta-}] = [T_{\alpha\beta \leftarrow abc}] [T_{abc-}] [T_{abc \leftarrow \alpha\beta}] [F_{\alpha\beta}], \quad [F_{\alpha\beta-}] = [T_{\alpha\beta-}] [F_{\alpha\beta}] \quad (3.59b)$$

where $[T_{\alpha\beta+}] = \frac{1}{2} \begin{bmatrix} 1 & -q \\ q & 1 \end{bmatrix}$, $[T_{\alpha\beta-}] = \frac{1}{2} \begin{bmatrix} 1 & q \\ -q & 1 \end{bmatrix} \begin{bmatrix} F_{\alpha} \\ F_{\beta} \end{bmatrix}$

and q is a phase-shift operator in the time-domain, which can be obtained by dealing the signal by a quadrature-phase shift (90°) from its original signal. In fact, this signal delay can be used for sequential components extractor or modeling the imaginary part “ j ” of the complex number in the real-time. Therefore, different quadrature single generation techniques have been presented such as all-pass filter [131], [144], adaptive notch filter (AF) [72], [129], [145], second-order adaptive filter [146], [147], Hilbert transformation-based phase lock loop (PLL) (HT-PLL) [148], [149], and inverse park transformation-based PLL (IPT-PLL). However, some of them are also complex or only operate at fixed frequency. In the next section, a brief discussion of the most popular techniques including the proposed one is provided.

3.3.2. Quadrature-signal generation (QSG) techniques

3.3.2.1. Adaptive filters based on generalized integration

To date, many techniques based on adaptive filter have been proposed. The most common one is the adaptive filter based on generalized integration (GI) or second order adaptive filter based generalized integration (SOGI), which was discussed in Chapter 1, section § 1.3.5, and further information can be found in [146], [147], [150].

3.3.2.2. Hilbert transform

The Hilbert filter is also used for phase detection or Quadrature-signal delay generation that can be used for SCE, it is based on Fourier analysis of the input signals, which presents two main features:

- Generating $\pm 90^\circ$ phase-angle shifts of the spectral components of the input signal depending on the sign of their frequency;
- Only effects on the phase shift and there is no effect on signal amplitude.

Therefore, as presented in reference [150], a PLL based on the Hilbert transform can be implemented as shown in Fig. 3.4. The time domain expression of the Hilbert transform of a given input signal v is defined as:

$$H(F) = \frac{1}{\pi} \int_{-\infty}^{\infty} \frac{F(\tau)}{t - \tau} d\tau = \frac{1}{\pi t} * F \quad (3.60)$$

which describes the convolution product of the function $h(t) = 1/\pi t$ with the signal $F(t)$. In the frequency domain, the Hilbert transform can be defined as

$$F_T(H(F)) = F_T\left(\frac{1}{\pi t}\right)F_T(F) = [-j \text{sign}(\omega)]F_T(F) \quad (3.61)$$

where F_T is the Fourier transform and $\text{sign}(\omega)$ gives the sign of the F frequency. Therefore, in the frequency domain, the Hilbert filter can be understood as a multiplier operator $\sigma_H(\omega) = -j \text{sign}(\omega)$, which can take the following values:

$$\sigma_H(\omega) = \begin{cases} -j & \text{if } \omega > 0 \\ 0 & \text{if } \omega = 0 \\ j & \text{if } \omega < 0 \end{cases} \quad (3.62)$$

Thus, the Hilbert transform has the effect of shifting the phase-angle of positive frequency components by -90° [148], [149].

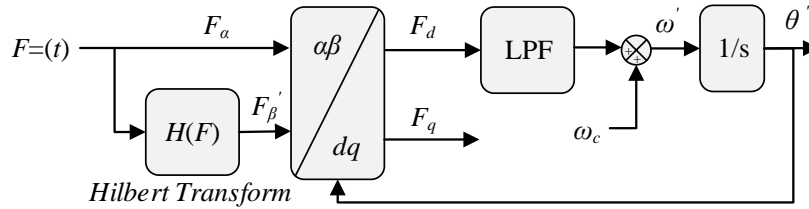


Fig. 3.4 PLL based on the Hilbert transform.

3.3.2.3. Implementation of new method of a quadrature-signal delay algorithm

When $T_s = 1/f_s$ is the fundamental frequency period, then $T_s/4$ is the simplest way to achieve a quarter signal generation. To implement such a delay under variable speeds, an algorithm based on the concept of variable integer sampling delay is written using MATLAB s-functions. This algorithm does not provide any filtering capability. It is able to delay the discrete-time input signals at the *In port* by integer numbers of samples equal to $T_s/4$. The variable integer delay stores the information (magnitude) of the most recent samples received from the input signal, then the outputs is the stored sample(s) shifted by the input to the delay port. i.e., if $F(t)$ is a periodic scalar input signal, the algorithm stores a vector of $V+1$, the most recent signal samples. When the current input sample is $F(1)$, the previous input sample is $F(2)$, and so on, then the program output is $Y(1)=V(1+D(1))$, where $D(1)$ is the integer number of the samples at input of the delay port in which a quarter signal delay is satisfied. For variable speed, the 90° phase shift can be calculated in samples using the expression $D(1) = \frac{1}{4 T_s f_s(1)}$, where $f_s(1)$ is the fundamental frequency at the instant of sampling one. This process is

repeated instantaneously for all samples. In this manner, it can ensure the fast and effective way to generate quadrature-signal delay.

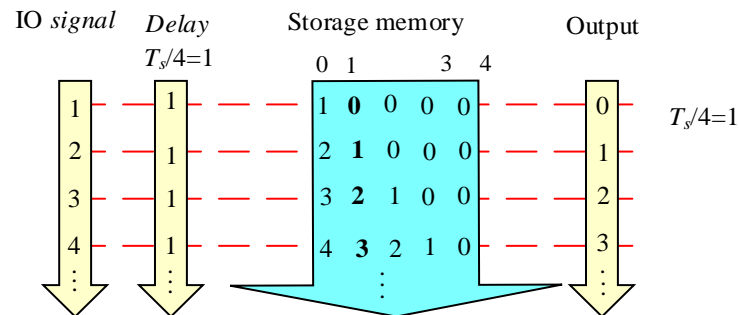


Fig. 3.5 Proposed quarter signal generation based on the integer sample delay.

The input to the unit is initially a set of balanced three-phase sinusoidal waveforms, since the system is balanced and the negative-sequence components do not exist. Then, at $t=0.4s$ a gain of 0.2 is subtracted from phase A amplitude, and at $t=0.7$ another gain of 0.2 is added to phase C. These cases simulate one-phase and three-phase unbalances, respectively. It is clear from Fig. 3.6 that the proposed algorithm has a fast dynamic response and accurate performance in terms of extraction of the positive and negative-sequence components. After the extraction of positive and negative components, a DSRF strategy is employed. Fig. 3.6(a) shows the schematic diagram of the conventional DSRF, while the proposed DSRF is shown in Fig. 3.6(b), and the structure of the positive and negative-sequence extraction unit is shown in Fig. 3.6(c). It can be seen that the proposed approach does not require any filters. Therefore, it has very simple structure, but powerful to control the currents under unbalanced condition, as will be verified by detailed experimental results.

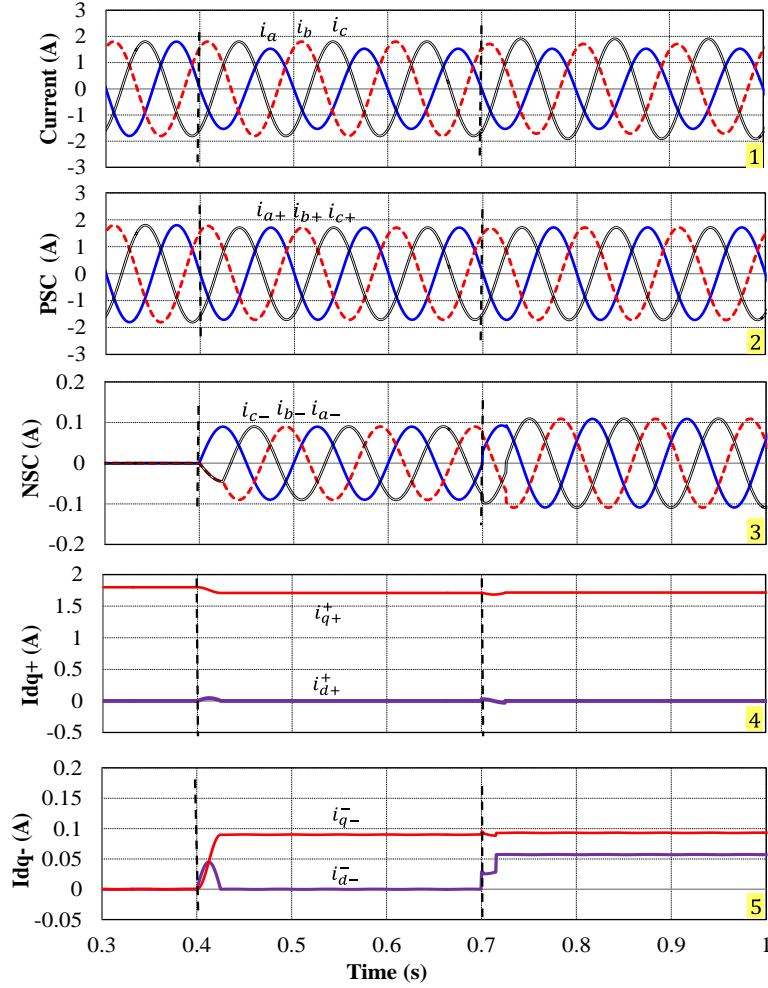


Fig. 3.6 Current behavior in the DSRF.

3.4. Proposed Current Control Method

Current control based on single-SRF is one of the most common strategy for electrical machines under balanced condition. The major benefits of this scheme is that all voltages and currents have DC values in the SRF, which are the projection of i_{abc} in the stationary frame. As long as the DC quantities are involved, the implementation of the classical PI-regulator will be suitable to achieve the desired performance. However, when the machine windings are asymmetric, the negative-sequence components will exist as shown in Fig. 3.7. Thus, the voltages or currents in the stationary $\alpha\beta$ reference frame can be represented by the sum of their positive and negative sequences components as

$$\vec{F}_{\alpha\beta} = \vec{F}_{\alpha\beta+} + \vec{F}_{\alpha\beta-} = \vec{F}_{dq+} e^{j\omega_r t} + \vec{F}_{dq-} e^{-j\omega_r t} \quad (3.63)$$

where F represent the stator voltage, current, or flux linkage vectors. Moreover, the vector F can be represent in the rotational positive synchronous (dq^+) reference frame, or negative synchronous (dq^-) reference frame as [151], [152]

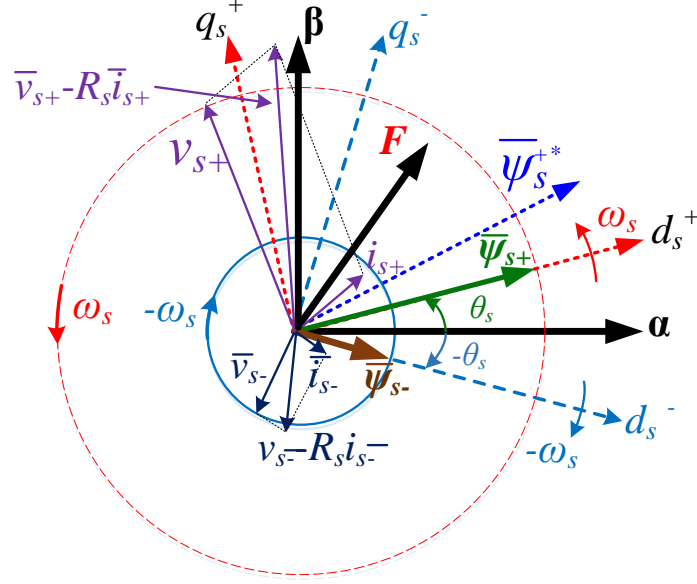


Fig. 3.7 Spatial relations between different reference frames.

$$\vec{F}_{dq}^+ = \vec{F}_{dq+}^+ + \vec{F}_{dq-}^- e^{-j2\omega_s t}, \quad \begin{bmatrix} F_d^+ \\ F_q^+ \end{bmatrix} = \underbrace{\begin{bmatrix} F_{d+}^+ \\ F_{q+}^+ \end{bmatrix}}_{DC \text{ terms}} + \underbrace{\begin{bmatrix} F_{d-}^- \cos(2\theta_r^+) + F_{q-}^- \sin(2\theta_r^+) \\ -F_{d-}^- \sin(2\theta_r^+) + F_{q-}^- \cos(2\theta_r^+) \end{bmatrix}}_{AC \text{ terms}} \quad (3.64a)$$

$$\vec{F}_{dq}^- = \vec{F}_{dq-}^- + \vec{F}_{dq+}^+ e^{j2\omega_s t}, \quad \begin{bmatrix} F_d^- \\ F_q^- \end{bmatrix} = \underbrace{\begin{bmatrix} F_{d-}^- \\ F_{q-}^- \end{bmatrix}}_{DC \text{ terms}} + \underbrace{\begin{bmatrix} F_{d+}^+ \cos(2\theta_r^-) + F_{q+}^+ \sin(2\theta_r^-) \\ -F_{d+}^+ \sin(2\theta_r^-) + F_{q+}^+ \cos(2\theta_r^-) \end{bmatrix}}_{AC \text{ terms}} \quad (3.64b)$$

where $\theta_r^+ = \omega_r t$ and $\theta_r^- = -\omega_r t$, in (3.64) the currents in both positive (i_{dq}^+) and negative (i_{dq}^-) SRFs are not pure DC components due to the cross-coupling effect. It can be deduced that the amplitude of the AC components $|i_{dq-}^-|$ in the positive SRF is matched to the DC components in the negative SRF and oscillating at the frequency of $2\omega_r$ and vice versa. Fig. 3.9 shows the unbalanced three phase currents and their projection in the positive and negative SRFs. The negative sequence components can cause rapid heating and have more damaging effect on the rotor because of producing the $2\omega_r$ frequency in the rotor.

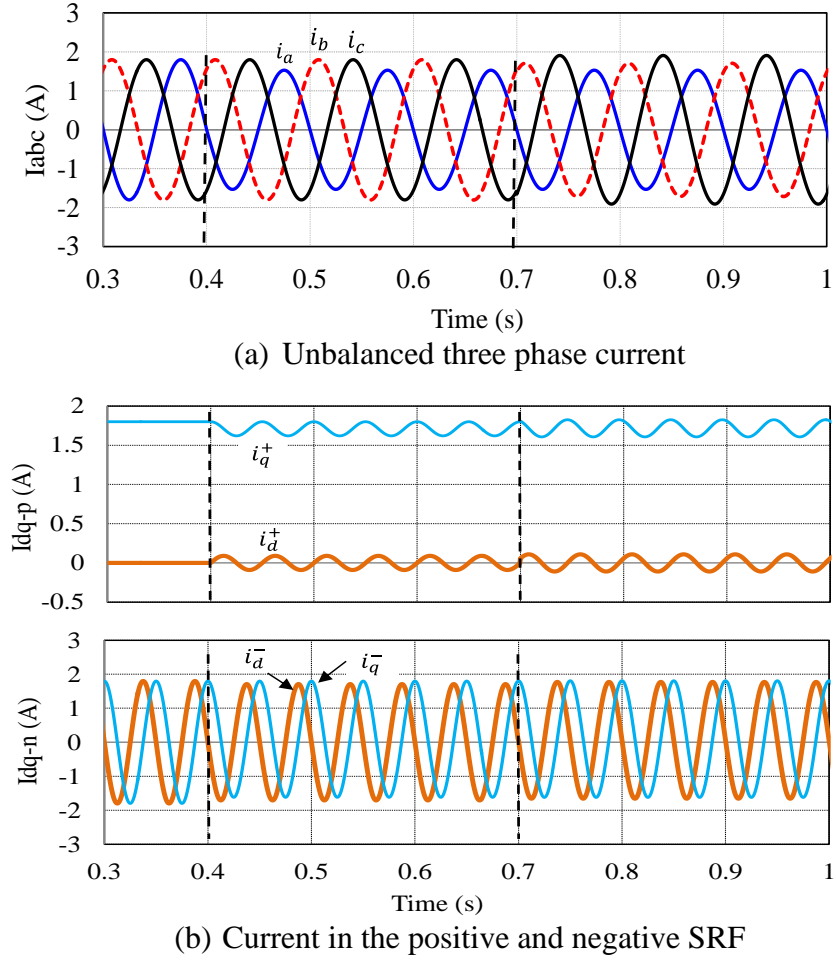


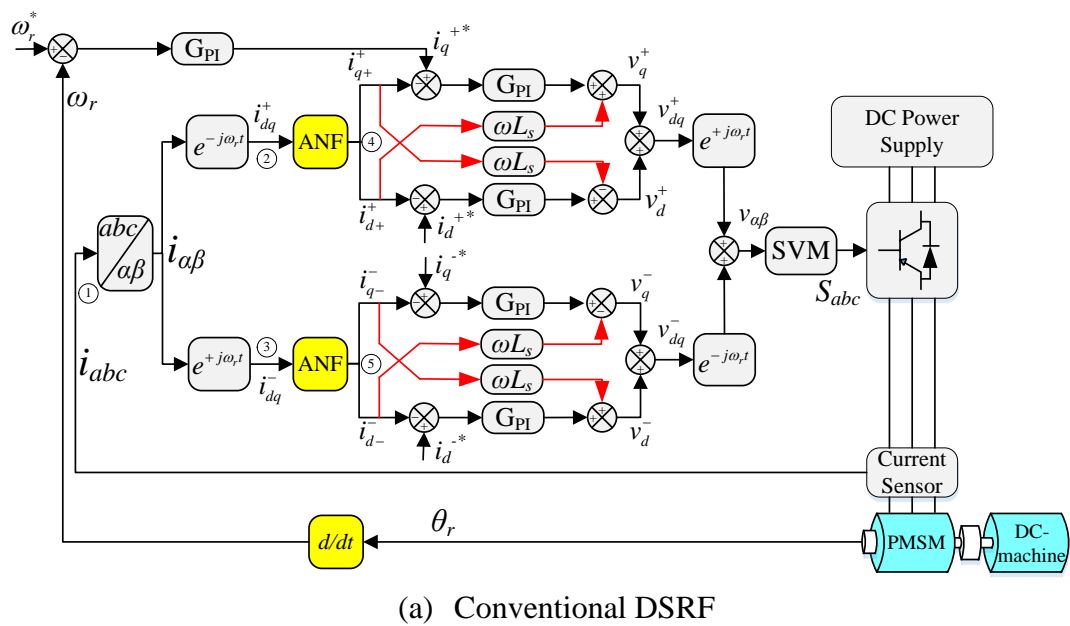
Fig. 3.8 Current behavior in the DSRF.

Hence, a DSRFs control strategy is one of most popular strategies [72], [73], [80]. It utilized two independent SRF controller, one for the positive sequence component (two PI-regulators for d - and q -axes) rotating in positive SRF, and another for the negative-sequence components (two PI-regulators for d - and q -axes) rotates in the negative-sequence direction. Essentially, when the tracking references are DC quantities, the resulting errors between the reference and the measured feedback currents will oscillate at twice of the fundamental frequency at the input of PI-controller. These errors cannot be control by using the conventional PI-regulator due to its limited bandwidth [77]. Therefore, many contributions were presented to cancel out these oscillations before delivering to the PI-regulators, such as filtering the measured currents in conventional DSRF, decoupling network and specified reference currents generation [72], [79], [129] (see Chapter 1 section §1.3.4 for further discussion), which are significantly increased the computational burdens and deteriorate the dynamic performance.

3.5. Experimental Validations

The experimental hardware platform to evaluate the effectiveness of the proposed control strategy is constructed based on dSPACE DS1006 in which the sampling frequency of the current control loop is 10 kHz, which is the same as the modulation frequency of SVM. The surface mounted PM motor, whose design parameters are given in Chapter 2 [25] is used.

Fig. 3.9 shows the schematic diagram of the conventional DSRF with AF and the proposed strategy. Furthermore, to simulate the unbalanced condition in a PM motor, the impedance ($Z_{exA}=0.6\Omega+2mH$) and resistance ($R_{exB}=0.9\Omega$) are deliberately connected in series with phase A and phase B, respectively. The system operates in the constant torque region, and the reference current in the positive SRF i_q^{*+} is 1.8A. The steady-state performances of the conventional, Fig. 3.9 (a), and the proposed DSRFs control strategies, Fig. 3.9 (b), are compared.



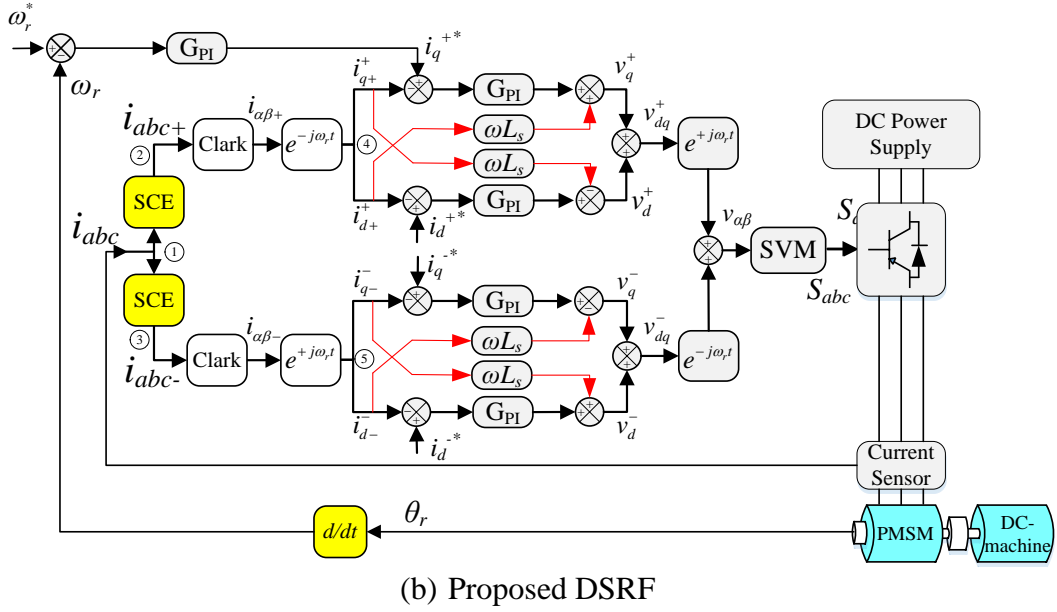


Fig. 3.9 Schematic diagram of the conventional and proposed DSRF strategies.

In the conventional DSRF control strategy, the currents i_{dq}^+ and i_{dq}^- in the positive and negative SRFs are obtained from the unbalanced three-phase currents shown in Fig. 3.10(1) using the classic Clark-Park transformations. According to equation (3.64), both AC and DC components exist in the i_{dq}^+ and i_{dq}^- waveforms before using filters, as shown in Fig. 3.10(2) and Fig. 3.10(3). Then, after the employment of filters, both the positive sequence components i_{dq+}^+ in positive SRFs and negative sequence components i_{dq-}^- in negative SRFs are pure DC components, Fig. 3.10(4) and Fig. 3.10(5). However, there is a little distortion in the negative sequence components due to the effect of cut-off frequency of the filters.

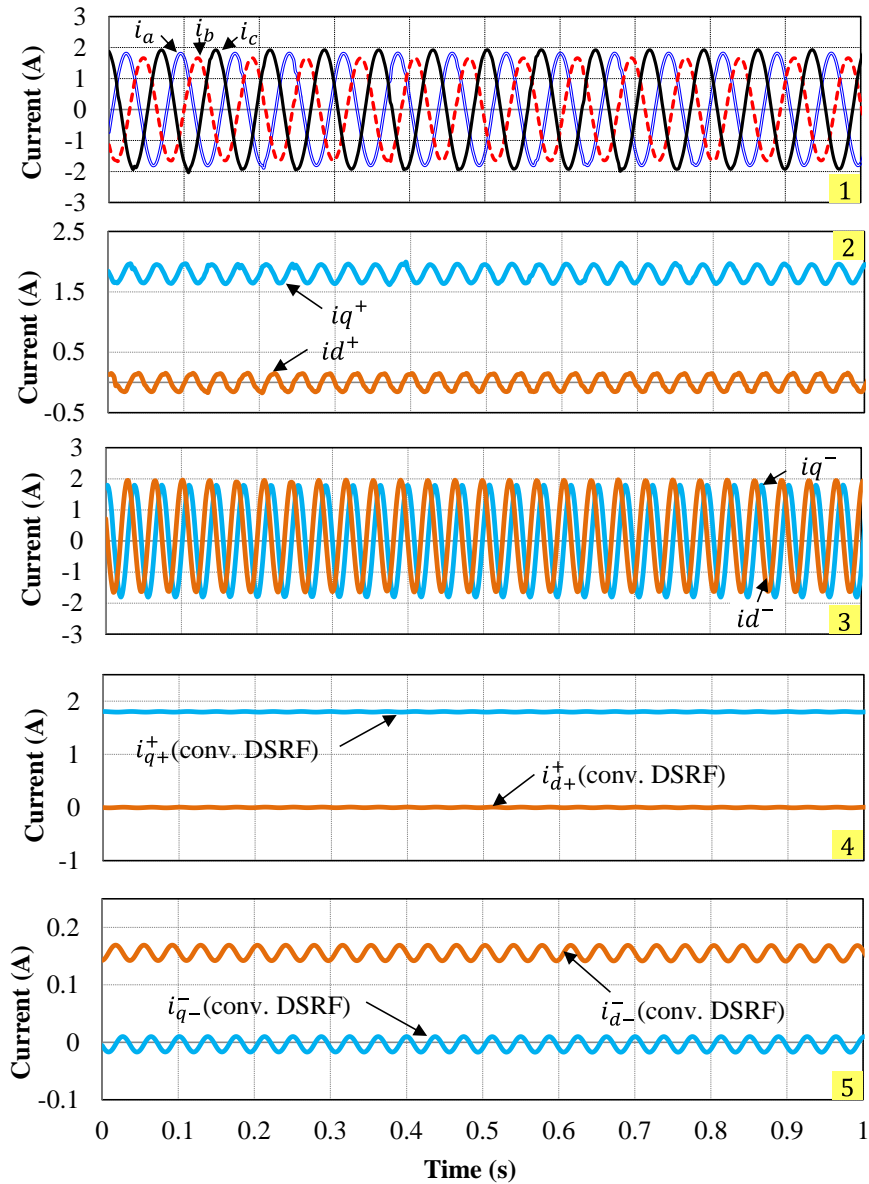


Fig. 3.10 Currents behavior in the conventional DSRF control strategy.

On the other hand, for the proposed control strategy, the positive i_{abc+} and negative i_{abc-} sequence components, Fig. 3.11(2) and Fig. 3.11(3), are firstly extracted from the unbalanced three-phase currents given in Fig. 3.11(1). These components in the positive and negative phase frames are balanced with sinusoidal waveform. Furthermore, the transformation of the positive and negative-sequence components to the positive and negative SRFs produces a pure DC variable as shown in Fig. 3.11(4) and Fig. 3.11(5). These results are compared with those obtained for the conventional DSRF after the adoption of filters, Fig. 3.11(4) and Fig. 3.11(5), it can be observed that they are DC variables.

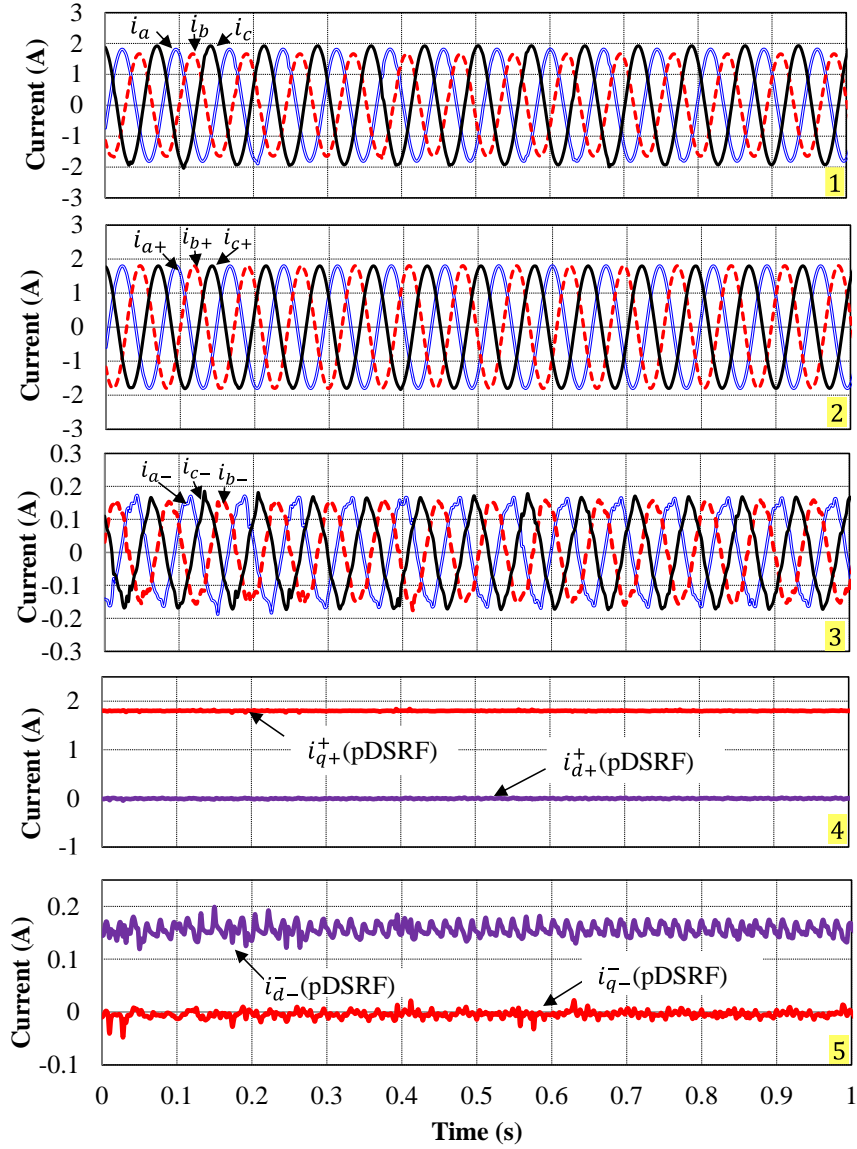


Fig. 3.11 Currents behavior in the proposed DSRF control.

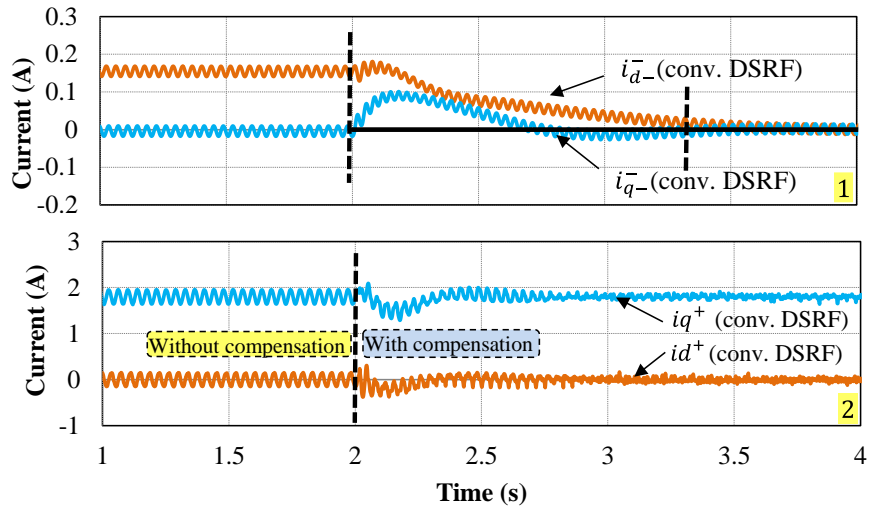
3.5.1. Steady-state performance

The steady-state performance is carried out by setting the reference current i_q^{*+} to 1.8A in the positive SRF, while i_d^{*+} is zero. Asymmetric conditions are similar to those discussed in the above. At $0 < t < 2s$, the motor operates as a conventional single-SRF controller, since the current control in the negative SRF is disabled. The i_{dq-}^- in the negative SRF are shown in Fig. 3.12 (a1) for the conventional DSRF with AF, and Fig. 3.12 (b1) for the proposed DSRF. Also, at this time interval, i.e. $0 < t < 2s$, the i_{dq}^+ in the positive SRF will have oscillations at twice of the fundamental frequency for both DSRF control strategies as shown in Fig. 3.12 (a2) and Fig. 3.12 (b2).

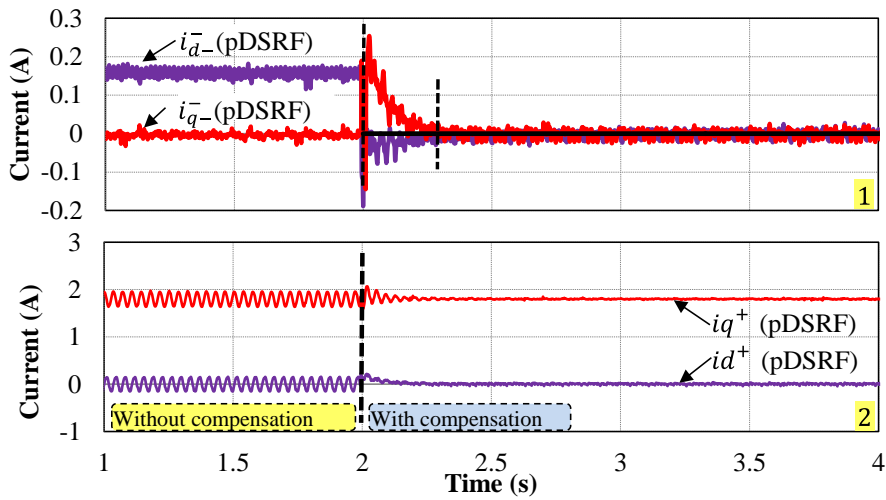
At $t=2s$, the control of the negative sequence current compensation is enabled in both DSRF strategies, the reference currents in the negative SRF i_{dq-}^{*-} are set to zero. It is clear that the transient response of the negative sequence current components i_{dq-}^- in the conventional DSRF strategy is slower than that of the proposed DSRF strategy, Fig. 3.12 (a1) and Fig. 3.12 (b1). Meanwhile, the transient responses of the positive sequence currents as well as the oscillation minimization in the positive SRF for the proposed strategy are better than those of the conventional strategy, as shown in Fig. 3.12 (a2) and Fig. 3.12 (b2). It should be noted that K_p and K_i used in both DSRF strategies are listed in Table 3.1, together with K_p and K_i of single SRF. These PI parameters are obtained by using the trial and error method in the real time system.

TABLE 3.1 PI-REGULATOR PARAMETERS

		Single-SRF	Conventional and proposed DSRFs	
			Positive SRF	Negative SRF
d-axis	Proportional gain (K_p)	15	9	6
	Integral gain (K_i)	150	650	550
q-axis	Proportional gain (K_p)	18	10	7
	Integral gain (K_i)	250	150	750



(a) Conventional DSRF



(b) Proposed DSRFs

Fig. 3.12 Comparison of current responses at steady-state between the conventional and proposed DSRFs strategies.

Furthermore, the steady-state responses of the estimated electromagnetic torque for the conventional and proposed DSRF control strategies are shown in Fig. 3.13(a) and Fig. 3.13(b), respectively. It is clear that the time required to reach the steady-state region in the conventional strategy is longer than that in the proposed strategy. Fig. 3.13 (c) shows thire spectrum analysis comparison. It is evident that the 2nd order harmonic in the electromagnetic torque is high in the single SRF strategy, while it is significantly reduced when DSRF strategies are used, and between them, the proposed DSRF strategy exhibits better torque performance.

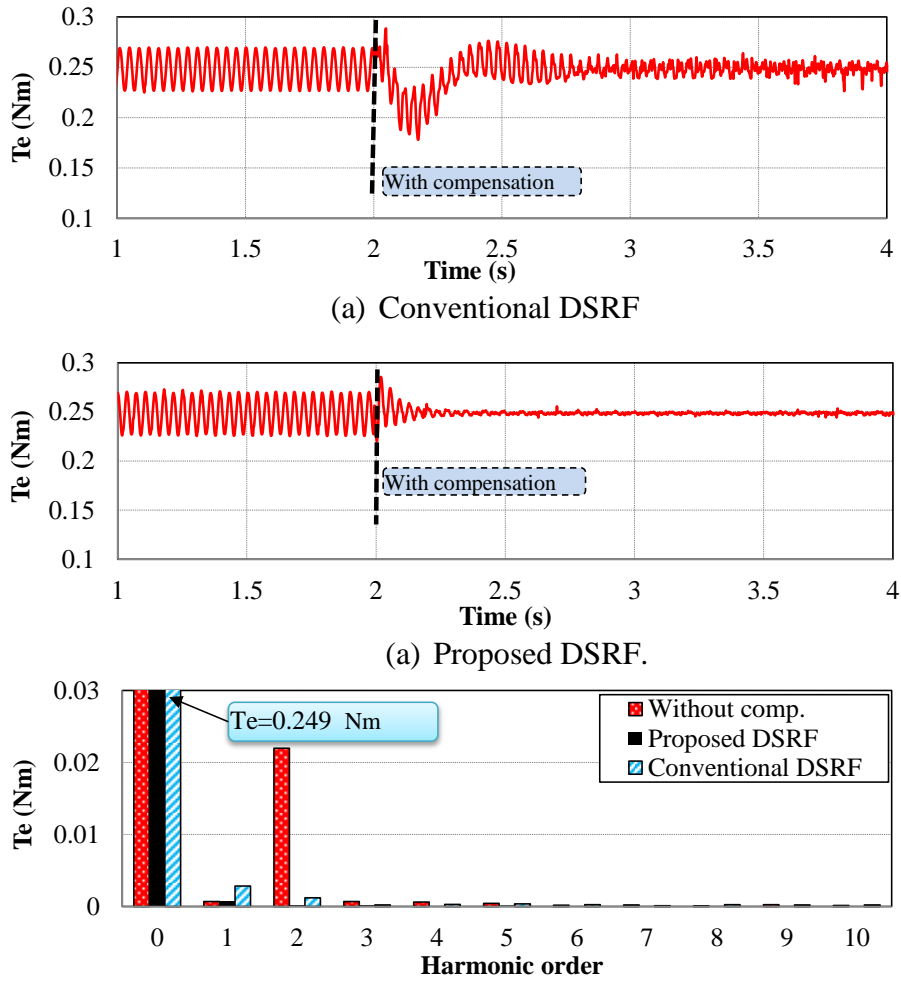
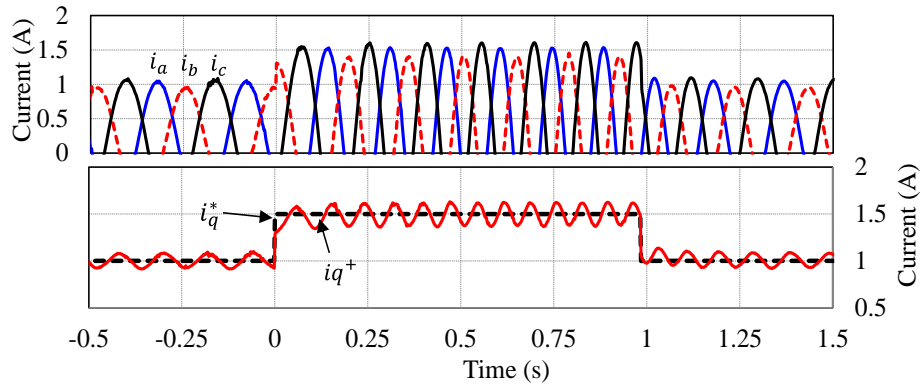


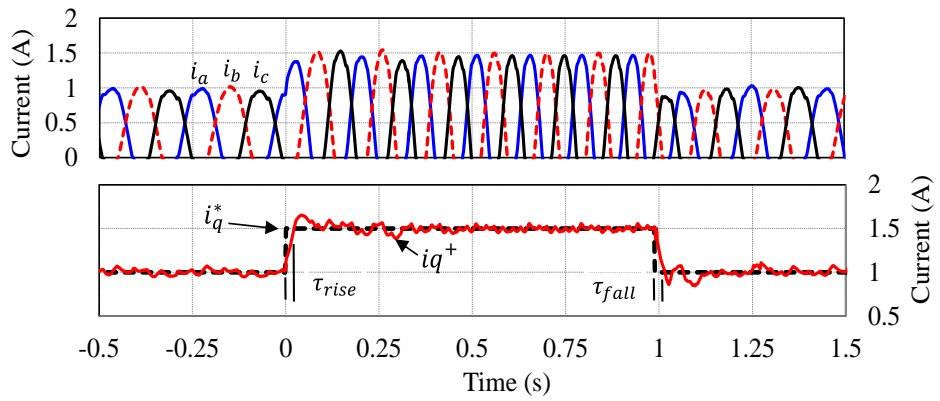
Fig. 3.13 Electromagnetic torques.

3.5.2. Dynamic performance

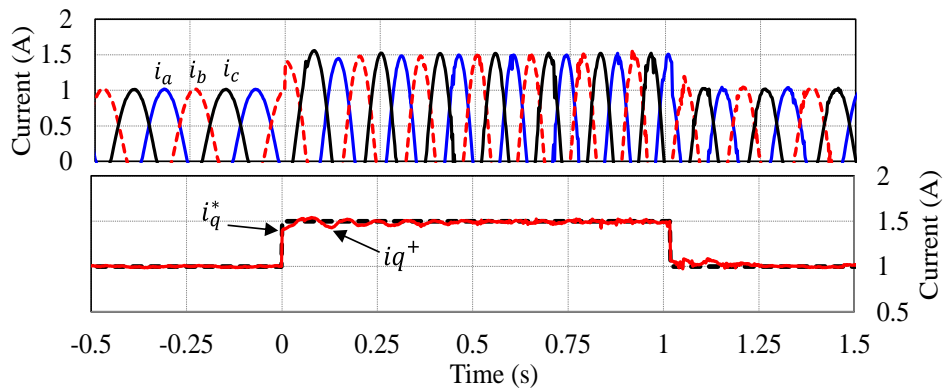
The dynamic performance of the proposed control strategy and two other control strategies, i.e. single SRF and conventional DSRF, are investigated in this section. The current reference i_q^{*+} is 1A-1.5A-1A. Fig. 3.14(a) shows the three-phase currents (top) and i_q^+ (bottom) by using the single-SRF strategy. It is obvious that the currents are unbalanced, since the machine is asymmetric and only the currents in the positive SRF are controlled. Fig. 3.14(b) and Fig. 3.14(c) show the performance of the conventional DSRF and the proposed DSRF strategies, respectively. It can be seen that the rising (τ_{rise}) and falling (τ_{fall}) times of i_q^+ in the conventional DSRF, Fig. 3.14(b) (bottom) are longer than those in the proposed DSRF, Fig. 3.14(c) (bottom). Furthermore, the steady-state error in the proposed strategy is smaller than that of the conventional DSRF strategy.



(a) Single SRF



(b) Conventional DSRF



(c) Proposed DSRF

Fig. 3.14 Dynamic performances of different strategies.

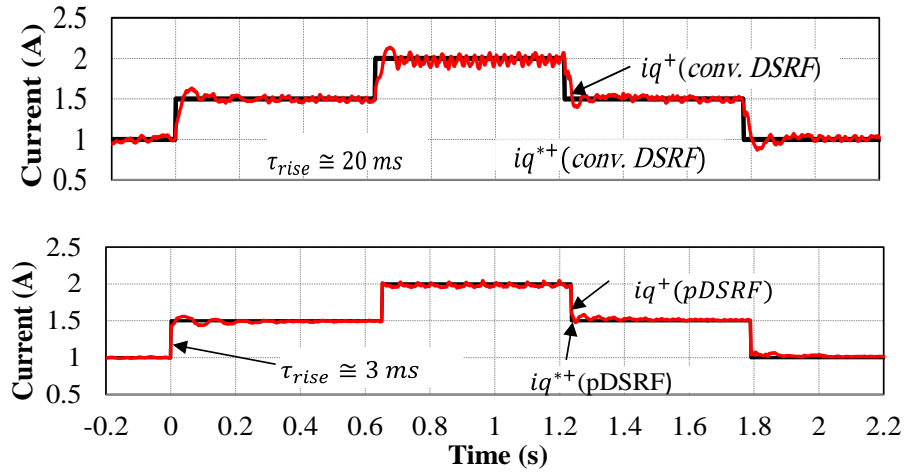


Fig. 3.15 Dynamic response comparison.

Fig. 3.15 shows the dynamic response of i_q^+ at different demand steps for the conventional DSRF (top) and the proposed DSRF (bottom), respectively. It is evident that the rising time in the conventional DSRF is approximately $20ms$. While in the proposed strategy, it is around $3ms$. Moreover, the distortion of i_q^+ is increased if the fundamental frequency is increased by using the conventional DSRF strategy, Fig. 3.15 (top). This is due to the low cut-off frequency of the AF, which needs to be modified according to the change of the fundamental frequency. However, the proposed strategy is able to overcome these problems since it does not require any filters.

Fig. 3.16 shows the speed step responses for single-SRF, conventional DSRF and proposed DSRF control strategies, respectively. As can be seen from Fig. 3.16 the responses of all strategies are similar.

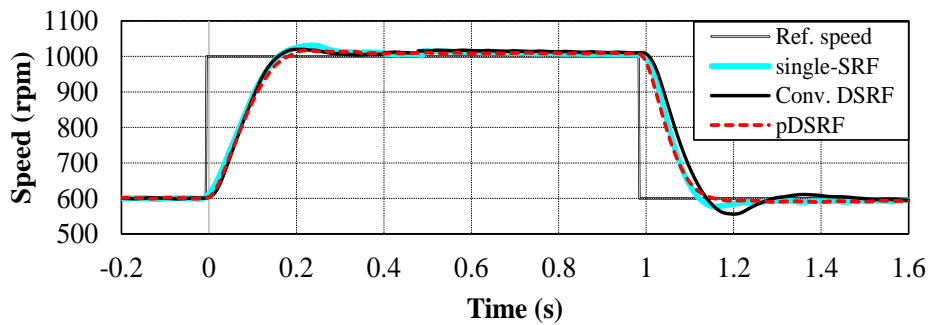


Fig. 3.16 Speed step response of the three control strategies.

3.5.3. Influence of adding extra resistance

The influence of different unbalance conditions on the single-SRF, conventional and proposed DSRFs is compared in Fig. 3.17. It has been accomplished by connecting additional resistances on phase A, from 0% to 100% of phase resistance. For the sake of quantitative comparison, the torque ripple factor (TRF) is defined as

$$TRF = \frac{T_{r(pk-pk)}}{T_e^*} 100\% \quad (3.65)$$

where is T_e^* is the reference torque, and $T_{r(pk-pk)}$ is the estimated peak-to-peak torque ripple. It can be seen from Fig. 3.17 that a positive correlation exists between the level of unbalanced conditions and the extra resistances for all three strategies, and among them, the proposed DSRF can achieve lower TRF compared with the other two strategies under different unbalanced conditions.

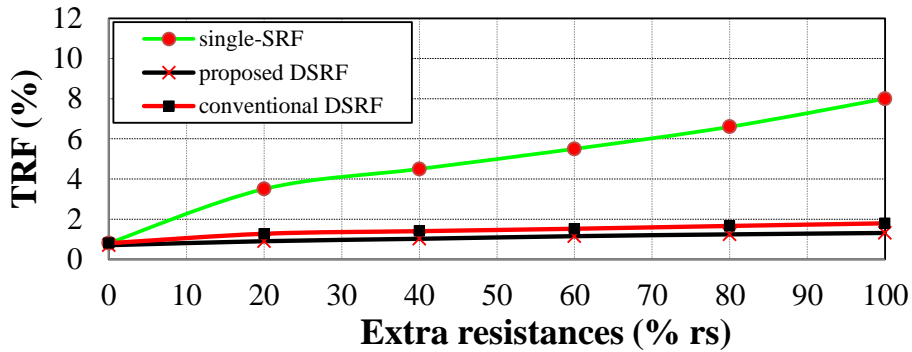
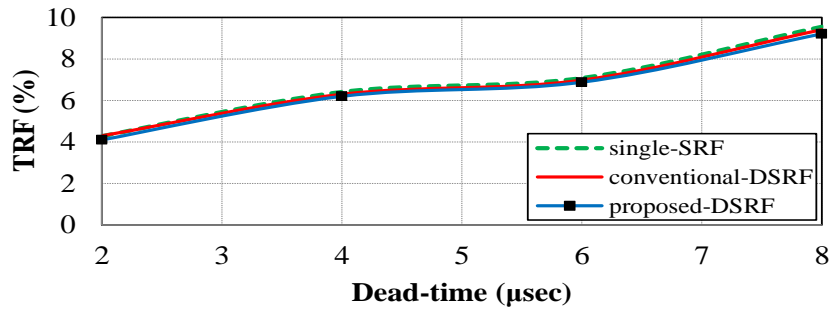


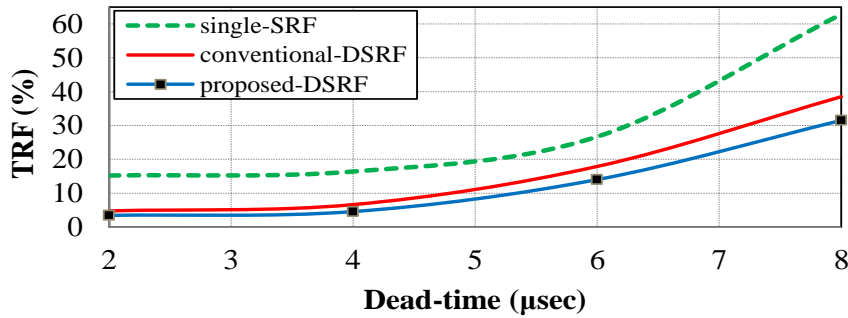
Fig. 3.17 Influence of unbalanced condition on TRF for different control strategies.

3.5.4. Inverter dead-time effects

The influence of the converter dead time on the controller behavior is investigated. The performances of single-SRF, conventional DSRF and proposed DSRF with different dead-times under symmetric and asymmetric conditions are presented in Fig. 3.18. It can be concluded that the increase of dead time leads to high TRF, no matter whether the motor is symmetric or asymmetric. It is also evident that the three strategies obtain almost the same TRF under the symmetric conditions, Fig. 3.18(a). However, under asymmetric conditions, the proposed DSRF strategy can achieve lower TRF values compared with those of the other two methods.



(a) Balanced condition



(b) Unbalanced condition

Fig. 3.18 Influence of dead-time on TRF.

3.6. Summary

In this chapter, a modified DSRF current control strategy of the asymmetric three-phase PMSM is presented. It is based on the extraction of positive and negative sequence components from the unbalanced three-phase currents, and then uses a DSRFs controller. Moreover, a new implementation of a 90^0 phase shift is used, which is based on the principle of integer sample delay, this implementation increases the speed of sequential component extraction compared with the conventional one based on filter implementation. The proposed strategy ensures the feedback currents in both positive and negative SRFs are pure DC components. Therefore, it is not necessary to use any filter, decoupling network, and particular reference current generation, which are used in the existing methods. Experimental results of the proposed DSRF strategy under dynamic and steady-state conditions are provided and compared with single SRF and conventional DSRF strategies. It is validated that the proposed strategy exhibits a fast dynamic response, low steady-state error under various unbalanced conditions. Moreover, it can provide advanced performance under the conditions of unbalanced back-EMF, variable speed, and dead-time variation.

CHAPTER 4

CASCADED DIRECT TORQUE CONTROL OF UNBALANCED PMSM WITH LOW TORQUE AND FLUX RIPPLES

Abstract—During operation or manufacturing, the electrical machines are exposed to parasitic impedance in the phases, causing unbalanced three-phase currents, and increased torque and flux ripples. To mitigate the undesired torque/flux ripples, this paper presents a modified cascaded direct torque control strategy for three-phase PMSMs, having asymmetric phase impedances. The proposed method aims to generate the positive and negative reference voltage vectors by extracting the sequential components of the stator flux and current in the stationary $\alpha\beta$ frame. Then, these two vectors are combined to produce the modified reference voltage vector for space vector modulation. Moreover, for further torque ripple suppression, a standard PI regulator has enhanced by a resonant controller tuning at twice of the fundamental frequency. Various experimental results verify the feasibility of the proposed strategy under dynamic and steady state conditions.

4.1. Introduction

In the current control based FOC strategy, the torque is indirectly controlled by adjusting the armature currents in the synchronous reference frame (SRF). In this frame, the rotor inductance and PM flux are constant if the back-EMF and variation of inductances are sinusoidal. However, when considering the effect of harmonics of the back-EMF and inductance (refer to Chapter 1), temperature change, and flux linkage saturation, the torque response under current control will be limited by the time constant of the armature winding [21], [153]. Therefore, a hysteresis direct torque control (DTC) strategy has become popular in recent years. However, as they have many drawbacks (as mentioned in Chapter 1), numerous control strategies have been proposed in literature [13], [154]. The most common way is the integration of the space vector pulse width modulation (SVM) algorithm and DTC strategy (DTC-SVM) to deal with the aforementioned issues of hysteresis DTC strategy. Different SVM algorithms were presented, such as right aligned sequence, symmetrical sequence, alternating zero

vector sequence, and highest current non-switched sequence [155], [156]. Among them, symmetrical sequence SVM topology is employed in this paper, since it produces lower total harmonic distortion (THD) [156].

DTC strategy was first proposed for IM drives [9], [154], [157], and then applied to PMSMs drives [37], [42], [21], [158], including the DTC-SVM strategy for PMSM [39], [21], [158], [159]. Compared with FOC [153], the DTC-SVM directly manipulates the final reference voltage vector (RVV) without the requirement of inner current control loops. Therefore, it can eliminate the effect of inherent delay caused by current loops, and hence, improve the dynamic performance [43], [21]. Furthermore, due to the constant switching frequency, which can be realized by DTC-SVM, they can significantly reduce torque and stator flux ripples compared with the hysteresis DTC strategy [37], [42], [39]. The DTC-SVM can be implemented by utilizing either one PI-regulator (cascaded) DTC-SVM [39], [158], [160] (the target of this chapter), or two PI-regulators (parallel) DTC-SVM [42], [43], [161]. For cascaded DTC-SVM [37], [42], [39], the PI-regulator is located in the torque control loop while the stator flux linkage is controlled in an open-loop fashion. The output of torque loop PI-regulator represent the change of the torque angle ($\Delta\delta_\psi$). According to this change, the error in the stator flux vector ($\Delta\psi_s$) can be predicted by comparing the instant value with the previous value. Afterward, the final reference voltage vector (RVV) can be calculated.

Despite the advantages above of the conventional DTC-SVM strategies [39], [40], [21], they present some drawbacks when used to drive unbalanced machines such as unbalanced three phase currents and increased torque and flux ripples [8], [43], [161], [162]. To date, cascaded DTC-SVM strategy is widely used under symmetrical conditions [39], [40], [158], while information under unbalanced conditions can scarcely be found. Therefore, in this chapter, a modified cascaded DTC-SVM strategy for unbalanced 3-phase surface-mounted PMSMs is presented. It is implemented by extracting the positive and negative sequence components of the stator flux and current in the stationary $\alpha\beta$ frame, and then calculating the positive and negative RVV in the real-time domain. These two vectors are combined to generate a modified vector for SVM module. The new RVV includes the information of the positive and negative sequence components and therefore the torque/flux ripples can be reduced. Moreover, the PIR controller tuning at twice of the fundamental frequency has been employed instead of the standard PI-regulator for further torque harmonic reduction, which can provide zero steady state error and fast dynamic response. The feasibility of the

proposed strategy is verified under dynamic and steady state conditions with various experimental results. It shows advanced performance in terms of low torque and flux ripples while keeping the merit of the fast dynamic response of the DTC strategy.

4.2. Conventional Cascaded DTC-SVM Strategy for Balanced PMSM

4.2.1. Machine model represented in stator flux reference frame

The principle of the cascaded DTC-SVM strategy is based on the analysis of the torque equation in stator flux reference frame. Fig. 4.1 describes the relationship between different variables in the PMSM represented in rotational dqr , stator dqs , and stationary $\alpha\beta$ reference frames. The mathematical model of the symmetrical machine derived in the rotating dqr reference frame can be represented as:

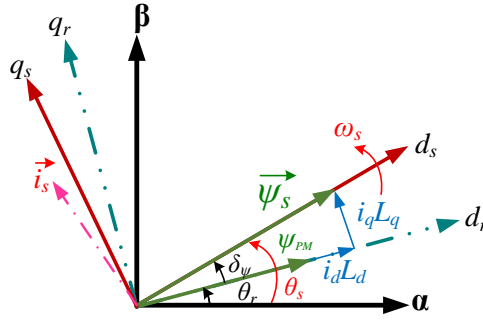


Fig. 4.1 Spatial relationship of PMSM variables represented in different frames.

$$\begin{aligned} v_{dr} &= R_s i_{dr} + \rho \psi_{dr} - \omega_r \psi_{qr} \\ v_{qr} &= R_s i_{qr} + \rho \psi_{qr} + \omega_r \psi_{dr} \end{aligned} \quad (4.1)$$

$$\begin{aligned} \psi_{dr} &= L_{dr} i_{dr} + \psi_{PM} \\ \psi_{qr} &= L_{qr} i_{qr} \end{aligned} \quad (4.2)$$

$$T_e = \frac{3}{2} p_n (\psi_{dr} i_{qr} - \psi_{qr} i_{dr}) \quad (4.3)$$

where ω_r refers to the rotor fundamental angular speed, v_{dr} , v_{qr} , i_{dr} , i_{qr} , ψ_{dr} , ψ_{qr} , and L_{dr} , L_{qr} are the voltages, currents, fluxes, and self-inductances in the dqr -axis, respectively. These variables can be transformed into the stator flux dqs -reference frame using the following matrix [21], [163]:

$$\begin{bmatrix} F_{ds} \\ F_{qs} \end{bmatrix} = \begin{bmatrix} \cos(\delta_\psi) & \sin(\delta_\psi) \\ -\sin(\delta_\psi) & \cos(\delta_\psi) \end{bmatrix} \begin{bmatrix} F_{dr} \\ F_{qr} \end{bmatrix}. \quad (4.4)$$

where F represents current, voltage, or flux-linkage, and δ_ψ is the torque angle between the rotor and stator flux linkage vectors. Then the voltage in the stator flux frame when the stator flux vector is fixed at ds -axis, i.e., $\psi_{qs}=0$ and $\psi_{ds}=\psi_s$, can be written as:

$$\begin{aligned} v_{ds} &= R_s i_{ds} + \frac{d\vec{\psi}_s}{dt} \\ v_{qs} &= R_s i_{qs} + \omega_s \vec{\psi}_s. \end{aligned} \quad (4.5)$$

Then, the stator flux vector can be transformed into the stationary $\alpha\beta$ reference frame using stator flux position angle θ_s as:

$$\begin{bmatrix} F_\alpha \\ F_\beta \end{bmatrix} = \begin{bmatrix} \cos(\theta_s) & \sin(\theta_s) \\ -\sin(\theta_s) & \cos(\theta_s) \end{bmatrix} \begin{bmatrix} F_{ds} \\ F_{qs} \end{bmatrix} \quad (4.6)$$

Moreover, the torque angle in Fig. 4.1 can be calculated from as:

$$\begin{aligned} \sin \delta_\psi &= \frac{\psi_{qr}}{|\vec{\psi}_s|} \\ \cos \delta_\psi &= \frac{\psi_{dr}}{|\vec{\psi}_s|} \end{aligned} \quad (4.7)$$

Substituting (4.4) for current and (4.7) into the torque equation (4.3) gives:

$$\begin{aligned} T_e &= \frac{3}{2} P_n [\psi_{dr} (i_{ds} \sin \delta_\psi + i_{qs} \cos \delta_\psi) + \psi_{qr} (i_{ds} \cos \delta_\psi - i_{qs} \sin \delta_\psi)] \\ &= \frac{3}{2} P_n \left[\frac{\psi_{dr} \psi_{qr}}{|\psi_s|} i_{ds} + \frac{\psi_{dr}^2}{|\psi_s|} i_{qs} - \frac{\psi_{dr} \psi_{qr}}{|\psi_s|} i_{ds} - \frac{\psi_{dr}^2}{|\psi_s|} i_{qs} \right] = \frac{3}{2} P_n |\psi_s| i_{qs} \end{aligned} \quad (4.8)$$

The torque in (4.8) is directly proportional to the qs -axis current component (i_{qs}) when the amplitude of the stator flux linkage is kept constant. The rotor flux equation of (4.2) can be transformed into stator flux dqs -reference frame as follows:

$$\begin{bmatrix} \cos(\delta_\psi) & -\sin(\delta_\psi) \\ \sin(\delta_\psi) & \cos(\delta_\psi) \end{bmatrix} \begin{bmatrix} \psi_{ds} \\ \psi_{qs} \end{bmatrix} = \begin{bmatrix} L_{dr} & 0 \\ 0 & L_{qr} \end{bmatrix} \begin{bmatrix} \cos(\delta_\psi) & -\sin(\delta_\psi) \\ \sin(\delta_\psi) & \cos(\delta_\psi) \end{bmatrix} \begin{bmatrix} i_{ds} \\ i_{qs} \end{bmatrix} + \begin{bmatrix} \psi_{PM} \\ 0 \end{bmatrix} \quad (4.9)$$

Solving and reorganizing (4.9) gives:

$$\begin{bmatrix} \psi_{ds} \\ \psi_{qs} \end{bmatrix} = \begin{bmatrix} \cos(\delta_\psi) & \sin(\delta_\psi) \\ -\sin(\delta_\psi) & \cos(\delta_\psi) \end{bmatrix} \begin{bmatrix} L_{dr} & 0 \\ 0 & L_{qr} \end{bmatrix} \begin{bmatrix} \cos(\delta_\psi) & -\sin(\delta_\psi) \\ \sin(\delta_\psi) & \cos(\delta_\psi) \end{bmatrix} \begin{bmatrix} i_{ds} \\ i_{qs} \end{bmatrix} + \begin{bmatrix} \cos(\delta_\psi) & \sin(\delta_\psi) \\ -\sin(\delta_\psi) & \cos(\delta_\psi) \end{bmatrix} \begin{bmatrix} \psi_{PM} \\ 0 \end{bmatrix}$$

$$\begin{aligned}
&= \begin{bmatrix} L_{dr} \cos^2(\delta_\psi) + L_{qr} \sin^2(\delta_\psi) & -L_{dr} \sin(\delta_\psi) \cos(\delta_\psi) + L_{qr} \sin(\delta_\psi) \cos(\delta_\psi) \\ -L_{dr} \sin(\delta_\psi) \cos(\delta_\psi) + L_{qr} \sin(\delta_\psi) \cos(\delta_\psi) & L_{dr} \sin^2(\delta_\psi) + L_{qr} \cos^2(\delta_\psi) \end{bmatrix} \begin{bmatrix} i_{ds} \\ i_{qs} \end{bmatrix} \\
&+ \begin{bmatrix} \psi_{PM} \cos(\delta_\psi) \\ -\psi_{PM} \sin(\delta_\psi) \end{bmatrix}.
\end{aligned} \tag{4.1}$$

- *Non-saliency pole PMSMs:* In these machines, $L_{dr}=L_{qr}=L_s$, thus, (4.10) can be simplified as:

$$\begin{bmatrix} \psi_{ds} \\ \psi_{qs} \end{bmatrix} = \begin{bmatrix} L_s & 0 \\ 0 & L_s \end{bmatrix} \begin{bmatrix} i_{ds} \\ i_{qs} \end{bmatrix} + \begin{bmatrix} \psi_{PM} \\ 0 \end{bmatrix} \begin{bmatrix} \cos(\delta_\psi) \\ -\sin(\delta_\psi) \end{bmatrix} \tag{4.2}$$

According to Fig. 4.1, ψ_{qs} is zero because the stator flux vector is aligned with ds -axis. Hence, i_{qs} in the second equation of (4.11) can be written as:

$$i_{qs} = \frac{1}{L_s} \psi_{PM} \sin \delta_\psi \tag{4.3}$$

Substituting (4.12) into the electromagnetic torque expression (4.8) gives:

$$T_e = \frac{3}{2} p_n \frac{|\vec{\psi}_s| \psi_{PM} \sin \delta_\psi}{L_s} \tag{4.4}$$

Equation (4.13) implies that the increase of torque is proportional to the increase of the torque angle δ_ψ at the constant stator flux magnitude. Hence, maximum torque can be achieved at $\delta_\psi=90^\circ$ [21].

- *Saliency pole PMSMs:* In this machines, $L_{dr} \neq L_{qr}$, and the torque equation as a function of stator flux linkage and δ_ψ can be obtained by solving i_{ds} from (4.11) as:

$$i_{ds} = \frac{2\psi_{PM} \sin \delta_\psi - [(L_{dr} + L_{qr}) + (L_{dr} - L_{qr}) \cos 2\delta_\psi]}{(L_{qr} - L_{dr}) \sin 2\delta_\psi} i_{qs} \tag{4.5}$$

Substituting (4.14) into the first equation of (4.10) gives:

$$i_{qs} = \frac{1}{2L_{dr}L_{qr}} [2\psi_{PM}L_{qr} \sin \delta_\psi - |\psi_s| (L_{qr} - L_{dr}) \sin 2\delta_\psi] \tag{4.6}$$

Then, the electromagnetic torque can be written as:

$$T_e = \frac{3}{2} p_n \left[\frac{|\vec{\psi}_s| \psi_{PM} \sin \delta_\psi}{L_{qr}} - \frac{|\vec{\psi}_s|^2 (L_{qr} - L_{dr}) \sin 2\delta_\psi}{2L_{qr}L_{dr}} \right]. \tag{4.7}$$

Equation (4.16) involves two terms: the PM torque and the reluctance torque due to rotor saliency. The stator voltage of the symmetrical PMSMs in stationary $\alpha\beta$ reference frame can be calculated using the following complex vector expression [37], [38], [21], [164]:

$$\vec{v}_s = \frac{d\vec{\psi}_s}{dt} + R_s \vec{i}_s. \quad (4.8)$$

where $\vec{v}_s = v_\alpha + jv_\beta$ is the stator voltage, $\vec{i}_s = i_\alpha + ji_\beta$ stator current.

On the other hand, the stator flux linkage can be estimated by utilizing either current model based on (4.18) [38], [21], or voltage-model based on (4.19) as [165] [166]:

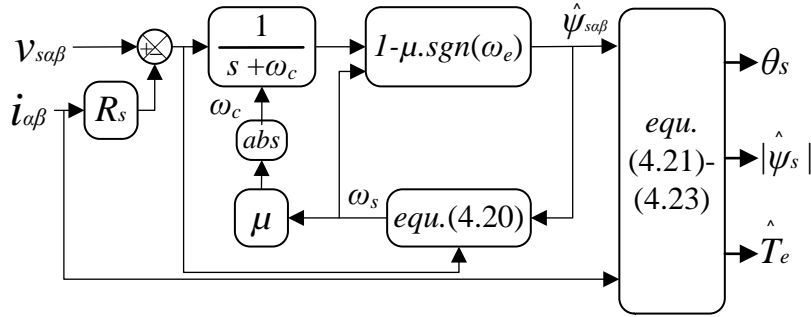


Fig. 4.2 Adaptive stator flux estimator.

$$\vec{\psi}_s = L_s \vec{i}_s + \vec{\psi}_r. \quad (4.9)$$

$$\hat{\vec{\psi}}_s = \int (\vec{v}_s - R_s \vec{i}_s) dt + \vec{\psi}_{r0}. \quad (4.19)$$

where $\psi_s = \psi_\alpha + j\psi_\beta$ stator flux linkage, $\psi_r = \psi_{PM} e^{-j\theta_r}$ is the flux produced by the rotor, and ψ_{r0} is the initial rotor flux. In Practice, the real-time integration in (4.19) is usually replaced by the transfer function of the lowpass filter (LPF) [167]. However, when the system fundamental frequency is below the cut-off frequency, the estimator performance will degrade if the conventional LPF with fixed cut-off frequency (ω_c) is employed. Very low cut-off frequency should mitigate this problem, but the dynamic performance will deteriorate. Therefore, an adaptive structure has been introduced in [165], [166]. Fig. 4.2 shows the schematic diagram of the adaptive stator flux estimator, the cut-off frequency varying according to the fundamental frequency, i.e., $\omega_c = \mu\omega_s$, where μ is usually chosen between 0.1 and 0.5 [165], [166]. The synchronous frequency ω_s can be calculated as:

$$\omega_s = \frac{\psi_\alpha(v_\beta - R_s i_\beta) - \psi_\beta(v_\alpha - R_s i_\alpha)}{\psi_\alpha^2 + \psi_\beta^2} \quad (4.20)$$

The stator flux magnitude, position and the electromagnetic torque in the stationary $\alpha\beta$ -frame can be calculated as:

$$|\hat{\vec{\psi}}_s| = \sqrt{\psi_\alpha^2 + \psi_\beta^2} \quad (4.21)$$

$$\hat{\theta}_\psi = a \tan\left(\frac{\psi_\beta}{\psi_\alpha}\right) \quad (4.22)$$

$$\begin{aligned} T_e &= 1.5p_n \text{Im}\{\vec{\psi}_s' \cdot \vec{i}_s\} \\ &= 1.5p_n \text{Im}\{(\psi_\alpha + j\psi_\beta)' \cdot (i_\alpha + ji_\beta)\} = 1.5p_n (\psi_\alpha i_\beta - \psi_\beta i_\alpha). \end{aligned} \quad (4.23)$$

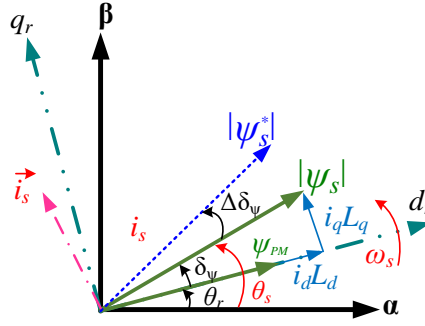


Fig. 4.3 Relationship between different quantities in different reference frames.

4.2.2. Torque and flux control

From equation (4.13), assuming the magnitude of the stator flux $|\vec{\psi}_s|$ and the rotor PM flux ψ_{PM} are constants, then the torque T_e can be regulated by controlling the torque angle δ_ψ . At steady-state and constant torque conditions, δ_ψ is constant corresponding to the machine load torque (T_L), whereas the stator and rotor flux vectors rotate at the synchronous speed. On the other hand, during the dynamic or transient conditions, δ_ψ varies, and the stator and rotor flux vectors rotate at different speeds. The positive torque is always satisfied when the torque angle is within the range of $-\pi/2 < \delta_\psi < \pi/2$ [21]. In (4.13), if the voltage drop across stator resistance is omitted, the stator flux vector $\vec{\psi}_s$ can be controlled by adjusting the terminal voltage vectors, which causes the change in δ_ψ . Assuming there is a slight change in the stator flux vector, the new reference stator flux becomes $|\psi_s^*|$, and the torque angle has a slight change in $\Delta\delta_\psi$ as shown in Fig. 4.3. Then, the error that presents in the torque expression can be represented as:

$$\Delta T_e = T_e^* - T_e = 1.5 p_n \left[\frac{|\vec{\psi}_s^*| \psi_{PM} \sin(\Delta\delta_\psi + \delta_\psi)}{L_s} - \frac{|\vec{\psi}_s| \psi_{PM} \sin(\delta_\psi)}{L_s} \right] \quad (4.24)$$

It is worth mentioning that the relationship between the torque error ΔT_e and the change of torque angle $\Delta\delta_\psi$ is nonlinear. Therefore, the PI-regulator is usually employed in the torque closed-loop to obtain the certain variation of $\Delta\delta_\psi$ to minimize the steady-state error between the reference and the actual torque values [38], [39], [40].

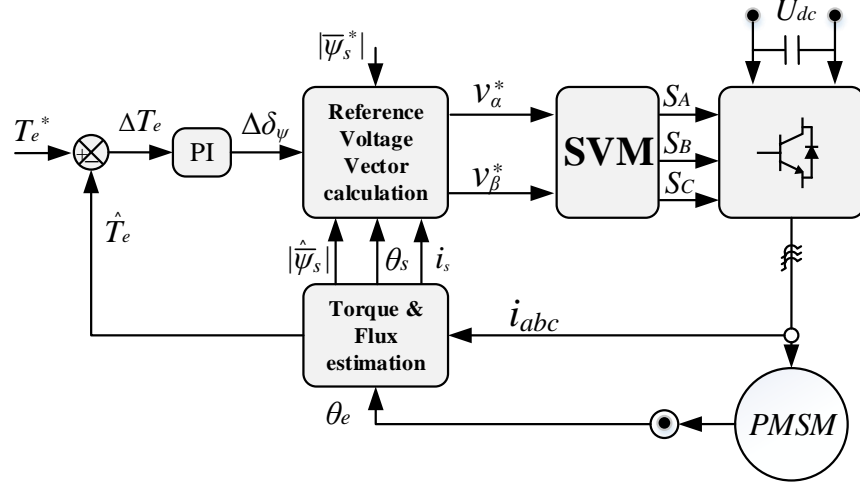


Fig. 4.4 Block diagram of the conventional cascaded DTC-SVM strategy.

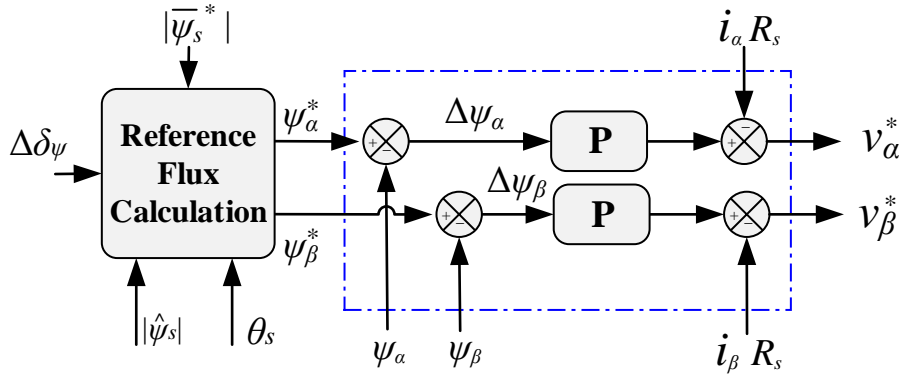


Fig. 4.5 Block diagram of the RVV calculation.

Fig. 4.4 shows the block diagram of the conventional cascaded DTC-SVM strategy. The torque error signal ΔT_e is delivered to the PI controller, which determines the change of torque angle $\Delta\delta_\psi$. Then, using this signal together with the information about the reference and actual stator flux magnitudes, the stator flux position θ_s , and the measured stator current i_s , the RVV easily obtained in the fundamental stator coordinates $\alpha\beta$ as shown in Fig. 4.5. Afterward, the RVV is delivered to the SVM, which generates the switching signals S_{abc} for the VSI.

Based on the change of the torque angle $\Delta\delta_\psi$, the reference stator flux magnitude $|\psi_s^*|$ and stator flux vector position θ_s , the reference flux components ψ_α^* and ψ_β^* are calculated as:

$$\begin{aligned}\psi_\alpha^* &= |\vec{\psi}_s^*| \cos(\Delta\delta_\psi + \theta_s) \\ \psi_\beta^* &= |\vec{\psi}_s^*| \sin(\Delta\delta_\psi + \theta_s)\end{aligned}\quad (4.25)$$

At constant flux operation region, the stator flux reference magnitude is equal to the PM flux, $|\psi_s^*| = \psi_{PM}$. The stator flux reference components are compared with the estimated values given by:

$$\begin{aligned}\psi_\alpha &= |\vec{\psi}_s| \cos(\theta_s) \\ \psi_\beta &= |\vec{\psi}_s| \sin(\theta_s)\end{aligned}\quad (4.26)$$

Moreover, the voltage commands in the stationary $\alpha\beta$ reference frame can be presented as:

$$\begin{aligned}v_\alpha^* &= i_\alpha R_s + \frac{\psi_\alpha^* - \psi_\alpha}{T_s} = i_\alpha R_s + \frac{\Delta\psi_\alpha}{T_s} \\ v_\beta^* &= i_\beta R_s + \frac{\psi_\beta^* - \psi_\beta}{T_s} = i_\beta R_s + \frac{\Delta\psi_\beta}{T_s}\end{aligned}\quad (4.27)$$

where T_s is the sampling time. Furthermore, the next two sections present a method for designing the torque and flux control loops [163], [168], [18].

4.2.2.1. Stator flux control loop

The flux control loop is based on the voltage equations given in (4.27). Taking the Laplace transformation, the equations (4.27) can be expressed as:

$$\begin{aligned}v_\alpha^* &= i_\alpha R_s + s\psi_\alpha \\ v_\beta^* &= i_\beta R_s + s\psi_\beta\end{aligned}\quad (4.28)$$

It corresponds to the flux model of the PMSM machine represented in the stationary $\alpha\beta$ reference frame as depicted in Fig. 4.6.

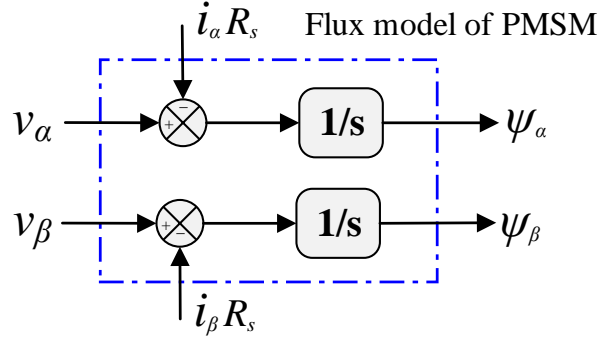


Fig. 4.6 Flux model of PMSM in stator coordinate.

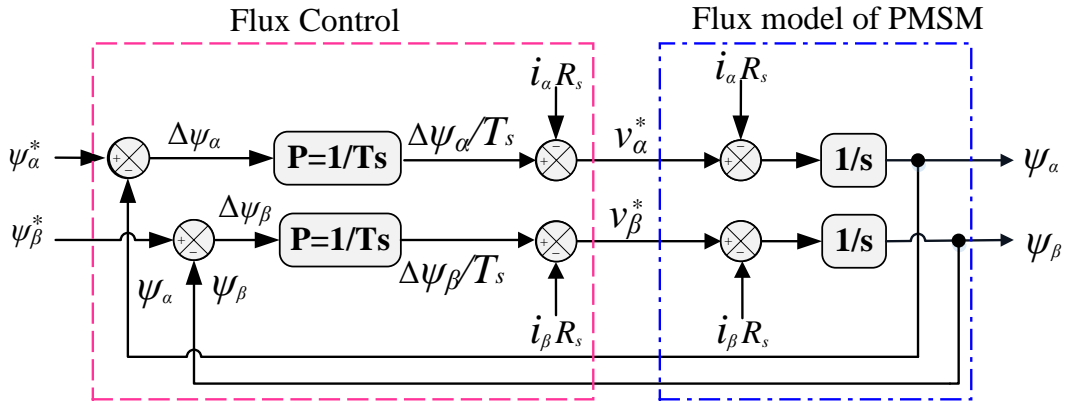


Fig. 4.7 Flux control loop in stationary $\alpha\beta$ reference frame.

Fig. 4.7 shows the block diagram of the flux components, and the P controller is a proportional gain, which can be obtained by considering the following assumption:

- The change in the torque angle $\Delta\delta_\psi$ is zero, which means that the torque is not produced.
- The rotor and stator flux vector positions are equal to zero, i.e., $\theta_s = \theta_r = 0$, which corresponds to the case when those two vectors lie along the α -axis.

In this manner, the stator flux reference magnitude $|\psi_s^*| = \psi_\alpha$ can be controlled by the stator voltage component $v_\alpha = |v_s^*|$, when the voltage drop across stator resistances is neglected. Therefore, the flux control loop can be simplified as shown in Fig. 4.8.

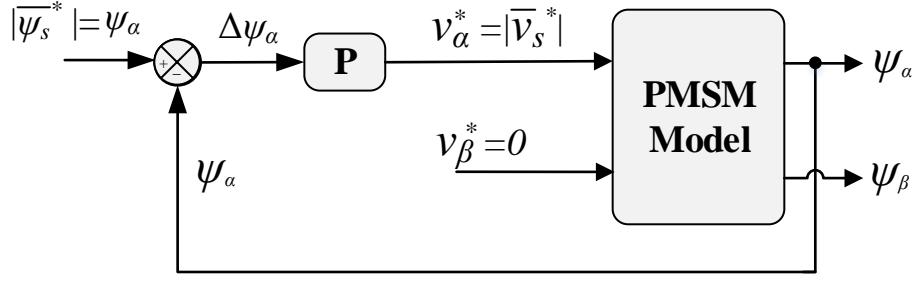


Fig. 4.8 Simplified flux control loop in stationary $\alpha\beta$ reference frame.

The equivalent representation of Fig. 4.8 in s-domain is shown in Fig. 4.9, where $C_\psi(s)$ is the transfer function (TF) of the proportional P controller, which is given by:

$$C_\psi(s) = K_{p\psi} \quad (4.29)$$

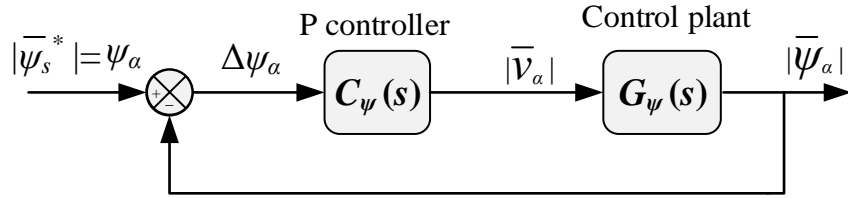


Fig. 4.9 Block diagram of the dynamic flux controller.

The TFs between the stator flux magnitude $|\psi_s^*| = \psi_\alpha$, and the stator voltage magnitude $|v_s|$ can be written as

$$G_\psi(s) = \frac{|\bar{\psi}_s|}{|\bar{v}_s|} = \frac{1}{s} \quad (4.30)$$

Then, the closed-loop TF of the system can be expressed as

$$G_{\psi,CL}(s) = \frac{|\psi_s^*|(s)}{|\psi_s|(s)} = \frac{C_\psi(s)G_\psi(s)}{1 + C_\psi(s)G_\psi(s)} \quad (4.31)$$

Substituting the TF of $C_\psi(s)$ and $G_\psi(s)$ into (4.31) gives

$$G_{\psi,CL}(s) = \frac{K_{p\psi} \left(\frac{1}{s} \right)}{1 + K_{p\psi} \left(\frac{1}{s} \right)} = \frac{K_{p\psi}}{s + K_{p\psi}} \quad (4.32)$$

4.2.2.2. Torque control loop

The torque control loop is shown in Fig. 4.10. From the equations (4.25) and (4.26), the stator flux errors in the stationary $\alpha\beta$ -frame can be expressed as:

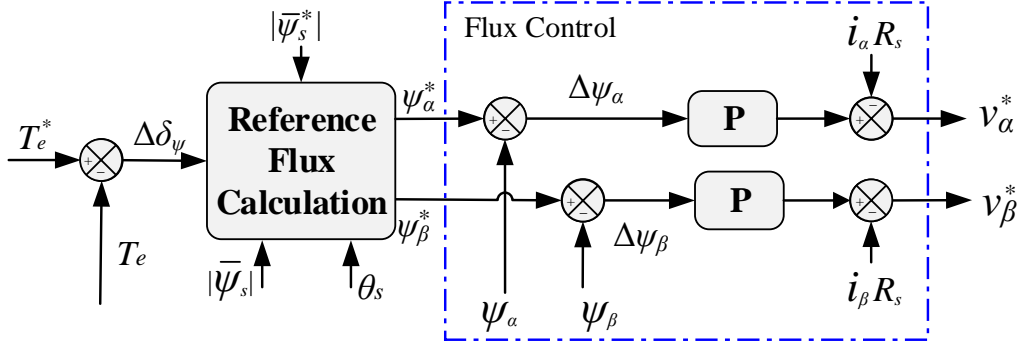


Fig. 4.10 Torque control loop with PI regulator.

$$\begin{aligned}\Delta\psi_\alpha &= |\vec{\psi}_s^*| \cos(\theta_s + \Delta\delta_\psi) - |\vec{\psi}_s| \cos(\theta_s) \\ \Delta\psi_\beta &= |\vec{\psi}_s^*| \sin(\theta_s + \Delta\delta_\psi) - |\vec{\psi}_s| \sin(\theta_s)\end{aligned}\quad (4.33)$$

Assuming that for small changes of $\Delta\delta_\psi$ the $\Delta\delta_\psi \approx 1$ and $\sin(\Delta\delta_\psi) \approx \Delta\delta_\psi$, and hence, equations (4.33) can be simplified as

$$\begin{aligned}\Delta\psi_\alpha &= |\vec{\psi}_s^*| \Delta\delta_\psi \sin(\theta_s) \\ \Delta\psi_\beta &= |\vec{\psi}_s^*| \Delta\delta_\psi \cos(\theta_s)\end{aligned}\quad (4.34)$$

To design the torque loop PI controller, the following assumptions have to be considered:

- The rotor and stator flux vector positions are equal to zero, i.e., $\theta_s = \theta_r = 0$, which corresponds to the situation, where those two flux vectors lie along the α -axis;
- Stator flux reference magnitude and PM flux are equal, i.e., $|\vec{\psi}_s^*| = \psi_{PM}$;
- Stator resistance is neglected.

Thus, the error of stator fluxes in stationary $\alpha\beta$ -reference frame can be expressed as

$$\begin{aligned}\Delta\psi_\alpha &= 0 \\ \Delta\psi_\beta &= \psi_{PM} \Delta\delta_\psi\end{aligned}\quad (4.35)$$

While the reference stator voltages are:

$$\begin{aligned}v_\alpha^* &= 0 \\ v_\beta^* &= \Delta\psi_\beta K_{p\psi}\end{aligned}\quad (4.36)$$

Further, because of $v_\beta^* = |\vec{v}_s^*|$, and with substituting of (4.35), equation (4.36) becomes:

$$|\vec{v}_s^*| = \psi_{PM} \Delta\delta_\psi K_{p\psi}\quad (4.37)$$

Then, the TF (C_{δ_ψ}) between stator voltage magnitude $|\bar{v}_s|$ and the change of torque angle $\Delta\delta_\psi$ can be expressed as:

$$C_{\delta_\psi}(s) = \frac{|\bar{v}_s^*|}{\Delta\delta_\psi} = K_{p\psi} \psi_{PM} \quad (4.38)$$

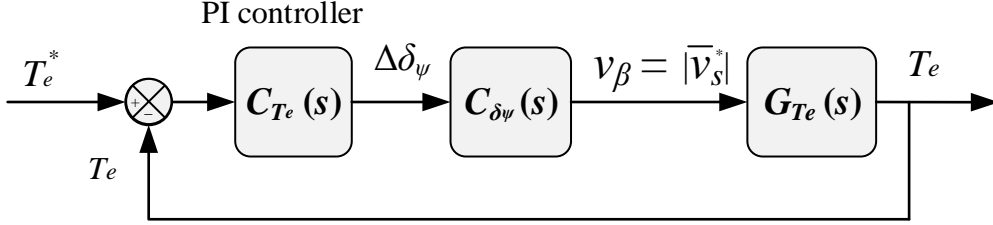


Fig. 4.11 Block diagram of the torque control loop represented in s-domain.

Fig. 4.11 shows the equivalent block diagram of the torque control loop described in s-domain. Moreover, the plant TF can be derived from the stator voltage equation (4.5) and the electromagnetic torque produced in SPMSM. Since the relationship between the load and the electromagnetic torque is:

$$\rho\omega_m = \frac{1}{J}(T_e - T_L) \quad (4.39)$$

and the torque angle can be calculated as:

$$\delta_\psi = \theta_s - p_n \theta_r \quad (4.40)$$

Taking the differentiation of (4.40), it can be written as:

$$\rho\delta_\psi = \rho\theta_s - p_n \rho\theta_r \quad (4.41)$$

$$\rho\delta_\psi = \omega_\psi - p_n \omega_m \rightarrow \omega_\psi = \rho\delta_\psi + p_n \omega_m \quad (4.42)$$

where ρ is a derivative operator. From the current equation (4.12) and under the assumption of small angle $\sin(\delta_\psi) = \delta_\psi$, the torque angle can be written as

$$\delta_\psi = \frac{i_{qs} L_s}{\psi_{PM}} \quad (4.43)$$

Substituting equations (4.42) and (4.43) into the second voltage equation (4.5) one can obtain

$$v_{qs} = R_s i_{qs} + |\vec{\psi}_s| \left(\frac{L_s}{\psi_{PM}} \cdot \rho i_{qs} + p_n \omega_m \right) \quad (4.44)$$

Taking the differentiation of the above equation gives

$$\rho v_{qs} = R_s \rho i_{qs} + \vec{\psi}_s \left(\frac{L_s}{\psi_{PM}} \cdot \rho^2 i_{qs} + p_n \rho \omega_m \right) \quad (4.45)$$

From (4.12) and (4.13), the relationship between current and torque in the qs -axis is $i_{qs} = (2T_e / 3p_n \psi_s)$, substituting i_{qs} and equation (4.39) at zero load torque into (4.45) gives

$$\rho v_{qs} = \frac{2R_s}{3p_n |\vec{\psi}_s|} \rho T_e + \left(\frac{L_s R_s}{3p_n \psi_{PM}} \cdot \rho^2 T_e + \frac{p_n T_e}{J} \right) \quad (4.46)$$

Taking the Laplace transformation of (4.46) with some arrangement yields

$$s v_{qs} = T_e \left(\frac{2L_s}{3p_n \psi_{PM}} s^2 + \frac{2R_s}{3p_n |\vec{\psi}_s|} s + \frac{p |\vec{\psi}_s|}{J} \right) \quad (4.47)$$

Then, the plant TF between the ds -axis voltage and electromagnetic torque can be written as

$$G_{T_e}(s) = \frac{T_e}{v_{qs}} = \left(\frac{A_{T_e} s}{s^2 + B_{T_e} s + C_{T_e}} \right) \quad (4.48)$$

where $A_{T_e} = \frac{3p_n \psi_{PM}}{2L_s}$, $B_{T_e} = \frac{R_s \psi_{PM}}{|\psi_s| L_s}$, and $C_{T_e} = \frac{3p_n^2 \psi_{PM}}{2J L_s}$. Substituting machine parameters

given in Chapter 1, one obtains: $A_{T_e} = 43.63$, $B_{T_e} = 146$ and $C_{T_e} = 1214$. Hence, the torque open-loop control TF can be written as

$$G_{T_e,OL}(s) = C_{T_e}(s) \cdot C_{\delta_\psi}(s) \cdot G_{T_e}(s) \quad (4.49)$$

where $C_{T_e}(s)$ is the TF of the standard PI controller given by

$$C_{T_e}(s) = \frac{K_{PT_e} \left(s + \frac{K_{IT_e}}{K_{PT_e}} \right)}{s} \quad (4.50)$$

The PI controller parameters can be obtained using either SISO tool of the MATLAB or online tuning in real-time system operation. Furthermore, the torque closed-loop control TF in Fig. 4.11 is given by:

$$G_{T_e,CL}(s) = \frac{T_e^*(s)}{T_e(s)} = \frac{C_{T_e}(s) \cdot C_{\delta_\psi}(s) \cdot G_{T_e}(s)}{1 + C_{T_e}(s) \cdot C_{\delta_\psi}(s) \cdot G_{T_e}(s)} \quad (4.51)$$

Substituting the TF of $C_{T_e}(s)$ and $C_{\delta_\psi}(s)$ into equation (4.51) yields

$$G_{T_e,CL}(s) = \frac{K_{P\psi} \psi_{PM} A_{T_e} K_{PT_e} \left(s + \frac{K_{IT_e}}{K_{PT_e}} \right)}{s^2 + (B_{T_e} + K_{PT_e} A_{T_e})s + (C_M + K_{IT_e} A_{T_e})} \quad (4.52)$$

4.3. Proposed Cascaded DTC-SVM Strategy for Unbalanced PMSM

4.3.1. Machine behavior under unbalanced conditions

As discussed in Chapter 3, the positive and negative sequence components exist under unbalanced conditions, which result in the rise of the second order torque and flux harmonics if the conventional cascaded DTC-SVM strategy is employed. Assuming there is no zero sequence, i.e., Y-connection with floating neutral point, the electrical machine quantities can be expressed in terms of their positive/negative sequence components in the stationary $\alpha\beta$ reference frame as [56], [83], [146]:

$$F_{\alpha\beta} = F_{\alpha\beta 1+} + F_{\alpha\beta 1-} = F_{dqs 1+} e^{j(\omega_s t + \varphi_+)} + F_{dqs 1-} e^{-j(\omega_s t + \varphi_-)} \quad (4.53)$$

where φ_+ and φ_- are the initial phase shift. Fig. 4.12(a) illustrates the relationship between different quantities under unbalanced conditions represented in the positive dqs^+ , negative dqs^- , and stationary $\alpha\beta$ reference frames. It can be seen that the positive and negative voltage vectors rotate in circular trajectories but in opposite directions with angular frequencies of $\pm\omega_s$. The combination of these two voltage vectors produced an ellipse trajectory, which describes the unbalanced situation as depicted in Fig. 4.12(b). The current and stator flux can be rewritten in terms of their positive/negative sequence components referred to the positive dqs^+ reference frame as:

$$\vec{i}_{dqs}^+ = \vec{i}_{dqs+} + \vec{i}_{dqs-} = \vec{i}_{dqs+} + \vec{i}_{dqs-} e^{-j2\omega_s t} \quad (4.54a)$$

$$\vec{\psi}_{dqs}^+ = \vec{\psi}_{dqs+} + \vec{\psi}_{dqs-} = \vec{\psi}_{dqs+} + \vec{\psi}_{dqs-} e^{-j2\omega_s t} \quad (4.54b)$$

In (4.54), the negative sequence components behave as an AC pulsating at the frequency of $2\omega_s$ in the fundamental stator flux dqs^+ reference frame. Taking into consideration the positive and negative sequence components, the torque can be expressed as:

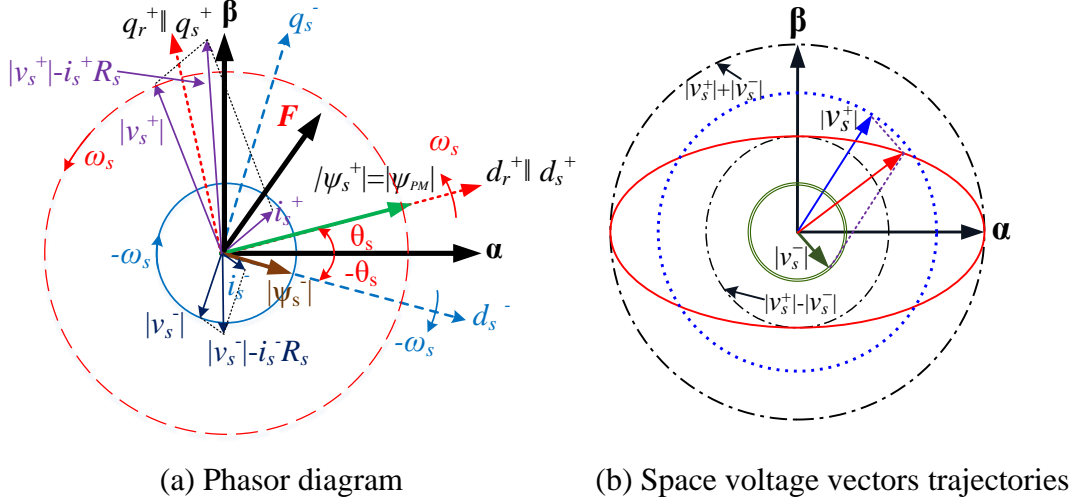


Fig. 4.12 Relationship between different quantities in different reference frames under unbalanced conditions.

$$T_e = 1.5p_n \text{Im} \{ \vec{\psi}_{dqs}^+ \cdot \vec{i}_{dqs}^+ \} = 1.5p_n [T_{e0} + T_{es2} \sin(2\omega_s t) + T_{ec2} \cos(2\omega_s t)] \quad (4.55a)$$

$$\begin{aligned} \bar{T}_{e0} &= (\psi_{ds+}^+ \cdot i_{qs+}^+ - \psi_{qs+}^+ \cdot i_{ds+}^+ + \psi_{ds-}^- \cdot i_{qs-}^- - \psi_{qs-}^- \cdot i_{ds-}^-) \\ \tilde{T}_{es2} &= (\psi_{ds-}^- \cdot i_{ds+}^+ + \psi_{qs-}^- \cdot i_{q1+}^+ - \psi_{ds+}^+ \cdot i_{ds-}^- - \psi_{qs+}^+ \cdot i_{qs-}^-) \\ \tilde{T}_{ec2} &= (\psi_{ds-}^- \cdot i_{qs+}^+ - \psi_{qs-}^- \cdot i_{d1+}^+ + \psi_{ds+}^+ \cdot i_{qs-}^- - \psi_{qs+}^+ \cdot i_{ds-}^-) \end{aligned} \quad (4.55b)$$

Equation (4.55) comprises of one direct term \bar{T}_{e0} correlated with equal harmonic sequence products, and two pulsating terms, i.e., \tilde{T}_{es2} and \tilde{T}_{ec2} , at twice of the fundamental frequency $2\omega_s$ produced by unequal harmonic sequence products [83], [43], [160], [161], [130]. These two terms are responsible for the existence of the second order torque harmonic. In a conventional cascaded DTC-SVM, single voltage vector in the positive dqs^+ reference frame is applied. This structure fails to achieve low torque/flux ripples for unbalanced machines. To mitigate this problem, a modified, cascaded DTC-SVM structure has been presented by employing two compensation models, of which the first one (as will be explained in section §4.3.3) is based on generating the positive and negative RVVs individually and then combining them together to produce the modified RVV as shown in Fig. 4.13.

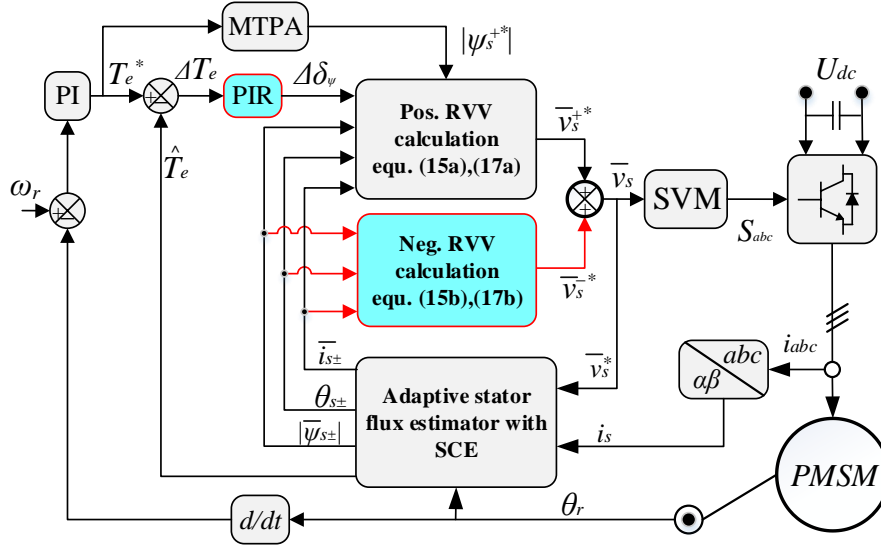


Fig. 4.13 Proposed cascaded DTC-SVM strategy.

4.3.2. Sequential components extraction

Under balanced conditions, the instantaneous current and flux linkage in α frame are equal in magnitude and displacement by 90° from those in β frame, i.e., $|\psi_\alpha|=|\psi_\beta|$ and $|i_\alpha|=|i_\beta|$. Hence, there are no negative sequence components. However, under unbalanced conditions, they will vary in magnitude and/or phase shift, which lead to the emergence of negative sequence components [83], [146]. Therefore, the sequential components extractor (SCE) has been used to obtain the positive and negative sequence components of the current and flux in the $\alpha\beta$ reference frame. It is based on the principle of signal delay, by adding or subtracting the real-time signals and the signals delayed by a quarter of the fundamental period, which is mathematically described as follows [146], [169]:

$$x_{\alpha+}(t) = \frac{1}{2} \left[x_\alpha(t) - x_\beta \left(t - \frac{\pi}{2} \omega_s \right) \right] \quad (4.56a)$$

$$x_{\beta+}(t) = \frac{1}{2} \left[x_\beta(t) + x_\alpha \left(t - \frac{\pi}{2} \omega_s \right) \right].$$

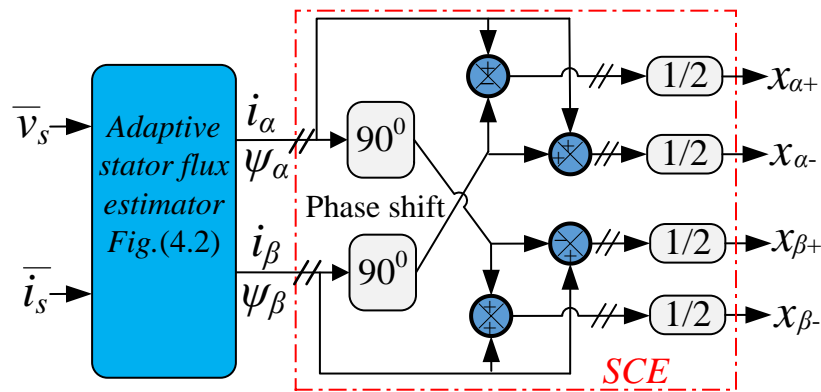
$$x_{\alpha-}(t) = \frac{1}{2} \left[x_\alpha(t) + x_\beta \left(t - \frac{\pi}{2} \omega_s \right) \right] \quad (4.56b)$$

$$x_{\beta-}(t) = \frac{1}{2} \left[x_\beta(t) - x_\alpha \left(t - \frac{\pi}{2} \omega_s \right) \right].$$

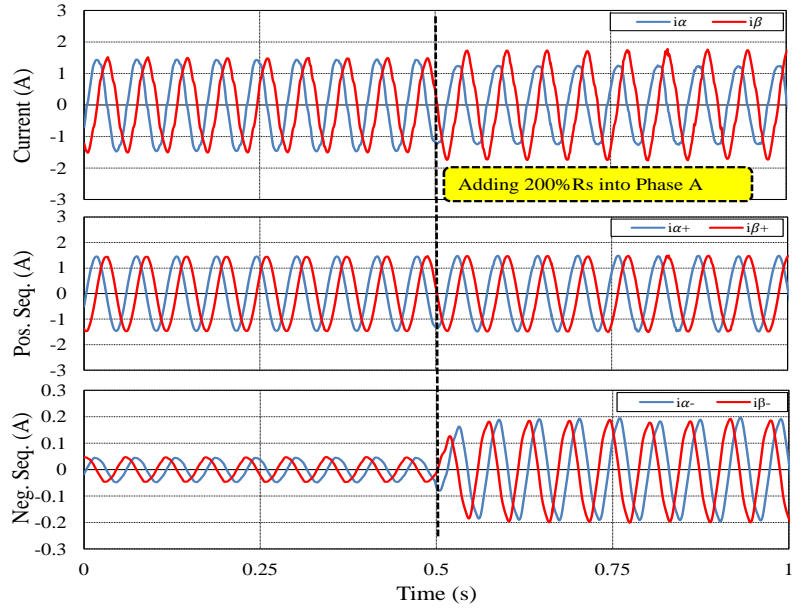
Factor x refers to current or flux variables. The phase shift delay by 90° is an interesting target, and therefore, many researchers have tried to obtain the easiest and

most effective way to achieve such a delay under variable frequency. Some effort such as all pass filter, adaptive notch filter (ANF) [170], and second order generalized filter [146], [169] have already been developed in the past few years. In this chapter, an algorithm using MATLAB s-function has been written based on the concept of the variable integer sampling delay as described in [171].

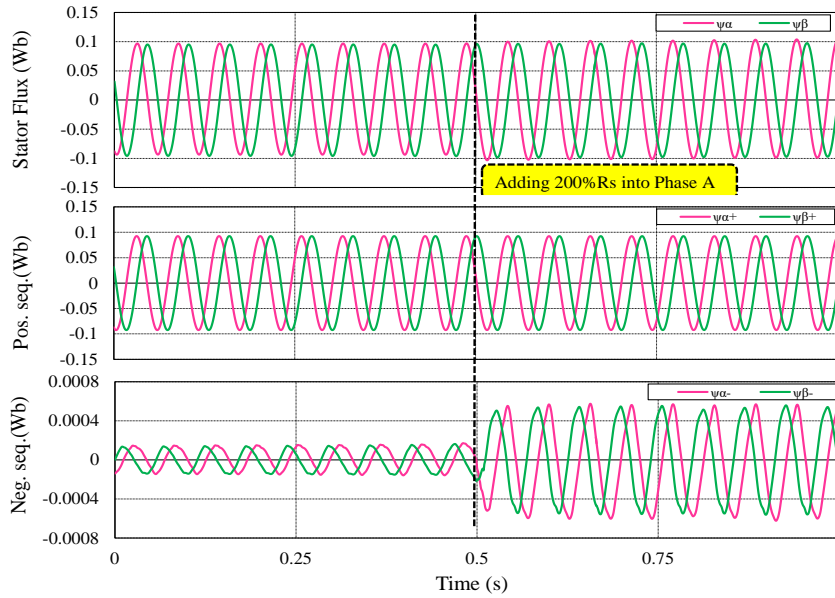
Fig. 4.14 shows the schematic diagram of the SCE and its performance, the unbalanced conditions in Fig. 4.14 are created by connecting extra resistance ($R_{ex}=200\%R_a$) in series with phase a . The stator current and flux behaviors without/with considering the effect of R_{ex} are shown in Fig. 4.14(b) and Fig. 4.14(c), respectively. It can be seen that when R_{ex} is connected, the negative sequence components of flux and current are significantly increased due to unbalance, Fig. 4.14(b) and Fig. 4.14(c) at $t > 0.5$. The transient time consumed in SCE is relatively small due to the fast digital signals processing when creating the 90° phase shift. It is worth mentioning that the negative sequence components of both current and flux without additional resistance, i.e., $t < 0.5$, is not equal to zero since the motor under test has a slightly inherent unbalanced back-EMF caused by designing process, further discussion can be found in section §4.4.2.



(a) Schematic diagram of SCE



(b) Current components



(c) Flux components

Fig. 4.14 Performance of SCE without/with adding extra resistance.

4.3.3. Positive and negative RVVs generation

As the sequential components are obtained, the positive and negative RVVs can be calculated individually by predicting the stator flux vector variation in each sampling interval. This change can be described as the difference between the expectation and current values of the stator flux in the next cycle, which can be mathematically expressed as:

$$\begin{aligned}\Delta\psi_{\alpha}^{+} &= |\vec{\psi}_{s}^{+*}| \cos(\Delta\delta_{\psi} + \theta_s) - |\psi_{s+}| \cos(\theta_s) \\ \Delta\psi_{\beta}^{+} &= |\vec{\psi}_{s}^{+*}| \sin(\Delta\delta_{\psi} + \theta_s) - |\psi_{s+}| \sin(\theta_s)\end{aligned}\quad (4.57a)$$

$$\begin{aligned}\Delta\psi_{\alpha}^{-} &= |\psi_{s-}| \cos(-\theta_s + \gamma) \\ \Delta\psi_{\beta}^{-} &= |\psi_{s-}| \sin(-\theta_s + \gamma).\end{aligned}\quad (4.57b)$$

where γ is the phase shift compensation angle between the stator flux and voltage vectors in the stationary $\alpha\beta$ reference frame, $\gamma=90^0$, $|\psi_{s}^{+*}|$ is the stator flux reference and can be obtained from the reference torque based on the principle of maximum torque per ampere (MTPA) to promote the system efficiency [42], [172]. Usually, for surface-mounted PMSM with $L_d = L_q = L_s$, the stator flux reference trajectory can be obtained online using motor parameters (L_s , p_n , and ψ_{PM}) as:

$$|\psi_{s}^{+*}| = \sqrt{(\psi_{PM})^2 + \left(\frac{L_s T_e^*}{\frac{3}{2} p_n \psi_{PM}}\right)^2} \quad (4.58)$$

Although the variations of motor parameters may affect the performance of MTPA, a comprehensive discussion regarding this issue can be found in [42], [172]. Afterward, the modified RVV is computed by combining both positive and negative RVVs as follows:

$$\vec{v}_s^{+*} = \frac{\Delta\vec{\psi}_s^+}{T_s} + R_s \vec{i}_{s+} \quad (4.59a)$$

$$\vec{v}_s^{-*} = \frac{\Delta\vec{\psi}_s^-}{T_s} + R_s \vec{i}_{s-} \quad (4.59b)$$

$$\vec{v}_s^* = \vec{v}_s^{+*} + \vec{v}_s^{-*} \quad (4.59c)$$

4.3.4. Torque ripple minimization

For further torque ripple reduction, the PIR controller tuning at twice of the fundamental frequency has been used instead of standard PI regulator [77], [151], [173]. This modification provides high gain at the selected resonant frequency, which can sufficiently minimize the 2nd harmonic of the torque signal and improve the steady-state error [77], [174]. The ideal R controller transfer function can be expressed in s-domain as:

$$G_R(s) = \frac{K_r s}{s^2 + (h\omega_s)^2} \quad (4.60)$$

where K_r is the resonant gain that provides infinite gain at the desired frequency, h refers to the selected harmonic order to be regulated. Practically, the resonant controller is usually implemented by using non-ideal R controller to avoid stability problem associated with an infinite gain [151], [175], [176], which can be expressed by the given transfer function:

$$G_{R2}(s) = \frac{2K_r \omega_c s}{\underbrace{s^2 + 2\omega_c s + (h\omega_s)^2}_{G_h(s)}} \quad (4.61)$$

Expression (4.61) provides a finite gain but is still relatively high for enforcing a small steady-state error and good tracking for the selected harmonics. Another feature can be obtained using the non-ideal R controller is that the bandwidth can be widened by properly adjusting ω_c [95], [177]. The sensitivity and stability of the R regulator have been verified theoretically in [77]. Since the resonant frequency is variable, the transfer function of (4.60) can be implemented by decomposition the term $G_h(s)$ into two integrators [158], [178] as shown in Fig. 4.15. Further analysis and discussion regarding the improvement of frequency accuracy and stability margin for digital resonant controllers, by performing delay compensation and pole correction, is also available in [178], [179]. In this thesis, the structure without delay compensation is used since the magnitude of the compensation harmonic is low. The complete transfer function of the PIR controller is given by:

$$G_{PIR}(s) = K_P + \frac{K_I}{s} + \frac{2K_{r2} \omega_{c2} s}{\underbrace{s^2 + 2\omega_{c2} s + (h\omega_s)^2}_{G_h(s)}} \quad (4.62)$$

where K_P and K_I are the proportional and integral gains of the classic PI-regulator. The input frequency ω_s is obtained in the real-time from the stator flux position θ_s , the dominated torque harmonic is $h=2$, and the cut-off frequency is chosen as $\omega_c = \omega_s/200$ while the resonant gain is set to be the same as the integral gain of the PI control [178].

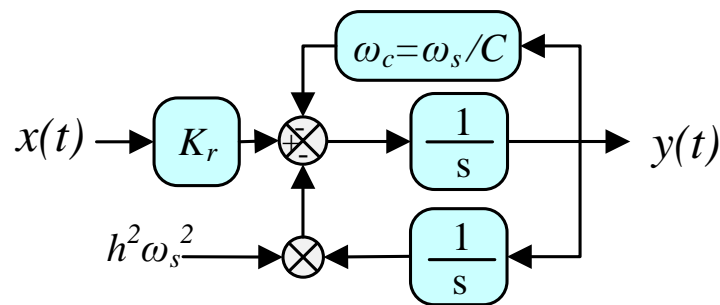


Fig. 4.15 Simulation model of the resonant controller.

TABLE 4.1 CONTROLLER PARAMETERS

Torque loop regulator	$K_{PTe}=0.061$	$K_{ITe}=5.32$	$K_{r2}=5.32$	$\omega_{c2}=\omega_s/200$
Speed loop regulator	$K_P=0.00012$	$K_I=0.0014$		
Switching frequency	$f_{sw}=5\text{kHz}$			
Sampling frequency	$f_s=10\text{kHz}$			
DC-Link voltage	38 V			
Inverter Dead time	$T_D=5\mu s$			

4.4. Experimental Verification

The experimental tests are conducted on balanced (with the possibility of manual conversion to unbalanced) three-phase surface-mounted PM synchronous motor. The information regarding hardware, software, and test rig are discussed in Chapter 2. The controller parameters are listed in Table 4.1.

4.4.1. Compensation under steady-state conditions

As aforementioned in Chapter 2, the motor under test has a slightly inherent unbalanced back-EMF due to the manufacturing process, which appears in the spectrum analysis of the three-phase back-EMF given in Table 4.2 (symmetrical) [38]. The influence of this unbalanced back-EMF is slight, which can be neglected, and the motor can be regarded as a symmetrical machine.

On the other hand, to investigate the proposed strategy under realistic unbalanced conditions, the asymmetry has been created in different phases by adding extra winding ($\approx 10\%N_s$) into phase b as shown in Fig. 4.16. The measured impedance of the additional winding is $Z_{exb}=R_{exb}+L_{exb}=0.098\ \Omega + 0.102\ \text{mH}$.

Moreover, a resistance of $R_{exa}=100\%R_s$ has been deliberately connected in series with phase a . These modifications increased the influence of unbalanced back-EMF as shown in the spectrum analysis presented in Table 4.2 (unbalanced). Therefore, all experimental results are carried out based on this assumption.

Under steady state, the motor is driven at a constant torque of $T_e=0.25\ \text{Nm}$, where the amplitude of the demand phase current is $i_{abc}\approx 1.9\ \text{A}$. The stator flux reference is obtained according to (4.58). Then, three operating modes are employed, which can be defined as follows:

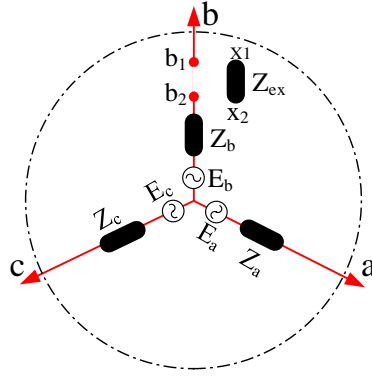


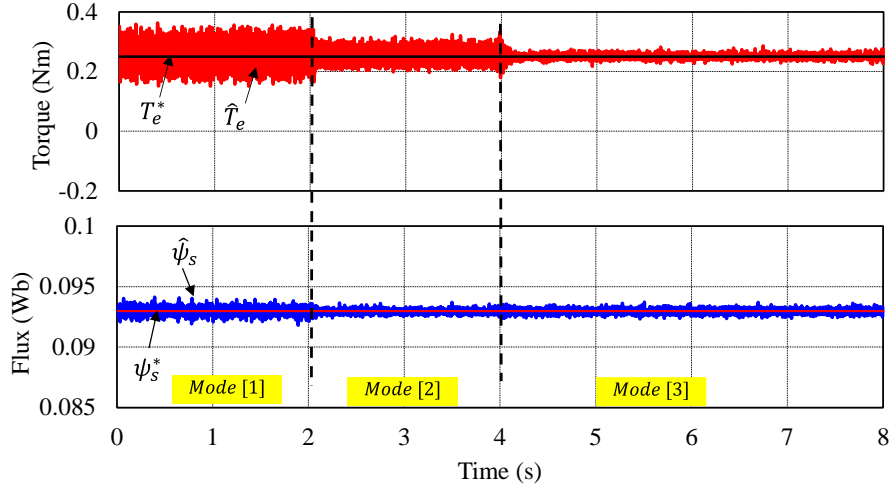
Fig. 4.16 Additional winding placement.

TABLE 4.2 PHASE BACK-EMF HARMONICS (V) AT 1500 RPM

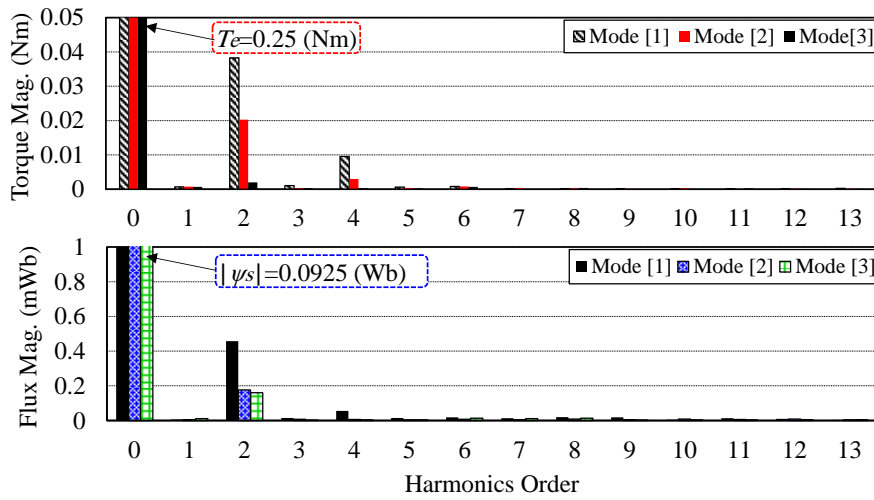
	<i>Phases</i>	<i>Fundamental</i>	<i>2nd</i>	<i>3rd</i>	<i>5th</i>	<i>7th</i>
Balanced	A	14.516	0.412	0.048	0.318	0.197
	B	14.2880	0.321	0.212	0.2483	0.186
	C	15.3256	0.422	0.264	0.220	0.247
Unbalanced	A	16.423	0.421	0.132	0.201	0.192
	B	14.825	0.312	0.101	0.335	0.187
	C	15.630	0.262	0.171	0.221	0.200

- *Mode* [1] without compensation, i.e., conventional cascaded DTC-SVM.
- *Mode* [2] compensation using positive and negative RVV, while keeps the classic PI-regulator.
- *Mode* [3] combines between *Mode* [2] and employing PIR instead of classic PI-regulator.

Fig. 4.17 shows the experimental results of torque and flux and their spectrum analysis under different modes. It can be seen that the 2nd harmonics in both torque and flux are the most dominated under *Mode* [1] while it can be reduced by 50% in torque signal and 60% in flux signal when using *Mode* [2] due to the use of modified RVV. Consequently, the best results can be obtained when using *Mode* [3], the 2nd harmonic torque is reduced by 90%, while the effect on the flux is negligible, Fig. 4.17(b), since the flux is controlled in an open-loop fashion and independent of torque loop. It is worth mentioning that the 4th harmonic appears in both torque and flux linkage due to the correlating of unequal sequence product of flux and current signals. Nevertheless, this harmonic is also reduced because of the compensation of 2nd harmonic.



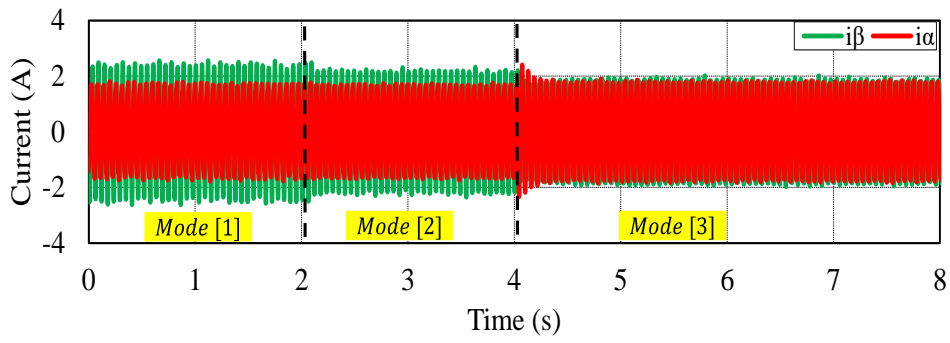
(a) Instantaneous torque and flux



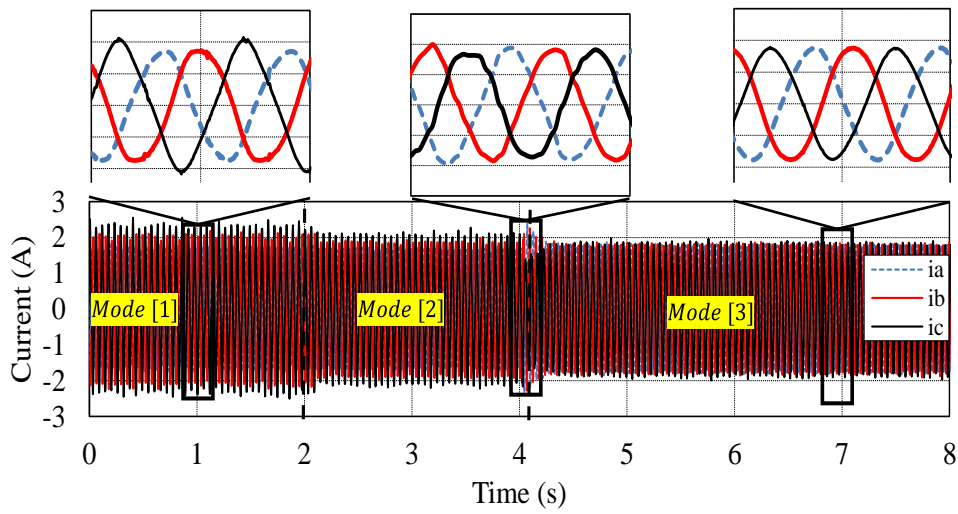
(b) Spectrum analysis

Fig. 4.17 Steady-state performance with/without compensation.

Furthermore, the currents behaviors in the $\alpha\beta$ - and abc -reference frames are depicted in Fig. 4.18(a) and Fig. 4.18(b), respectively. The total harmonic distortion (THD) of phase a current under Mode [1] is 4.88% and becomes 1.81% with Mode [3], which means such asymmetric machine can achieve balanced current. However, the unbalanced in the demand voltage is increased under Mode [2] and Mode [3] compared with Mode [1] as shown in Fig. 4.19 since it is impossible to achieve balanced current and voltage simultaneously for such asymmetric machines [28]. Moreover, the voltage trajectory angle is modified with compensation, Mode [3], compared without compensation. This correction is due to the PIR controller, which reduced the steady-state error.

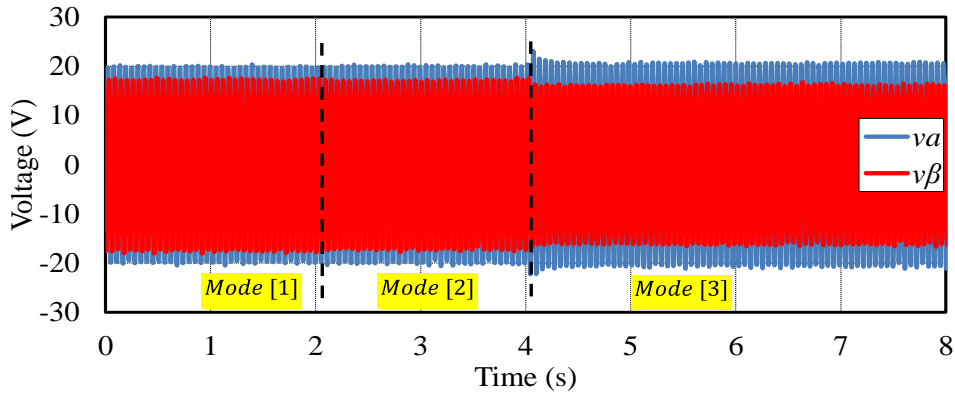


(a) Currents in $\alpha\beta$ frame

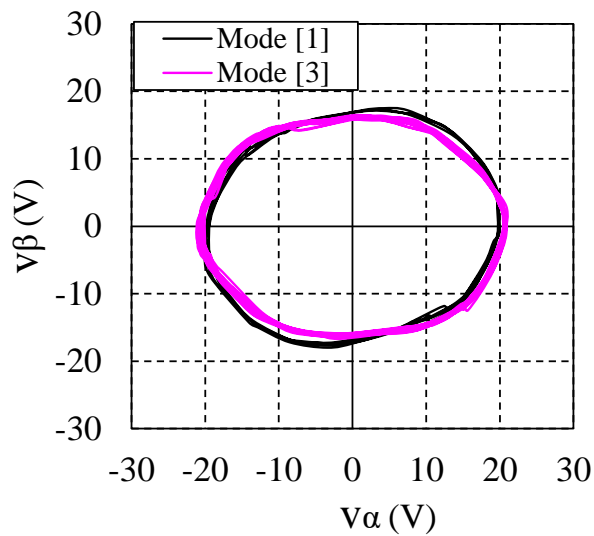


(b) Three-phase currents i_{abc}

Fig. 4.18 Current behaviours with/without compensation.



(a) Voltages in $\alpha\beta$ frame



(b) Voltage trajectories

Fig. 4.19 Voltage behaviours with/without compensation.

4.4.2. Compensation under dynamic conditions

Apart from the steady-state test, the feasibility of the proposed strategy is further experimentally verified under dynamic conditions. The demanded torque is stepped as 0.1-0.25-0.1 Nm while the system has similar asymmetric conditions that given in section 4.4.2. Fig. 4.20 shows the estimated torque and flux without/with compensation (for simplicity, only Mode [1] and Mode [3] are used since Mode [2] is already included in Mode [3]). As can be seen from Fig. 4.20, the torque/flux quickly responds to their demand changes under both Modes, in addition to less torque/flux ripples producing under Mode [3].

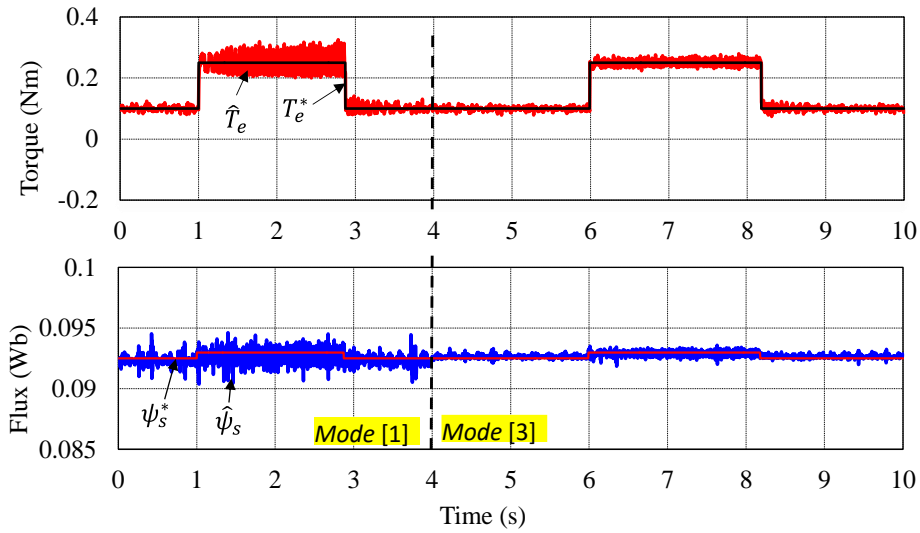


Fig. 4.20 Torque and flux dynamic responses with/without compensation.

Fig. 4.21-4.23 show the motor starting from a standstill under symmetrical condition using Mode [1], asymmetric condition using Mode [1], and asymmetric condition using Mode [3], respectively. From top to bottom, plots in Fig. 4.21-4.23 show the reference and estimated torques, the reference and estimated fluxes, and the measured three-phase currents. Besides reducing the torque and flux ripples by using Mode [3], Fig. 4.23, the proposed strategy can keep the merits of fast dynamic response inherent in the conventional DTC-SVM.

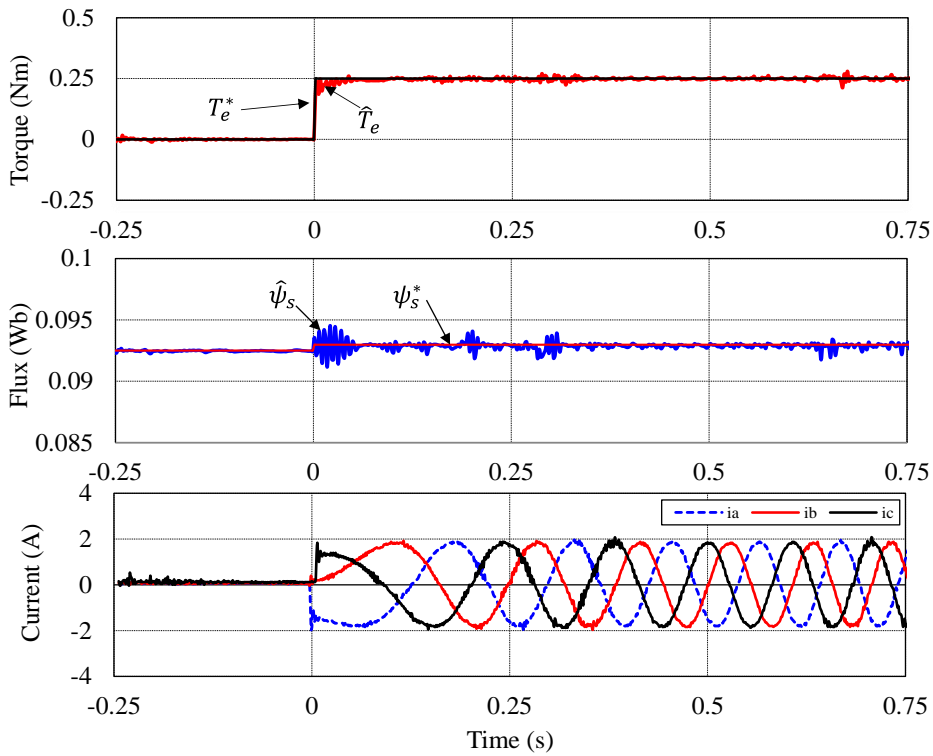


Fig. 4.21 Start-up response under symmetrical conditions using Mode [1].

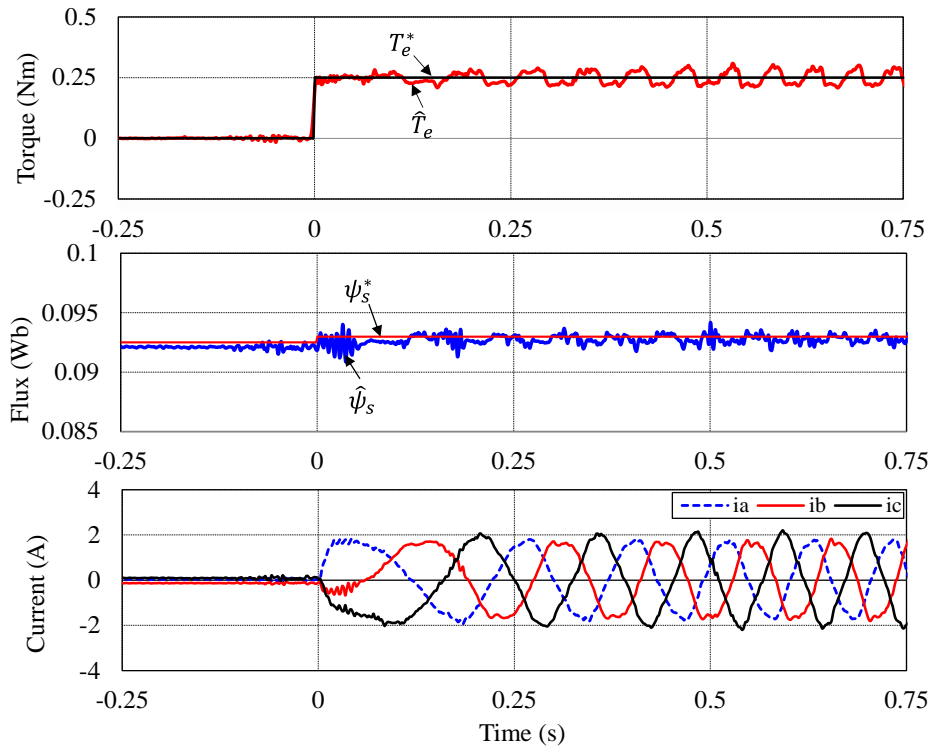


Fig. 4.22 Start-up response under asymmetric conditions using Mode [1].

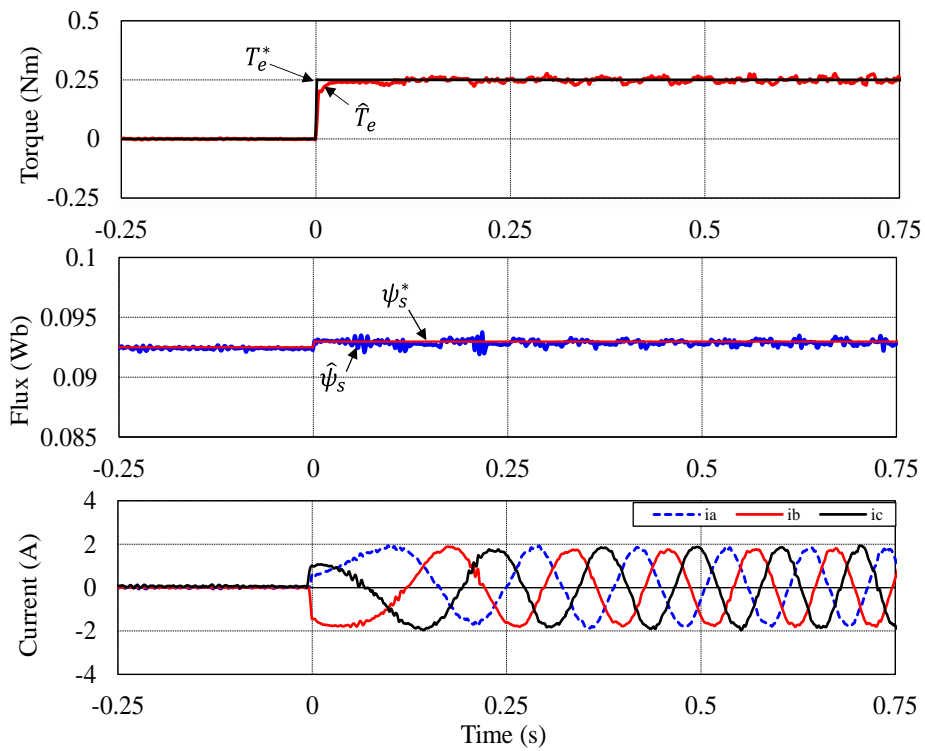


Fig. 4.23 Start-up response under asymmetric conditions using Mode [3].

Fig. 4.24 compares the torque responses obtained from Fig. 4.21-4.23. The rise time t_r under symmetrical ($t_r \approx 3.8ms$) and asymmetric ($t_r \approx 3.7ms$) conditions using Mode [1] is approximately the same while it is less ($t_r \approx 2.8ms$) with a slight overshoot (OS) under asymmetric condition using Mode [3]. The fastest dynamic response under Mode [3] is because of the resonant gain [77], [176], [179]. However, a large resonant gain led to a fast dynamic response, but it imposes high overshoot and vice versa [95]. Therefore, there is a tradeoff between the transient error (large OS) and the fast dynamic response when selecting the resonant controller parameters. Thus, a compromise between those two characteristics should be taken into consideration when tuning with the controller parameters.

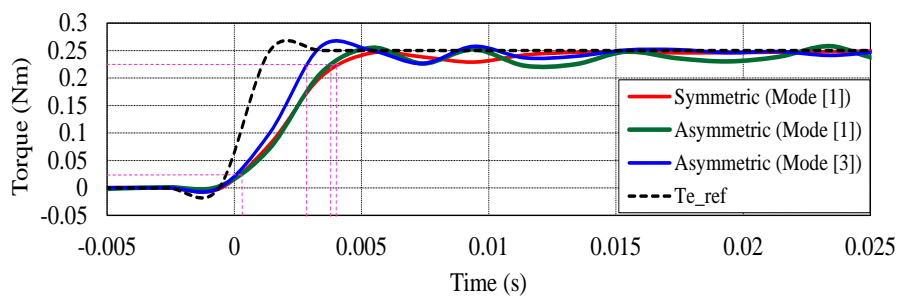


Fig. 4.24 Comparative of torque step responses under different modes.

4.4.3. Speed control

The speed control is also investigated, where the speed, torque, and flux signals are all depicted in Fig. 4.25. At $t=5s$ the Mode [3] is applied, thus, the torque/flux ripples are reduced.

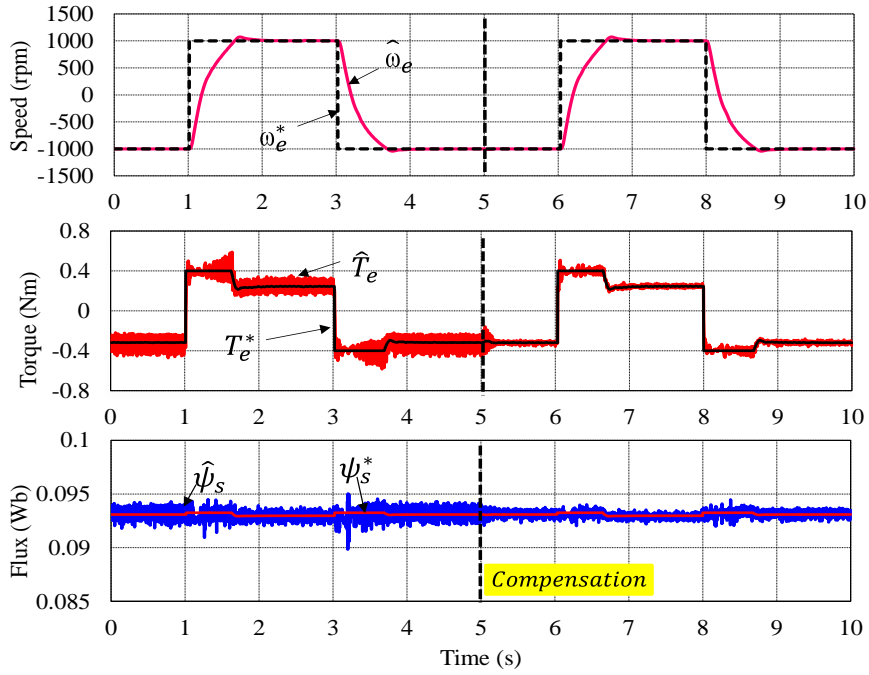


Fig. 4.25 Speed reversal response with/without compensation.

It can be seen that the proposed compensation method is working effectively in both speed directions to keep the merits of fast speed response compared with that of the conventional method.

4.5. Summary

In this chapter, the cascaded DTC-SVM strategy has been modified to suppress the second-order torque and flux harmonic components that reside in asymmetric three-phase PMSMs. It is based on using two compensators of which the first one is by generating the positive and negative sequence voltage vectors independently, and then combined them together to produce a modified RVV. For further torque ripple reduction, the second compensator is used PIR controller tuning at $2\omega_s$ instead of the standard PI-regulator. This modification ensures zero steady state error at the selected frequency. The experimental results have verified the effectiveness of the proposed method under dynamic and steady state conditions, which shows an excellent capability to reduce torque and flux ripples under asymmetric conditions while keeping the merits of fast dynamic response inherent in DTC-SVM strategies.

CHAPTER 5

REDUCTION OF TORQUE AND FLUX RIPPLES IN DIRECT TORQUE CONTROL OF ASYMMETRIC PERMANENT MAGNET SYNCHRONOUS MACHINE

Abstract— Due to asymmetric three-phase system and influence of inverter nonlinearity, large torque and stator flux harmonics would exist in the space vector modulation based direct torque controlled (DTC-SVM) three-phase permanent magnet synchronous machines (PMSMs). A general expression for electromagnetic torque is derived for DTC of asymmetric three-phase PMSMs considering the influence of inverter nonlinearity. To mitigate the influence of the undesired harmonics, a compensation method is developed by enhancing the standard PI-regulator in the torque and flux loops with appropriate resonant controllers. Since the second and sixth order harmonics are the most dominant components, two resonant controllers tuning at the 2nd and 6th of stator angular frequency respectively are utilized. The proposed method can achieve good steady-state performance in terms of low torque and flux ripples while keeping the merits of the conventional DTC-SVM strategy such as good dynamic torque response and machine parameter independence. The experimental results validate the effectiveness of the proposed strategy.

5.1. Introduction

In high-performance motion control such as precision machine tools, robotics, and servo drives, low torque ripple is obligatory [8]. Therefore, the direct torque control (DTC) strategy is often employed, which directly control the torque and stator flux linkage without the coordinate transformation and the inner current loops compared to vector control (VC) [127]. Unlike the cascaded DTC-SVM that presents in Chapter 4, parallel DTC-SVM strategy employs two PI-regulators for flux and torque control, thus, it is less sensitive to the stator flux disturbance and achieves a satisfactory performance when the machine is balanced [45], [163], [164], [180]. However, during operation or manufacturing, it is common that the electric machines are exposed to various types of asymmetries such as stator flux linkage distortion [8], non-sinusoidal back-EMF [181],

[182] unequal phase impedance [161], inverter nonlinearity, etc. [95], [183]. Such abnormal conditions lead to the rise of negative sequence components and parasitic harmonics at low frequency in the torque and flux linkage, i.e., 2nd, 4th, 6th, and 12th [95], [181]. These harmonics behave as alternative components (AC) overlapped with the original direct (DC) quantities. The classic PI-regulator cannot control the AC components due to its bandwidth limitation [95], [174], [184]. Therefore, different control techniques have been presented to mitigate these harmonics [77], [95], [181], [185], [186]. In [181], the authors compensate the influence of non-sinusoidal back EMF and cogging torque by improving the torque estimator, which requires the information about cogging torque, and only the torque improvement is considered. In addition, an iterative learning control (ILC) topology for compensating any periodic components in the torque is inserted between two PI regulators [184]. Moreover, repetitive compensation is often employed for torque ripple reduction [186]. However, it presents drawbacks such as complex tuning process [174], [182]. Furthermore, modified DTC-SVM to deal with this issue is rarely studied so far.

Recently, the resonant controller (R controller) is widely employed in vector control (VC) strategy under asymmetric and distorted conditions [95], [182], [186]. It can be used in stationary reference frame by simply replacing the integral controller with resonant controller (proportional resonant PR controller) [77], [132], [174], or in synchronous reference frame by utilizing resonant controller together with the classical PI-regulator (PIR controller) [95], [151], [187], [188], [189]. In [182], a multi-resonance controller is used in synchronous frame to improve the q -axis current in order to reduce the torque ripple caused by non-sinusoidal back EMFs. In the same manner, a dead time compensation for a dual three-phase machine using a resonant controller is reported in [95], [189].

This chapter focuses on compensating the dominating harmonics in the torque and stator flux linkage caused by unbalanced back EMF and influence of inverter nonlinearity in DTC-SVM for PMSMs. A general expression for electromagnetic torque is derived for DTC of asymmetric 3-phase PMSMs considering the influence of inverter nonlinearity. A modified parallel DTC-SVM strategy being able to reduce the 2nd and 6th harmonics in both torque and flux linkage is presented. The compensation is achieved by enhancing the standard PI-regulators with two resonant controllers tuning at the 2nd and 6th of stator angular frequency respectively. This method does not require a sequential component decomposition and presents desirable performance in terms of

low torque and flux ripples while keeping the merit of conventional DTC-SVM strategy such as fast torque dynamic response and parameter independence.

5.2. Conventional Parallel DTC-SVM Strategy for Balanced PMSM

5.2.1. Mathematical model represented in stator flux reference frame

The mathematical model of PMSM in the stationary $\alpha\beta$ -reference frame can be expressed as [181], [190]:

$$\vec{v}_s = R_s \vec{i}_s + \frac{d\vec{\psi}_s}{dt} \quad (5.1)$$

where $\vec{v}_s = (v_\alpha + jv_\beta)$ is the stator voltage, $\vec{i}_s = (i_\alpha + ji_\beta)$ is the stator current, and $\vec{\psi}_s = (\psi_\alpha + j\psi_\beta)$ is the stator flux-linkage. Then, the stator flux-linkage magnitude and position can be obtained by utilizing either current (5.2) [45], [181], or voltage-model (5.3) [163], [190] based estimator as:

$$\hat{\vec{\psi}}_s = L_s \vec{i}_s + \vec{\psi}_r \quad (5.2)$$

$$\hat{\vec{\psi}}_s = \int (\vec{v}_s - R_s \vec{i}_s) dt \quad (5.3)$$

$$|\hat{\vec{\psi}}_s| = \sqrt{\psi_\alpha^2 + \psi_\beta^2} \quad (5.4)$$

$$\hat{\theta}_s = \tan^{-1} \left(\frac{\psi_\beta}{\psi_\alpha} \right) \quad (5.5)$$

where $\vec{\psi}_r = (\psi_{PM} \cos\theta_r + j\psi_{PM} \sin\theta_r)$ is the flux produced by the rotor, ψ_{PM} is the rotor PM flux, θ_s and θ_r are the stator and rotor flux positions, respectively, and L_s is the stator self-inductance. Then the electromagnetic torque (T_e) can be expressed as:

$$\begin{aligned} T_e &= 1.5p_n \text{Im}\{\vec{\psi}_s' \cdot \vec{i}_s\} \\ &= 1.5p_n \text{Im}\{(\psi_\alpha + j\psi_\beta)' \cdot (i_\alpha + ji_\beta)\} = 1.5p_n (\psi_\alpha i_\beta - \psi_\beta i_\alpha). \end{aligned} \quad (5.6)$$

where p_n denotes the number of pole pairs, and the superscript “'” refers to the complex conjugate vector. The relationship of rotor and stator flux vectors represented in the rotor flux dqr , stator flux dqs , and stationary $\alpha\beta$ reference frames under the symmetric

conditions is depicted in Fig. 5.1. The stator flux dqs -reference frame rotates at the stator angular frequency (ω_s) and the ds -axis is aligned to the stator flux vector $\vec{\psi}_s$. The machine model in the rotational dqr -reference frame can be expressed as [163], [181]:

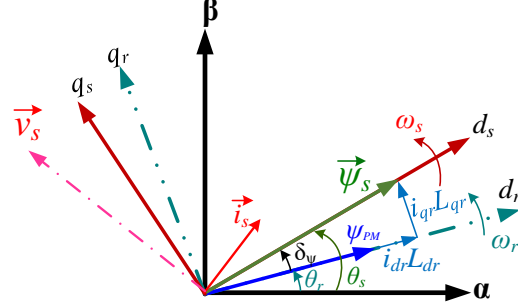


Fig. 5.1 Spatial relationship between different reference frames.

$$\begin{aligned} v_{dr} &= R_s i_{dr} + \frac{d\psi_{dr}}{dt} - \omega_r \psi_{qr} \\ v_{qr} &= R_s i_{qr} + \frac{d\psi_{qr}}{dt} + \omega_r \psi_{dr}. \end{aligned} \quad (5.7)$$

$$\begin{aligned} \psi_{dr} &= L_{dr} i_{dr} + \psi_{PM} \\ \psi_{qr} &= L_{qr} i_{qr} \end{aligned} \quad (5.8)$$

where ω_r refers to the rotor angular frequency, v_{dr} , v_{qr} , i_{dr} , i_{qr} , ψ_{dr} , ψ_{qr} , and L_{dr} , L_{qr} are the voltages, currents, fluxes, and self-inductances in the dqr reference frame, respectively. These voltages in (5.7) can be transformed into the stator flux dqs -reference frame using the following matrix [163], [181]:

$$\begin{bmatrix} F_{ds} \\ F_{qs} \end{bmatrix} = \begin{bmatrix} \cos(\delta_\psi) & \sin(\delta_\psi) \\ -\sin(\delta_\psi) & \cos(\delta_\psi) \end{bmatrix} \begin{bmatrix} F_{dr} \\ F_{qr} \end{bmatrix}. \quad (5.9)$$

where F represents voltage, current or flux-linkage, and δ_ψ is the torque angle. Furthermore, the voltage command of surface mounted PMSM (where $L_{dr} \approx L_{qr}$) in the stator flux dqs -reference frame is given by [45], [181]:

$$\begin{aligned} v_{ds}^* &= R_s i_{ds} + \frac{d|\vec{\psi}_s|}{dt} - \omega_s \psi_{qs} \\ v_{qs}^* &= R_s i_{qs} + \omega_s |\vec{\psi}_s| = \frac{2R_s}{3p_n |\vec{\psi}_s|} T_e + \omega_s |\vec{\psi}_s|. \end{aligned} \quad (5.10)$$

where $i_{qs} = 2T_e / 3p_n |\psi_s|$, $\psi_{qs} = 0$. From (5.10), it can be deduced that the stator flux can be directly controlled by adjusting ds -axis voltage command v_{ds}^* , while the torque can be easily regulated by controlling qs -axis voltage command v_{qs}^* .

5.2.2. Torque and flux control

In the parallel DTC-SVM strategy, the torque and flux quantities can be controlled by employing two closed-loop systems. The estimated torque and flux are compared with their references, and then, the resulting errors signals, i.e., ΔT_e and $\Delta \psi_s$, are delivered to the PI-regulators, whose outputs are the command voltage components v_{ds}^* and v_{qs}^* in the stator flux dqs -reference frame as shown in Fig. 5.2. The final RVV can be formed by transforming this voltage commands into stationary $\alpha\beta$ -reference frame as:

$$\begin{bmatrix} v_{\alpha}^* \\ v_{\beta}^* \end{bmatrix} = \begin{bmatrix} \cos(\theta_s) & -\sin(\theta_s) \\ \sin(\theta_s) & \cos(\theta_s) \end{bmatrix} \begin{bmatrix} v_{ds}^* \\ v_{qs}^* \end{bmatrix}. \quad (5.11)$$

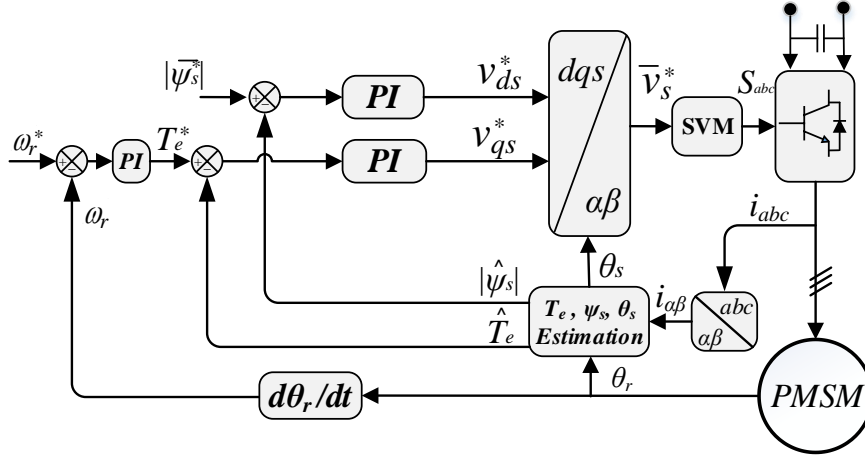


Fig. 5.2 Block diagram of the parallel DTC-SVM structure.

5.2.2.1. Stator flux control loop

Back to the mathematical model of SPMSM derived in Chapter 4, the current in the ds -axis (refer to equation 4.11 in Chapter 4) can be put in the form bellow:

$$i_{ds} = \frac{|\psi_s| - \psi_{PM} \cos \delta_\psi}{L_s} \quad (5.12)$$

Substituting equation (5.12) in the first equation of (5.10) one can obtains:

$$v_{ds} = R_s \left(\frac{|\psi_s| - \psi_{PM} \cos \delta_\psi}{L_s} \right) + \frac{d\vec{\psi}_s}{dt} = \frac{R_s}{L_s} |\vec{\psi}_s| + \frac{d\vec{\psi}_s}{dt} - \frac{R_s \psi_{PM}}{L_s} \cos \delta_\psi \quad (5.13)$$

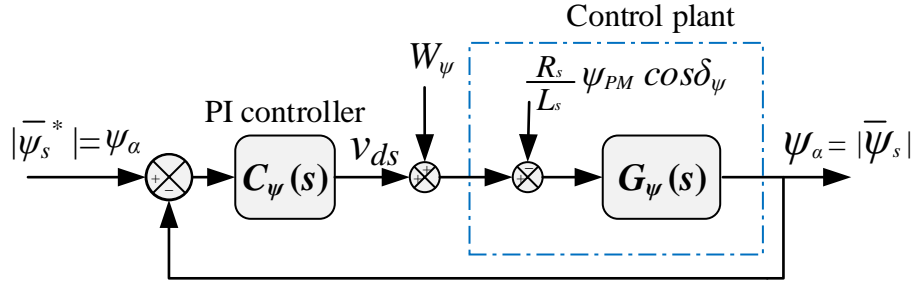


Fig. 5.3 Block diagram of the flux control loop.

Taking the Laplace transformation of (5.13) gives:

$$v_{ds} = \left(s + \frac{R_s}{L_s}\right) |\bar{\psi}_s| - \frac{R_s \psi_{PM}}{L_s} \cos \delta_\psi \quad (5.14)$$

Assuming small changes in δ_ψ , hence $\cos \delta_\psi \cong 1$, and equation (5.14) becomes:

$$v_{ds} = \left(s + \frac{R_s}{L_s}\right) |\bar{\psi}_s| - W_\psi \quad (5.15)$$

where, $W_\psi = \frac{R_s \psi_{PM}}{L_s} \cos \delta_\psi \cong \frac{R_s \psi_{PM}}{L_s}$, the TF between the stator flux magnitude and the ds -axis voltage is

$$G_\psi(s) = \frac{|\bar{\psi}_s|}{v_{ds} + W_\psi} = \frac{1}{s + \frac{R_s}{L_s}} = \frac{1}{s + A_\psi} \quad (5.16)$$

where, $A_\psi = \frac{R_s}{L_s}$. The flux control loop is shown in Fig. 5.3, where $C_\psi(s)$ is a TF of the conventional PI controller given by:

$$C_\psi(s) = \frac{K_{P\psi} \left(s + \frac{K_{I\psi}}{K_{P\psi}} \right)}{s} \quad (5.17)$$

and the TF of the closed-loop stator flux magnitude control is

$$G_{\psi,CL}(s) = \frac{|\bar{\psi}_s|}{|\bar{\psi}_s^*|} = \frac{C_\psi(s) G_\psi(s)}{1 + C_\psi(s) G_\psi(s)} \quad (5.18)$$

Substituting $C_\psi(s)$ and $G_\psi(s)$ into (5.18) yields:

$$G_{\psi,CL}(s) = \frac{\frac{K_{P\psi} \left(s + \frac{K_{I\psi}}{K_{P\psi}} \right)}{s} \left(\frac{1}{s + A_{\psi}} \right)}{1 + \frac{K_{P\psi} \left(s + \frac{K_{I\psi}}{K_{P\psi}} \right)}{s} \left(\frac{1}{s + A_{\psi}} \right)} = \frac{K_{P\psi} \left(s + \frac{K_{I\psi}}{K_{P\psi}} \right)}{s^2 + (A_{\psi} + K_{P\psi})s + K_{I\psi}} \quad (5.19)$$

5.2.2.2. Torque control loop

The torque control loop of the parallel structure DTC-SVM represented in s-domain is shown in Fig. 5.4. $G_{T_e}(s)$ is the TF between the qs -axis voltage and the electromagnetic torque (similar to that obtained in Chapter 4, section §4.2.2.2), and $C_{T_e}(s)$ is the TF of the standard PI controller defined as:

$$C_{T_e}(s) = \frac{K_{PT_e} \left(s + \frac{K_{IT_e}}{K_{PT_e}} \right)}{s} \quad (5.20)$$

Hence, the torque closed-loop control TF in Fig. 5.4 can be expressed as:

$$G_{T_e,CL}(s) = \frac{T_e^*(s)}{T_e(s)} = \frac{C_{T_e}(s) \cdot G_{T_e}(s)}{1 + C_{T_e}(s) \cdot G_{T_e}(s)} \quad (5.21)$$

Substituting the TF of $C_{T_e}(s)$ and $G_{T_e}(s)$ into equation (5.21) yields:

$$G_{T_e,CL}(s) = \frac{K_{P\psi} \psi_{PM} A_{T_e} K_{PT_e} \left(s + \frac{K_{IT_e}}{K_{PT_e}} \right)}{s^2 + (B_{T_e} + K_{PT_e} A_{T_e})s + (C_M + K_{IT_e} A_{T_e})} \quad (5.22)$$

The PI controller parameters of both torque and flux control loops can be obtained using either SISO tool of MATLAB software or online tuning in the real-time operating system.

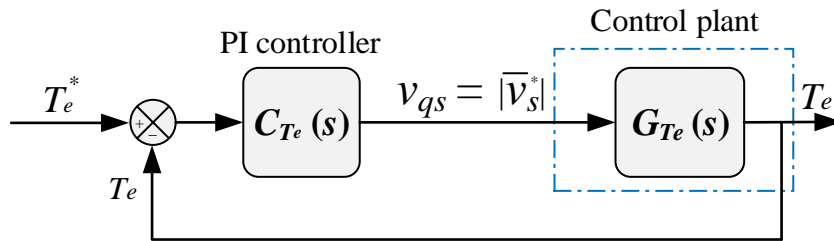


Fig. 5.4 Block diagram of the torque control loop in s-domain.

5.3. Influence of Unbalanced and Inverter nonlinearity

5.3.1. Inverter nonlinearity

Most of the VSIs suffer from different non-ideal characteristics such as a change in the junction temperature of the power switch devices, DC-Link voltage/current fluctuation, and phase current unbalanced [191], [192], [193]. These factors result in current distortion, torque pulsating, and degradation of control performance. The most significant non-linearity causes include [191], [192], [193], [194]:

- A voltage drop across the power switch devices.
- Dead time effect.
- Pulsating of the DC-link voltage.

5.3.1.1. Voltage drop across power switch devices

In the real VSI, the power switches do not conduct ideally. When they are conducting, the voltage across them is not zero and equal to the voltage drop on the conducted transistor V_T . Whereas, in the blocking mode, the power switches have voltage drop on the conducted diode V_D . The voltage drop across the power devices depending on the phase current direction. It has an influence on the output voltage, especially at the low-speed range and high load current. Fig. 5.5 shows the influence of the voltage drop across power switch devices on the inverter output voltage. It can be seen that the output voltage is asymmetric (having offset) and the voltage drop decreases the output voltage when the phase current is positive and increases the output voltage when the phase current is negative [193], [194], [195].

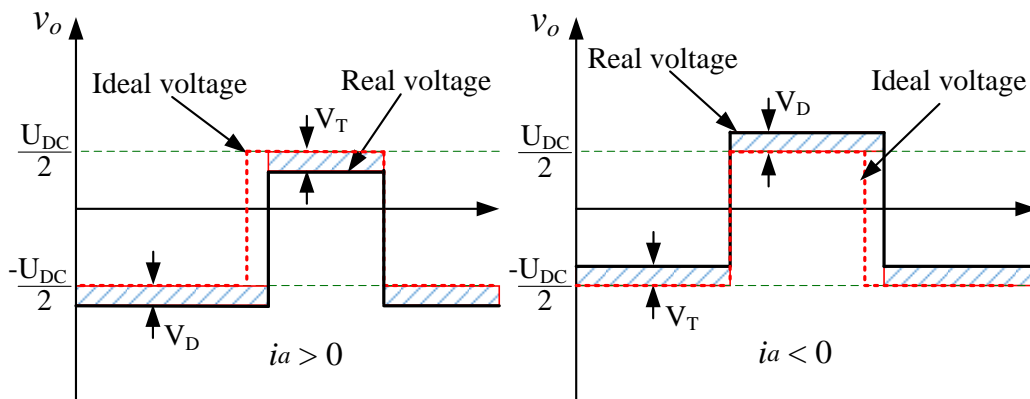


Fig. 5.5 Output voltage with the influence of voltage drop across power devices.

5.3.1.2. Dead time

In the practice, all power switches have non-ideal characteristics. Hence, they do not turn ON or OFF instantaneously. To avoid a short circuit in the DC-link, a protection time is necessary when two switching devices are in the same leg. This time is known as the dead time (T_D), and included in the control signals. It guarantees safe operation of the inverter. The typical value of T_D is between $1\mu s$ to $5\mu s$, where the lowest value is for small power IGBT and is increased in respect to increasing of IGBT power [193]. The effect of dead time can be examined from one phase of PWM inverter since each inverter leg consists of upper (T_1) and lower (T_2) power switch device, and reverse recovery diodes D_1 and D_2 , connected between the positive and negative rails of the power supply. The gate signals S_a and \bar{S}_a come from the control block, which forms the output voltage V_o . Fig. 5.6 shows the ideal control signals and real control signals with inserted dead time T_D . It can be seen that the time duration of the real drive signal of upper transistor is shorter than the ideal drive signal and for the lower transistor is longer than ideal. Therefore, when the phase current is positive ($i_a > 0$), the output voltage is reduced while for negative phase current ($i_a < 0$), the output voltage is increased as shown in Fig. 5.7 [185], [196]. It is worth mentioning that the effect of dead time is more obvious at low-speed operation range, whilst it is almost disappeared in the high-speed range.

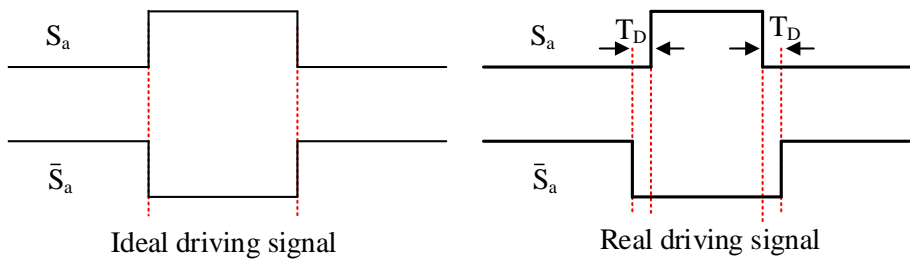


Fig. 5.6 Gate drive signal control on one inverter lag.

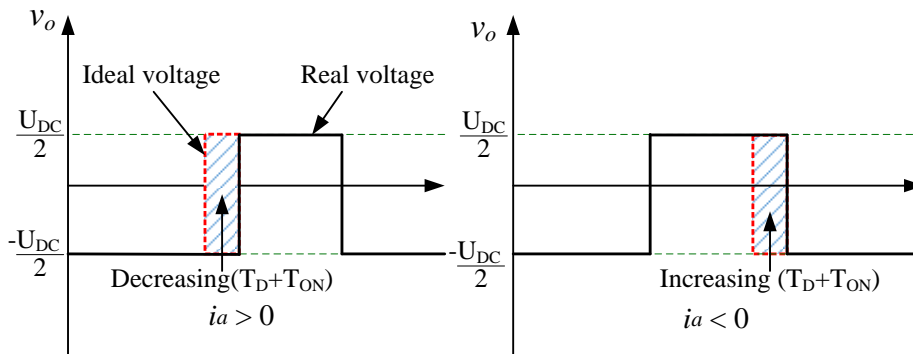


Fig. 5.7 Dead time effect on the inverter output voltage.

5.3.1.3. Pulsating of DC-link voltage

Actually, the real DC-link voltage contains ripple and fluctuation due to low capacitor value or bad filtering, and the disadvantage of diode rectifier and non-ideal characteristic. Therefore, the quality of DC-link voltage has a direct influence on the inverter output voltage in which the inverter output voltage can be expressed as [195], [195].

$$v_o = D \cdot U_{DC} \quad (5.23)$$

where D is the duty cycle ratio, U_{DC} is the DC-Link voltage, and v_o represent inverter output voltage. Hence, it can be easily observed that any change in DC-link voltage will contribute in variation of the output voltage. To overcome this problem:

- Using the measured DC-link voltage in the calculation of the modulation index of SVM instead of constant value.
- Replacing the diode rectifier circuit by active rectifier circuit, which provides a controllable DC-link voltage.
- Using high capacitor value in the DC-link side to increase the possibility of filtering out the undesired ripples and ensure smooth DC-link voltage.

The above factors will result in the rise of the odd low order harmonics in the three-phase current, especially the 5th and 7th [197].

5.3.2. Impact of unbalanced Back-EMF and Inverter nonlinearity

Due to unbalanced back-EMF caused by winding asymmetry and influence of inverter nonlinearity, the stator voltage, current, and flux in a three-phase system can be expressed in terms of their positive-, negative-, zero-sequence components of ω_s and the harmonic components of $-5\omega_s$ and $+7\omega_s$ [95], [189], [197], [83], [198]. Since the model under investigation is a three-wire connection system, i.e., floating neutral point, the zero-sequence component is neglected [83]. Fig. 5.8 shows the spatial relationship between different reference frames under asymmetric condition. It is worth mentioning that only the positive, negative sequence and harmonic components of fifth and seventh are taken into consideration in this paper. Therefore, the voltage, current, and stator flux linkage vectors can be expressed in the stationary $\alpha\beta$ frame as [151], [198]:

$$\vec{F}_{\alpha\beta} = \vec{F}_{\alpha\beta 1+} + \vec{F}_{\alpha\beta 1-} + \vec{F}_{\alpha\beta 5-} + \vec{F}_{\alpha\beta 7+} \quad (5.24)$$

where the subscript of 1+, 1-, 5-, 7+ refer to the positive-, negative-sequence components, fifth, and seventh harmonic components, respectively. According to Fig. 5.8, the dqs^{1+} reference frame rotates at the stator angular frequency of ω_s .

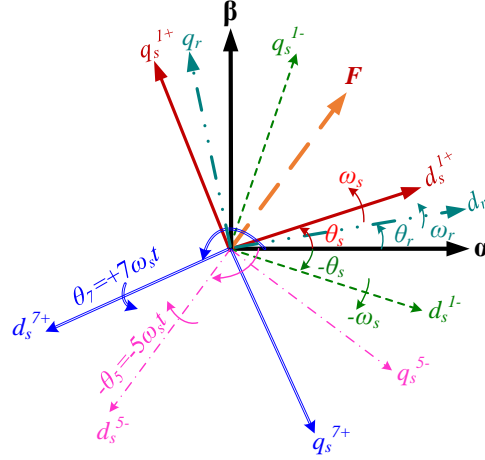


Fig. 5.8 Asymmetric condition (unbalanced back-EMF and inverter nonlinearity).

Whereas, the harmonic reference frames, dqs^{1-} , dqs^{5-} , and dqs^{7+} rotate at the angular frequencies of $-\omega_s$, $-5\omega_s$, and $+7\omega_s$, respectively. These harmonics can be represented in the dqs^{1+} reference frame as:

$$\vec{F}_{dqs}^{1+} = \vec{F}_{dqs1+}^{1+} + \vec{F}_{dqs1-}^{1-} e^{-j2\omega_s t} + \vec{F}_{dqs5-}^{5-} e^{-j6\omega_s t} + \vec{F}_{dqs7+}^{7+} e^{j6\omega_s t} \quad (5.25)$$

where the superscripts of 1+, 1-, 5-, and 7+ represent the positive, negative, and harmonic components of $-5\omega_s$ and $+7\omega_s$ in the dqs^{1+} reference frame, respectively, and $e^{\pm jh\omega_s t} = (\cos(h\omega_s t) \pm j\sin(h\omega_s t))$. From (5.25), it can be deduced that the negative sequence component due to unbalanced back EMF behaves as the AC oscillation at the frequency of $2\omega_s$ in the dqs^{1+} reference frame [181], [182]. Whereas, the harmonic components of $-5\omega_s$ and $+7\omega_s$ caused by inverter nonlinearity behave as the AC oscillation at the frequency of $\pm 6\omega_s$ in the dqs^{1+} reference frame [151], [189], [198], [199]. According to Fig. 5.8 and (5.25), the current and stator flux in the dqs^{1+} reference frame can be expressed as:

$$\vec{\psi}_{dqs}^{1+} = \vec{\psi}_{dqs1+}^{1+} + \vec{\psi}_{dqs1-}^{1-} e^{-j2\omega_s t} + \vec{\psi}_{dqs5-}^{5-} e^{-j6\omega_s t} + \vec{\psi}_{dqs7+}^{7+} e^{j6\omega_s t} \quad (5.26)$$

$$\vec{i}_{dqs}^{1+} = \vec{i}_{dqs1+}^{1+} + \vec{i}_{dqs1-}^{1-} e^{-j2\omega_s t} + \vec{i}_{dqs5-}^{5-} e^{-j6\omega_s t} + \vec{i}_{dqs7+}^{7+} e^{j6\omega_s t} \quad (5.27)$$

Then, the electromagnetic torque can be expressed as [83], [198], [199]:

$$\begin{aligned}
T_e &= 1.5p_n \operatorname{Im} \{ \vec{\psi}_{dqs}^{1+} \cdot \vec{i}_{dqs}^{1+} \} \\
&= 1.5p_n [T_{e0} + T_{es2} \sin(2\omega_s t) + T_{ec2} \cos(2\omega_s t) + T_{es6} \sin(6\omega_s t) + T_{ec6} \cos(6\omega_s t)]
\end{aligned} \tag{5.28a}$$

where the variables of T_{es2} , T_{ec2} , T_{es6} , and T_{ec6} can be expressed in the following matrix:

$$\begin{bmatrix} T_{e0} \\ T_{es2} \\ T_{ec2} \\ T_{es6} \\ T_{ec6} \end{bmatrix} = \begin{bmatrix} -\psi_{qs1+}^{1+} & \psi_{ds1+}^{1+} & -\psi_{qs1-}^{1-} & \psi_{ds1-}^{1-} \\ \psi_{ds1-}^{1-} & \psi_{qs1-}^{1-} & -\psi_{qs1+}^{1+} & -\psi_{ds1+}^{1+} \\ -\psi_{qs1-}^{1-} & \psi_{ds1-}^{1-} & -\psi_{qs1+}^{1+} & \psi_{ds1+}^{1+} \\ \psi_{ds5-}^{5-} - \psi_{ds7+}^{7+} & \psi_{qs5-}^{5-} - \psi_{qs7+}^{7+} & 0 & 0 \\ -\psi_{qs5-}^{5-} - \psi_{qs7+}^{7+} & \psi_{ds5-}^{5-} + \psi_{ds7+}^{7+} & 0 & 0 \end{bmatrix} \begin{bmatrix} i_{ds1+}^{1+} \\ i_{qs1+}^{1+} \\ i_{ds1-}^{1-} \\ i_{qs1-}^{1-} \\ i_{ds5-}^{5-} \\ i_{qs5-}^{5-} \\ i_{ds7+}^{7+} \\ i_{qs7+}^{7+} \end{bmatrix} \tag{5.28b}$$

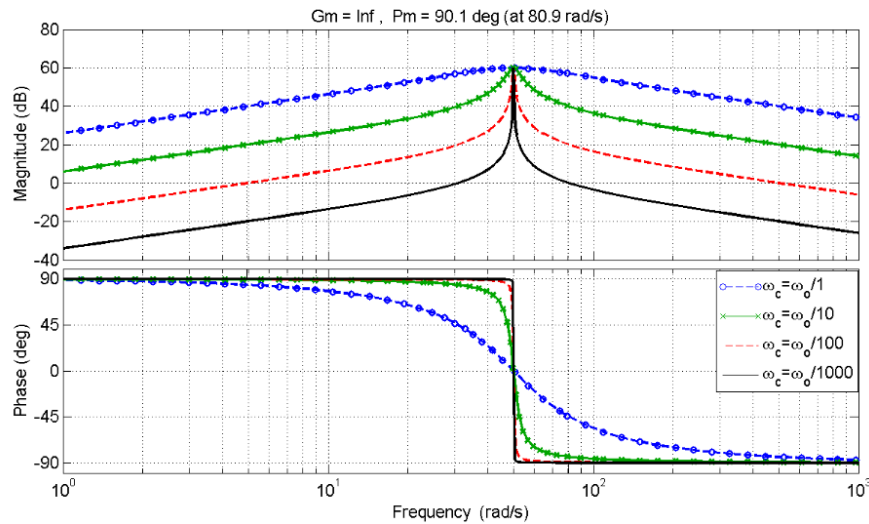
From (5.28), it can be deduced that the electromagnetic torque is composed of a DC term T_{e0} , which is correlated with equal sequence product of flux and current. While the alternative terms of T_{es2} , T_{ec2} , T_{es6} , T_{ec6} oscillate at $2\omega_s$ and $6\omega_s$ of the fundamental frequency, respectively. These harmonic terms are produced by unequal sequence product as illustrated in (5.28b) [151], [83], [198]. It should be emphasized that the harmonic components of 4th, 8th, and 12th also exist in the estimated torque [198], which are correlated with different unequal sequence product.

It is worth noting that for symmetric case, the torque can be calculated according to (5.6), which is established upon the assumption that current and back-EMF are sinusoidal. For an asymmetric machine, (5.28) should be used in which the dominant second and sixth harmonic components are considered. However, the proposed method is designed to suppress the second and sixth harmonics in the output torque and stator flux linkage using resonant controllers, as shown in Fig. 5.11. Thus, when such harmonics are suppressed with compensation using the resonant controllers, the asymmetric machine becomes equivalent to that of the symmetrical case, and then (5.6) can be used to estimate the torque as it is much simpler than (5.28) for practical implementation. Consequently, since the resonant controllers are machine parameters independent, as will be discussed later, the measurement of unknown components in (5.28b) are not required.

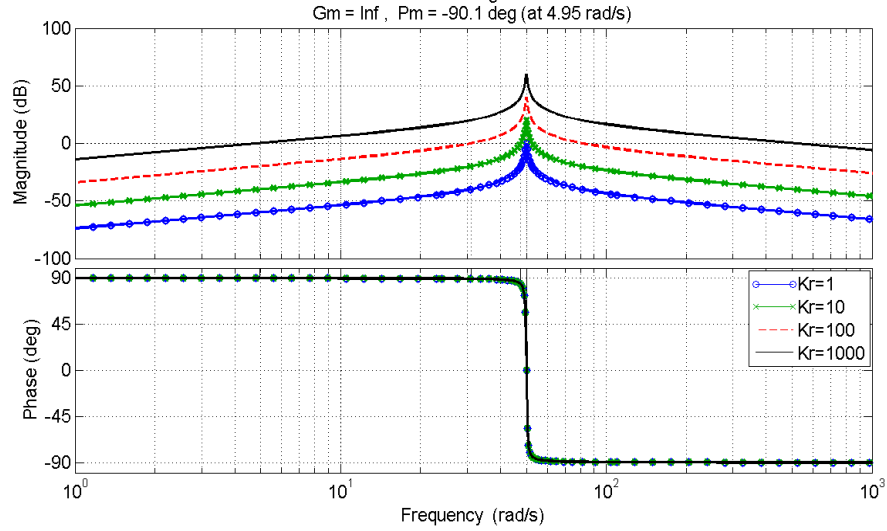
5.4. Proposed Parallel DTC-SVM Strategy for Unbalanced and Distorted PMSM

5.4.1. Resonance controller

As discussed in Chapter 4 section 4.3.4, the conventional PI-controller has been enhanced by a resonant controller to increase the bandwidth at the selected frequencies. Therefore, a non-ideal R controller (described by equation 4.61, and Fig 4.15 [52], [189]) is employed together with the conventional PI controller to mitigate the steady-state error [178]. The frequency response of the resonant controller (shown in Fig 4.15) at $K_r=200$, $\omega_s =157$ rad/s, and different ω_c is illustrated in Fig. 5.9(a), while at fixed ω_c and variable resonant gain $K_r =\text{variable}$ is shown in Fig. 5.9(b). It can be deduced that for a small value of ω_c , better performance can be achieved when the resonant gain is constant. Usually, the cut-off frequency is far lower than the fundamental frequency $\omega_c \ll \omega_s$ [95], [189]. In this chapter, the cut-off frequency of two resonant controllers (ω_{c2} , ω_{c6}) are online modified with respect of the variable fundamental frequency ω_s to ensure better selectivity of the required harmonic [189], [178].



(a) Conditions at $f_s=25\text{Hz}$, $\omega_o=157$ rad/s, $h=2$, $K_r=1000$, and variable ω_c



(b) Conditions at $f_s=25\text{Hz}$, $\omega_o=157\text{ rad/s}$, $h=2$, $\omega_c=0.25\text{ Hz}$, and variable K_r

Fig. 5.9 Frequency response of non-ideal resonant controller.

5.4.2. Dynamic behavior of PIR controller

The final transfer function of the torque and flux controllers with the 2nd and 6th harmonics compensation can be represented as:

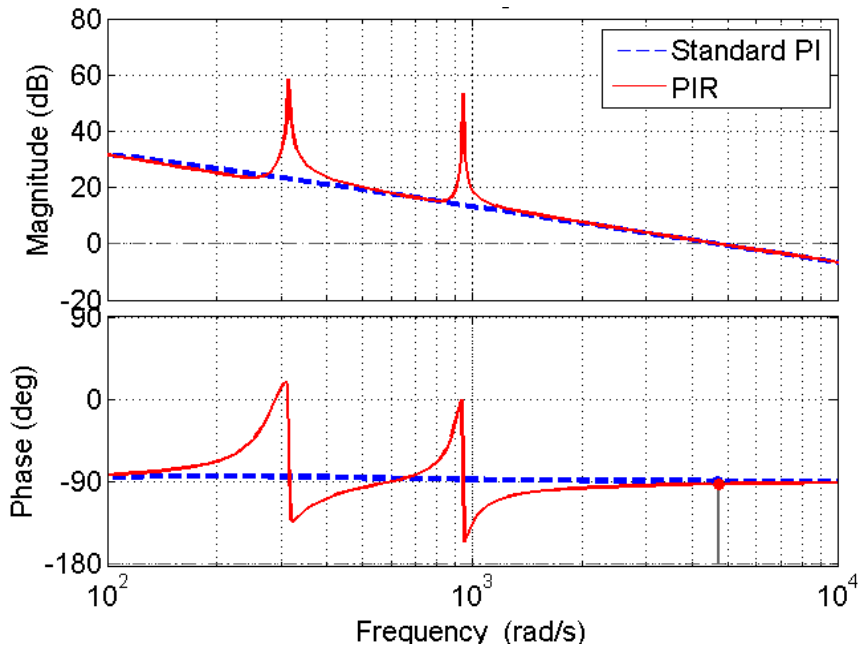
$$G_{PIR}(s) = G_{PI} + G_{R2} + G_{R6} = K_p + \frac{K_i}{s} + \frac{K_{r2}\omega_{c2}s}{s^2 + \omega_{c2}s + (2\omega_s)^2} + \frac{K_{r6}\omega_{c6}s}{s^2 + \omega_{c6}s + (6\omega_s)^2} \quad (5.29)$$

where K_p and K_i are the proportional and integral gains of the standard PI-regulator, respectively. K_{r2} , K_{r6} , are the resonant gains, and ω_{c2} , ω_{c6} , are the cut-off frequencies of the second and sixth order harmonics controllers, respectively. Assume that the inverter TF is unity, i.e. $G_{INV}(s) = 1$, and PMSM plant is RL circuit with the transfer function of $G_{PL} = 1/(L_s s + R)$. Then, the open- and closed-loop system TF can be expressed as:

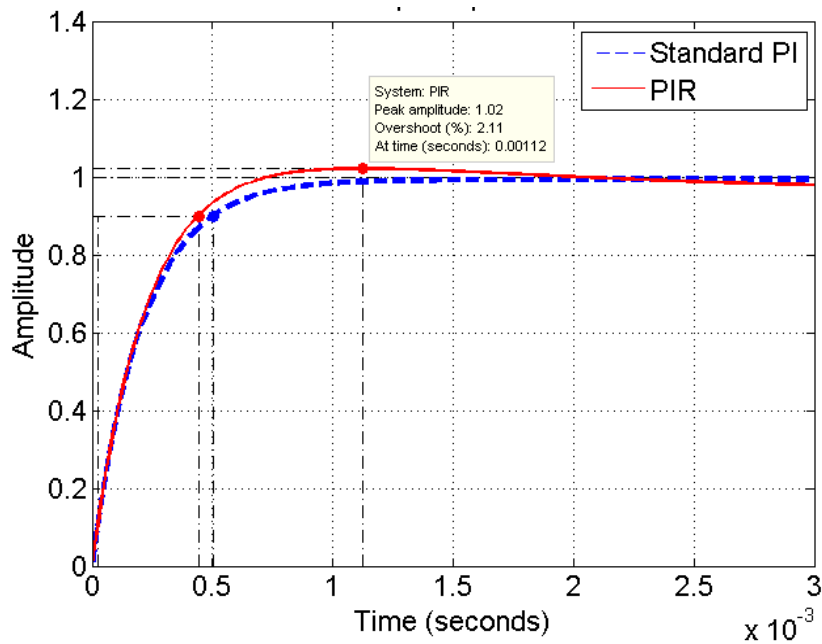
$$G_{OL}(s) = G_{PIR}(s)G_{INV}(s)G_{PL}(s) \quad (5.30)$$

$$G_{CL}(s) = \frac{G_{PIR}(s)G_{INV}(s)G_{PL}(s)}{1 + G_{PIR}(s)G_{INV}(s)G_{PL}(s)} \quad (5.31)$$

The frequency response of the open-loop TF (5.30) is shown in Fig. 5.10(a). The cut-off frequencies and resonant gains are given in Table I. It can be seen that compared to classical PI, the PIR only provides high gain around the frequencies of $2\omega_s$ and $6\omega_s$, which imposes zero steady-state error at these frequencies. Fig. 5.10(b) shows the dynamic behavior comparison without/with considering the resonant controller, which is obtained from the closed-loop TF of (5.31).



(a) Bode-plot without/with resonant controller



(b) Step responses without/with a resonant controller

Fig. 5.10 Frequency response of the proposed compensation.

It should be emphasized that the torque loop, flux loop, and speed loop regulators are conventional controllers and their tunings can be widely found in existing papers [163], [168]. It should be emphasized that the torque loop, flux loop, and speed loop regulators are conventional controllers. Since they are conventional controllers, their tunings can be widely found in [163], [168], [18], or using commercial software such as MATLAB. The method used for the determination of the PI parameters of the

three conventional regulators is based on the analysis of transfer function in the frequency domain, and the SISO tool of MATLAB is then used to determine the optimized PI parameters. Thus, in fact, there are only four parameters viz. two resonant gains and two cut-off frequencies need to be adjusted. Our main contribution is the development of two resonant controllers, being able to self-adjust with respect to the variable fundamental frequency, to suppress the 2nd and 6th harmonics. For decent control performance, the easiest way to obtain the resonant gains can be utilized in which their values can be set around or as same as the value of the integral gain of current or torque PI controllers [95], [168], [182]. Since an overshoot in the torque step response can be observed if the high resonant gain is employed [132], [188], the values of resonant gains are selected to be around the values of integral PI controllers gains. Furthermore, the step responses with and without resonant controllers are presented in Fig 3(b). It can be found that a good dynamic response and low overshoot (*OS*) is achieved when considering resonant controllers, i.e., the rising time and *OS* for PIR are $t_r=0.41ms$, $OS=2.11\%$, respectively, while they are $t_r=0.52ms$, $OS=0\%$ for the standard PI-controller. Hence, there is a trade-off between fast dynamic response and low overshoot [77], [188], [189]. On the other hand, the influence of cut-off frequencies (ω_{c2} , ω_{c6}) of two resonant controllers is usually dominant in control performance. In this paper, the gains for the online adjustment of two cut-off frequencies ($\omega_{c2}=\omega_s/200$ and $\omega_{c6}=\omega_s/100$) with respect to the variable fundamental frequency are based on the bode-plot analysis shown in Fig. 2(b). Thus, their tuning is also straightforward [95], [77], [151], [189].

Furthermore, assuming an ideal resonant controller tuning at $2\omega_s$ is used in (5.31) for simplicity, then the closed-loop transfer function can be expressed as:

$$\begin{aligned}
G_{CL}(s) &= \frac{G_{PIR}(s)G_{INV}(s)G_{PL}(s)}{1+G_{PIR}(s)G_{INV}(s)G_{PL}(s)} \\
&= \frac{F_N(s)}{s[s^2+(2\omega_s)^2].(Ls+R)+s[s^2+(2\omega_s)^2]K_p+F_N(s)}
\end{aligned} \tag{5.32}$$

where $G_{PIR}(s)=K_p+\frac{K_i}{s}+\frac{K_{r2}s}{s^2+(2\omega_s)^2}$, and $F_N(s)=s[s^2+(2\omega_s)^2]K_p+[s^2+(2\omega_s)^2]K_i+s^2K_{r2}$.

Substituting $s=j2\omega_s$ into (5.32) yields:

$$G_{CL}(s) = \frac{F_N(j2\omega_s)}{j2\omega_s \cdot ((j2\omega_s)^2 + (2\omega_s)^2) \cdot (j2\omega_s L + R) + F_N(j2\omega_s)} \quad (5.33)$$

$$= \frac{F_N(j2\omega_s)}{j2\omega_s \cdot (0) \cdot (2\omega_s L + R) + F_N(j2\omega_s)} = 1$$

The analysis above implies that the proposed method is machine parameter independent. This method provides zero state-steady error at the selected frequency $2\omega_s$ [151]. The similar conclusion can be easily extended to other frequencies. Consequently, to implement $G_R(s)$ controller in discrete time-domain, several discretization methods can be used [178]. The two integration model is utilized shown in Fig. 5.9(a), where the forward integrator is discretized with a forward Euler method, i.e., $s=(z-1)/T_s$, and the feedback one uses the backward Euler method, i.e., $s=(z-1)/zT_s$, where T_s is the sample time [132], [178].

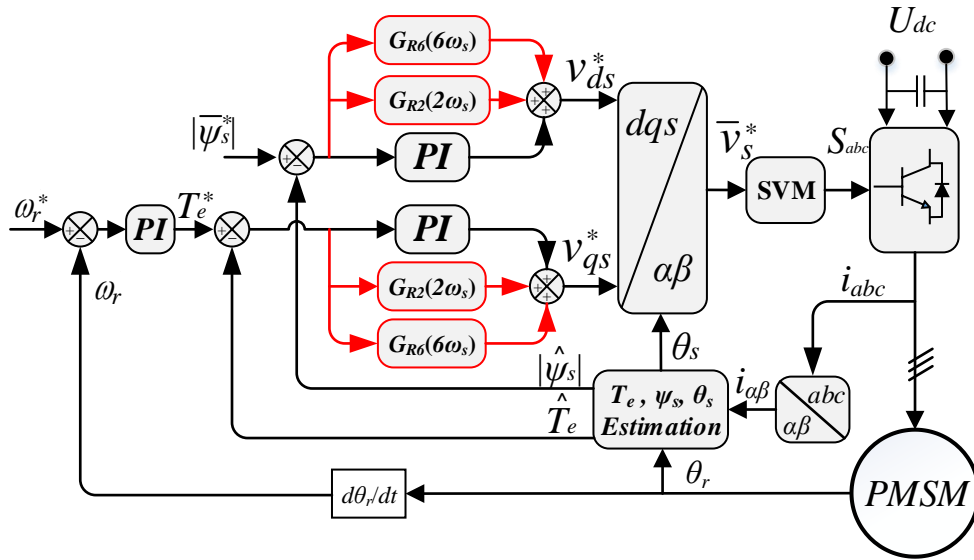


Fig. 5.11 Schematic diagram of the proposed strategy.

5.5. Experimental Verification

The feasibility of the proposed strategy is verified by many experiments in which the sampling frequency and the switching frequency of SVM are 10 kHz. A permanent magnet DC motor is mechanically coupled to the prototype PMSM and is connected with an adjustable power resistor to provide a load. The parameters of the prototype machine are given in Chapter 2 section § 2.4, while the controllers are listed in Table 5.1. The block diagram of the proposed method is shown in Fig. 5.11.

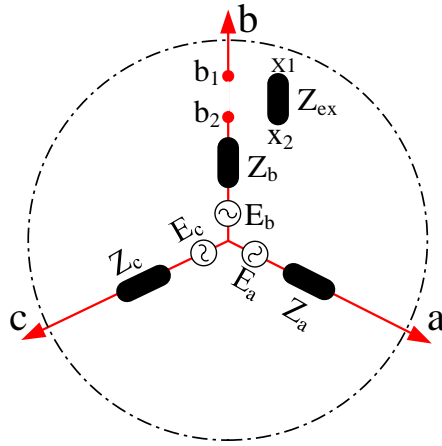
TABLE 5.1 EXPERIMENTAL SYSTEM PARAMETERS

Controller parameters		
Torque loop regulator	$K_p=45$	$K_i=2500$
Flux loop regulator	$K_p=528$	$K_i=1000$
Resonant gain	$K_{r2}=1000$	$K_{r6}=1800$
Cut-of frequency	$\omega_{c2}=\omega_s/200$	$\omega_{c6}=\omega_s/100$
Speed loop regulator	$K_p=0.0001$	$K_i=0.0014$

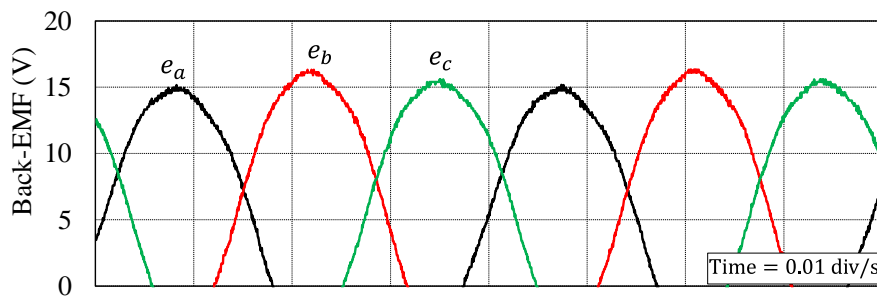
5.5.1. Compensation under steady-state conditions

The asymmetric conditions have been created by adding extra coil inside the machine with the number of turns equal to 10% of phase *b* windings as shown in Fig. 5.12(a). The extra coil is adaptable, i.e., it can be connected, disconnected, and reversely connected to any phase manually via mechanical switch. The measured impedance of the additional coil is $Z_{ex}=R_{ex}+L_{ex}=0.098\ \Omega+0.102\ \text{mH}$. Therefore, depending on the phase and the way of the additional coil connection, the flux linkage produced by this phase will be different from that produced by other healthy phases. Hence, the unbalanced back-EMFs can be generated.

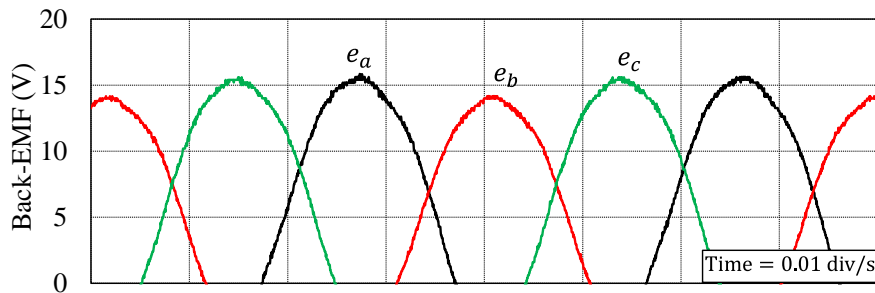
In this section, two cases (case A and case B) of unbalanced back EMF have been considered. In the case A, the extra coil is connected in series with phase *b* as $b_1x_1-b_2x_2$, Fig. 5.12(a), where the main and extra coils are in the same winding direction. Therefore, the total flux linkage produced by phase *b* will increase, which makes the back-EMF of phase *b* higher, Fig. 5.12(b). On the other hand, for case B, the direction of the extra coil is reversed, i.e., $b_1x_2-b_2x_1$, and thus the total flux linkage is reduced, which makes the back-EMF of phase *b* smaller, Fig. 5.12(c). The steady-state performance is investigated under both cases to show the influence of different situations of unbalanced back-EMF on the proposed strategy. The torque and stator flux-linkage references are set to $T_e^*=0.2\ \text{Nm}$ and $|\psi_{s'}^*|=928\ \text{mWb}$.



(a) Extra windings connection



(b) Back-EMF under case A

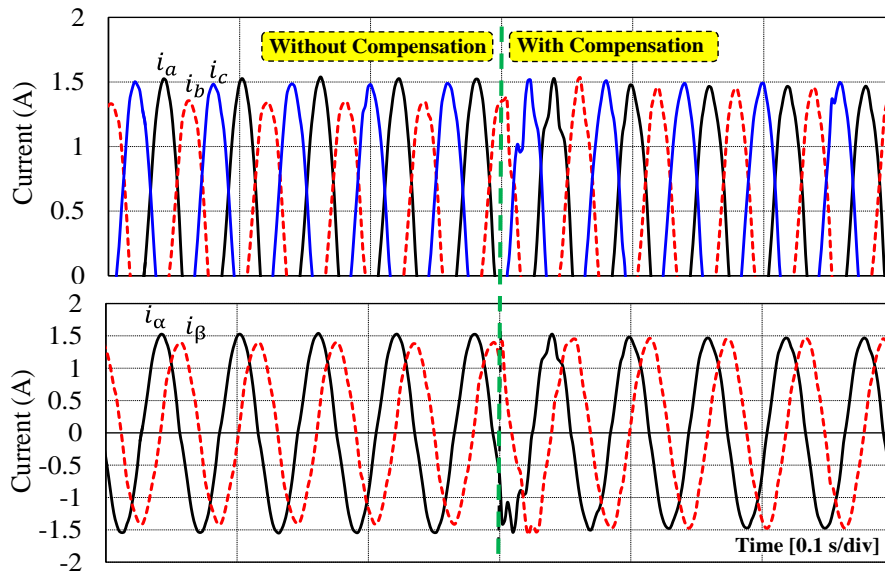


(c) Back-EMF under case B

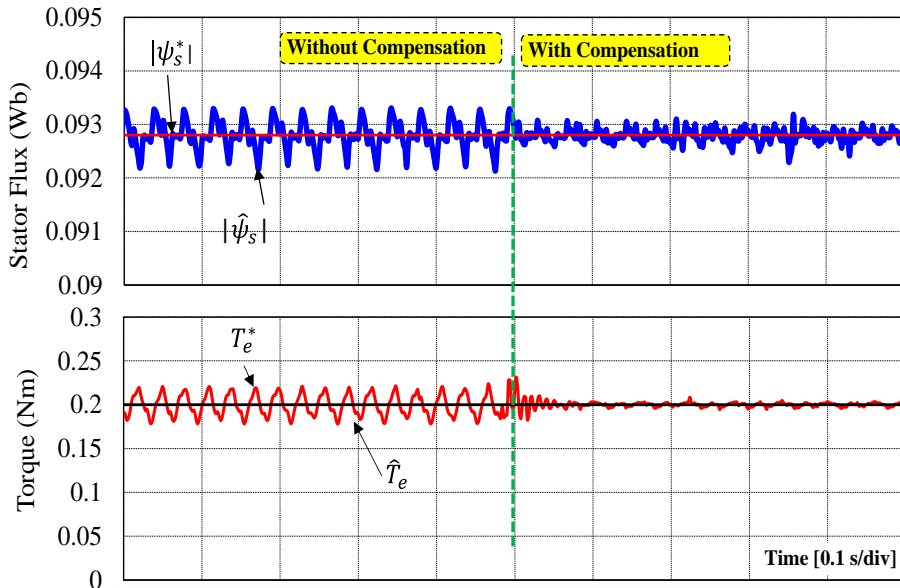
Fig. 5.12 Stator winding configuration with measured back-EMF at 1500 rpm.

Fig. 5.13(b) shows the estimated torque and flux without/with compensation obtained by using the current model (2), and their relevant spectrum analysis is shown in Fig. 5.13(c). It can be seen that the 2nd and 6th harmonics of torque and flux are significantly reduced with compensation. From the spectrum analysis, there exist other harmonics, i.e., 4th, 8th, and 12th, and their amplitudes are also reduced as a result of compensation of the 2nd and 6th harmonic components. The voltage waveforms in the stator flux v_{dqs} and stationary $v_{\alpha\beta}$ reference frames are shown in Fig. 5.13(d).

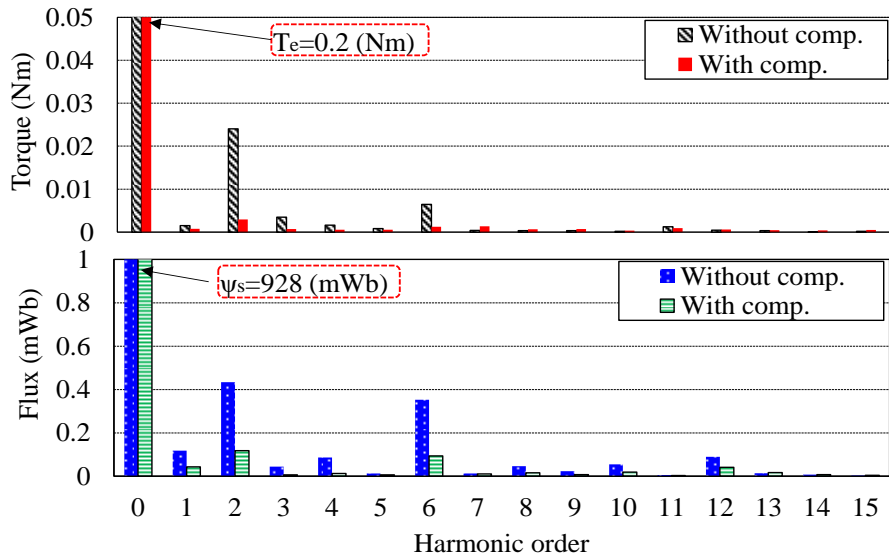
It is worth mentioning that with compensation there is a slight increase of the voltage ripples in the stator dqs and stationary $\alpha\beta$ reference frames since it is impossible to obtain balanced current and voltage simultaneously for the asymmetric structure.



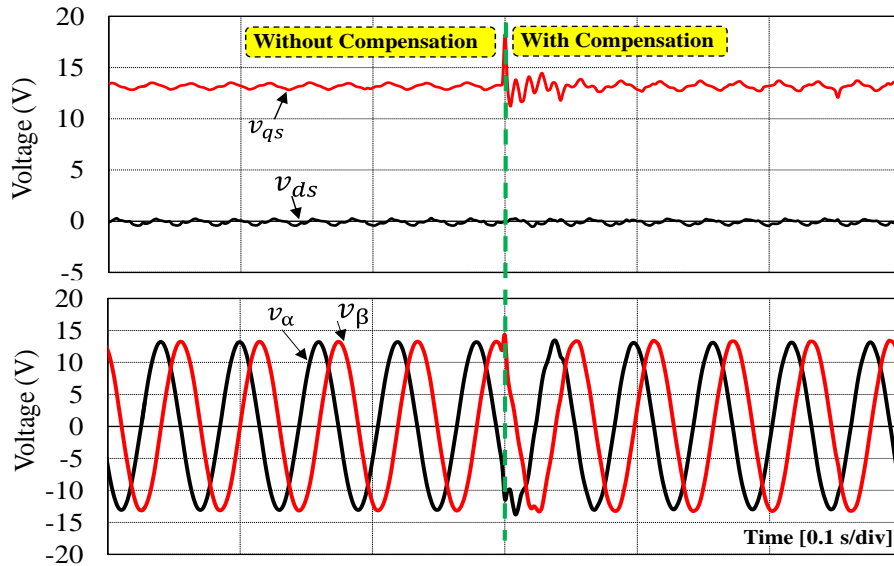
(a) Currents in abc and $\alpha\beta$ reference frames



(b) Instantaneous torque and stator flux



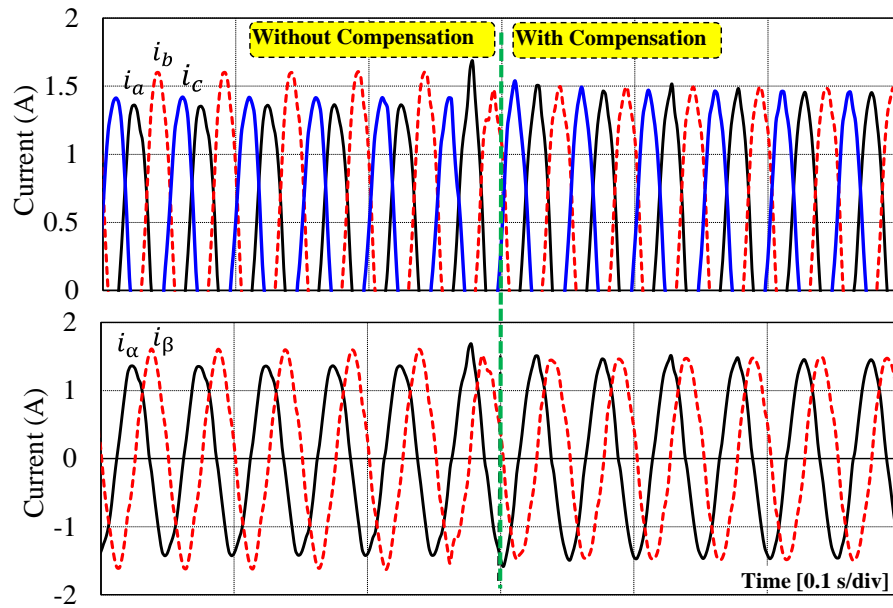
(c) Spectrum analysis of torque and stator flux



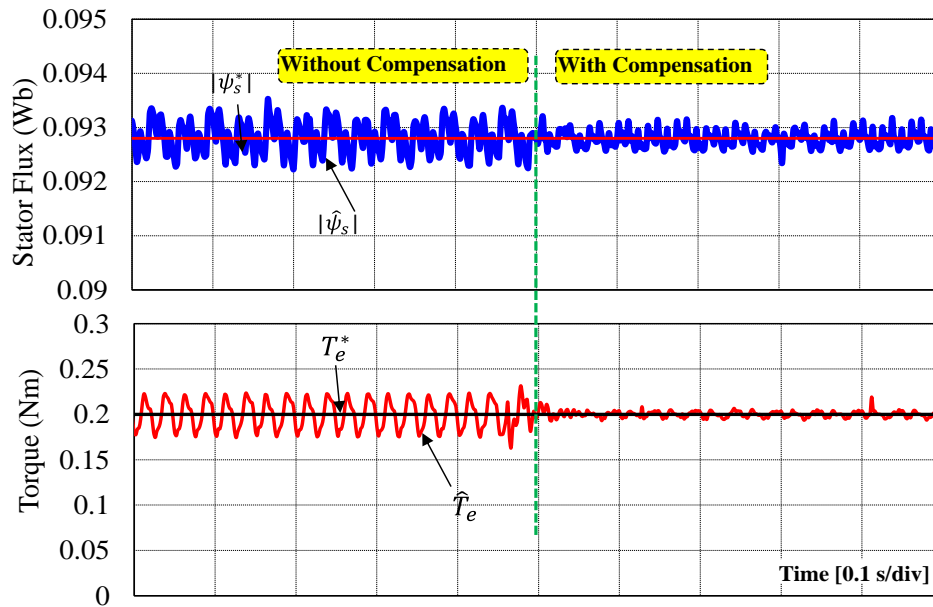
(d) Voltage in dq and $\alpha\beta$ reference frames

Fig. 5.13 Steady-state performance without/with compensation for case A.

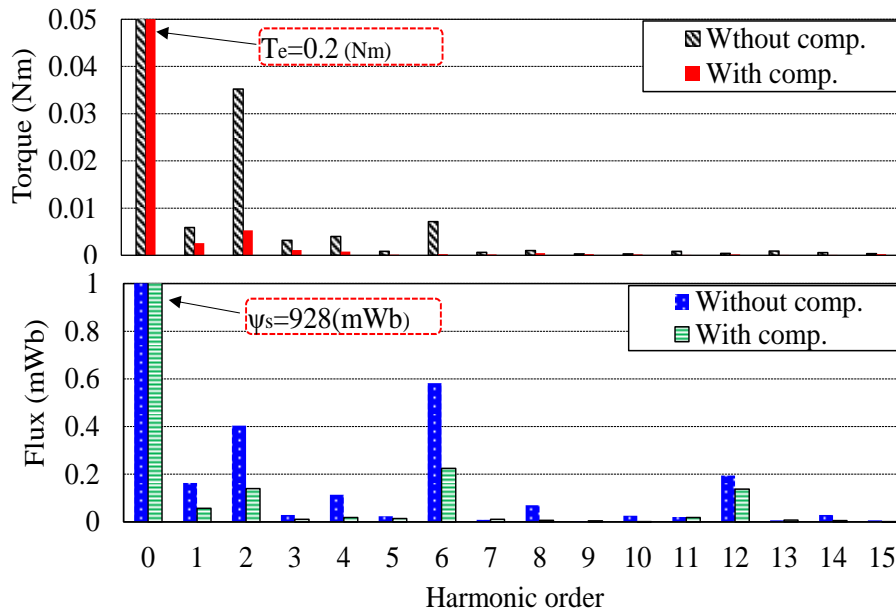
In the case B, the amplitude of phase b current i_b is higher than that of i_a and i_c due to the lower back-EMF in this phase as shown in Fig. 5.14. When the compensation is enabled, similar performance as that of case A can be achieved, which means that the proposed strategy is independent on the state of asymmetric phase, since it is irrespective on machine parameters.



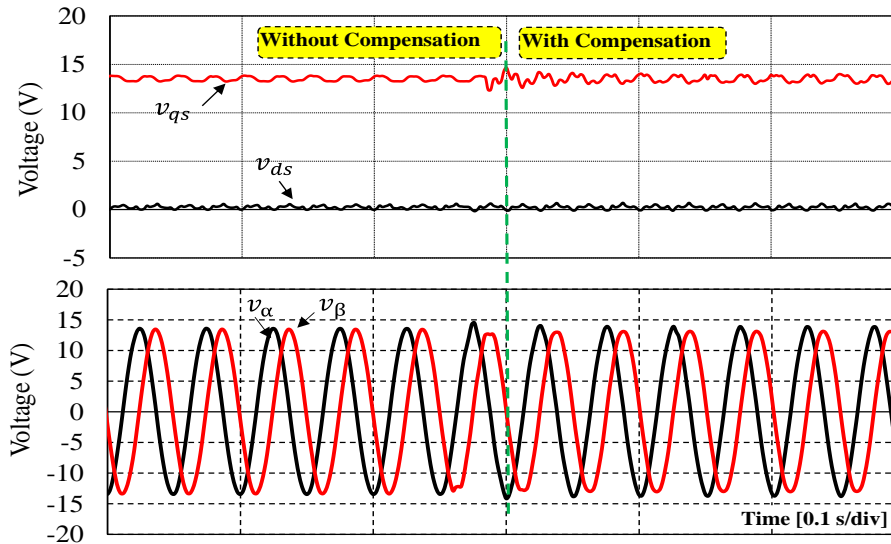
(a) Currents in abc and $\alpha\beta$ reference frames



(b) Instantaneous torque and stator flux



(c) Spectra analysis of torque and stator flux



(d) Voltage in dqs and $\alpha\beta$ reference frames

Fig. 5.14 Steady-state performance without/with compensation for case B.

Fig. 5.15 presents the compensation of the 6th, 2nd, and 6th+2nd harmonic components separately. It can be seen that the best result is obtained when both 6th and 2nd harmonics are compensated together. Furthermore, the corresponding three-phase currents and their spectrum analysis are shown in Fig. 5.16. It can be seen that the 3rd, 5th, and 7th are the dominant harmonic components, and they are significantly reduced due to the compensation of the 2nd and 6th harmonics in the torque and stator flux linkage.

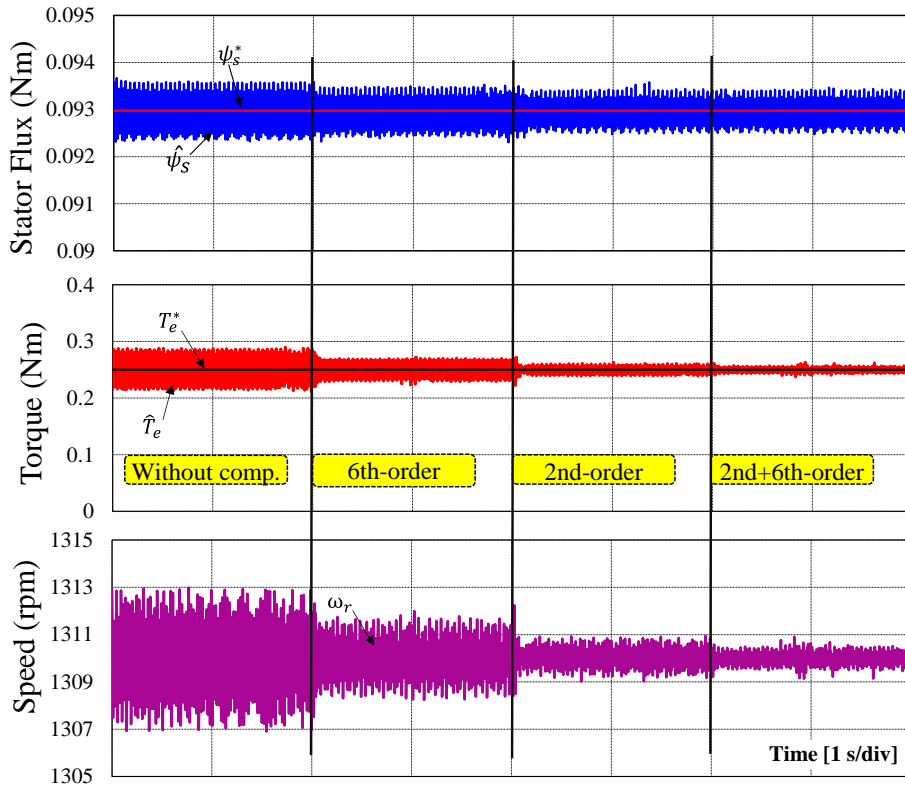
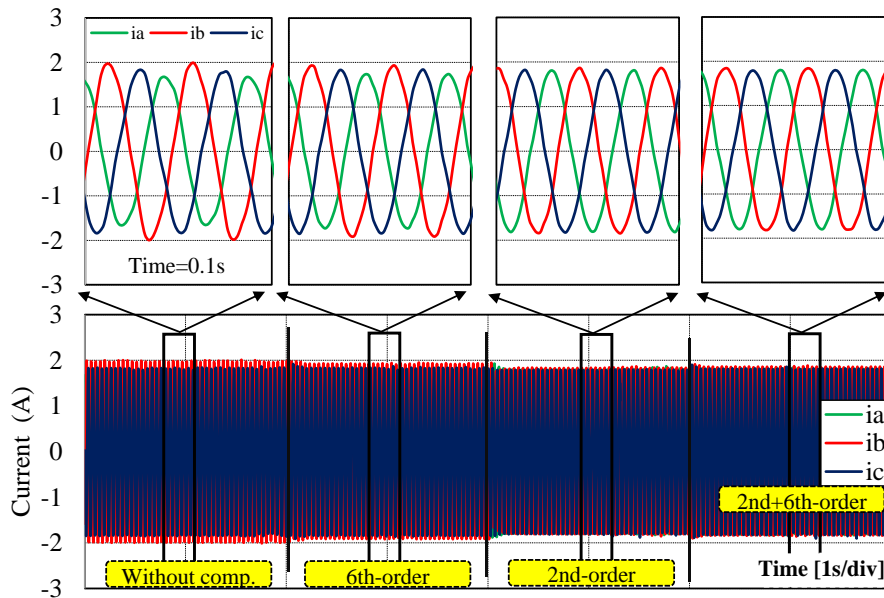
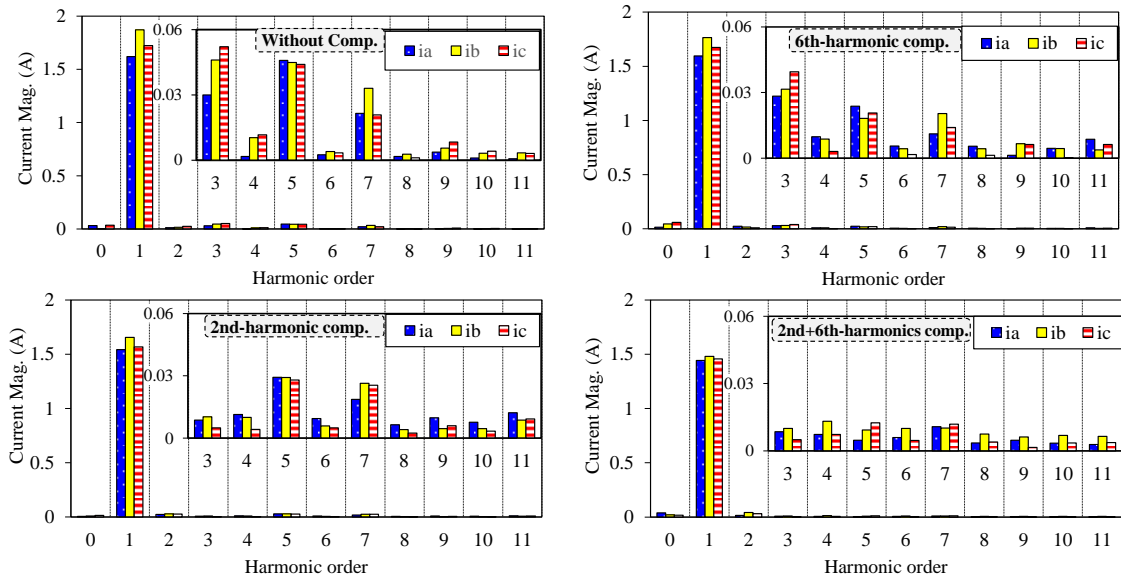


Fig. 5.15 Compensation of 6th and 2nd harmonic under steady-state conditions.



(a) Three-phase current

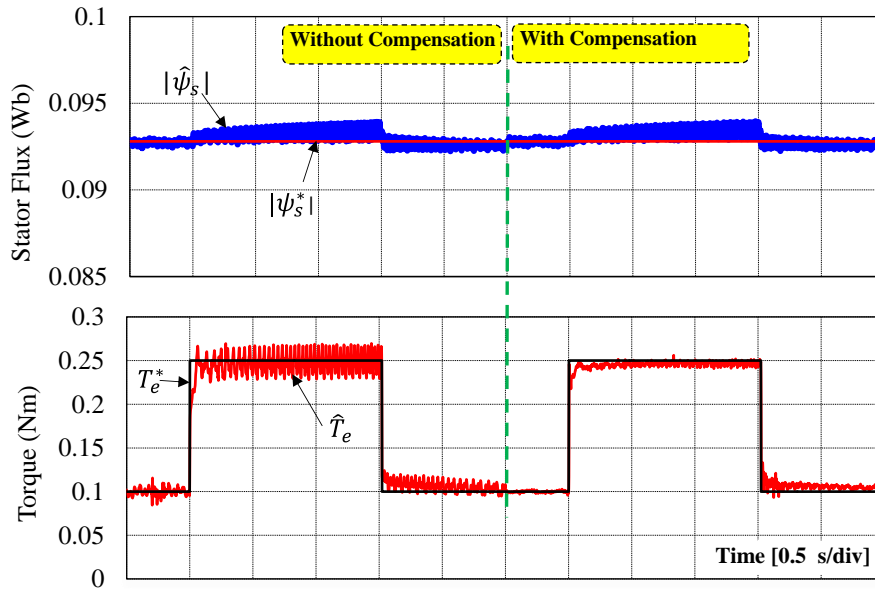


(b) Three-phase current spectra analysis

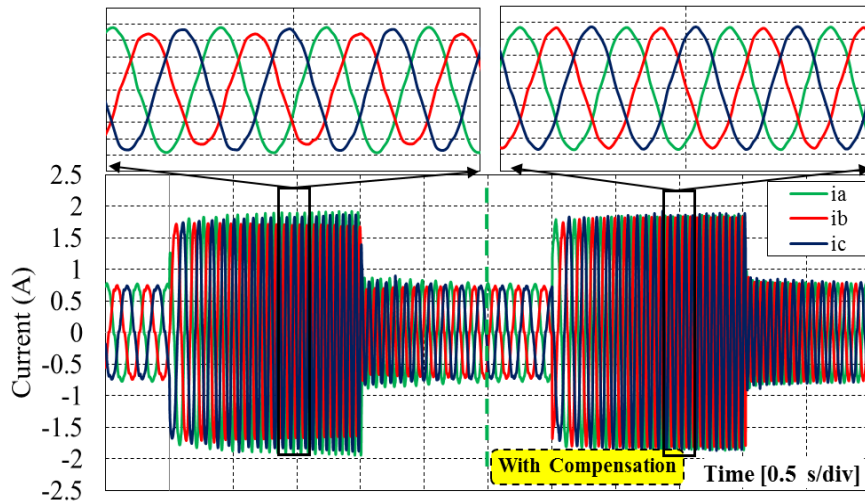
Fig. 5.16 Compensation of 6th and 2nd harmonic in the dqs reference frame.

5.5.2. Compensation under dynamic condition

The feasibility of the proposed control strategy is further experimentally verified under dynamic condition. The demanded torque is stepped as 0.1-0.25-0.1Nm while the system has the similar asymmetric condition as that discussed in the case A in section 5.5.1. Fig. 5.17(a) shows the estimated stator flux and torque without/with compensation while the three-phase currents are shown in Fig. 5.17(b). As can be seen from Fig. 5.17, besides the reduction in torque and flux ripples, the merit of fast dynamic torque response of the conventional DTC-SVM can be maintained in the proposed strategy. It is worth mentioning that the motor speed will change with respect to the changes in demand torque.



(a) Estimated stator flux and torque



(b) Three-phase currents

Fig. 5.17 Experimental results under dynamic condition without/with compensation.

Moreover, the responses of the speed control and the corresponding torque without/with compensation are shown in Fig. 5.18. It can be seen that the rising and falling times without/with compensation are approximately $t_r=0.22\text{s}$ and $t_f=0.1\text{s}$, respectively, which means the influence of the compensation on the torque and speed dynamic responses can be neglected. Moreover, the speed ripples without compensation are higher than that with compensation as shown in the magnified scale in Fig. 5.18.

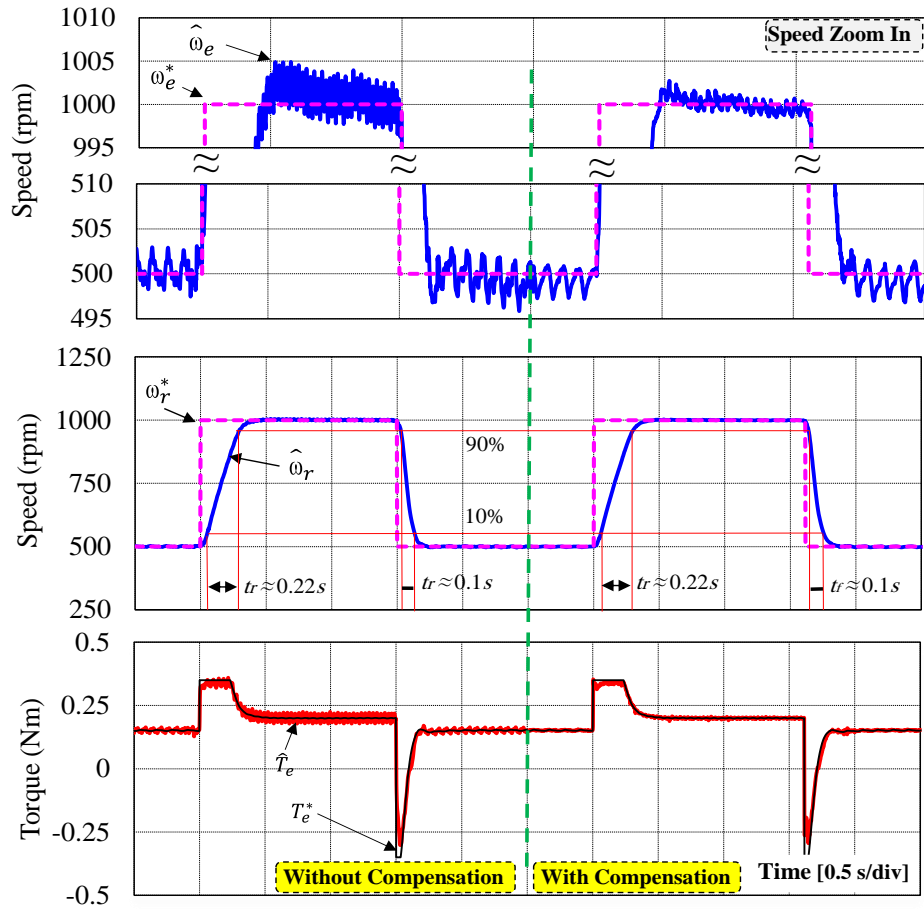
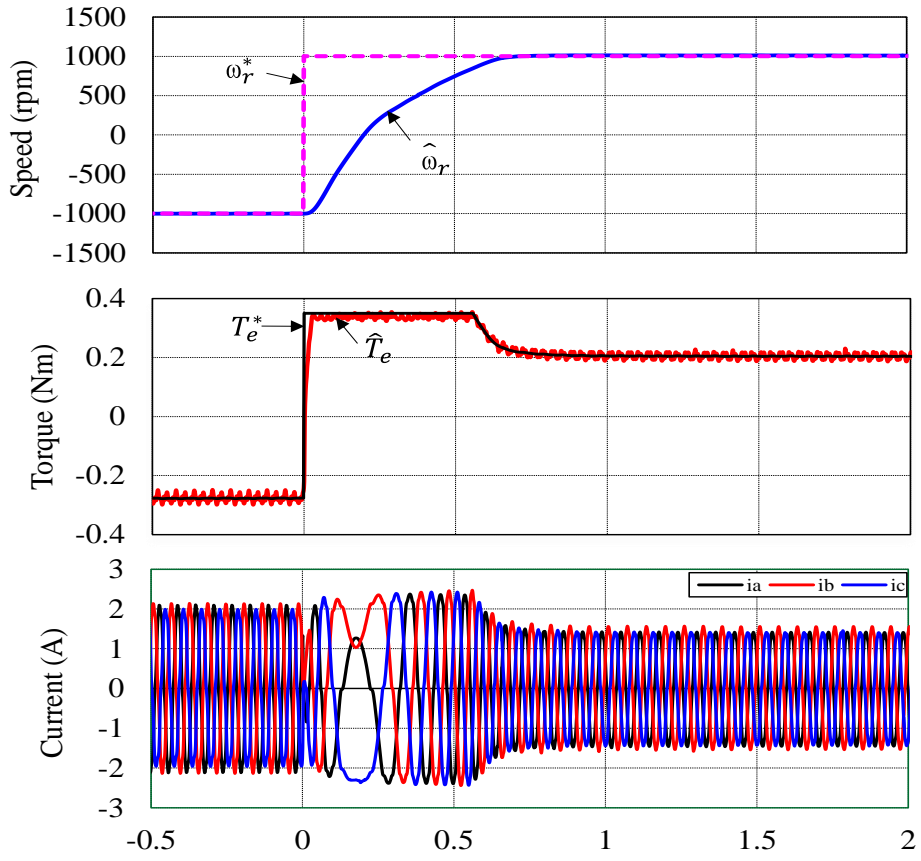
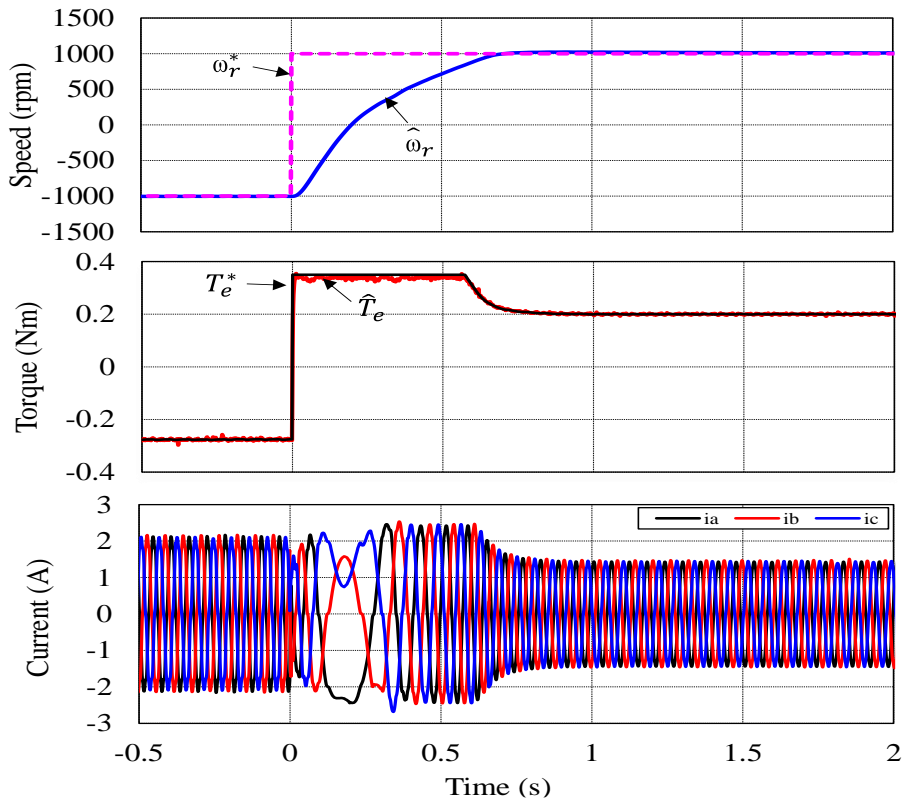


Fig. 5.18 Speed and corresponding torque responses without/with compensation.

On the other hand, the speed-reversing test is presented in Fig. 5.19. The speed reference has been changed from -1000 rpm to 1000 rpm. It can be seen from Fig. 5.19 that the proposed method can be applied in both rotational directions and the dynamic performance without/with compensation are similar. Furthermore, the steady-state performance of both current and torque are improved with compensation.



(a) Without compensation



(b) With compensation

Fig. 5.19 Speed-reversing test.

5.5.3. Machine start-up

Machine start-up without/with compensation under case A is depicted in Fig. 5.20, where the reference torque is stepped from 0 to 0.25 Nm. The steady-state performance of both current and torque with compensation are better than those without compensation. The torque step responses without/with compensation of the 2nd and 6th harmonic components are compared in Fig. 5.21. The rise time with compensation $t_r=1.8ms$ is shorter than that without compensation, i.e. $t_r=2.2ms$, due to the use of the resonant controllers [132], [189].

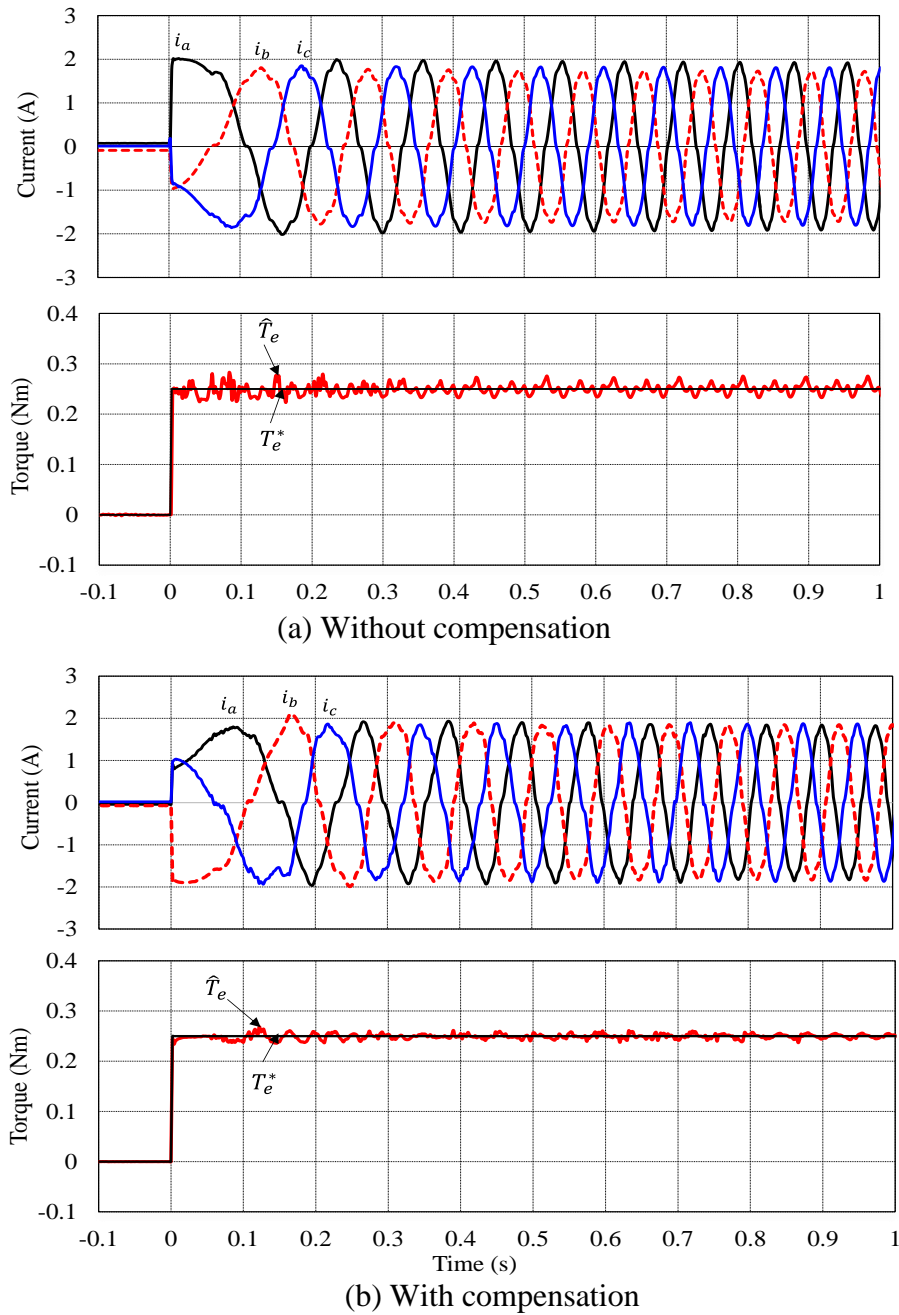


Fig. 5.20 Machine start-up.

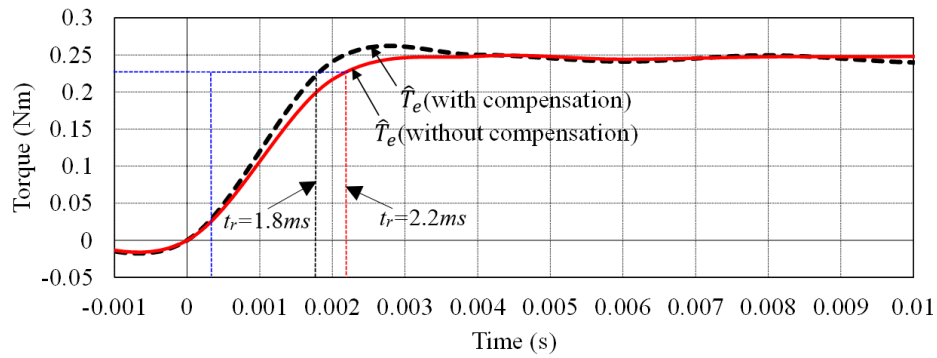


Fig. 5.21 Torque step responses without/with compensation.

5.6. Summary

In this paper, a modified parallel DTC-SVM strategy for asymmetric three-phase PMSM considering the influence of inverter nonlinearity has been presented. The standard PI-regulators in the torque and flux loops are enhanced by two resonant controllers tuning at $2\omega_s$ and $6\omega_s$ to reduce the 2nd and 6th torque and flux harmonics. In addition to the reduction of torque and flux harmonics, the currents harmonics can be suppressed as well. Moreover, the proposed method keeps the merits of fast dynamic torque response and machine parameter independence as in conventional DTC-SVM. The feasibility of the proposed method is verified by experimental results under dynamic and steady state conditions.

CHAPTER 6

REDUCTION OF TORQUE AND FLUX RIPPLES OF UNBALANCED PERMANENT MAGNET SYNCHRONOUS MACHINES BY DIRECT TORQUE CONTROL WITH ADAPTIVE FILTER

Abstract—This chapter presents a modified space vector modulation based direct torque control (DTC-SVM) for asymmetric three-phase PMSMs. Under asymmetric conditions, the current and voltage will suffer from harmonic distortion, which leads to the increase of torque and flux ripples. Therefore, to mitigate this problem, a control method of torque and flux linkage loops is developed by coupling the conventional PI-controller with two harmonic compensators based on the adaptive filter (AF) for suppression of the second and sixth harmonics. The developed method is mathematically analyzed and experientially verified under steady and dynamic states under different asymmetric scenarios. Compared with the conventional DTC-SVM scheme based on the PI controller, the proposed compensation scheme can significantly reduce both torque and flux ripples as well as the three-phase current harmonics under asymmetric and distorted conditions.

6.1. Introduction

Torque smoothness is often a major concern in high-performance motion control for medical, automation, robotic, and servo motor applications. Even in the domestic applications, torque smoothness is necessary to meet the user expectations since high torque ripple will contribute to the noise and vibrations [8], [54]. The major sources of torque pulsation in the PMSMs are extensively discussed in Chapter 5 [8]. Therefore, to mitigate the torque and flux ripples, two major groups of techniques are proposed, [39], [43], [53], [200]. In the first group, torque ripples are minimized by employing the machine design techniques such as magnet sizing and shaping, distributed windings, and stator and/or rotor skewing, etc., to reduce the cogging torque and torque ripples [53], [54]. Although the design techniques provide a valuable solution in terms of reducing torque ripples, they may not achieve similar performance under the load operation conditions. Moreover, they may impose additional manufacturing costs and

reduce the torque density. Whereas the second group involves the techniques that are based on control strategies [163], [164], [201], including space vector modulation based direct torque control (DTC-SVM) strategy [163], [164], [201], [202]. In the DTC-SVM strategy, the torque and stator flux are independently controlled via PI-controller as in cascaded DTC-SVM [39] (refer to Chapter 4), or parallel DTC-SVM (refer to Chapter 5) [43], [163], [180], [200].

The above DTC-SVM strategies can achieve decent performance when the machine is balanced. However, in the unbalanced case, their performance will be deteriorated, and the low order torque and flux harmonics, i.e. 1st, 2nd, 4th, 6th, and 12th as discussed in Chapter 5 [8], will be increased. These harmonics can be regarded as various AC components overlapped with their original DC values, which cannot be controlled by using the standard PI-controller due to its limited bandwidth [77], [95], [160]. Previously, many methods have been proposed to address this problem [77], [95], [174], [203], [204]. However, their application on DTC-SVM strategy can rarely be found. In [203] an iterative learning control (ILC) for compensating any periodic components in the torque has been added between two PI controllers. For current control strategies, the resonant controller is widely employed under unbalanced conditions. Furthermore, a reference or multi-reference generation of current, torque, or active and reactive power, is one of the proposed solutions [83], [198]. The adaptive filter (AF) provides an attractive technique in signal processing and control applications [205], [206], [207], [208], [209]. Hence, depending on the selecting output node, it can remove or pass a specified harmonic at a certain frequency (band-pass/band-stop filter). This feature is interesting when it is utilized together with a standard PI-controller, in order to increase the capability of the PI-controller to respond to the AC components.

In this chapter, a modified parallel DTC-SVM strategy for unbalanced three-phase PMSMs is presented. It is implemented by enhancing each of the standard PI-controller in the torque and flux loops with two AF tuned at twice and six times of the fundamental frequency. This combination is mathematically analyzed and then applied to suppress the second and sixth order torque and flux harmonics. The proposed scheme provides high gain and narrow bandwidth at the selected AC frequency, and therefore, compensation of undesired torque and flux harmonics can be achieved. The improved control strategy is further experimentally investigated under steady state and dynamic conditions when the motor suffers from unbalanced winding impedance and back-EMF. Compared with the conventional parallel DTC-SVM scheme based on standard

PI controller, the proposed compensation scheme leads to the significant reduction of both torque and flux ripples as well as the three-phase current harmonics under asymmetric and distorted conditions.

6.2. Conventional Parallel DTC-SVM Strategy

The mathematical model of the conventional parallel DTC-SVM strategy of PMSMs is derived in Chapter 5, section §5.2. It is based on the analysis of the torque and flux linkage in the stator flux dqs -reference frame. Hence, the torque and stator flux linkage are controlled via two PI-controllers independently and simultaneously (refer to Fig. 5.2). The outputs of the PI-controllers represented as a voltage command in the dqs -reference frame, which can be transformed into the $\alpha\beta$ -reference frame using stator flux positions θ_s to trigger the inverter via SVM.

The detailed block diagram of the torque and stator flux control loops are given in Fig. 6.1 [163], [18], [168] and further discussion is given in Chapter 5.

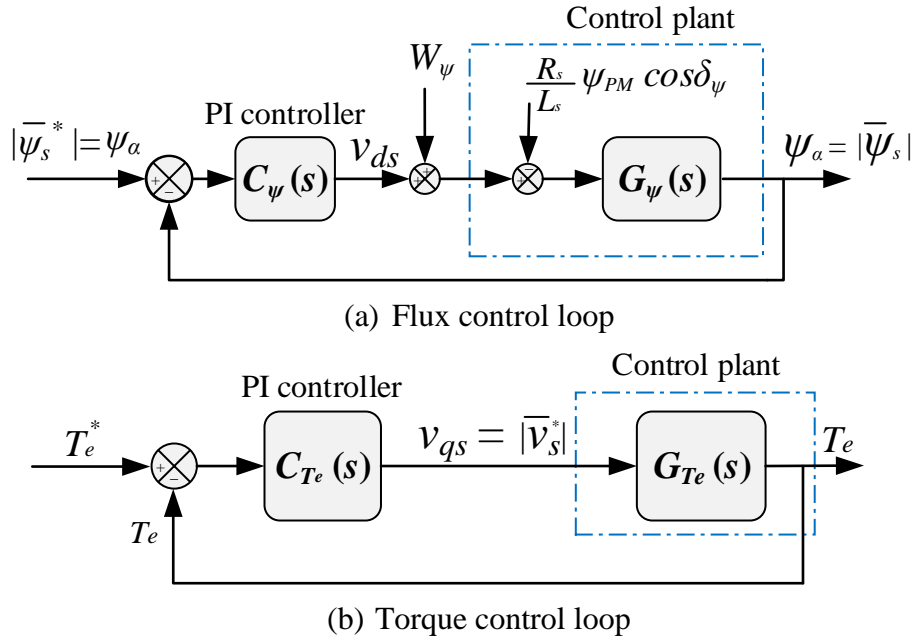


Fig. 6.1 Block diagram of the torque and flux control loops.

where

- $|\psi_\alpha|$ and $|\psi_s^*|$ are the actual and reference stator flux magnitudes.
- $C_\psi(s) = K_{p\psi} + K_{i\psi}/s$, $C_{Te}(s) = K_{pTe} + K_{iTe}/s$ represent the flux and torque standard PI-regulator transfer function (TF), and K_p and K_i are the proportional and integral gains, respectively.

- $W_\psi = \frac{R_s \psi_{PM}}{L_s} \cos(\delta_\psi) \approx \frac{R_s \psi_{PM}}{L_s}$ is an outer weight disturbance.
- $G_\psi(s) = 1/(s + A_\psi)$ is the TF between the stator flux and the ds -axis voltage, and $A_\psi = R_s/L_s$.
- $G_{T_e}(s) = \frac{T_e}{v_{qs}} = \frac{A_{T_e} s}{s^2 + B_{T_e} s + C_{T_e}}$ is the TF between the torque and the qs -axis voltage, and A_{T_e} , B_{T_e} , and C_{T_e} are the TF parameters, which can be obtained as given in section §4.2.2.2 of Chapter 4.

Consequently, the closed-loop TF of the stator flux linkage can be written as:

$$G_{\psi,CL}(s) = \frac{|\psi_s|}{|\psi_s^*|} = \frac{C_\psi(s)G_\psi(s)}{1 + C_\psi(s)G_\psi(s)} = \frac{K_{p\psi} \left(s + \frac{K_{i\psi}}{K_{p\psi}} \right)}{s^2 + (K_{p\psi} + A_\psi)s + K_{i\psi}} \quad (6.1)$$

and for the torque loop it is

$$G_{T_e,CL}(s) = \frac{T_e(s)}{T_e^*(s)} = \frac{C_{T_e}(s) \cdot G_{T_e}(s)}{1 + C_{T_e}(s) \cdot G_{T_e}(s)} = \frac{K_{p\psi} \psi_{PM} A_{T_e} K_{pT_e} \left(s + \frac{K_{pT_e}}{K_{pT_e}} \right)}{s^2 + (B_{T_e} + K_{pT_e} A_{T_e})s + (C_M + K_{iT_e} A_{T_e})} \quad (6.2)$$

6.3. Proposed Control Strategy

Under asymmetric and distorted conditions, considering the positive- negative-sequence and the 5th and 7th harmonic components, the electromagnetic torque equation can be expressed as (further explanation is given in Chapter 5)

$$\begin{aligned} T_e &= 1.5p_n \operatorname{Im} \{ \vec{\psi}_{dqs}^{1+} \cdot \vec{i}_{dqs}^{1+} \} \\ &= 1.5p_n [T_{e0} + T_{es2} \sin(2\omega_s t) + T_{ec2} \cos(2\omega_s t) + T_{es6} \sin(6\omega_s t) + T_{ec6} \cos(6\omega_s t)] \end{aligned} \quad (6.3)$$

It can be deduced that the negative sequence components exhibit oscillation at twice of the fundamental frequency in the electromagnetic torque, whereas the harmonics of $-5\omega_s$ and $7\omega_s$ behave as AC components at the angular speed of $\pm 6\omega_s$.

In general, the electromagnetic torque in (6.3) is composed of a constant term (T_{e0}), which is correlated with equal sequence products, and oscillating terms (T_{es2} , T_{ec2} , T_{es4} , T_{ec4} , T_{es6} , T_{ec6} , T_{es8} , T_{ec8} , T_{es12} , T_{ec12} ...) at $2\omega_s$, $4\omega_s$, $6\omega_s$, $8\omega_s$, $12\omega_s$ of the fundamental frequency produced by unequal sequence products [209]. It is worth mentioning that the 2nd and 6th are the dominant harmonics. Hence, the other harmonics ($4\omega_s$, $8\omega_s$, and $12\omega_s$) are not considered in this investigation.

6.3.1. Compensation of torque and flux ripples by means of adaptive filters

When the reference and estimated torque/flux signals are DC values, zero steady-state error can be expected by employing the standard PI-controller. However, when there are AC components overlapped with their original DC values, the straightforward use of standard PI-controller contributes in a steady-state error due to its finite bandwidth to AC components [77], [106]. Therefore, to suppress the undesired torque and flux ripples, a proportional resonant control (PIR) can be used as investigated in Chapter 5. Unlike the method presented in Chapter 5, in this chapter, a digital adaptive filter (AF) will be utilized with the standard PI-controller to suppress the undesired harmonics. Fig. 6.2(a) shows the AF based on the concept of adaptive noise cancelling with least mean square algorithm (LMS). The detailed block diagram of AF with two orthogonal references is illustrated in Fig. 6.2 (b). In this scheme, $U(s)$ represents the initial distorted input signal, $R(s)$ denotes the reference signal for the adaptive algorithm, which can be obtained by applying two sinusoidal signals shifted by 90° , i.e., *sin* and *cosine* functions at the interested frequency $h\omega_s$, where h is the specified harmonic to be filter out, i.e., $h=2$ for the second and $h=6$ for the sixth order harmonics. There is one feedback loop needed for each selected harmonic to diminish the component adopting the AF as shown in Fig. 6.2 (b). The feedback loops for all harmonics have the same structure and characteristic. Taking the *cosine* loop as an example for analysis, the coefficient $x_1(t)$ can be expressed as

$$x_1(t) = \int (\gamma \cdot u(t) \cdot \cos h\omega_s t) dt \quad (6.4)$$

where γ is the adaption gain. Taking the *Laplace* transform of (6.4) yields:

$$X_1(s) = L(x_1(t)) = L\left(\int \gamma \cdot u(t) \cdot \frac{e^{jh\omega_s t} + e^{-jh\omega_s t}}{2}\right) = \frac{\gamma}{2s} U(s + jh\omega_s) + U(s - jh\omega_s) \quad (6.5)$$

where L refers to the *Laplace* operator. Noting that $h_1(t) = x_1(t) \cos(h\omega_s t)$, taking the *Laplace* of $h_1(t)$ yields:

$$\begin{aligned} H_1(s) &= L(h_1(t)) \\ &= \frac{\gamma}{4(s + jh\omega_s)} (U(s) + U(s + 2jh\omega_s)) + \frac{\gamma}{4(s - jh\omega_s)} (U(s) + U(s - 2jh\omega_s)) \end{aligned} \quad (6.5)$$

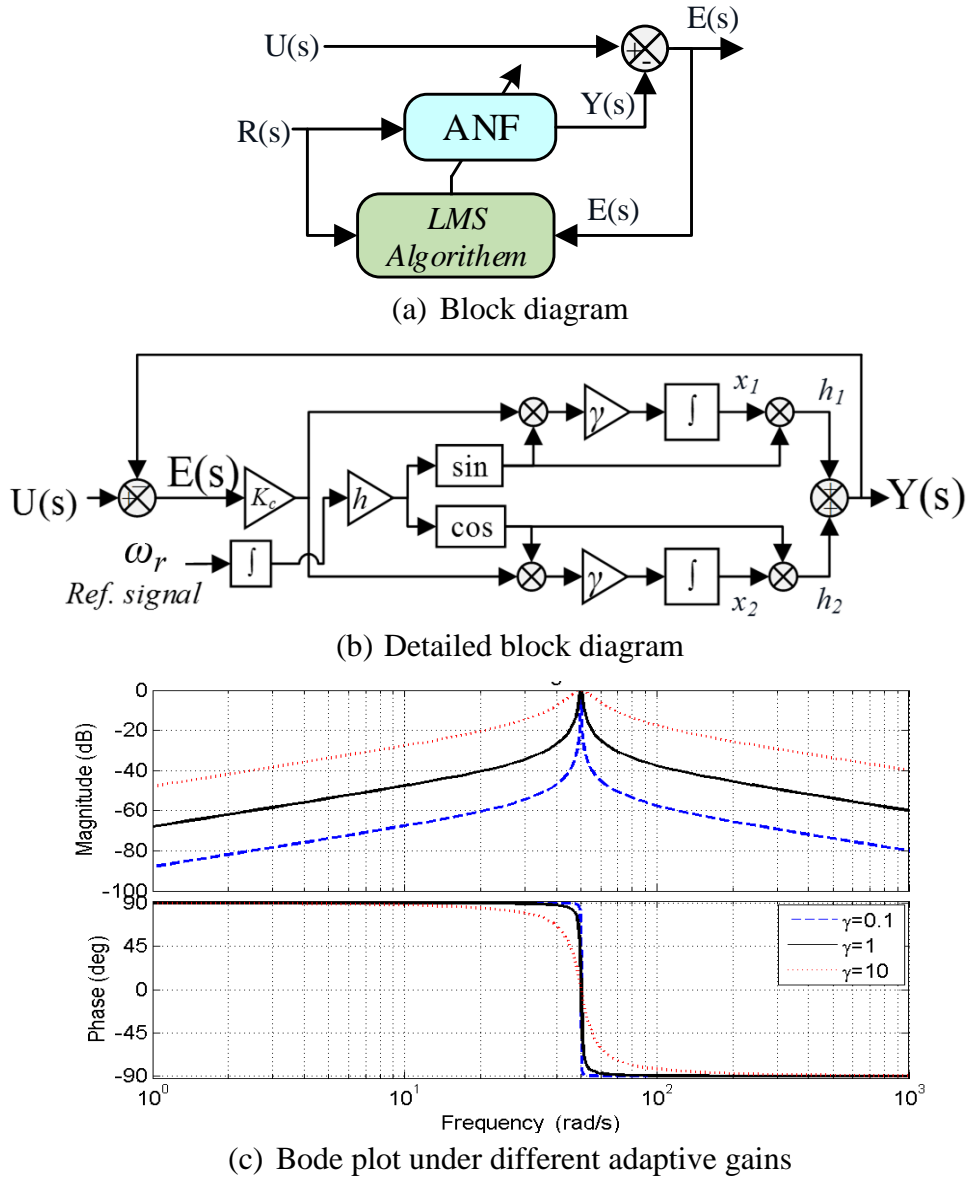


Fig. 6.2 Second order adaptive filter.

Likewise, the *Laplace* transform of $h_2(t)$ is

$$\begin{aligned}
 H_2(s) &= L(h_2(t)) \\
 &= \frac{\gamma}{4(s + jh\omega_s)} (U(s) - U(s + 2jh\omega_s)) + \frac{\gamma}{4(s - jh\omega_s)} (U(s) - U(s - 2jh\omega_s)) \quad (6.6)
 \end{aligned}$$

Hence, the response of AF can be defined by two transfer functions depending on node outputs, being adaptive band-pass filter (ABPF) and adaptive band-stop (or notch) filter (ANF), which can be expressed as follows:

$$AF(s) = \frac{Y(s)}{E(s)} = \frac{\gamma s}{s^2 + (h\omega_s)^2} \quad (6.7)$$

$$ABPF(s) = \frac{Y(s)}{U(s)} = \frac{AF}{1+AF} = \frac{\gamma s}{s^2 + \gamma s + (h\omega_s)^2} \quad (6.8)$$

$$ANF = \frac{E(s)}{U(s)} = 1 - ABPF = \frac{s^2 + (h\omega_s)^2}{s^2 + \gamma s + (h\omega_s)^2} \quad (6.9)$$

According to the analysis mentioned earlier, it can be seen that the block diagram shown in Fig. 6.2 (b) is equivalent to a conventional second-order adaptive filter. The gain γ is chosen such that the magnitude of the output can be controlled. In this investigation, the value of γ is set as the integral gain of the conventional PI-controller. In practice, the filter is designed to be underdamping to increase the convergence rate, i.e., $0 < \gamma < 2\omega_s$. The bandwidth of the adaptive filter can be adjusted by controlling the adaption gain γ . When γ is larger the bandwidth of the filter becomes larger and the setting time will be smaller, and therefore the system response is faster, but the steady-state error is increased. On the other hand, for a small γ , the bandwidth will be reduced and the filter performance approaches to its ideal state. However, the dynamic response is significantly slower. Therefore, the convergence rate has to compromise with the steady-state error and the fast dynamic response [206]. The frequency responses of the adaptive band pass filter (ABPF) at different adaptive gain γ values are depicted in Fig. 6.2 (c). It is worth mentioning that the characteristic of ABPF is the same as the nonlinear resonant controller [106], [174], although a different implementation is used.

6.3.2. Robustness and system response analysis

According to (6.1), the stator flux closed-loop TF can be modified after considering the AF transfer function with the standard PI-controller as follows:

$$G_{\psi,CL}(s) = \frac{|\psi_s|}{|\psi_s^*|} = \frac{C_{\psi,ABPF}(s)G_{\psi}(s)}{1 + C_{\psi,ABPF}(s)G_{\psi}(s)} = \frac{F_N(s)}{s \times (s^2 + (2\omega_s)^2) \times (s + A_{\psi}) + F_N(s)} \quad (6.10)$$

where $C_{\psi,ABPF}(s) = K_{p\psi} + \frac{K_{i\psi}}{s} + ABPF(2\omega_s)$, and $F_N(s) = K_{p\psi}s(s^2 + (h\omega_s)^2) + K_{i\psi}(s^2 + (h\omega_s)^2) + \gamma s^2$

Substituting $s=j2\omega_s$ into (6.11) yields:

$$\begin{aligned} \frac{|\psi_s|}{|\psi_s^*|} &= \frac{F_N(2\omega_s)}{2\omega_s \cdot ((j2\omega_s)^2 + (2\omega_s)^2) \cdot ((2\omega_s) + A_{\psi}) + F_N(2\omega_s)} \\ &= \frac{F_N(2\omega_s)}{2\omega_s \cdot (0) \cdot ((2\omega_s) + A_{\psi}) + F_N(2\omega_s)} = 1 \end{aligned} \quad (6.11)$$

In the same manner, equation (6.2) can be modified by adding the SBPF to the standard PI-controller TF as:

$$\frac{T_e(s)}{T_e^*(s)} = \frac{C_{Te,ABPF}(s)G_{Te}(s)}{1+C_{Te,ABPF}(s)G_{Te}(s)} = \frac{T_N(s)}{s \times (s^2 + (h\omega_s)^2) \times (s^2 + B_m s + C_m) + T_N(s)}. \quad (6.12)$$

where $C_{Te,ABPF}(s) = K_{pTe} + \frac{K_{iTe}}{s} + ABPF(2\omega_s)$, and

$$T_N(s) = A_m s (K_{pTe} s (s^2 + (h\omega_s)^2) + K_{iTe} (s^2 + (h\omega_s)^2) + \gamma s)$$

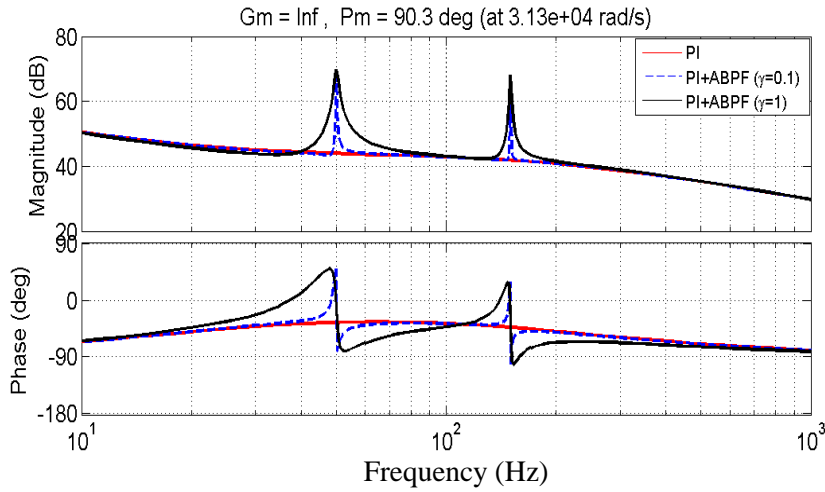
Substituting $s=j2\omega_s$ into (6.13) yields:

$$\frac{T_e(s)}{T_e^*(s)} = \frac{T_N(2\omega_s)}{2\omega_s \times 0 \times ((2\omega_s)^2 + B_m(2\omega_s) + C_m) + T_N(2\omega_s)} = 1 \quad (6.13)$$

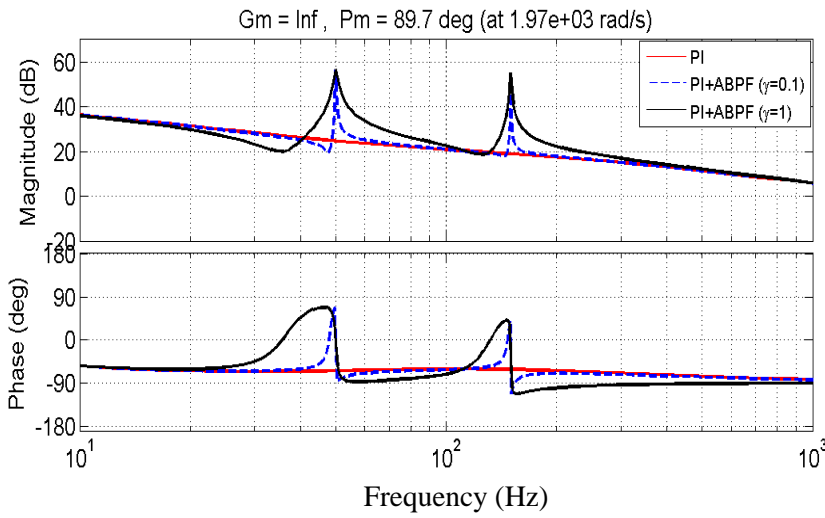
The above analysis implies that the modified PI+ABPF controller has zero steady-state error at the selected harmonic frequency, regardless the machine parameters, which is a good indication of the robustness and effectiveness of the proposed modification. In the same way, it can be solved for the frequency of $\pm 6\omega_s$.

Fig. 6.3 shows the flux and torque open-loop frequency responses of the conventional PI and the modified PI+ABPF controllers, the fundamental frequency being set to $\omega_s=25$ Hz. The motor parameters are given in Chapter 2 while the controller parameters are obtained using SISOTOOL of MATLAB. As can be seen in Fig. 6.3, the modified PI+ABPF controller provides high proportional gain with very narrow bandwidth at the selected harmonic frequency, i.e., the second and sixth harmonics in this test, which means high capability to suppress these harmonics, regardless the influence on system stability.

Another interesting feature is that the bandwidth of the filter can be widened by properly adjusting the value of γ as shown in Fig. 6.3, for $\gamma=0.1$ and $\gamma=1$. The gain margin will be infinite if the phase margin never crosses -180 degrees, which implies that the phase margin plot always remains above the -180 degree line. Hence, the gain margin will be infinite since there is no phase crossover frequency, and therefore, the corresponding gain margin cannot be determined graphically. Infinite gain margin means that the system is inherently stable [178].



(a) Flux-loop response at $K_p=100$, $K_i=\gamma=2000$

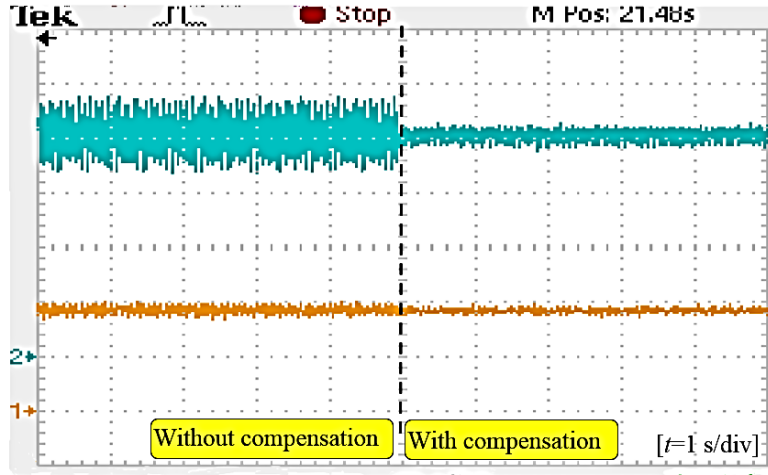


(b) Torque loop response at $K_p=35$, $K_i=\gamma=3200$

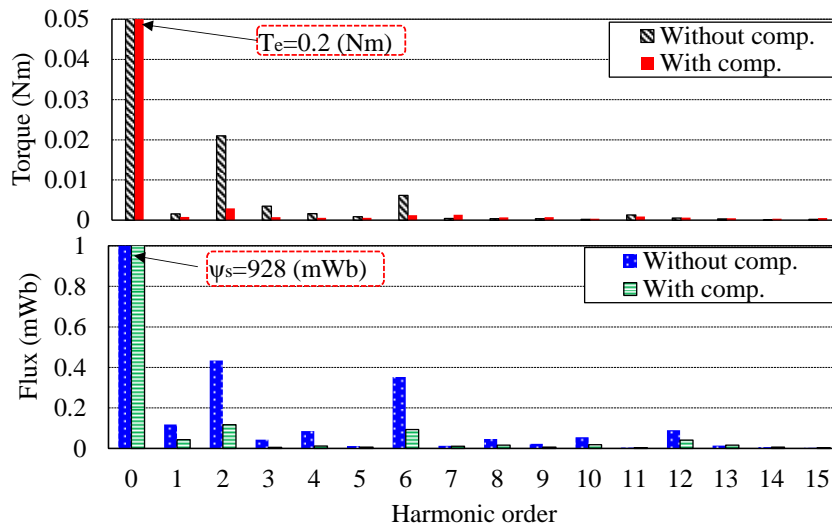
Fig. 6.3 System open-loop response with/without ABPF.

6.4. Experimental Verification

In this test, the sampling and switching frequencies are set to $f_s=f_{sw}=10$ kHz. The PM motor information is given in Chapter 2. Fig. 6.4 shows the block diagram of the proposed control strategy. Based on this, all experiments under steady state and dynamic operating conditions are carried out, and then compared with those obtained from the conventional control strategy.



(a) Torque and stator flux with and without compensation, channel 1: $|\hat{\psi}_s|$ (50 mWb/div), channel 2: T_e (0.05 Nm/div), horizontal: Time (1 s/div)



(b) Spectrum analysis of torque and stator flux

Fig. 6.5 Steady state performance.

On the other hand, when the compensation method is enabled, these two harmonics, i.e., the 2nd and the 6th, are significantly reduced by approximately 70% as depicted in Fig. 6.5 (a) (with compensation) and its spectrum in Fig. 6.5(b). The modified PI+ABPF controller parameters are listed in Table 6.1.

Consequently, the three-phase currents are also improved and become more balanced due to the compensation of torque ripples as shown in Fig. 6.6. However, there is a slightly increase of voltage unbalance in both dqs and $\alpha\beta$ reference frames as depicted in Fig. 6.7. Normally, this is true since it is impossible to achieve balanced voltage and current simultaneously for asymmetric machine [198].

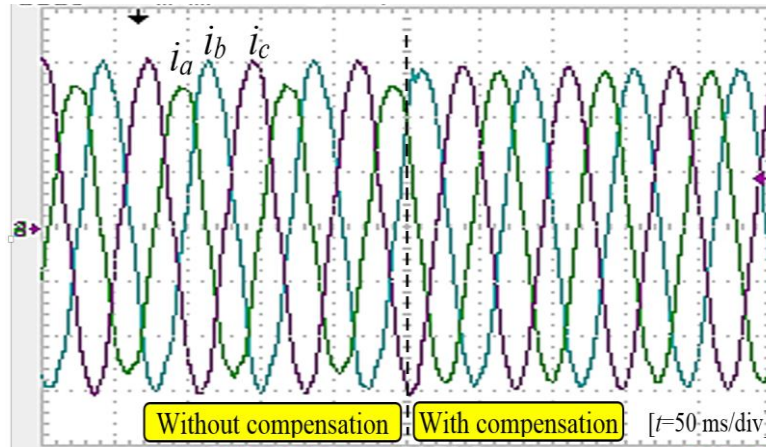
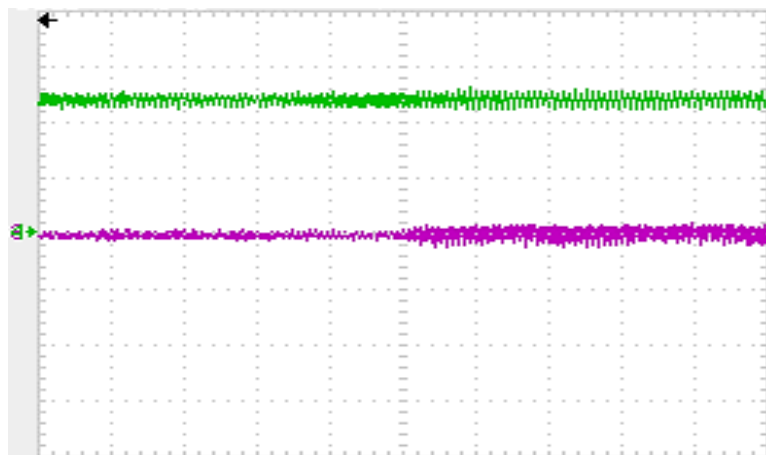
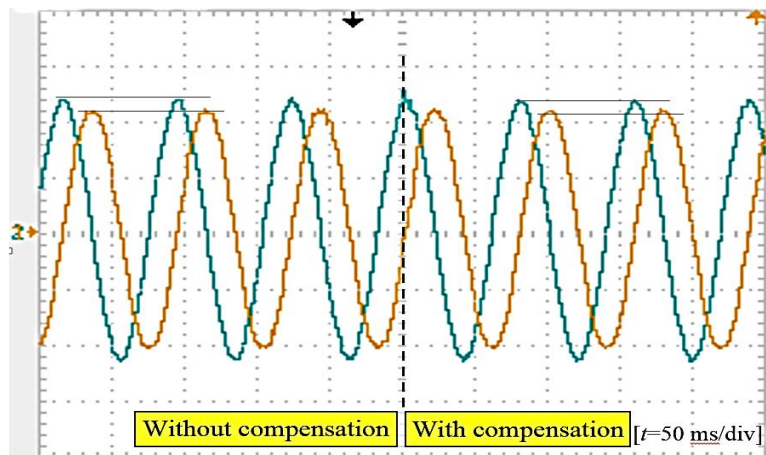


Fig. 6.6 Phase current without/with compensation, channels: i_{abc} (0.5 A/div), horizontal: time (50 ms/div).



(a) Voltage command, channels: v_{dq} (5 V/div), horizontal: time (50 ms/div)



(b) Stator voltage, channels: $v_{\alpha\beta}$ (5 V/div), horizontal: time (50 ms/div)

Fig. 6.7 Voltage command without/with compensation.

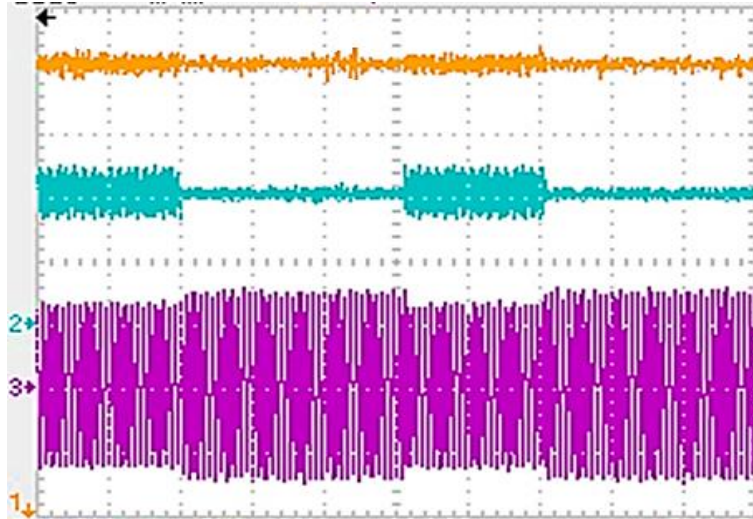


Fig. 6.8 Compensation under steady state conditions, channel 1: $|\hat{\psi}_s|$ (5 mWb/div), channel 2: T_e (0.1 Nm/div), channel 3: i_a (1 A/div), horizontal: time (1 s/div).

Fig. 6.8 shows of the estimated torque, flux, and the measured phase A currents with/without compensation under steady state conditions. The influence of variable asymmetric winding resistance on the second order torque harmonic is further investigated. It is accomplished by changing the additional resistance and then the corresponding torque ripple factor (TRF) is calculated with/without compensation according to

$$TRF = \frac{T_{r(pk-pk)}}{T_m} 100\% \quad (6.15)$$

where T_m is the demand torque, and $T_{r(pk-pk)}$ is the estimated peak-to-peak torque ripple. Fig. 6.9 shows the relationship between the increment of the stator resistance and the TRF.

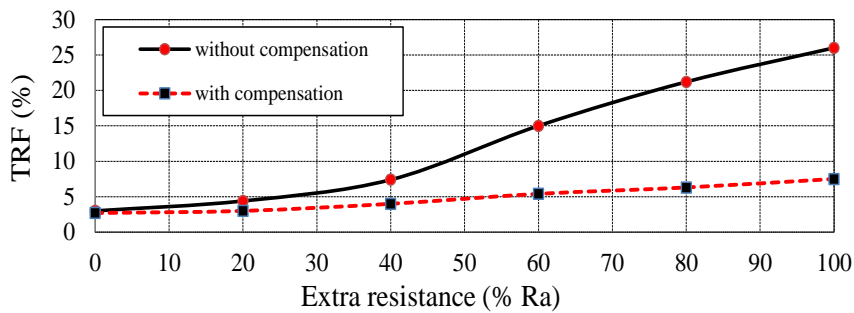
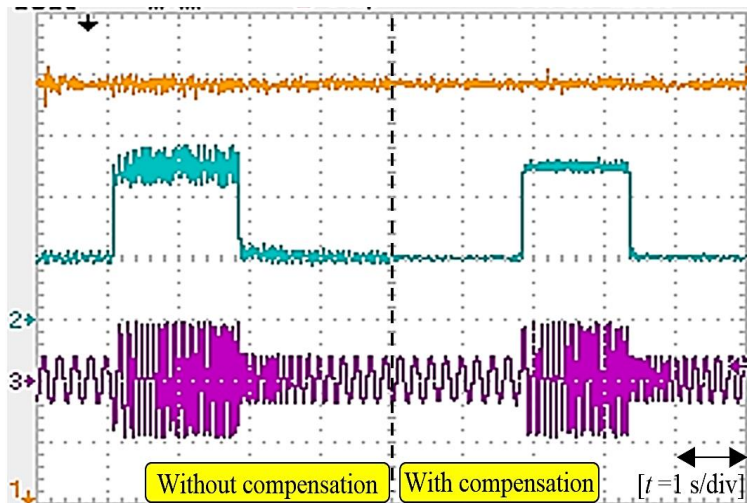


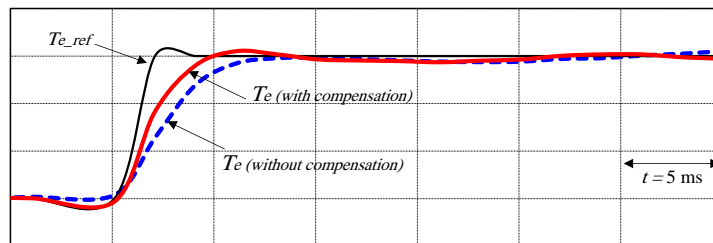
Fig. 6.9 Influence of added extra resistance on TRF.

6.4.2. Investigation under dynamic conditions

The feasibility of the proposed control strategy is further experimentally verified under dynamic conditions. The step reference of torque is 0.1-0.25-0.1 Nm while the asymmetric conditions are the same as that discussed in section 6.4.1. Fig. 6.10(a) shows the estimated stator flux linkage, torque, and the measured phase A currents with/without compensation. As can be seen from Fig. 6.10(a), the torque ripple is significantly reduced with compensation. Fig. 6.10 (b) shows the comparison between the torque step responses with/without compensation. It can be deduced that the transient response with compensation is slightly faster than that without compensation, i.e. $t_r \approx 4$ ms with compensation and $t_r \approx 5$ ms without compensation, because of the higher proportional gain at the selected AC frequency. Therefore, although the proposed compensation method is simple, it can merit the fast dynamic response of DTC strategy.



(a) Channel 1: $|\psi_s|$ (50 mWb/div), channel 2: T_e (0.1 Nm/div), channel 3: i_a (2 A/div), horizontal: time (1 s/div)

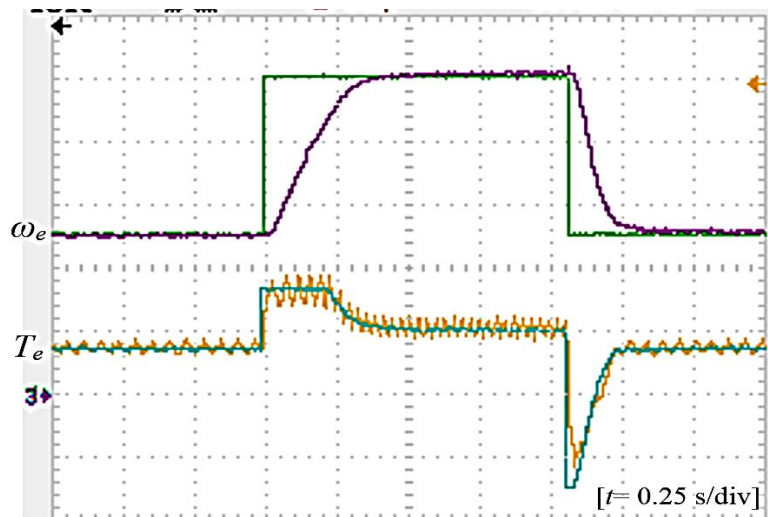


(b) Torque step responses, channels: T_e (0.05 Nm/div), horizontal: time (5 ms/div)

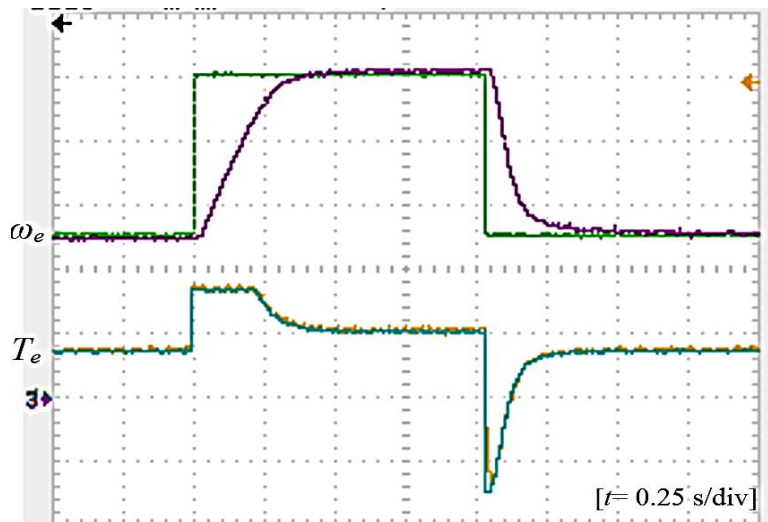
Fig. 6.10 Dynamic responses with/without compensation.

Consequently, the speed control and the corresponding torque response with/without compensation are shown in Fig. 6.11. The motor is asymmetric and the

step speed reference is $\omega_r=500-1000-500$ rpm, the torque ripple is remarkable when the conventional DTC-SVM employed, Fig. 6.11(a), while it is reduced as the compensation enabled as shown in Fig. 6.11(b). It should be emphasized that the torque increases as the speed becomes higher since the load torque is manually adjusted by using either the field excitation voltage or the load power resistor connected to the load machine. Therefore, under dynamic conditions, it is difficult to obtain the same load torque by manual adjustment.



(a) Without compensation



(b) With compensation

Fig. 6.11 Speed control, channels 1&2: reference and estimated torques, T_e (0.2 Nm/div), channels 3&4: reference and estimated speeds, ω_r (1000 rpm/div), horizontal: time (5 s/div).

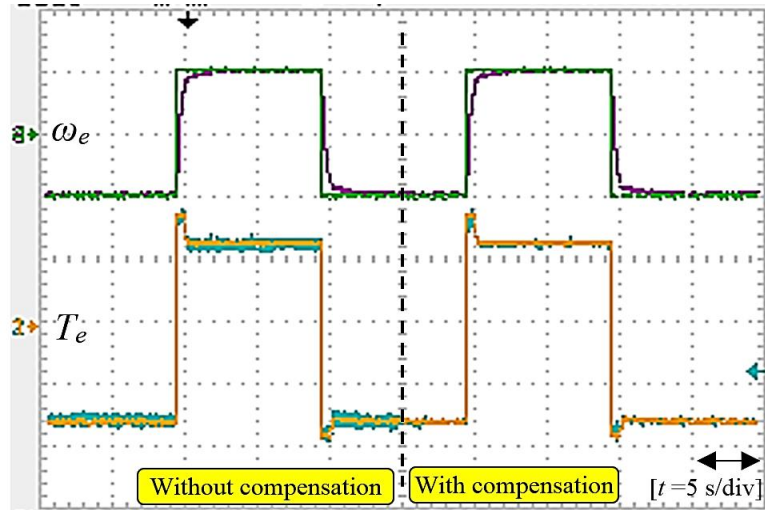
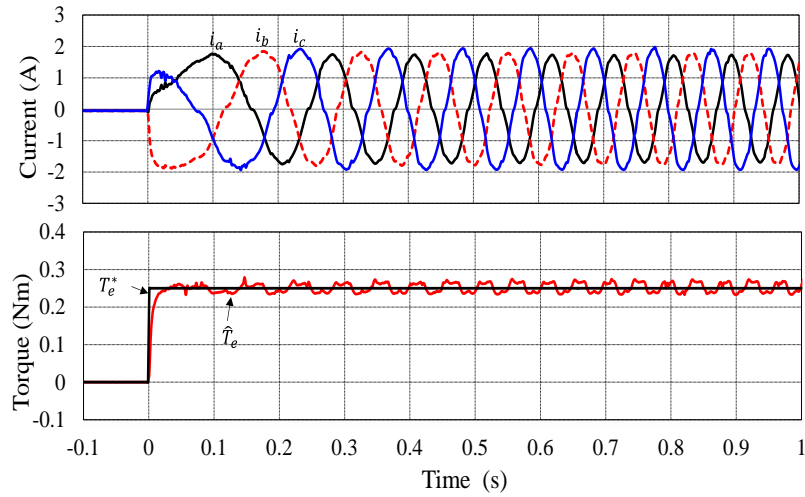


Fig. 6.12 Speed control with/without compensation, channels 1&2: reference and estimated torques, T_e (0.2 Nm/div), channel 3&4: reference and estimated speeds, ω_r (1000 rpm/div), horizontal: time (5 s/div).

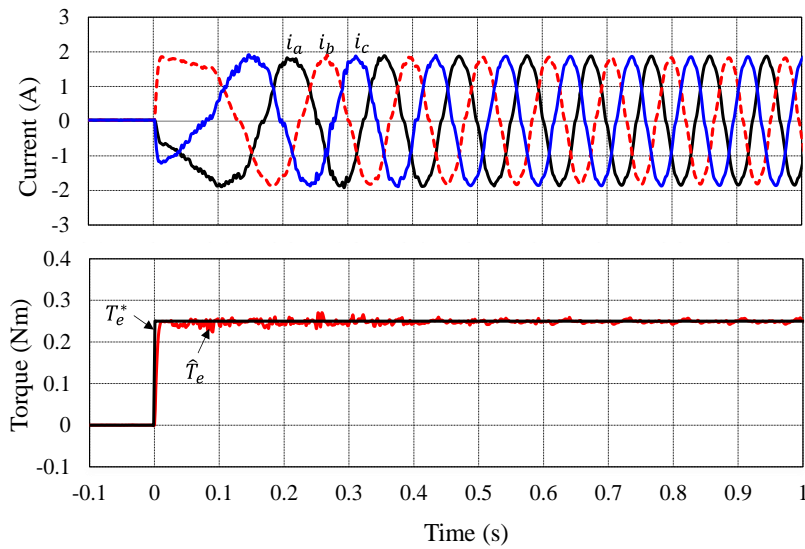
Fig. 6.12 shows the change in speed directions from -1000 rpm to 1000 rpm. The speed PI-controller parameters are given in Table 6.1. It can be deduced that the compensation method is independent of the speed direction. It can effectively operate in both forward and backward directions.

6.4.3. System start-up

In this test, a realistic phenomenon of unbalanced back-EMF is investigated. To implement unbalanced back-EMF, the number of turns in phase b has been increased to $N_{sb}=110\%N_s$, where N_s represents the number of turns at healthy condition (refer to Chapter 5). The measured impedance of the additional winding N_{sb} is $Z_{exb}=R_{exb}+L_{exb}=0.078\ \Omega+0.102\ \text{mH}$. Moreover, a resistor of $R_{exa}=100\%R_s$ has been deliberately connected in series with phase A. Therefore, three-phase asymmetric case can be achieved. The controller parameters are kept constant as in the previous tests, Table 6.1. Fig. 6.13(a) shows the phase current and electromagnetic torque when the motor start-up from standstill without compensation (conventional-DTC). Fig. 6.13(b) shows the performance when the compensation method is employed. Therefore, it can be deduced that in spite of different reasons which may cause unbalanced and harmonic distortion, the compensation method results in a satisfactory performance in terms of reducing the second order harmonics in the torque and flux linkage.



(a) Without compensation



(b) With compensation

Fig. 6.13 Motor start up from a standstill.

6.5. Summary

This chapter presents a modified parallel DTC-SVM strategy for asymmetric three-phase PMSM to mitigate the torque and flux ripples. The torque and stator flux linkage are harmonically distorted, which impose AC components onto their original DC components. Since the standard PI-controlled cannot respond to the AC components due to its finite bandwidth, the proposed control method suppresses the second and sixth order harmonics by enhancing the standard PI-controller via two harmonic compensators based on the adaptive filter. The modified control scheme provides relatively high gain at the selected AC frequency, which is regarded as a competitive method for elimination of the torque and flux ripples under unbalanced and

distorted conditions. The feasibility of the proposed method is experimentally verified under dynamic and steady state conditions based on deferent asymmetric conditions. The results show advanced performance in terms of low torque and flux ripples while keeping the merit of the fast dynamic response of conventional DTC strategy.

CHAPTER 7

CONCLUSIONS AND FUTURE RESEARCH

7.1. Introduction

This thesis addresses the drawbacks associated with asymmetric three-phase PMSMs by indirect and direct torque control strategies. It presents some valuable solutions by using modified control strategies to minimize these disadvantages, including current, torque and flux ripples. The main contributions and conclusions of this thesis are summarised as follows:

7.2. Current Control of Unbalanced Three-phase PMSMs Based on Double Synchronous Reference Frame Controller

The analytical models of the symmetrical and asymmetric PMSMs are derived, and then the conventional double synchronous reference frame control strategy is modified by extracting the positive- and the negative-sequence components in the abc reference frame. Then, employing the Clark-Park transformations into the extracted components to obtain pure DC components in the positive and negative SRFs. Hence, the need of using the adaptive filter, decoupling network, and reference current generation can be eliminated. Consequently, the dynamic performance can be improved, and the current and torque ripples can be reduced. Moreover, an algorithm based on the integer sampling delay is developed to generate a quarter signal delay, which is required for sequential components extraction. The main benefits of the proposed DSRFs method and its comparison with the conventional DSRFs strategy are summarised in Table 7.1.

TABLE 7.1 COMPARISON BETWEEN CONVENTIONAL AND PROPOSED DSRFS

	Conventional DSRF	Proposed DSRF
Steady-state	Poor	Good
Dynamic-state	Medium	Fast
Torque and flux control	Indirectly	Indirectly
Implementation	Complex	Simple
Decoupling network or ANF	Required	Not required
Limitations	Only the negative sequence components can be compensated	Only the negative sequence components can be compensated

7.3. Cascaded Direct Torque Control of Unbalanced PMSMs with Low Torque and Flux Ripples

Since there is a lack of the investigations that explore space vector modulation based direct torque control, this thesis fills this gap by proposing a modified cascaded DTC-SVM method for asymmetric three-phase PMSM. The implementation of the proposed method is based on generating the reference voltage in the negative SRF from the negative sequence variables, which, together with the reference voltage vector in the PSR, produce the final voltage vector that is delivered to the SVM. Moreover, the standard PI regulator has been enhanced by using the resonant controller tuned at twice of the fundamental frequency, and therefore significantly reduces the 2nd order torque harmonic and minimizes the steady-state error. Table 7.2 shows the main differences between the conventional and proposed cascaded DTC-SVM strategies.

TABLE 7.2 COMPARISON BETWEEN CONVENTIONAL CASCADED DTC
AND PROPOSED CASCADED DTC-SVM

	Conventional cascaded DTC-SVM	Proposed cascaded DTC-SVM
Steady-state performance	Poor (TRF @ adding 100% $R_a \approx 27\%$)	Good (TRF @ adding 100% $R_a \approx 12\%$)
Steady-state error	High	Low
Dynamic-state	Fast ($\approx 3.7ms$)	Faster ($\approx 2.8ms$)
Compensation	No	Yes (2 nd order)
Implementation	Simple	Simple
Limitations	Suitable for symmetrical machines	Suitable for asymmetric machines with 2 nd order torque and flux harmonics

7.4. Reduction of Torque and Flux Ripples in Direct Torque Control of Unbalanced PMSMs by Means of Resonant Controllers

A modified parallel DTC-SVM which is able to reduce the 2nd and 6th harmonics in the torque and flux due to asymmetric and inverter nonlinearities is presented. Since the conventional PI controller cannot achieve zero steady-state error for alternate current signals, the standard PI-regulators are enhanced by two resonant controllers, which are tuned at $2\omega_s$ and $6\omega_s$, respectively. It is proved that without sequential component decomposition, an advanced performance in terms of low torque and flux ripples while keeping the merit of simple structure and fast dynamic response of the conventional DTC strategy can be achieved. Furthermore, the proposed strategy is parameter independent, since it does not require information about faulty phases. Table 7.3 shows the comparison between the conventional and proposed parallel DTC-SVM strategies.

TABLE 7.3 COMPARISON BETWEEN CONVENTIONAL PARALLEL DTC-SVM AND PROPOSED PARALLEL DTC-SVM STRATEGIES

	Conventional parallel DTC	Proposed parallel DTC
Implementation	Simple	Simple
Torque and flux control	Directly in a closed loop fashion	Directly in a closed loop fashion
Steady-state	Poor	Good
Steady state error	High	Low
Dynamic-state performance	Fast ($\approx 2.2ms$)	Faster ($\approx 1.8 ms$)
Compensation	No	Yes (2 nd and 6 th order)
Robustness	High	High
Limitation	Suitable for symmetrical machines	Suitable for asymmetric machines with multi harmonics compensation

7.5. Reduction of Torque and Flux Ripples in Direct Torque Control of Unbalanced PMSMs by Means of Adaptive Filter

It is proved that the adaptive filter (AF) based on the noise cancelation algorithm has the same characteristic as that of the resonant controller but with a different way of implementation. The AF can select and reject any harmonics depending on its design frequency, and thus, can be used to compensate the dominant 2nd and 6th harmonics in the parallel structure DTC-SVM strategy. Moreover, Table 7.4 illustrates the main differences between the proportional resonant controller and adaptive filter to compensate the undesired harmonics.

TABLE 7.4 COMPARISON BETWEEN PR AND AF

	PIR	AF
Implementation	Two integration in forward and backward directions	Reference signals are generated using <i>sin</i> and <i>cosine</i> functions
Transfer function	Second order	Second order
Requirements	Integral gain and setting of a cut-off frequency	Gain and setting of a proper damping factor
Applications	Alternative current control, harmonic compensation	Noise cancelation, band pass or band reject of a specific harmonics

7.6. Future Research

In this thesis, all the investigations are applied on a three-phase surface-mounted PMSM. Therefore, the following suggestions and ideas can be considered as future work for further investigation, for example:

- Application of the proposed strategies to a different type of machines, such as interior PMSM, multi-phase PMSM, and switched reluctance machine.
- This study is mainly focused on compensation the 2nd and 6th harmonic components due to unbalanced back-EMF and inverter nonlinearity. Therefore, further investigations can be carried on the study of the influence of other sources of imbalance, such as fluctuation of DC-link voltage due to the limited value of the DC-link capacitor, unbalanced load, and machine rotor eccentricity.
- Sensorless control for an asymmetric machine.

7.7. Publications

During the research of this thesis, several papers have been published as detailed as follows:

- Atheer H. Abosh and Z. Q. Zhu, “Current control of the permanent magnet synchronous machine with asymmetric phases,” in *7th IET International Conference on Power Electronics Machines and Drives (PEMD)*, April 2014, Manchester, pp.1-6.

- Atheer H. Abosh, Z. Q. Zhu, and Y. Ren, “Reduction of torque and flux ripples in space-vector modulation based direct torque control of asymmetric permanent magnet synchronous machine,” *IEEE Trans. on Power Electron.* (*accepted*).
- Atheer H. Abosh and Z. Q. Zhu, “Cascaded direct torque control of unbalanced PMSM with low torque and flux ripples,” *drafted and to be submitted*.
- Atheer H. Abosh and Z. Q. Zhu, “Adaptive filter for torque and flux ripples reduction of asymmetric permanent magnet synchronous machine based direct torque control,” *drafted and to be submitted*.

REFERENCES

- [1] K. Krishnan, "Permanent magnet synchronous and brushless DC motor drives," CRC Press 2009, pp. 3–133.
- [2] R. Krishnan, "Permanent magnet synchronous and brushless DC motor drives," in Electrical and Computer Engineering Department, Virginia Tech., Blacksburg, U.S.A., 2010.
- [3] A. Cimpoeu, "Encoderless vector control of PMSG for wind turbine applications," MSc. thesis, Aalborg University, 2010.
- [4] P. Vas, "Electrical machines and drives," Oxford University Press, 1992.
- [5] J. R. Hendershot and T. J. E. Miller, "Design of brushless permanent magnet motor," Magnatic Physics, Oxford Science Publications, 1994.
- [6] P. Pillay and R. Krishnan, "Modeling of permanent magnet motor drives," *IEEE Trans. on Ind. Electron.*, vol. 35, pp. 537-541, 1988.
- [7] P. L. Chapman, S. D. Sudhoff, and A. C. Whithcomb, "Optimal current control strategies for surface-mounted permanent-magnet synchronous machine drives," *IEEE Trans. Energy Conv.*, vol. 14, no. 4, pp. 1043-1050, Dec. 1999.
- [8] T. M. Jahns and W. L. Soong, "Pulsating torque minimization techniques for permanent magnet AC motor drives-a review," *IEEE Trans. Ind. Electron.*, vol. 43, no. 2, pp. 321–330, Apr. 1996.
- [9] G. S. Buja and M. P. Kazmierkowski, "Direct torque control of PWM inverter-fed AC motors - a survey," *IEEE Trans. Ind. Electron.*, vol. 51, no. 4, pp. 744–757, Aug. 2004.
- [10] M. Kazmierkowski, R. Krishnan, and F. Blaabjerg, "Control in power electronics – selected problems," Academic Press, 2002.
- [11] F. Blaschke, "The principle of field orientation as applied to the new transvector closed-loop control system for rotating field machine," *Siemens Review*, vol. 34, pp. 217-220, May 1972.
- [12] G. Pfaff, A. Weschta, and A. F. Wick, "Design and experimental results of a brushless AC servo drive," *IEEE Tran. Ind. Appl.*, Vols. IA-20, no. 4, pp. 814-821, Jul. 1984.
- [13] I. Takahashi and T. Noguchi, "A new quick-response and high efficiency control strategy of an induction machine," *IEEE Trans. Ind. Appl.*, vol. 22, pp. 820–827, Sept./Oct. 1986.
- [14] L. Zhong, M. F. Rahman, W. Y. Hu, and K. W. Lim, "Analysis of direct torque control in permanent magnet synchronous motor drives," *IEEE Trans. Power Electron.*, vol. 12, no. 3, pp. 528–536, May 1997.
- [15] E. Clarks, "Circuit analysis of AC power system," Wiley, 1950.

- [16] R. Park, "Two reaction theory of synchronous machine," AIEE Transection, bol 48, pp 716-730, 1929.
- [17] E. Simon, "Implementation of a speed field oriented control of 3-phase PMSM motor using TMS320F240," Application Report SPRA588, Texas instrument, 1999.
- [18] M. Zelechowski, "Direct torque control with space vector modulation (DTC-SVM) of inverter-fed permanent magnet synchronous motor drive," Ph.D. Thesis, Warsaw University of Technology, 2005.
- [19] C. Perera, "Sensorless control of permanent magnet synchronous motor drives," PhD thesis, Institute of Energy Technology, 2002.
- [20] R. Krishnan, "Electric motor drives: modeling , analysis , and control," Prentice Hall, First Edition, 2001.
- [21] L. Zhong, M. F. Rahman, W. Y. Hu and K. W. Lim, "Analysis of direct torque control in permanent magnet synchronous motor drives," *IEEE Trans. Power Electron.*, vol. 12, no. 3, pp. 528–536, May 1997.
- [22] M. Depenbrock, "Direct self control for high dynamics performance of inverter feed AC machines," *ETZ Arch*, vol. 7, no. 7, pp. 211–218, 1985.
- [23] M. Depenbrock, "Direct self control of the flux and rotary moment of a rotary-field machine," United States Patent, patent number 4678248, 7 Jul. 1987.
- [24] U. Baader, M. Depenbrock, and G. Gierse, "Direct self control (DSC) of inverter-fed induction machine: a basis for speed control without speed measurement," *IEEE Trans. on Ind. Appl.*, vol. 28, pp. 581-588, 1992.
- [25] C. French and P. Acarnley, "Direct torque control of permanent magnet drives," *IEEE Trans. on Ind. Appl.*, vol. 32, pp. 1080-1088, 1996.
- [26] M. R. Zolghadri, E. M. Olasagasti, and D. Roye, "Steady state torque correction of a direct torque controlled PM synchronous machine," IEEE International Conference in Electric Machines and Drives, 1997, pp. MC3/4.1-MC3/4.3.
- [27] Y. Liu, Z. Q. Zhu, and D. Howe, "Direct torque control of brushless DC drives with reduced torque ripple," *IEEE Ind. Appl. Conf., 39th IAS Annual Meeting*, 2004, vol. 4, pp. 2390-2396.
- [28] D. Casadei, F. Profumo, G. Serra, and A. Tani, "FOC and DTC: two viable schemes for induction motors torque control," *IEEE Trans.on Power Electron*, vol. 17, no. 5, pp. 779-787, Sep 2002.
- [29] D. Casadei, G. Serra, and A. Tani, "Implementation of a direct torque control algorithm for induction motors based on discrete space vector modulation," *IEEE Trans. Power Electron.*, vol. 15, pp. 769–777, Jul. 2000.
- [30] D. Sun, W. Fang, and Y. He, "Study on the direct torque control of permanent magnet synchronous motor drives," in *Proceedings of the 5th International Conference on Electrical Machines and Systems, ICEMS*, 2001, vol.1, pp. 571-574.

- [31] M. F. Rahman, L. Zhong, W. Y. Hu, K. W. Lim, and M. A. Rahman, "A direct torque controller for permanent magnet synchronous motor drives," *IEEE International Conference in Electric Machines and Drives*, 1997, pp. TD1/2.1-TD1/2.3.
- [32] J. Luukko and P. J, "Selection of the flux linkage reference in a direct torque controlled permanent magnet synchronous motor drive," in *Advanced Motion Control (AMC), 5th International Workshop*, 1998, pp. 198-203.
- [33] Y. Hu, C. Tian, Y. Y. Z. Gu, T. L. X, and F. M. Rahman, "In-depth research on direct torque control of permanent magnet synchronous motor," *IEEE Industrial Electronics Society, 28th Annual Conference*, 2002, vol. 2, pp. 1060-1065.
- [34] J. N. Nash, "Direct torque control, induction motor vector control without an encoder," *IEEE Tran. Ind. Appl.*, vol. 33, pp. 333-341, 1997..
- [35] M. P. Kazmierkowski and A. B. Kasprowicz, "Improved direct torque and flux vector control of PWM inverter-fed induction motor drives," *IEEE Transactions on Ind. Electron.*, vol. 42, pp. 344-350, 1995.
- [36] M. F. Rahman, M. E. Haque, L. Tang, and L. Zhong, "Problems associated with the direct torque control of an interior permanent-magnet synchronous motor drive and their remedies," *IEEE Trans. Ind. Electron*, vol. 51, pp. 799–809, Aug. 2004.
- [37] T. Lixin, Z. Limin, M. F. Rahman, and Y. Hu, "A novel direct torque control for interior permanent-magnet synchronous machine drive with low ripple in torque and flux-a speed-sensorless approach," *IEEE Trans. Ind. Appl.*, vol. 39, pp. 1748–1756, Nov./Dec. 2003.
- [38] K. D. Hoang, Z. Q. Zhu, and M. P. Foster, "Influence and compensation of inverter voltage drop in direct torque-controlled four-switch three-phase PM brushless AC drives," *IEEE Trans. Power Electron.*, vol. 8, no. 28, pp. 2343–2357, Aug. 2011.
- [39] L. Tang, L. Zhong, M. F. Rahman, and Y. Hu, "A novel direct torque controlled interior permanent magnet synchronous machine drive with low ripple in flux and torque and fixed switching frequency," *IEEE Trans. Power Electron.*, vol. 19, no. 2, p. 346–354, Mar. 2004.
- [40] Z. Xu and M. F. Rahman, "Direct torque and flux regulation of an IPM synchronous motor drive using variable structure control approach," *IEEE Trans. Power Electron.*, vol. 22, no. 6, p. 2487–2498, Nov. 2007.
- [41] J. Singh, B. S. Singh, P. Singh, and M. Naim, "Investigation of performance parameters of PMSM drives using DTC-SVPWM technique," in *Engineering and Systems Students Conference (SCES)*, 2012, pp. 1-6.
- [42] G. Foo and M. F. Rahman, "Sensorless direct torque and flux-controlled IPM synchronous motor drive at very low speed without signal injection," *IEEE Trans. Ind. Electron.*, vol. 57, no. 1, pp. 395–403, Jan. 2010.

- [43] J. H. Leong, Z. Q. Zhu, and J. M. Liu, "Space-vector PWM based direct torque control of PM brushless machine drives having non-ideal characteristics," in *Ecological Vehicles and Renewable Energies (EVER), 8th International Conf. and Exhibition*, 2013, pp.1-6.
- [44] B. B. Pimple, V. Y. Vekhande, and B. G. Fernandes, "New direct torque control of DFIG under balanced and unbalanced grid voltage," in *Proc. TENCON, IEEE Region Conf.*, 2010, pp. 2154–2158.
- [45] J. Zhang, M. F. Rahman, and C. Grantham, "A New Scheme to Direct Torque Control of Interior Permanent Magnet Synchronous Machine Drives for Constant Inverter Switching Frequency and Low Torque Ripple," in *International Power Electronics and Motion Control Conference (IPEMC)*, Shanghai, 2006, pp. 1-5.
- [46] F. M. Abdel-kader, A. El-Saadawi, A. E. Kalas, and O. M. Elbaksawi, "Study in direct torque control of induction motor by using space vector modulation," in *Power System Conference, 12th International Middle-East*, 2008, pp. 224 - 229.
- [47] H. W. V. D. Broexk, H.-C. Skudelny, and C. V. Stanke, "Analysis and realization of a pulse width modulator based on voltage space vector," *IEEE Trans. Ind. Appl.*, vol. 24, pp. 142–150, Jan./Feb. 1988.
- [48] K. Zhou and D. Wang, "Relationship between space-vector modulation and three-phase carrier based PWM: A comprehensive analysis," *IEEE Trans. Ind. Electron.*, vol. 49, no. 1, pp. 186–196, Feb. 2002.
- [49] C. Martins, X. Roboam, T. A. Meynard, and A. S. Caryalho, "Switching frequency imposition and ripple reduction in DTC drives by using a multilevel converter," *IEEE Trans. Power Electron.*, vol. 17, pp. 286–297, Mar. 2002.
- [50] D. Swierczynski, M. Kazmierkowski, and F. Blaabjerg, "DSP based direct torque control of permanent magnet synchronous motor (PMSM) using space vector modulation (DTC-SVM)," in *Proc. IEEE-ISIE Annu. Meeting*, vol. 3, May 2002, pp. 723–727.
- [51] j.-H. Lee, C.-G. Kim and M.-J. Youn, "A dead-beat type digital controller for the direct torque control of an induction motor," *IEEE Trans. on Power Electron.*, vol. 17, no. 5, pp. 739–746, Sept. 2002.
- [52] M. Preindl and S. Bolognani, "Model predictive direct speed control with finite control set of PMSM drive systems," *IEEE Trans. Power Electron.*, vol. 28, no. 8, pp. 1007–1015, Feb. 2013.
- [53] D. Wang, X. Wang and S.-Y. Jung, "Cogging torque minimization and torque ripple suppression in surface-mounted permanent magnet synchronous machines using different magnet widths," *IEEE Trans. Magnetics*, vol. 49, no. 5, pp. 2295–2298, 2013.

- [54] W. Chu and Z. Q. Zhu, "Investigation of torque ripples in permanent magnet synchronous machines with skewing," *IEEE Trans. Magnetics*, vol. 49, no. 3, pp. 1211–1220, 2013.
- [55] S. Buso, L. Malesani, and P. Mattavelli, "Comparison of current control techniques for active filter applications," *IEEE Trans. On Ind. Electron.*, vol. 45, no. 4, pp. 722-729, Oct. 1998.
- [56] J. Eloy-Garcia, S. Arnaltes, and J. L. Rodriguez-Amenedo, "Direct power control of voltage source inverters with unbalanced grid voltages," *IET Power Electron.*, vol. 1, no. 3, p. 395–407, Sep. 2008.
- [57] W. Stefanutti and P. Mattavelli, "Full digital hysteresis modulation with switching-time prediction," *IEEE Trans. on Ind. Appl.*, vol. 42, no. 3, pp. 763-769, May 2006.
- [58] M. Mohseni and S. Islam, "A new vector-based hysteresis current control scheme for three-phase PWM voltage-source inverter," *IEEE Trans. on power Electron.*, vol. 25, no. 9, pp. 2299-2309, Sep. 2010 .
- [59] P. Mattavelli, L. Tubiana, and M. Zigliotto, "Torque-ripple reduction in PM synchronous motor drives using repetitive current control," *IEEE Trans. Power Electron.*, vol. 20, no. 6, pp. 1423–1431, Nov. 2005.
- [60] Y.-Y. Tzou, R.-S. Ou, S.-L. Jung, and M.-Y. Chang, "High-performance programmable AC power source with low harmonic distortion using DSP-based repetitive control technique," *IEEE Trans. on Power Electro.*, vol. 12, no. 4, pp. 715-725, Jul 1997.
- [61] Y. Wang, F. Gao, and F. J. Doyle, "Survey on iterative learning control, repetitive control, and run-to-run control," *Journal of process control*, 2009, pp 1589–1600.
- [62] M.-C. Tsai and W.-S. Yao, "Design of a plug-in type repetitive controller for periodic inputs," *IEEE Trans. on control System Technology*, vol. 10, no. 4, pp. 547-555, Jul. 2002.
- [63] J. M. Espi, J. Castello, R. García-Gil, G. Garcera, and E. Figueres, "An adaptive robust predictive current control for three-phase grid-connected inverters," *IEEE Trans. on Ind. Electron*, vol. 58, no. 8, pp. 3537-3546, Aug. 2011.
- [64] Y. A.-R. I. Mohamed and E. F. El-Saadany, "An improved deadbeat current control scheme with a novel adaptive self-tuning load model for a three-phase PWM voltage-source inverter," *IEEE Trans. on Ind. Electron.*, vol. 54, no. 2, pp. 747-759, April 2007.
- [65] J. W. Kolar, H. Ertl, and F. C. Zach, "Analysis of on- and off-line optimized predictive current controllers for PWM converter systems," *IEEE Trans. on Power Electron.*, vol. 6, no. 3, pp. 451–462, July 1991.
- [66] R. Wu, S. B. Dewan, and G. R. Slemon, "Analysis of a PWM AC to DC voltage source converter under the predicted current control with a fixed switching

- frequency," *IEEE Transactions on Industry Applications*, vol 2, no. 4, pp. 756–764, July/August 1991.
- [67] P. Mattavelli, "An improved deadbeat control for UPS using disturbance observers," *IEEE Trans. on Ind. Electron.*, vol. 52, no. 1, pp. 206-212, Feb. 2005.
- [68] H. Fujita, "A single-phase active filter using an h-bridge PWM converter with a sampling frequency quadruple of the switching frequency," *IEEE Trans. on power Electron.*, vol. 24, no. 4, pp. 934-941, Apr. 2009.
- [69] S. Buso and P. Mattavelli, "Digital control in power electronic," Ed. Morgan and Claypool Publishers, 2006..
- [70] G. F. Franklin and P. J. D, "Feedback control of dynamic systems," Addison-Wesley Publishing Company, 1994.
- [71] K. Nishida, M. Rukonuzzman, and M. Nakaoka, "Advanced current control implementation with robust deadbeat algorithm for shunt single-phase voltage-source type active power filter," in *IEE proceeding- Electric Power Applications*, vol. 151, no. 3, pp. 283-288, Mar. 2002.
- [72] H.-S. Song and K. Nam, "Dual current control scheme for PWM converter under unbalanced input voltage conditions," *IEEE Trans. on Ind. Electron.*, vol. 46, no. 5, pp. 953-959, Oct 1999.
- [73] P. Rodriguez, J. Pou, J. Bergas, J. I. Candela, R. P. Burgos, and D. Boroyevich, "Decoupled double synchronous reference frame PII for power converters control," *IEEE Transactions on Power Electron.*, vol. 22, no. 2, pp. 584–592, Mar. 2007.
- [74] Y. Suh and T. A. Lipo, "A control scheme in hybrid synchronous-stationary frame for PWM AC/DC converter under generalized unbalanced operating conditions," in *Proc. IEEE-IAS Annu. Meeting*, Oct. 2004, vol. 4, pp. 2244–2251.
- [75] Y. Suh and T. A. Lipo, "Control scheme in hybrid synchronous stationary frame for PWM AC/DC converter under generalized unbalanced operating conditions," *IEEE Trans. on Ind. Appl.*, vol. 42, no. 3, pp. 825-835, May-June 2006.
- [76] M. Reyes, P. Rodriguez, S. Vazquez, A. Luna, J. M. Carrasco, and R. Teodorescu, "Decoupled double synchronous reference frame current controller for unbalanced grid voltage conditions," in *IEEE Energy Conversion Congress and Exposition (ECCE)*, 15-20 Sept. 2012, pp.4676-468.
- [77] D. N. Zmood and D. G. Holmes, "Stationary frame current regulation of PWM inverters with zero steady-state error," *IEEE Trans. Power Electron.*, vol. 18, no. 3, pp. 814–822, May 2003.
- [78] I. Jeong, B. JoHyon, and K. Nam, "Dynamic modeling and control for SPMSMS with internal turn short fault," *IEEE Trans. Power Elect.*, vol. 28, no. 7, pp. 3495-3508, July 2013.

- [79] F. Blaabjerg, R. Teodorescu, M. Liserre, and A. V. Timbus, "Overview of control and grid synchronization for distributed power generation systems," *IEEE Trans. on Ind. Electron.*, vol. 53, pp. 1398-1409, Oct. 2006.
- [80] P. Rodriguez, A. Luna, R. Teodorescu, and F. Blaabjerg, "Grid synchronization of wind turbine converters under transient grid faults using a double synchronous reference frame PLL," in *IEEE Energy 2030 Conf.*, 2008, pp.1-8.
- [81] G. Bergna et al., "An energy-based controller for HVDC modular multilevel converter in decoupled double synchronous reference frame for voltage oscillation reduction," *IEEE Trans. on Ind. Electron.*, vol. 60, no. 6, pp. 2360-2371, 2013.
- [82] P. Rodriguez, A. Lunar, R. Teodorescu, F. Iov, and F. Blaabjerg, "Fault ride-through capability implementation in wind turbine converters using a decoupled double synchronous reference frame PLL," in *Power Electronics and Applications, European Conference*, Aalborg, 2007, pp. 1-10.
- [83] G. Abad, M. A. Rodriguez, G. Iwanski, and J. Poza, "Direct power control of doubly-fed-induction-generator-based wind turbines under unbalanced grid voltage," *IEEE Trans. Power Electron.*, vol. 25, no. 2, pp. 442–452, Feb. 2010.
- [84] M. Aredes, E. H. Watanabe, and H. Akagi, "Instantaneous power theory and applications to power conditioning," IEEE Press Series on Power Engineering, March 2007, ISBN 0470107618.
- [85] Y. Suh, V. Tijeras, and T. A. Lipo, "A nonlinear control of the instantaneous power in dq synchronous frame for PWM AC/DC converter under generalized unbalanced operating conditions," in *Industry Applications Conference, 37th Annual Meeting*, Oct. 2002, vol.2, pp.1189-1196.
- [86] L. Hsu, R. Ortega, and G. Damm, "A globally convergent frequency estimator," *IEEE Trans. Automat. Contr.*, vol. 44, no. 4, pp. 698–713, Apr. 1999.
- [87] B. Widrow and E. A. Glover, "Adaptive noise cancelling: principles and applications," in *Proceedings of the IEEE*, vol. 63, no. 12, Dec. 1975, pp. 1692-1716.
- [88] B. Burger and E. Engler, "Fast signal conditioning in single phase systems," in *European Conference on Power Electronics and Applications (EPE'01)*, Graz, Aug. 2001, pp. 00287.
- [89] K. De Brabandere and e. al, "Design and operation of a phase-locked loop with kalman estimator-based filter for single-phase applications," in *proceeding of the IEEE Industrial Electronics Conference (IECON,06)*, 2006, pp. 525-530.
- [90] M. Mojiri and A. Bakhshai, "An adaptive notch filter for frequency estimation of a periodic signal," *IEEE Trans. on Automatic Control*, vol. 49, no. 2, pp. 314–318, February 2004.
- [91] P. Rodriguez, R. Teodorescu, I. Candela, A. V. Timbus, M. Liserre, and F. Blaabjerg, "New positive-sequence voltage detector for grid synchronization

- of power converters under faulty grid conditions," in *In Proceedings of the IEEE Power Electronics Special conference (PESC'06)*, June 2006, pp. 1-7.
- [92] R. Teodorescu, M. Liserre, and P. Rodríguez, "Grid converters for photovoltaic and wind power systems," A John Wiley and Sons, Ltd., Publication, 1st Edition, 2011.
- [93] C. Lascu, L. Asiminoaei, I. Boldea, and F. Blaabjerg, "High-performance current controller for selective harmonic compensation in active power filters," *IEEE Trans. on Power Electron.*, vol. 22, no. 5, pp. 1826-1835, Sep. 2007.
- [94] P. Mattavelli, "A closed-loop selective harmonic compensation for active power filter," *IEEE Trans. Ind. Appl.*, vol. 37, no. 1, pp. 81-89, Jan./Feb. 2001.
- [95] H. S. Che, E. Levi, M. Jones, W. P. Hew and N. A. Rahim, "Current control methods for an asymmetrical six-phase induction motor drive," *IEEE Trans. Power Electron.*, vol. 29, no. 1, pp. 407-417, 2014.
- [96] A. G. Yepes, F. D. Freijedo, J. Doval-Gandoy, O. Lopez, P. Fernandez-Comesana and, J. Malvar, "Harmonic identification algorithms based on DCT for power quality applications," *ETRI Journal*, vol. 32, no. 1, pp. 33-43, Feb. 2010.
- [97] I. Gabe, V. Montagner, and H. Pinheiro, "Design and implementation of a robust current control for VSI connected to the grid through an LCL filter," *IEEE Trans. on Power Electron.*, vol. 24, no. 6, pp. 1444-1452, Jun. 2009.
- [98] J. Dannehl, F. Fuchs, and P. Thoandgersen, "PI state space current control of grid-connected PWM converters with LCL filters," *IEEE Trans. on Power Electron.*, vol. 25, no. 9, pp. 2320-2330, Sep. 2010.
- [99] M.-C. Chou and L. C.-M., "Development of robust current 2-DOF controllers for a permanent magnet synchronous motor drive with reaction wheel load," *IEEE Trans. on Power Electron.*, vol. 24, no. 5, pp. 1304-1320, May 2009.
- [100] P. Degobert, G. Remy, J. Zeng, P.-J. Barre, and J.-P. Hautier, "High performance control of the permanent magnet synchronous motor using self-tuning resonant controllers," in *in Proceeding of the Southeastern Symposium on System Theory, SSST*, Mar. 2006, pp. 382-386.
- [101] J. Zeng, P. Degobert, and H. J.-P., "Minimum torque ripple control of permanent magnet synchronous motor in the stationary reference frame," in *Proceeding of IET Conference on power electronics, Machine and Drives, PEMD*, 15 May 2005, pp. 667-673.
- [102] H. Yu, "A novel digital current control strategy for torque ripple reduction in permanent magnet synchronous motor drives," in *proceeding of IEEE applied power Electron. Conference, APEC*, Feb. 2010, pp. 2025-2029.
- [103] S. Fukuda and R. Imamura, "Application of sinusoidal internal model to current control of three-phase utility-interface converter," *IEEE Trans. on Ind. Electron.*, vol. 52, no. 2, pp. 420-426, Apr. 2005.

- [104] G. Escobar, A. de, J. Leyva-Ramos, and P. Martinez, "A controller for boost converter with harmonic reduction," *IEEE Trans. on Control System Technology*, vol. 12, no. 5, pp. 717-726, Sep. 2004.
- [105] J. Hu, H. Nian, H. Xu, and Y. He, "Dynamic modeling and improved control of DFIG under distorted grid voltage conditions," *IEEE Trans. Energy Conv.*, vol. 26, no. 1, pp. 163–175, Mar. 2011.
- [106] M. Liserre, R. Teodorescu, and F. Blaabjerg, "Multiple harmonics control for three-phase grid converter system with the use of PI-RES current controller in a rotating frame," *IEEE Trans. on Power Electron*, vol. 21, no. 3, pp. 836-841, May. 2006.
- [107] V.-T. Phan and H.-H. Lee, "control strategy for harmonic elimination in stand-alone DFIG applications with nonlinear load," *IEEE Trans on Power Electron.*, vol. 26, no. 9, pp. 2662-2675, Sep. 2011.
- [108] A. G. Yepes, F. D. Freijedo, P. Fernandez-Comesana, J. Malvar, O. Lopez, and J. Doval-Gandoy, "Torque ripple minimization in surface-mounted PM drives by means of PI+multi-resonant controller in synchronous reference frame," in *Proceedings of IEEE Industrial Electronics Conference, IECON*, Nov. 2010.
- [109] R. Bojoi, L. Limongi, D. Ruiu, and A. Tenconi, "Frequency-domain analysis of resonant current controller for active power conditioners," in *Proceedings of IEEE Industrial Electronics Conference*, Nov. 2008, pp. 3141-3148.
- [110] L. Harnefors, L. Zhang, and M. Bongiono, "Frequency-domain passivity-based current controller design," *IET Power Electronics*, vol. 1, no. 4, pp. 455-465, Dec. 2008.
- [111] L. Limongi, R. Bojoi, G. Griva, and A. Tenconi, "Digital current-control schemes," *IEEE Industrial Electronics Magazine*, vol. 3, no. 1, pp. 30-31, Mar. 2009.
- [112] R. I. Bojoi, G. Griva, V. Bostan, M. Guerriero, F. Farina, and F. Profumo, "Current control strategy for power conditioners using sinusoidal signal integrators in synchronous reference frame," *IEEE Trans. on Power Electron.*, vol. 20, no. 6, pp. 1402-1412, Nov. 2005.
- [113] dSPACE, "Hardware installation and configuration reference," Release 6.6, May 2010.
- [114] B. K. Bose, "Modern Power Electronics and AC drives," Prentice-Hall, 2002.
- [115] A. M. Trzynadlowski and S. Legowski, "Minimum-loss vector PWM strategy for three-phase inverter," *IEEE Trans. on Power Electron*, vol. 9, no. 1, pp. 26-34, Jan. 1994.
- [116] J. Holtz, "Pulsewidth modulation for electronic power conversion," in *Proceedings of the IEEE*, vol. 83, no. 8, Aug. 1994, pp. 1194-1214.
- [117] A. M. Hava, R. J. Kerkman and T. A. Lipo, "A high performance generalized discontinuous PWM algorithm," in *Proceeding in Applied Power Electronics Conf. and exposition (APEC), 12th*, vol. 2, 23-27 Feb., 1997, pp. 886-894.

- [118] H. W. V. D Broeck, H.-C. Skudelny, and G. V. Stanke, "Analysis and realization of a pulsewidth modulator based on voltage space vectors," *IEEE Transactions on Ind. Appl.*, vol. 24, pp. 142-150, 1988.
- [119] W. Zhang and Y.-H. Yu, "Comparison of Three SVPWM Strategies," *Journal of electrical science and technology of China*, vol. 5, no. 3, Sep. 2007.
- [120] G. Narayanan and V. T. Ranganathan, "Triangle-comparison approach and space vector approach to pulsewidth modulation in inverter fed drives," *Journal of Indian Institute of Science*, vol. 80, pp. 409–427, Sep.-Oct. 2000.
- [121] X. Mao, A. K. Jain, and R. Ayyanar, "Hybrid interleaved space vector PWM for ripple reduction in modular converters," *IEEE Trans. on Power Electron.*, vol. 26, no. 7, pp. 1954–1967, 2011.
- [122] G. Narayanan and V. T. Ranganathan, "Extension of operation of space vector PWM strategies with low switching frequency using different overmodulation algorithms," *IEEE Transactions on Power Electronics*, vol. 17, no. 5, pp. 788–798, 2002.
- [123] V. Blasko, "Analysis of a hybrid PWM based on modified space-vector and triangle-comparison methods," *IEEE Trans. on Ind. Appl.*, vol. 33, no. 3, pp. 756-764, May-June 1997.
- [124] D.-C. Lee and C. Lee, "A novel overmodulation technique for space-vector PWM inverters," *IEEE Trans. on Power Electron.*, vol. 13, no. 6, pp. 1144-1151, Nov, 1998.
- [125] A. Diax and E. G. Strangas, "A novel wide range pulse width overmodulation method [for voltage source inverter]," in *Applied Power Electronics Conference and Exposition (APEC), 5th IEEE*, vol. 1, 6-10 Feb. 2000, pp. 556-561.
- [126] Z. Q. Zhu, K. Ng, and D. Howe, "Design and analysis of high-speed brushless permanent magnet motor," in *Proc. 8th Int. Conf. Elec. Mach. Drives*, Sept.1-3, 1997, pp. 381-385.
- [127] T. Ohtani, N. Takada and K. Tanaka, "Vector control of induction motor without shaft encoder," *IEEE Trans. Ind. Appl*, vol. 28, no. 1, p. 157–165, Jan./Feb. 1992.
- [128] F. Briz, M. Degner, and R. Lorenz, "Analysis and design of current regulators using complex vectors," *IEEE Trans. Ind. Appl*, vol. 36, no. 3, pp. 817-825, May/Jun. 2000.
- [129] I. Jeong, B. JoHyon, and K. Nam, "Dynamic modeling and control for SPMSMS with internal turn short fault," *IEEE Trans. Power Elect.*, vol. 28, no. 7, pp. 3495-3508, July 2013.
- [130] M. Reyes, P. Rodriguez, S. Vazquez, A. Luna, R. Teodorescu, and J. M. Carrasco, "Enhanced decoupled double synchronous reference frame current controller for unbalanced grid-voltage conditions," *IEEE Trans. Power Electron.*, vol. 27, no. 9, pp. 3934–3943, Sep. 2012.

- [131] K.-H. Kim, N.-J. Park, and D.-S. Hyun, "Advanced synchronous reference frame controller for three-phase UPS powering unbalanced and nonlinear loads," in *IEEE Power Electronics Specialists Conference (PESC, 36th)*, pp. 1699-1704.
- [132] R. Teodorescu, F. Blaabjerg, M. Liserre, and P. C. Loh, "Proportional-resonant controllers and filters for grid-connected voltage-source converters," *IEE Proceedings In Electric Power Appl.*, vol. 153, no. 5, pp. 750–762, Sep. 2006.
- [133] A. G. Yepes, A. Vidal, O. Lopez and J. Doval-Gandoy, "Evaluation of techniques for cross-coupling decoupling between orthogonal axes in double synchronous reference frame current control," *IEEE Trans. Ind. Electron.*, vol. 61, no. 7, pp. 3527,3531, July 2014.
- [134] Z. Ivanovic, E. Adzic, M. Vekic, S. Grabic, N. Celanovic, and V. Katic, "HIL evaluation of power flow control strategies for energy storage connected to smart grid under unbalanced conditions," *IEEE Trans. Power Electron.*, vol. 27, no. 11, pp. 4699-4710, Nov. 2012.
- [135] D. Y. Ohm, J. W. Brown, and V. B. Chava, "Modeling and Parameter Characterization of Permanent Magnet synchronous Motors," in *Proceedings of the 24th Annual Symposium of Incremental Motion Control System and Devices*, San Jose, 5-8 June 1995, pp. 81-86.
- [136] T.-S. Low, C. Bi, and K.-T. Chang, "Motor "identity"- a motor model for torque analysis and control," *IEEE Trans. on ind. Electron.*, vol. 43, no. 2, pp. 285-291, April 1996.
- [137] V. Petrovi and A. M. Stankovic, "Modeling of PM synchronous motors for control and estimation tasks," in *Proceedings of the 40th IEEE Decision and Control Conference*, 2001, vol.3, pp. 2229-2234.
- [138] V. A. Petrovi and M. Stankovi, "Modeling of PM synchronous motors for control and estimation tasks," in *proceedings of the 40th IEEE Conference on Decision and Control*, Orlando, FL, vol.3, pp. 2229-2234 2001..
- [139] P. C. Kraus and O. Waszynuk, "Electromechanical Motion Devices," New York, McGraw-Hill, 1989.
- [140] B.-G. Gu, J.-H. Choi and I.-S. Jung, "A dynamic modeling and a fault detection scheme of a PMSM under an inter turn short," in *IEEE Vehicle Power and Propulsion Conference*, Seoul, 2012, pp. 1074-1080.
- [141] J. Wang and R. Hamilton, "A review of negative sequence current," in *Protective Relay Engineers Conf. (63rd)*, March 29-1April,2010, pp. 1-18.
- [142] J. Grainger and W. Stevenson, "Power system analysis," McGraw-Hill, Inc, 1994.
- [143] W. V. Lyon, "Application of the method of symmetrical components," New York: McGraw-Hill, 1937.

- [144] M. Karimi-Ghartemani and M. R. Iravani, "A nonlinear adaptive filter for online signal analysis in power system: applications," *IEEE Trans. on Power Delivery*, vol. 17, pp. 617-622, April 2002.
- [145] L. Hsu, R. Ortega, and G. Damm, "A globally convergent frequency estimator," *IEEE Trans. Automat. Contr.*, vol. 44, no. 4, pp. 698–71, Apr. 1999.
- [146] P. Rodriguez, R. Teodorescu, I. Candela, A. V. Timbus, M. Liserre and F. Blaabjerg, "New positive-sequence voltage detector for grid synchronization of power converters under faulty grid conditions," in *Proceedings of the IEEE Power Electron. Special conf. (PESC'06)*, June 2006, pp.1-7.
- [147] F. J. Rodriguez, E. Bueno, M. Aredes, L. G. B. Rolim, F. A. S. Neves, and M. C. Cavalcanti, "Discrete-time implementation of second order generalized integrators for grid converters," in *Proc. IEEE Ind. Electron Conf. (IECON)*, Nov. 2008, pp. 176-181.
- [148] C. M. Rader and L. B. Jackson, "Approximating noncausal IIR digital filters having arbitrary poles, including new hilbert transformer designs via forwars/backward block recursion," *IEEE Trans. on Circuits and systems I: Regular Paper*, vol. 53, no. 12, Dec. 06, pp. 2779-2787.
- [149] S. M. Silva et al., "Performance Evaluation of PLL Algorithms for single-phase Grid-connected system," in *Proceedings of the Ind. Appl. Conf. (IAC'04)*, vol. 4, Oct. 2004, pp. 2259-2263.
- [150] R. Teodorescu, M. Liserre and P. Rodríguez, "Grid converters for photovoltaic and wind power systems," 2011.
- [151] J. Hu, H. Nian, H. Xu and Y. He, "Dynamic modeling and improved control of DFIG under distorted grid voltage conditions," *IEEE Trans. Energy Convers.*, vol. 26, no. 1, pp. 163–175, Mar. 2011.
- [152] A. H. Abosh and Z. Q. Zhu, "Current control of permanent magnet synchronous machine with asymmetric phases," in *7th IET International Conference on Power Electronics Machines and Drives (PEMD)*, April 2014, Manchester, pp.1-6.
- [153] T. Ohtani, N. Takada and K. Tanaka, "Vector control of induction motor without shaft encoder," *IEEE Trans. Ind. Appl.*, vol. 28, no. 1, pp. 157–165, Jan./Feb. 1992.
- [154] I. Takahashi and T. Noguchi, "A new quick-response and high efficiency control strategy of an induction machine," *IEEE Trans. Ind. Appl.*, vol. 22, pp. 820–827, Sept./Oct. 1986.
- [155] K. Zhou and D. Wang, "Relationship between space-vector modulation and three-phase carrier based PWM: A comprehensive analysis," *IEEE Trans. Ind. Electron.*, vol. 49, no. 1, pp. 186-196, Feb. 2002.
- [156] V. D. Broeck, H. C. Skudelny and G. Stanke, "Analysis and realization of a pulse width modulator based on voltage space vector," *IEEE Trans. Ind. Electron*, vol. 24, no. 1, pp. 142-150, Jan./Feb. 1988.

- [157] K.-K. Shyu and J.-K. Lin, "Global minimum torque ripple design for direct torque control of induction motor drives," *IEEE Trans. Ind. Electron.*, vol. 57, no. 9, pp. 3148 - 3156, Sept. 2010.
- [158] S. Fukuda and T. Yoda, "A novel current-tracking method for active filter based on a sinusoidal internal model," *IEEE Trans. on Ind. Appl.*, vol. 37, no. 3, pp. 888–895, May/June. 2001.
- [159] M. Fu and L. Xu, "A novel sensorless control technique for permanent magnet synchronous motor (PMSM) using digital signal processor (DSP)," in *Proc. IEEE Aerospace and Electronics Conf.*, 1997, vol. 1, pp. 403-408.
- [160] B. B. Pimple, V. Y. Vekhande and B. G. Fernandes, "A new direct torque control of doubly fed induction generator for wind power generation," in *India International Power Electron. Conf. (IICPE)*, Jan. 2011, pp. 1-5.
- [161] Y. Xu, N. Parspour and U. Vollmer, "Torque ripple minimization using online estimation of the stator resistances with consideration of magnetic saturation," *IEEE Trans. Ind. Electron.*, vol. 61, no. 9, pp. 5105–5114, Sep. 2014.
- [162] Z. Xunhao, Q. Huang, Z. Hu and K. Guangqiang, "A control method for permanent-magnet synchronous motor with unbalanced cable resistor," in *6th International Conference on Power Electronics Systems and Applications (PESA)*, Hong Kong, 2015, pp. 1-3.
- [163] G. Foo, C. Goon, and M. F. Rahman, "Analysis and design of the SVM direct torque and flux control scheme for IPM synchronous motors," in *Int. Conf. on Electrical Machines and Systems*, Nov. 15-18, 2009, pp. 1-6.
- [164] C. Lascau, I. Boldea and F. Blaabjerg, "A modified direct torque control for induction motor sensorless drive," *IEEE Trans. Ind. Appl.*, vol. 36, no. 1, p. 122–130, Jan/ Feb 2000.
- [165] M.-H. Shin, D.-S. Hyun, S.-B. Cho and S.-Y. Choe, "An improved stator flux estimation for speed sensorless stator flux orientation control of induction motors," *IEEE Trans. Power Electron.*, vol. 15, no. 2, pp. 312–318, Mar. 2000.
- [166] M. Hinkkanen and J. Luomi, "Modified integrator for voltage model flux estimation of induction motors," *IEEE Trans. Ind. Electron.*, vol. 50, no. 4, pp. 818–820, Aug. 2003.
- [167] M. Minkkanen and J. Luomi, "Modified integrator for voltage model flux estimation of induction motors," *IEEE Trans. Ind. Electron.*, vol. 50, no. 4, pp. 818–820, Aug. 2003.
- [168] C. Y. Chen, C. H. Hsu, S. H. Yu, C. F. Yang and H. H. Huang, "Cascade PI controller designs for speed control of permanent magnet synchronous motor drive using direct torque approach," in *4th International Conf. in Innovative Computing Information and Control (ICIC)*, 2009, pp.938-941.
- [169] P. Rodríguez, J. Pou, J. Bergas, I. Candela, R. Burgos and D. Boroyevich, "Double synchronous reference frame PLL for power converters," in *Proc. IEEE Power Electron. Spec. Conf. (PESC'05)*, 2005, pp. 1415-1421.

- [170] L. Hsu, R. Ortega and G. Damm, "A globally convergent frequency estimator," *IEEE Trans. Automat. Contr.*, vol. 44, no. 4, pp. 698–713, Apr. 1999.
- [171] Mathworks (r2014a). [on line] Available, <http://dali.feld.cvut.cz/ucebna/matlab/toolbox/dspblks/variableintegerdelay.html>.
- [172] S.-M. Sue and C.-T. Pan, "Voltage-constraint-tracking-based field weakening control of IPM synchronous motor drives," *IEEE Trans. Ind. Electron.*, vol. 55, no. 1, pp. 340–347, Jan. 2008.
- [173] I. Etxeberria-Otadui, U. Viscarret, M. Caballero, A. Rufer and S. Bacha, "New optimized PWM VSC control structures and strategies under unbalanced voltage transients," *IEEE Trans. Ind. Electron.*, vol. 54, no. 5, pp. 2902–2914, Oct. 2007.
- [174] X. Yuan, W. Merk, H. Stemmler, and J. Allmeling, "Stationary-frame generalized integrators for current control of active power filters with zero steady-state error for current harmonics of concern under unbalanced and distorted operating conditions," *IEEE Trans. Ind. Appl.*, vol. 38, no. 2, pp. 523–532, Mar./Apr. 2002.
- [175] D. N. Zmood, D. G. Holmes and G. H. Bode, "Frequency-domain analysis of three-phase linear current regulators," *IEEE Trans. Ind. Appl.*, vol. 37, no. 2, pp. 601–610, 2001.
- [176] Y. S. Hu, Z. Q. Zhu and K. Liu, "Current control for dual three-phase permanent magnet synchronous motors accounting for current unbalance and harmonics," *IEEE J. Emerging Sel. Topics Power Electron.*, vol. 2, no. 2, pp. 272–284, Jun. 2014.
- [177] R. Teodorescu, F. Blaabjerg, M. Liserre, and P. C. Loh, "Proportional-resonant controllers and filters for grid-connected voltage-source converters," *IEE Proceedings In Electric Power Appl.*, vol. 153, no. 5, pp. 750–762, Sep. 2006.
- [178] A. G. Yepes, F. D. Freijedo, J. Doval-Gandoy, O. Lopez, J. Malvar and P. Fernandez-Comesana, "Effects of discretization methods on the performance of resonant controllers," *IEEE Trans. Power Electron.*, vol. 25, no. 7, pp. 1692–1712, Jul. 2010.
- [179] A. G. Yepes, F. D. Freijedo, O. Lopez and J. Doval-Gandoy, "High performance digital resonant controllers implemented with two integrators," *IEEE Trans. Power Electron.*, vol. 26, no. 2, pp. 563–576, Feb. 2011.
- [180] Y. Xue, X. Xu, T. G. Habetler and D. M. Divan, "A low cost stator flux oriented voltage source variable speed drive," in *IEEE Industry Applications Society Annual Meeting*, 7-12 Oct., 1990, vol.1, pp.410-415.
- [181] Z. Q. Zhu, J. H. Leong, and X. Liu, "Control of stator torsional vibration in PM brushless AC drives due to non-sinusoidal back-EMF and cogging torque by improved direct torque control," in *International Conf. in Electrical Machines and Systems (ICEMS)*, 20-23 Aug., 2011, pp. 1-6.

- [182] A. G. Yepes, F. D. Freijedo, P. Fernandez-Comesana, J. Malvar, O. Lopez and J. Doval-Gandoy, "Torque ripple minimization in surface-mounted PM drives by means of PI+multi-resonant controller in synchronous reference frame," in *Proceedings of IEEE Industrial Electronics Conference, IECON*, Nov. 2010, pp. 1017-1022.
- [183] S. Hwang and J. Kim, "Dead time compensation method for voltage-fed PWM inverter," *IEEE Trans. Energy Convers.*, vol. 25, no. 1, pp. 1-10, Mar. 2010.
- [184] J. X. Xu, S. K. Panda, Y. J. Pan, T. J. Lee, and B. H. Lam, "A modular control scheme for PMSM speed control with pulsating torque minimization," *IEEE Trans. Ind. Electron.*, vol. 51, no. 3, pp. 526–536, Jun. 2004.
- [185] S.-H. Hwang and J.-M. Him, "Dead time compensation method for voltage-fed PWM inverter," *IEEE Trans. on Energy Conv.*, vol. 25, no. 1, pp. 1-10, March 2010.
- [186] P. Mattavelli, L. Tubiana and M. Zigliotto, "Torque-ripple reduction in PM synchronous motor drives using repetitive current control," *IEEE Trans. Power Electron.*, vol. 20, no. 6, pp. 1423-1431, Nov. 2005.
- [187] I. Etxeberria-Otadui, U. Viscarret, M. Caballero, A. Rufer and S. Bacha, "New optimized PWM VSC control structures and strategies under unbalanced voltage transients," *IEEE Trans. Ind. Electron.*, vol. 54, no. 5, pp. 2902–2914, Oct. 2007.
- [188] A. Vidal, F. Freijedo, A. Yepes, P. Fernandez-Gomesana, J. Malvar, O. Lopez and J. Doval-Gandoy, "Assessment and optimization of the transient response of proportional–resonant current controllers for distributed power generation systems," *IEEE Trans. Ind. Electron*, vol. 60, no. 4, pp. 1367–1383, Apr. 2013.
- [189] Y. Hu, Z. Q. Zhu, and K. Liu, "Current Control for Dual Three-Phase Permanent Magnet Synchronous Motors Accounting for Current Unbalance and Harmonics," *IEEE Trans. in Power Electron*, vol. 2, no. 2, pp. 272-284, June 2014.
- [190] G. S. Buja and M. P. Kazmierkowski, "Direct torque control of PWM inverter-fed AC motors - a survey," *IEEE Trans. Ind. Electron*, vol. 51, no. 4, pp. 744–757, Aug. 2004.
- [191] J. W. Choi and S. K. Sul, "Inverter output voltage synthesis using novel dead time compensation," *IEEE Trans. on Power Electron.*, vol. 11, no. 2, pp. 221-227, March 1996.
- [192] L. Ben-Brahim, "The analysis and compensation of dead-time effects in three phase PWM inverters," in *in Proceedings of the Industrial Electronics Society, IECON*, vol. 2d, 31 Aug.-4 Sept. 1998, pp.792-797.
- [193] J. L. Lin, "A new approach of dead-time compensation for PWM voltage inverters," *IEEE Transactions on Circuits and Systems I: Fundamental Theory and Applications*, vol. 49, no. 4, pp. 476-483, April 2002.

- [194] N. Urasaki, T. Senjyu, K. Uezato and T. unabashi, "On-line dead-time compensation method for permanent magnet synchronous motor drive," in *IEEE International on Industrial Technology, CIT '02*, 11-14 Dec. 2002, Vol. 1, pp. 268 –273.
- [195] F. Blaabjerg, J. K. Pedersen and P. Thøgersen, "Improved modulation techniques for PWM-VSI drives," *IEEE Transactions on Industrial Electronics*, vol. 44, pp. 87 – 95, Feb. 1997.
- [196] S. Buso and P. Mattavelli, *Digital Control in Power Electronics*, J. Hudgins, Ed. San Rafael, CA: Morgan and Claypool, 2006.
- [197] S. Kaitwanidvilai, W. Khan-Ngern and M. Panarut, "The impact of deadtime effect on unwanted harmonics conducted emission of PWM inverters," in *Proceedings Asia-Pacific Conference on Environmental Electromagnetics*, Shanghai, 2000, pp. 232 - 237.
- [198] M. A. Amirian, A. Rashidi, S. M. S. Nejad and M. Mojiri, "Multiple reference frame control of permanent magnet synchronous motor with non-sinusoidal back EMF using adaptive notch filter," in *23rd Iranian Conf. Electr. Eng. (ICEE)*, 10-14 May 2015, pp.1480-1485.
- [199] J. Zeng, D. P and J. Hautier, "Minimum Torque Ripple Control of Permanent Magnet Synchronous Motor in the Stationary Reference Frame," in *IEEE International Conference on Electric Machines and Drives, San Antonio, TX*, 2005, pp. 667-673.
- [200] Y.-S. Lai and J.-H. Chen, "A new approach to direct torque control of induction motor drives for constant inverter switching frequency and torque ripple reduction," *IEEE Trans. Energy Conv.*, vol. 16, no. 3, pp. 220–227, Sep. 2001.
- [201] H. Zhu, X. Xiao and Y. Li, "Torque ripple reduction of the torque predictive control scheme for permanent-magnet synchronous motors," *IEEE Trans. Ind. Electron.*, vol. 59, no. 2, pp. 871–877, Feb. 2012.
- [202] Y. Cho, K.-B. Lee, J.-H. Song, and Y. Lee, "Torque ripple minimization and fast dynamic scheme for torque predictive control of permanent magnet synchronous motors," *IEEE Trans. Power Electron.*, vol. 30, no. 4, pp. 2182–2190, April 2015.
- [203] J. X. Xu, S. K. Panda, Y. J. Pan, T. H. Lee, and B. H. Lam, "A modular control scheme for PMSM speed control with pulsating torque minimization," *IEEE Trans. Ind. Electron*, vol. 51, no. 3, pp. 526–536, Jun. 2004.
- [204] J. Zeng, P. Degobert, and J.-P. Hautier, "Minimum torque ripple control of permanent magnet synchronous motor in the stationary reference frame," in *Proceeding of IET Conference on power electronics, Machine and Drives, PEMD*, 15 May 2005, pp. 667-673.
- [205] D. Yazdani, A. Bakhshai, and P. K. Jain, "A three-phase adaptive notch filter-based approach to harmonic/reactive current extraction and harmonic

- decomposition," *IEEE Trans. Power Electron.*, vol. 25, no. 4, pp. 914–923, Apr. 2010.
- [206] M. Cirrincione, M. Pucci, G. Vitale, and A. Miraoui, "Current harmonic compensation by a single-phase shunt active power filter controlled by adaptive neural filtering," *IEEE Trans. Ind. Electron.*, vol. 56, no. 8, pp. 3128–3143, Aug. 2009.
- [207] R. L. Ortolan et al., "Evaluation of adaptive-nonadaptive filtering and wavelet transform techniques for noise reduction in EMG mobile acquisition equipment," *IEEE Trans. Neural Syst. Rehab. Eng.*, vol. 11, no. 1, pp. 60–69, Mar. 2003.
- [208] R. R. Pereira, C. H. da Silva, L. E. B. da Silva, G. Lambert-Torres, and J. O. P. Pinto, "New strategies for application of adaptive filters in active power filters," *IEEE Trans. Ind. Appl.*, vol. 47, no. 3, pp. 1136–1141, May/Jun. 2011.
- [209] P. L. Chapman and S. D. Sudhoff, "A multiple reference frame synchronous estimator/regulator," *IEEE Trans. on Energy Conv.*, vol. 15, no. 2, p. 197–202, 2000.
- [210] E. Clarke, "Circuit analysis of AC power system," in *Vol.I-symmetrical and Related Components*, Wiley, 1943.
- [211] P. Vas, "Sensorless vector and direct torque control," Oxford University Press, 1998..
- [212] P. C. Krause and C. H. Thomas, "Simulation of symmetrical induction machinery," *IEEE Transactions on Power Apparatus*, vol. 84, pp. 1038-1053, 1965.
- [213] P. Pillay and R. Krishnan, "Modeling of permanent magnet motor drives," *IEEE Trans. on Ind. Electron.*, vol. 35, pp. 537 – 541, Nov. 1988.
- [214] P. D. C. Perera, "Sensorless control of permanent magnet synchronous motor drives," PhD thesis, Institute of Energy Technology, 2002.

APPENDICES

APPENDIX A. Machine Basic Transformation

A.1. Stationary abc coordinates to $\alpha\beta 0$ transformation (Clark-transformation)

A dynamic model for a two-phase machine can be derived from the three-phase machine if the equivalence between the two and three phases is established [210], [211]. The equivalence is based on the equality of the magneto motive force (MMF) produced in the two-phase and three-phase windings and on equal current magnitudes. The stationary $\alpha\beta 0$ presented by Clarke [210] is more applicable in DTC strategy, whereas implementation in the rotational $dq0$ reference frame related to Clarke-Park transformations [212], is necessary for VC strategy. Fig. A.1 shows the three-phase and two-phase windings. Assuming that each of the three-phase windings has N_s turns per phase, and equal current magnitudes, then, the two-phase windings will have $\frac{3}{2}N_s$ turns per phase.

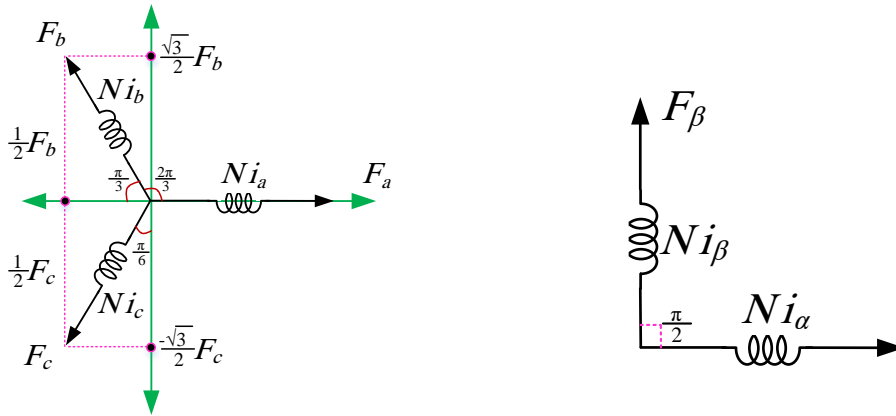


Fig. A. 1 Two axes representation of three-phase windings

As can be seen from Fig. A.1 the three-phase windings is equivalent with equal number of MMF turn N_s , and each winding is physically placed in 120° degree apart to other. The MMF produced by each winding is in the same direction of the winding axis with the magnitude being $N_s i_x$, where $x = \text{phase } a, b, \text{ or } c$. To calculate the vector sum of the airgap MMF. It can be resolved the individual MMF vector along two orthogonal axes α and β .

TABLE A.1 RELATIONSHIP BETWEEN THREE-PHASE AND TWO-PHASE WINDINGS

	F_a	F_b	F_c
F_a	$F_a = N i_a$	$-\frac{1}{2}F_b = -\frac{1}{2}Ni_b$	$-\frac{1}{2}F_c = -\frac{1}{2}Ni_c$
F_β	0	$\frac{\sqrt{3}}{2}F_b = \frac{\sqrt{3}}{2}Ni_b$	$-\frac{\sqrt{3}}{2}F_c = -\frac{\sqrt{3}}{2}Ni_c$
F_0	$F_a = \frac{1}{2}Ni_a$	$F_b = \frac{1}{2}Ni_b$	$F_c = \frac{1}{2}Ni_c$

The Clarke transformation of the three-phase stator winding from the stationary abc reference frame to an orthogonal two-phase windings $\alpha\beta 0$ of the above relationship in Table A.1 can be generalized to transformation as shown in the equation (A1.1)

$$\begin{bmatrix} F_\alpha \\ F_\beta \\ F_0 \end{bmatrix} = \frac{2}{3} \underbrace{\begin{bmatrix} 1 & -\frac{1}{2} & -\frac{1}{2} \\ 0 & \frac{\sqrt{3}}{2} & -\frac{\sqrt{3}}{2} \\ \frac{1}{2} & \frac{1}{2} & \frac{1}{2} \end{bmatrix}}_{[T_{\alpha\beta 0 \leftarrow abc}]} \begin{bmatrix} F_a \\ F_b \\ F_c \end{bmatrix}, \quad \begin{bmatrix} F_\alpha \\ F_\beta \\ F_0 \end{bmatrix} = [T_{\alpha\beta 0 \leftarrow abc}] \begin{bmatrix} F_a \\ F_b \\ F_c \end{bmatrix} \quad (\text{A.1})$$

where F can be any stator voltage, current, flux linkage, or MMF. The factor $2/3$ is chosen for magnitude invariant conversion. In Y-connection stator winding, the zero sequence current i_0 does not produce a resultant magnetic field and it becomes zero. Moreover, the Clarke-transformation from time variant $\alpha\beta 0$ reference frame to a three-phase abc reference frame can be obtained as

$$\begin{bmatrix} F_a \\ F_b \\ F_c \end{bmatrix} = \underbrace{\begin{bmatrix} 1 & 0 & 1 \\ -\frac{1}{2} & \frac{\sqrt{3}}{2} & 1 \\ -\frac{1}{2} & -\frac{\sqrt{3}}{2} & 1 \end{bmatrix}}_{[T_{abc \leftarrow \alpha\beta 0}]} \begin{bmatrix} F_\alpha \\ F_\beta \\ F_0 \end{bmatrix}; \quad \begin{bmatrix} F_a \\ F_b \\ F_c \end{bmatrix} = [T_{abc \leftarrow \alpha\beta 0}] \begin{bmatrix} F_\alpha \\ F_\beta \\ F_0 \end{bmatrix} \quad (\text{A.2})$$

A.2 Stationary $\alpha\beta 0$ to rotational $dq 0$ transformation (Park-transformation)

The transformation is to obtain constant inductances achieved by replacing the actual stator and its windings with a fictitious stator having windings on the d - and q -axes as shown in Fig.A.2. In this process, the fictitious stator will have the same number of turns for each phase as the actual stator phase windings and should produce the equivalent MMF. The actual stator MMF in any axis, i.e. α or β , is the product of the number of turns and current in the respective axis winding. The machine rotor produces a rotational field, which can be represented by the flux linkage vector coincident with d -axis. The axis is chosen to be dq -rotational reference frame. The q -axis is defined to be perpendicular to the d -axis according to the right hand corkscrew convention in direction of the rotation as shown in Fig. A.2. θ_r is the electrical angle between rotor d -axis and α -axis. If initially the two axes coincide and the rotor rotate at asynchronous speed ω_r , then, $\theta_r = \omega_r t$. The MMF vector in the $\alpha\beta$ reference frame can be represented by their equivalence in $dq 0$ reference frame as shown in Table A.2.

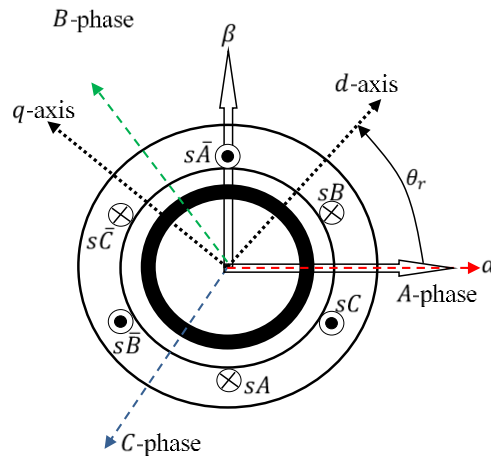


Fig.A.2 Rotational dq axes in reference frame

Table A.2 Relationship between $dq 0$ and $\alpha\beta$ reference frames

	F_α	F_β	F_0
F_d	$\cos(\theta_e)$	$\sin(\theta_e)$	0
F_q	$-\sin(\theta_e)$	$\cos(\theta_e)$	0
F_0	0	0	1

The mathematical transformation from stationary $\alpha\beta$ frame to the rotational $dq0$ reference frame is known as Park-transformation. Returning to Table A.1, this relationship can be written in the following transformation matrix:

$$\begin{bmatrix} F_d \\ F_q \\ F_0 \end{bmatrix} = \underbrace{\begin{bmatrix} \cos(\theta_e) & \sin(\theta_e) & 0 \\ -\sin(\theta_e) & \cos(\theta_e) & 0 \\ 0 & 0 & 1 \end{bmatrix}}_{[T_{dq0\leftarrow\alpha\beta0}]} \begin{bmatrix} F_\alpha \\ F_\beta \\ F_0 \end{bmatrix}, \quad \begin{bmatrix} F_d \\ F_q \\ F_0 \end{bmatrix} = [T_{dq0\leftarrow\alpha\beta0}] \begin{bmatrix} F_\alpha \\ F_\beta \\ F_0 \end{bmatrix} \quad (\text{A.3})$$

The inverse of Park transformation $[T_{dq0\leftarrow\alpha\beta0}]^{-1} = [T_{\alpha\beta0\leftarrow dq0}]$ is

$$\begin{bmatrix} F_\alpha \\ F_\beta \\ F_0 \end{bmatrix} = \underbrace{\begin{bmatrix} \cos(\theta_e) & -\sin(\theta_e) & 0 \\ \sin(\theta_e) & \cos(\theta_e) & 0 \\ 0 & 0 & 1 \end{bmatrix}}_{[T_{dq0\leftarrow\alpha\beta0}]^{-1}} \begin{bmatrix} F_d \\ F_q \\ F_0 \end{bmatrix}, \quad [T_{\alpha\beta0\leftarrow dq0}] = \begin{bmatrix} \cos(\theta_e) & -\sin(\theta_e) & 0 \\ \sin(\theta_e) & \cos(\theta_e) & 0 \\ 0 & 0 & 1 \end{bmatrix} \quad (\text{A.4})$$

A. 3 Stationary abc to rotational $dq0$ transformation (Clark-Park transformation)

The $dq0$ reference frame can be obtained by transforming the variables in the abc reference frame into $\alpha\beta0$ and then transform to $dq0$ as

$$\begin{bmatrix} F_d \\ F_q \\ F_0 \end{bmatrix} = \underbrace{[T_{dq0\leftarrow\alpha\beta0}][T_{\alpha\beta0\leftarrow abc}]}_{[T_{dq0\leftarrow abc}]} \begin{bmatrix} F_a \\ F_b \\ F_c \end{bmatrix}$$

$$[T_{dq0\leftarrow abc}] = \frac{2}{3} \begin{bmatrix} \cos(\theta_e) & \cos(\theta_e - \frac{2\pi}{3}) & \cos(\theta_e - \frac{4\pi}{3}) \\ \sin(\theta_e) & \sin(\theta_e - \frac{2\pi}{3}) & \sin(\theta_e - \frac{4\pi}{3}) \\ \frac{1}{2} & \frac{1}{2} & \frac{1}{2} \end{bmatrix} \quad (\text{A.5})$$

This transformation namely Clarke-Park transformation. The inverse of Clarke-Parke transformation can be expressed as

$$\begin{bmatrix} F_a \\ F_b \\ F_c \end{bmatrix} = [T_{dq0\leftarrow abc}]^{-1} \begin{bmatrix} F_d \\ F_q \\ F_0 \end{bmatrix}, \quad [T_{dq0\leftarrow abc}]^{-1} = [T_{abc\leftarrow dq0}] = \begin{bmatrix} \cos(\theta_e) & \sin(\theta_e) & 1 \\ \cos(\theta_e - \frac{2\pi}{3}) & \sin(\theta_e - \frac{2\pi}{3}) & 1 \\ \cos(\theta_e - \frac{4\pi}{3}) & \sin(\theta_e - \frac{4\pi}{3}) & 1 \end{bmatrix} \quad (\text{A.6})$$

APPENDIX B. Derivative of the Dynamic Model of Symmetrical and Asymmetric PMSMs

B.1. Representation in $\alpha\beta 0$ reference frame

- **Symmetrical and asymmetric resistances' equations**

This derivation is based on the assumption that the phase A stator impedance is slightly higher by ΔZ_a than the other two phases.

$$R_{abc} = \begin{bmatrix} (1+\Delta)R_a & 0 & 0 \\ 0 & R_b & 0 \\ 0 & 0 & R_c \end{bmatrix} = \underbrace{\begin{bmatrix} R_a & 0 & 0 \\ 0 & R_b & 0 \\ 0 & 0 & R_c \end{bmatrix}}_{R_{abc+}} + \underbrace{\begin{bmatrix} \Delta R_a & 0 & 0 \\ 0 & 0 & 0 \\ 0 & 0 & 0 \end{bmatrix}}_{R_{abc-}} \quad (\text{B.1})$$

$$R_{\alpha\beta 0} = [T_{\alpha\beta \leftarrow abc}] \begin{bmatrix} (1+\Delta)R_a & 0 & 0 \\ 0 & R_b & 0 \\ 0 & 0 & R_c \end{bmatrix} [T_{abc \leftarrow \alpha\beta}], \quad R_{\alpha\beta 0} = R_{\alpha\beta 0+} + R_{\alpha\beta 0-} \quad (\text{B.2})$$

$$R_{\alpha\beta 0_sym} = \frac{2}{3} \begin{bmatrix} 1 & -\frac{1}{2} & -\frac{1}{2} \\ 0 & \frac{\sqrt{3}}{2} & -\frac{\sqrt{3}}{2} \\ \frac{1}{2} & \frac{1}{2} & \frac{1}{2} \end{bmatrix} \underbrace{\begin{bmatrix} R_a & 0 & 0 \\ 0 & R_b & 0 \\ 0 & 0 & R_c \end{bmatrix}}_{R_{abc_sym}} \begin{bmatrix} 1 & 0 & 1 \\ -\frac{1}{2} & \frac{\sqrt{3}}{2} & 1 \\ -\frac{1}{2} & -\frac{\sqrt{3}}{2} & 1 \end{bmatrix} \quad (\text{B.3})$$

$$= \frac{2}{3} \begin{bmatrix} R_a & -\frac{1}{2}R_b & -\frac{1}{2}R_c \\ 0 & \frac{\sqrt{3}}{2}R_b & -\frac{\sqrt{3}}{2}R_c \\ \frac{1}{2}R_a & \frac{1}{2}R_b & \frac{1}{2}R_c \end{bmatrix} \begin{bmatrix} 1 & 0 & 1 \\ -\frac{1}{2} & \frac{\sqrt{3}}{2} & 1 \\ -\frac{1}{2} & -\frac{\sqrt{3}}{2} & 1 \end{bmatrix}$$

$$R_{\alpha\beta 0_sym} = \begin{bmatrix} \left(\frac{4}{6}R_a + \frac{1}{6}R_b + \frac{1}{6}R_c\right) & \left(\frac{1}{2\sqrt{3}}R_c - \frac{1}{2\sqrt{3}}R_b\right) & \left(\frac{2}{3}R_a - \frac{1}{3}R_b - \frac{1}{3}R_c\right) \\ \left(\frac{1}{2\sqrt{3}}R_c - \frac{1}{2\sqrt{3}}R_b\right) & R_b & \left(\frac{1}{2\sqrt{3}}R_b - \frac{1}{2\sqrt{3}}R_c\right) \\ \left(\frac{1}{3}R_a - \frac{1}{6}R_b - \frac{1}{6}R_c\right) & \left(\frac{1}{2\sqrt{3}}R_b - \frac{1}{2\sqrt{3}}R_c\right) & \left(\frac{1}{3}R_a + \frac{1}{3}R_b + \frac{1}{3}R_c\right) \end{bmatrix} \quad (\text{B.3a})$$

$$\text{If } R_a=R_b=R_c=R_s, \text{ then. } R_{\alpha\beta 0_sym} = \begin{bmatrix} R_s & 0 & 0 \\ 0 & R_s & 0 \\ 0 & 0 & R_s \end{bmatrix} \quad (\text{B.3b})$$

$$R_{\alpha\beta 0_asy} = \frac{2}{3} \begin{bmatrix} 1 & -\frac{1}{2} & -\frac{1}{2} \\ 0 & \frac{\sqrt{3}}{2} & -\frac{\sqrt{3}}{2} \\ \frac{1}{2} & \frac{1}{2} & \frac{1}{2} \end{bmatrix} \underbrace{\begin{bmatrix} \Delta R_a & 0 & 0 \\ 0 & 0 & 0 \\ 0 & 0 & 0 \end{bmatrix}}_{R_{abc_asy}} \begin{bmatrix} 1 & 0 & 1 \\ -\frac{1}{2} & \frac{\sqrt{3}}{2} & 1 \\ -\frac{1}{2} & -\frac{\sqrt{3}}{2} & 1 \end{bmatrix} = \begin{bmatrix} \frac{2}{3}\Delta R_a & 0 & \frac{2}{3}\Delta R_a \\ 0 & 0 & 0 \\ \frac{1}{3}\Delta R_a & 0 & 0 \end{bmatrix} \quad (\text{B.4})$$

- **Symmetrical and asymmetric inductances equations**

The asymmetric inductance equations can be derived as

$$L_{abc} = \begin{bmatrix} (1+\Delta)^2 L_{aa} & (1+\Delta)M_{ab} & (1+\Delta)M_{ac} \\ (1+\Delta)M_{ba} & L_{bb} & M_{bc} \\ (1+\Delta)M_{ca} & M_{cb} & L_{cc} \end{bmatrix} = \underbrace{\begin{bmatrix} L_{aa} & M_{ab} & M_{ac} \\ M_{ba} & L_{bb} & M_{bc} \\ M_{ca} & M_{cb} & L_{cc} \end{bmatrix}}_{L_{abc+}} + \underbrace{\begin{bmatrix} (\Delta^2 + 2\Delta)L_{aa} & \Delta M_{ab} & \Delta M_{ac} \\ \Delta M_{ba} & 0 & 0 \\ \Delta M_{ca} & 0 & 0 \end{bmatrix}}_{L_{abc-}}$$

$$L_{\alpha\beta 0_sym} = \frac{2}{3} \begin{bmatrix} 1 & -\frac{1}{2} & -\frac{1}{2} \\ 0 & \frac{\sqrt{3}}{2} & -\frac{\sqrt{3}}{2} \\ \frac{1}{2} & \frac{1}{2} & \frac{1}{2} \end{bmatrix} \underbrace{\begin{bmatrix} L_{aa} & M_{ab} & M_{ac} \\ M_{ba} & L_{bb} & M_{bc} \\ M_{ca} & M_{cb} & L_{cc} \end{bmatrix}}_{L_{abc_sym}} \begin{bmatrix} 1 & 0 & 1 \\ -\frac{1}{2} & \frac{\sqrt{3}}{2} & 1 \\ -\frac{1}{2} & -\frac{\sqrt{3}}{2} & 1 \end{bmatrix} \quad (\text{B.5})$$

$$L_{\alpha\beta 0_sym} = \frac{2}{3} \begin{bmatrix} (L_{aa} - \frac{1}{2}M_{ba} - \frac{1}{2}M_{ca}) & (M_{ab} - \frac{1}{2}L_{bb} - \frac{1}{2}M_{cb}) & (M_{ac} - \frac{1}{2}M_{bc} - \frac{1}{2}L_{cc}) \\ (\frac{\sqrt{3}}{2}M_{ba} - \frac{\sqrt{3}}{2}M_{ca}) & (\frac{\sqrt{3}}{2}L_{bb} - \frac{\sqrt{3}}{2}M_{cb}) & (\frac{\sqrt{3}}{2}M_{bc} - \frac{\sqrt{3}}{2}L_{cc}) \\ (\frac{1}{2}L_{aa} + \frac{1}{2}M_{ba} + \frac{1}{2}M_{ca}) & (\frac{1}{2}M_{ab} + \frac{1}{2}L_{bb} + \frac{1}{2}M_{cb}) & (\frac{1}{2}M_{ac} + \frac{1}{2}M_{bc} + \frac{1}{2}L_{cc}) \end{bmatrix}$$

$$\begin{bmatrix} 1 & 0 & 1 \\ -\frac{1}{2} & \frac{\sqrt{3}}{2} & 1 \\ -\frac{1}{2} & -\frac{\sqrt{3}}{2} & 1 \end{bmatrix}$$

$$L_{\alpha\beta 0_sym} = \frac{2}{3} \begin{bmatrix} A_{11} & A_{12} & A_{13} \\ A_{21} & A_{22} & A_{23} \\ A_{33} & A_{32} & A_{33} \end{bmatrix} \begin{bmatrix} 1 & 0 & 1 \\ -\frac{1}{2} & \frac{\sqrt{3}}{2} & 1 \\ -\frac{1}{2} & -\frac{\sqrt{3}}{2} & 1 \end{bmatrix} = \begin{bmatrix} L_{\alpha\alpha} & L_{\alpha\beta} & L_{\alpha 0} \\ L_{\beta\alpha} & L_{\beta\beta} & L_{\beta 0} \\ L_{0\alpha} & L_{0\beta} & L_{00} \end{bmatrix}. \quad (\text{B.5a})$$

Assuming $L_{aa}=L_{bb}=L_{cc}=L$ and $M_{ab}=M_{ba}=M_{ca}=M_{ac}=M_{bc}=M_{cb}=M$, then,

$$L_{\alpha\alpha} = \frac{2}{3} [(L_{aa} - \frac{1}{2}M_{ba} - \frac{1}{2}M_{ca}) - \frac{1}{2}(M_{ab} - \frac{1}{2}L_{bb} - \frac{1}{2}M_{cb}) - \frac{1}{2}(M_{ac} - \frac{1}{2}M_{bc} - \frac{1}{2}L_{cc})] = (L - M)$$

$$L_{\alpha\beta} = \frac{2}{3} [\frac{\sqrt{3}}{2}(M_{ab} - \frac{1}{2}L_{bb} - \frac{1}{2}M_{cb}) - \frac{\sqrt{3}}{2}(M_{ac} - \frac{1}{2}M_{bc} - \frac{1}{2}L_{cc})] = 0$$

$$L_{\beta\beta} = \frac{2}{3} \left[\frac{\sqrt{3}}{2} \left(\frac{\sqrt{3}}{2} L_{bb} - \frac{\sqrt{3}}{2} M_{cb} \right) - \frac{\sqrt{3}}{2} \left(\frac{\sqrt{3}}{2} M_{bc} - \frac{\sqrt{3}}{2} L_{cc} \right) \right]$$

$$= \frac{2}{3} \left[\frac{3}{4} L_{bb} - \frac{3}{4} M_{cb} - \frac{3}{4} M_{bc} + \frac{3}{4} L_{cc} \right] = (L - M)$$

$$L_{00} = \frac{2}{3} \left[\left(\frac{1}{2} L_{aa} + \frac{1}{2} M_{ba} + \frac{1}{2} M_{ca} \right) + \left(\frac{1}{2} M_{ab} + \frac{1}{2} L_{bb} + \frac{1}{2} M_{cb} \right) + \left(\frac{1}{2} M_{ac} + \frac{1}{2} M_{bc} + \frac{1}{2} L_{cc} \right) \right] = (L + 2M)$$

and, $L_{\alpha\beta} = 0$, $L_{\alpha 0} = 0$, $L_{\beta\alpha} = 0$, $L_{\beta 0} = 0$, $L_{0\alpha} = 0$, $L_{0\beta} = 0$,

$$L_{\alpha\beta 0_sym}(\theta_r) = \frac{2}{3} \begin{bmatrix} 1 & -\frac{1}{2} & -\frac{1}{2} \\ 0 & \frac{\sqrt{3}}{2} & -\frac{\sqrt{3}}{2} \\ \frac{1}{2} & \frac{1}{2} & \frac{1}{2} \end{bmatrix} \begin{bmatrix} L_2 \cos(2\theta_r) & M_2 \cos\left(2\theta_r - \frac{2\pi}{3}\right) & M_2 \cos\left(2\theta_r - \frac{4\pi}{3}\right) \\ M_2 \cos\left(2\theta_r - \frac{2\pi}{3}\right) & L_2 \cos\left(2\theta_r - \frac{4\pi}{3}\right) & M_2 \cos(2\theta_r) \\ M_2 \cos\left(2\theta_r - \frac{4\pi}{3}\right) & M_2 \cos(2\theta_r) & L_2 \cos\left(2\theta_r - \frac{2\pi}{3}\right) \end{bmatrix}$$

$$\begin{bmatrix} 1 & 0 & 1 \\ -\frac{1}{2} & \frac{\sqrt{3}}{2} & 1 \\ -\frac{1}{2} & -\frac{\sqrt{3}}{2} & 1 \end{bmatrix}$$

(B.5b)

$$= \frac{2}{3} \begin{bmatrix} L_2 \cos(2\theta_r) - \frac{1}{2} M_2 \cos\left(2\theta_r - \frac{2\pi}{3}\right) - \frac{1}{2} M_2 \cos\left(2\theta_r - \frac{4\pi}{3}\right) & M_2 \cos\left(2\theta_r - \frac{2\pi}{3}\right) - \frac{1}{2} L_2 \cos\left(2\theta_r - \frac{4\pi}{3}\right) - \frac{1}{2} M_2 \cos(2\theta_r) \\ \frac{\sqrt{3}}{2} M_2 \cos\left(2\theta_r - \frac{2\pi}{3}\right) - \frac{\sqrt{3}}{2} M_2 \cos\left(2\theta_r - \frac{4\pi}{3}\right) & \frac{\sqrt{3}}{2} L_2 \cos\left(2\theta_r - \frac{4\pi}{3}\right) - \frac{\sqrt{3}}{2} M_2 \cos(2\theta_r) \\ \frac{1}{2} L_2 \cos(2\theta_r) + \frac{1}{2} M_2 \cos\left(2\theta_r - \frac{2\pi}{3}\right) + \frac{1}{2} M_2 \cos\left(2\theta_r - \frac{4\pi}{3}\right) & M_2 \cos\left(2\theta_r - \frac{2\pi}{3}\right) + \frac{1}{2} L_2 \cos\left(2\theta_r - \frac{2\pi}{3}\right) + \frac{1}{2} M_2 \cos(2\theta_r) \\ M_2 \cos\left(2\theta_r - \frac{4\pi}{3}\right) - \frac{1}{2} M_2 \cos(2\theta_r) - \frac{1}{2} L_2 \cos\left(2\theta_r - \frac{2\pi}{3}\right) & \left[\begin{array}{ccc} 1 & 0 & 1 \\ -\frac{1}{2} & \frac{\sqrt{3}}{2} & 1 \\ -\frac{1}{2} & -\frac{\sqrt{3}}{2} & 1 \end{array} \right] \\ \frac{\sqrt{3}}{2} M_2 \cos(2\theta_r) - \frac{\sqrt{3}}{2} L_2 \cos\left(2\theta_r - \frac{2\pi}{3}\right) & \left[\begin{array}{ccc} L_{\alpha\alpha}(\theta_r) & L_{\alpha\beta}(\theta_r) & L_{\alpha 0}(\theta_r) \\ L_{\beta\alpha}(\theta_r) & L_{\beta\beta}(\theta_r) & L_{\beta 0}(\theta_r) \\ L_{0\alpha}(\theta_r) & L_{0\beta}(\theta_r) & L_{00}(\theta_r) \end{array} \right] \\ \frac{1}{2} M_2 \cos\left(2\theta_r - \frac{4\pi}{3}\right) + \frac{1}{2} M_2 \cos(2\theta_r) + \frac{1}{2} L_2 \cos\left(2\theta_r - \frac{2\pi}{3}\right) & \left[\begin{array}{ccc} 1 & 0 & 1 \\ -\frac{1}{2} & \frac{\sqrt{3}}{2} & 1 \\ -\frac{1}{2} & -\frac{\sqrt{3}}{2} & 1 \end{array} \right] \end{bmatrix}$$

$$L_{\alpha\alpha}(\theta_r) = \frac{2}{3} \left\{ \begin{array}{l} L_2 \cos(2\theta_r) - \frac{1}{2} M_2 \cos\left(2\theta_r - \frac{2\pi}{3}\right) - \frac{1}{2} M_2 \cos\left(2\theta_r - \frac{4\pi}{3}\right) \\ -\frac{1}{2} \left[M_2 \cos\left(2\theta_r - \frac{2\pi}{3}\right) - \frac{1}{2} L_2 \cos\left(2\theta_r - \frac{4\pi}{3}\right) - \frac{1}{2} M_2 \cos(2\theta_r) \right] \\ -\frac{1}{2} \left[M_2 \cos\left(2\theta_r - \frac{4\pi}{3}\right) - \frac{1}{2} M_2 \cos(2\theta_r) - \frac{1}{2} L_2 \cos\left(2\theta_r - \frac{2\pi}{3}\right) \right] \end{array} \right\}$$

$$L_{\alpha\alpha}(\theta_r) = \frac{2}{3} \left[L_2 \cos(2\theta_r) + \frac{1}{4} L_2 \cos\left(2\theta_r - \frac{4\pi}{3}\right) + \frac{1}{4} L_2 \cos\left(2\theta_r - \frac{2\pi}{3}\right) + \frac{1}{2} M_2 \cos(2\theta_r) - M_2 \cos\left(2\theta_r - \frac{2\pi}{3}\right) - M_2 \cos\left(2\theta_r - \frac{4\pi}{3}\right) \right]$$

$$L_{\alpha\alpha}(\theta_r) = \frac{2}{3} \left[\begin{array}{l} L_2 \cos(2\theta_r) + \frac{1}{4} L_2 \left(-\frac{1}{2} \cos(2\theta_r) + \frac{\sqrt{3}}{2} \sin(2\theta_r) \right) + \frac{1}{4} L_2 \left(-\frac{1}{2} \cos(2\theta_r) - \frac{\sqrt{3}}{2} \sin(2\theta_r) \right) \\ + \frac{1}{2} M_2 \cos(2\theta_r) - M_2 \left(-\frac{1}{2} \cos(2\theta_r) + \frac{\sqrt{3}}{2} \sin(2\theta_r) \right) - M_2 \left(-\frac{1}{2} \cos(2\theta_r) - \frac{\sqrt{3}}{2} \sin(2\theta_r) \right) \end{array} \right]$$

$$L_{\alpha\alpha}(\theta_r) = \frac{2}{3} \left[\frac{3}{4} L_2 \cos(2\theta_r) + \frac{3}{2} M_2 \cos(2\theta_r) \right] = \left(\frac{1}{2} L_2 + M_2 \right) \cos(2\theta_r)$$

$$L_{\alpha\beta}(\theta_r) = \frac{2}{3} \left[\begin{array}{l} \frac{\sqrt{3}}{2} \left[M_2 \cos\left(2\theta_r - \frac{2\pi}{3}\right) - \frac{1}{2} L_2 \cos\left(2\theta_r - \frac{4\pi}{3}\right) - \frac{1}{2} M_2 \cos(2\theta_r) \right] \\ - \frac{\sqrt{3}}{2} \left[M_2 \cos\left(2\theta_r - \frac{4\pi}{3}\right) - \frac{1}{2} M_2 \cos(2\theta_r) - \frac{1}{2} L_2 \cos\left(2\theta_r - \frac{2\pi}{3}\right) \right] \end{array} \right]$$

$$L_{\alpha\beta}(\theta_r) = \frac{2}{3} \left[\begin{array}{l} \frac{\sqrt{3}}{2} \left[-\frac{1}{2} M_2 \cos(2\theta_r) + \frac{\sqrt{3}}{2} M_2 \sin(2\theta_r) + \frac{1}{4} L_2 \cos(2\theta_r) - \frac{\sqrt{3}}{4} L_2 \sin(2\theta_r) \right] \\ - \frac{\sqrt{3}}{2} \left[-\frac{1}{2} M_2 \cos(2\theta_r) + \frac{\sqrt{3}}{2} M_2 \sin(2\theta_r) + \frac{1}{4} L_2 \cos(2\theta_r) - \frac{\sqrt{3}}{4} L_2 \sin(2\theta_r) \right] \end{array} \right]$$

$$L_{\alpha\beta}(\theta_r) = \frac{2}{3} \left[\frac{3}{4} M_2 \sin(2\theta_r) + \frac{3}{8} L_2 \sin(2\theta_r) + \frac{3}{4} M_2 \sin(2\theta_r) + \frac{3}{8} L_2 \sin(2\theta_r) \right] = \left(\frac{1}{2} L_2 + M_2 \right) \sin(2\theta_r)$$

$$L_{\beta\alpha}(\theta_r) = \frac{2}{3} \left[\begin{array}{l} \frac{\sqrt{3}}{2} M_2 \cos\left(2\theta_r - \frac{2\pi}{3}\right) - \frac{\sqrt{3}}{2} M_2 \cos\left(2\theta_r - \frac{4\pi}{3}\right) - \frac{1}{2} \left[\frac{\sqrt{3}}{2} L_2 \cos\left(2\theta_r - \frac{4\pi}{3}\right) \right. \\ \left. - \frac{\sqrt{3}}{2} M_2 \cos(2\theta_r) \right] - \frac{1}{2} \left[\frac{\sqrt{3}}{2} M_2 \cos(2\theta_r) - \frac{\sqrt{3}}{2} L_2 \cos\left(2\theta_r - \frac{2\pi}{3}\right) \right] \end{array} \right]$$

$$L_{\beta\alpha}(\theta_r) = \frac{2}{3} \left[\begin{array}{l} \frac{\sqrt{3}}{2} \left[\left(-\frac{1}{2} M_2 \cos(2\theta_r) + \frac{\sqrt{3}}{2} M_2 \sin(2\theta_r) - \frac{\sqrt{3}}{2} \left(-\frac{1}{2} M_2 \cos(2\theta_r) - \frac{\sqrt{3}}{2} M_2 \sin(2\theta_r)\right) \right. \right. \\ \left. - \frac{1}{2} \left[\frac{\sqrt{3}}{2} \left(-\frac{1}{2} L_2 \cos(2\theta_r) - \frac{\sqrt{3}}{2} L_2 \sin(2\theta_r)\right) - \frac{\sqrt{3}}{2} M_2 \cos(2\theta_r) \right] \right. \\ \left. - \frac{1}{2} \left[\frac{\sqrt{3}}{2} M_2 \cos(2\theta_r) - \frac{\sqrt{3}}{2} \left(-\frac{1}{2} L_2 \cos(2\theta_r) + \frac{\sqrt{3}}{2} L_2 \sin(2\theta_r)\right) \right] \right. \\ \left. - \frac{\sqrt{3}}{4} M_2 \cos(2\theta_r) + \frac{3}{4} M_2 \sin(2\theta_r) + \frac{\sqrt{3}}{4} M_2 \cos(2\theta_r) + \frac{3}{4} M_2 \sin(2\theta_r) \right] \\ \left. - \frac{1}{2} \left[-\frac{\sqrt{3}}{4} L_2 \cos(2\theta_r) - \frac{3}{4} L_2 \cos(2\theta_r) - \frac{\sqrt{3}}{2} M_2 \cos(2\theta_r) \right] \right. \\ \left. - \frac{1}{2} \left[\frac{\sqrt{3}}{2} M_2 \cos(2\theta_r) + \frac{\sqrt{3}}{4} L_2 \cos(2\theta_r) - \frac{3}{4} L_2 \cos(2\theta_r) \right] \right]$$

$$L_{\beta\alpha}(\theta_r) = \frac{2}{3} \left[\frac{3}{2} M_2 \sin(2\theta_r) + \frac{3}{4} L_2 \cos(2\theta_r) \right] = \left(\frac{1}{2} L_2 + M_2 \right) \sin(2\theta_r)$$

$$L_{\beta\beta}(\theta_r) = \frac{2}{3} \left[\frac{3}{4} L_2 \cos\left(2\theta_r - \frac{4\pi}{3}\right) - \frac{3}{4} M_2 \cos(2\theta_r) - \frac{3}{4} M_2 \cos(2\theta_r) + \frac{3}{4} L_2 \cos\left(2\theta_r - \frac{2\pi}{3}\right) \right]$$

$$L_{\beta\beta}(\theta_r) = \frac{2}{3} \left[\frac{3}{4} L_2 \left(-\frac{1}{2} \cos(2\theta_r) - \frac{\sqrt{3}}{2} \sin(2\theta_r)\right) - \frac{3}{2} M_2 \cos(2\theta_r) + \frac{3}{4} L_2 \left(-\frac{1}{2} \cos(2\theta_r) + \frac{\sqrt{3}}{2} \sin(2\theta_r)\right) \right]$$

$$L_{\beta\beta}(\theta_r) = \frac{2}{3} \left[\frac{3}{4} L_2 \left(-\frac{1}{2} \cos(2\theta_r) - \frac{3}{2} M_2 \cos(2\theta_r) + \frac{3}{4} L_2 \left(-\frac{1}{2} \cos(2\theta_r)\right) \right] \right]$$

$$L_{\beta\beta}(\theta_r) = \frac{2}{3} \left[-\frac{3}{4} L_2 \cos(2\theta_r) - \frac{3}{2} M_2 \cos(2\theta_r) \right] = -\left(\frac{1}{2} L_2 + \Delta M_2 \right) \cos(2\theta_r)$$

Then, the final symmetrical inductance equation in the stationary $\alpha\beta\theta$ reference frame is

$$L_{\alpha\beta\theta_sym} = \begin{bmatrix} (L-M) & 0 & 0 \\ 0 & (L-M) & 0 \\ 0 & 0 & (L+2M) \end{bmatrix} + \begin{bmatrix} \left(\frac{1}{2} L_2 + M_2\right) \cos(2\theta_r) & \left(\frac{1}{2} L_2 + M_2\right) \sin(2\theta_r) & - \\ \left(\frac{1}{2} L_2 + M_2\right) \sin(2\theta_r) & -\left(\frac{1}{2} L_2 + M_2\right) \cos(2\theta_r) & - \\ - & - & - \end{bmatrix}$$

(B.5c)

The asymmetric inductance equations can be derived as

$$L_{\alpha\beta 0_asy} = \frac{2}{3} \begin{bmatrix} 1 & -\frac{1}{2} & -\frac{1}{2} \\ 0 & \frac{\sqrt{3}}{2} & -\frac{\sqrt{3}}{2} \\ \frac{1}{2} & \frac{1}{2} & \frac{1}{2} \end{bmatrix} \underbrace{\begin{bmatrix} (\Delta^2 + 2\Delta)L_{aa} & \Delta M_{ab} & \Delta M_{ac} \\ \Delta M_{ba} & 0 & 0 \\ \Delta M_{ca} & 0 & 0 \end{bmatrix}}_{L_{abc-}} \begin{bmatrix} 1 & 0 & 1 \\ -\frac{1}{2} & \frac{\sqrt{3}}{2} & 1 \\ -\frac{1}{2} & -\frac{\sqrt{3}}{2} & 1 \end{bmatrix} \quad (\text{B.6})$$

$$L_{\alpha\beta 0_asy} = \frac{2}{3} \begin{bmatrix} [(\Delta^2 + 2\Delta)L_{aa} - \frac{1}{2}\Delta M_{ba} - \frac{1}{2}\Delta M_{ca}] & \Delta M_{ab} & \Delta M_{ac} \\ [\frac{\sqrt{3}}{2}\Delta M_{ba} - \frac{\sqrt{3}}{2}\Delta M_{ca}] & 0 & 0 \\ [\frac{1}{2}(\Delta^2 + 2\Delta)L_{aa} + \frac{1}{2}\Delta M_{ba} + \frac{1}{2}\Delta M_{ca}] & \frac{1}{2}\Delta M_{ab} & \frac{1}{2}\Delta M_{ac} \end{bmatrix} \begin{bmatrix} 1 & 0 & 1 \\ -\frac{1}{2} & \frac{\sqrt{3}}{2} & 1 \\ -\frac{1}{2} & -\frac{\sqrt{3}}{2} & 1 \end{bmatrix} \quad (\text{B.6a})$$

$$= \begin{bmatrix} L_{\alpha\alpha_asy} & L_{\alpha\beta_asy} & L_{\alpha 0_asy} \\ L_{\beta\alpha_asy} & L_{\beta\beta_asy} & L_{\beta 0_asy} \\ L_{0\alpha_asy} & L_{0\beta_asy} & L_{00_asy} \end{bmatrix}$$

$$L_{\alpha\alpha_asy} = \frac{2}{3} [(\Delta^2 + 2\Delta)L_{aa} - \frac{1}{2}\Delta M_{ba} - \frac{1}{2}\Delta M_{ca} - \frac{1}{2}\Delta M_{ab} - \frac{1}{2}\Delta M_{ac}] = [(\frac{2}{3}\Delta^2 + \frac{4}{3}\Delta)L - \frac{4}{3}\Delta M]$$

$$L_{\alpha\beta_asy} = [\frac{\sqrt{3}}{2}\Delta M_{ab} - \frac{\sqrt{3}}{2}\Delta M_{ac}] = 0$$

$$L_{\alpha 0_asy} = \frac{2}{3} [(\Delta^2 + 2\Delta)L_{aa} - \frac{1}{2}\Delta M_{ba} - \frac{1}{2}\Delta M_{ca} + \Delta M_{ab} + \Delta M_{ac}] = [(\frac{2}{3}\Delta^2 + \frac{4}{3}\Delta)L + \frac{2}{3}\Delta M]$$

$$L_{\beta\alpha_asy} = \frac{2}{3} [\frac{\sqrt{3}}{2}\Delta M_{ba} - \frac{\sqrt{3}}{2}\Delta M_{ca}] = 0$$

$$L_{\beta\beta_asy} = 0$$

$$L_{\beta 0_asy} = \frac{2}{3} [\frac{\sqrt{3}}{2}\Delta M_{ba} - \frac{\sqrt{3}}{2}\Delta M_{ca}] = 0$$

$$L_{0\alpha_asy} = \frac{2}{3} [\frac{1}{2}(\Delta^2 + 2\Delta)L_{aa} + \frac{1}{2}\Delta M_{ba} + \frac{1}{2}\Delta M_{ca} - \frac{1}{4}\Delta M_{ab} - \frac{1}{4}\Delta M_{ac}] = [(\frac{1}{3}\Delta^2 + \frac{4}{3}\Delta)L + \frac{1}{3}\Delta M]$$

$$L_{0\beta_asy} = \frac{2}{3} [\frac{\sqrt{3}}{4}\Delta M_{ab} - \frac{\sqrt{3}}{4}\Delta M_{ac}] = 0$$

$$L_{00_asy} = \frac{2}{3} [\frac{1}{2}(\Delta^2 + 2\Delta)L_{aa} + \frac{1}{2}\Delta M_{ba} + \frac{1}{2}\Delta M_{ca} + \frac{1}{2}\Delta M_{ab} + \frac{1}{2}\Delta M_{ac}] = [(\frac{1}{3}\Delta^2 + \frac{4}{3}\Delta)L + \frac{4}{3}\Delta M]$$

$$L_{\alpha\beta 0_asy} = \begin{bmatrix} (\frac{2}{3}\Delta^2 + \frac{4}{3}\Delta)L - \frac{4}{3}\Delta M & 0 & (\frac{2}{3}\Delta^2 + \frac{4}{3}\Delta)L + \frac{2}{3}\Delta M \\ 0 & 0 & 0 \\ (\frac{1}{3}\Delta^2 + \frac{4}{3}\Delta)L + \frac{1}{3}\Delta M & 0 & (\frac{1}{3}\Delta^2 + \frac{4}{3}\Delta)L + \frac{4}{3}\Delta M \end{bmatrix} \quad (\text{B.6b})$$

$$\begin{aligned}
\bar{L}_{\alpha\beta 0_asy}(\theta_r) &= \frac{2}{3} \begin{bmatrix} 1 & -\frac{1}{2} & -\frac{1}{2} \\ 0 & \frac{\sqrt{3}}{2} & -\frac{\sqrt{3}}{2} \\ \frac{1}{2} & \frac{1}{2} & \frac{1}{2} \end{bmatrix} \begin{bmatrix} (\Delta^2 + 2\Delta)L_2 \cos(2\theta_r) & \Delta M_2 \cos\left(2\theta_r - \frac{2\pi}{3}\right) & \Delta M_2 \cos\left(2\theta_r - \frac{4\pi}{3}\right) \\ \Delta M_2 \cos\left(2\theta_r - \frac{2\pi}{3}\right) & 0 & 0 \\ \Delta M_2 \cos\left(2\theta_r - \frac{4\pi}{3}\right) & 0 & 0 \end{bmatrix} \begin{bmatrix} 1 & 0 & 1 \\ -\frac{1}{2} & \frac{\sqrt{3}}{2} & 1 \\ -\frac{1}{2} & -\frac{\sqrt{3}}{2} & 1 \end{bmatrix} \\
&= \frac{2}{3} \begin{bmatrix} (\Delta^2 + 2\Delta)L_2 \cos(2\theta_r) - \frac{1}{2}\Delta M_2 \cos\left(2\theta_r - \frac{2\pi}{3}\right) - \Delta \frac{1}{2}M_2 \cos\left(2\theta_r - \frac{4\pi}{3}\right) & \Delta M_2 \cos\left(2\theta_r - \frac{2\pi}{3}\right) & \Delta M_2 \cos\left(2\theta_r - \frac{4\pi}{3}\right) \\ \frac{\sqrt{3}}{2}\Delta M_2 \cos\left(2\theta_r - \frac{2\pi}{3}\right) - \frac{\sqrt{3}}{2}\Delta M_2 \cos\left(2\theta_r - \frac{4\pi}{3}\right) & 0 & 0 \\ \frac{1}{2}(\Delta^2 + 2\Delta)L_2 \cos(2\theta_r) + \frac{1}{2}\Delta M_2 \cos\left(2\theta_r - \frac{2\pi}{3}\right) + \frac{1}{2}\Delta M_2 \cos\left(2\theta_r - \frac{4\pi}{3}\right) & \frac{1}{2}\Delta M_2 \cos\left(2\theta_r - \frac{2\pi}{3}\right) & \frac{1}{2}\Delta M_2 \cos\left(2\theta_r - \frac{4\pi}{3}\right) \end{bmatrix} \\
&= \begin{bmatrix} 1 & 0 & 1 \\ -\frac{1}{2} & \frac{\sqrt{3}}{2} & 1 \\ -\frac{1}{2} & -\frac{\sqrt{3}}{2} & 1 \end{bmatrix} = \begin{bmatrix} L_{11} & L_{12} & L_{13} \\ L_{21} & L_{22} & L_{23} \\ L_{31} & L_{32} & L_{33} \end{bmatrix}
\end{aligned}$$

(B.6c)

$$\begin{aligned}
L_{11} &= \frac{2}{3} \begin{bmatrix} (\Delta^2 + 2\Delta)L_2 \cos(2\theta_r) - \frac{1}{2}\Delta M_2 \cos\left(2\theta_r - \frac{2\pi}{3}\right) \\ -\frac{1}{2}\Delta M_2 \cos\left(2\theta_r - \frac{4\pi}{3}\right) - \frac{1}{2}\Delta M_2 \cos\left(2\theta_r - \frac{2\pi}{3}\right) - \frac{1}{2}\Delta M_2 \cos\left(2\theta_r - \frac{4\pi}{3}\right) \end{bmatrix} \\
L_{11} &= \frac{2}{3} \begin{bmatrix} (\Delta^2 + 2\Delta)L_2 \cos(2\theta_r) - \Delta M_2 \left(-\frac{1}{2}\cos(2\theta_r) + \frac{\sqrt{3}}{2}\cos(2\theta_r) \right) \\ -\Delta M_2 \left(-\frac{1}{2}\cos(2\theta_r) - \frac{\sqrt{3}}{2}\cos(2\theta_r) \right) \end{bmatrix} \\
&= \left[\left(\frac{2}{3}\Delta^2 + \frac{4}{3}\Delta \right) L_2 + \left(\frac{2}{3}\Delta \right) M_2 \right] \cos(2\theta_r) \\
L_{12} &= \frac{2}{3} \begin{bmatrix} \frac{\sqrt{3}}{2}\Delta M_2 \cos\left(2\theta_r - \frac{2\pi}{3}\right) - \frac{\sqrt{3}}{2}\Delta M_2 \cos\left(2\theta_r - \frac{4\pi}{3}\right) \end{bmatrix} \\
&= \frac{2}{3} \begin{bmatrix} \frac{\sqrt{3}}{2}\Delta M_2 \left(-\frac{1}{2}\cos(2\theta_r) + \frac{\sqrt{3}}{2}\sin(2\theta_r) \right) - \frac{\sqrt{3}}{2}\Delta M_2 \left(-\frac{1}{2}\cos(2\theta_r) - \frac{\sqrt{3}}{2}\sin(2\theta_r) \right) \end{bmatrix} \\
L_{12} &= \frac{2}{3} \begin{bmatrix} \frac{3}{4}\Delta M_2 \sin(2\theta_r) + \frac{3}{4}\Delta M_2 \sin(2\theta_r) \end{bmatrix} = \Delta M_2 \sin(2\theta_r) \\
L_{21} &= \Delta M_2 \sin(2\theta_r) \\
L_{22} &= 0
\end{aligned}$$

Then, the final asymmetric inductance matrix can be written as

$$\begin{aligned}
L_{\alpha\beta 0_asy} &= \begin{bmatrix} [(\frac{2}{3}\Delta^2 + \frac{4}{3}\Delta)L - \frac{4}{3}\Delta M] & 0 & [(\frac{2}{3}\Delta^2 + \frac{4}{3}\Delta)L + \frac{2}{3}\Delta M] \\ 0 & 0 & 0 \\ [(\frac{1}{3}\Delta^2 + \frac{4}{3}\Delta)L + \frac{1}{3}\Delta M] & 0 & [(\frac{1}{3}\Delta^2 + \frac{4}{3}\Delta)L + \frac{4}{3}\Delta M] \end{bmatrix} \\
&+ \begin{bmatrix} [(\frac{2}{3}\Delta^2 + \frac{4}{3}\Delta)L_2 + (\frac{2}{3}\Delta)M_2]\cos(2\theta_r) & (\Delta M_2)\sin(2\theta_r) & - \\ (\Delta M_2)\sin(2\theta_r) & 0 & - \\ - & - & - \end{bmatrix}.
\end{aligned} \tag{B.6d}$$

B.2 Representation in $dq\theta$ reference frame

- Symmetrical and asymmetric resistances equations

$$\begin{aligned}
R_{qd0_sym} &= \frac{2}{3} \begin{bmatrix} \cos(\theta_r) & \cos(\theta_r - \frac{2\pi}{3}) & \cos(\theta_r - \frac{4\pi}{3}) \\ \sin(\theta_r) & \sin(\theta_r - \frac{2\pi}{3}) & \sin(\theta_r - \frac{4\pi}{3}) \\ \frac{1}{2} & \frac{1}{2} & \frac{1}{2} \end{bmatrix} \underbrace{\begin{bmatrix} R_a & 0 & 0 \\ 0 & R_b & 0 \\ 0 & 0 & R_c \end{bmatrix}}_{R_{abc_sym}} \begin{bmatrix} \cos(\theta_r) & \sin(\theta_r) & 1 \\ \cos(\theta_r - \frac{2\pi}{3}) & \sin(\theta_r - \frac{2\pi}{3}) & 1 \\ \cos(\theta_r - \frac{4\pi}{3}) & \sin(\theta_r - \frac{4\pi}{3}) & 1 \end{bmatrix} \\
&= \frac{2}{3} \begin{bmatrix} R_a \cos(\theta_e) & R_b \cos(\theta_e - \frac{2\pi}{3}) & R_c \cos(\theta_e - \frac{4\pi}{3}) \\ R_a \sin(\theta_e) & R_b \sin(\theta_e - \frac{2\pi}{3}) & R_c \sin(\theta_e - \frac{4\pi}{3}) \\ R_a \frac{1}{2} & R_b \frac{1}{2} & R_c \frac{1}{2} \end{bmatrix} \begin{bmatrix} \cos(\theta_e) & \sin(\theta_e) & 1 \\ \cos(\theta_e - \frac{2\pi}{3}) & \sin(\theta_e - \frac{2\pi}{3}) & 1 \\ \cos(\theta_e - \frac{4\pi}{3}) & \sin(\theta_e - \frac{4\pi}{3}) & 1 \end{bmatrix} \\
&= \frac{2}{3} \begin{bmatrix} R_{dd} & R_{dq} & R_{d0} \\ R_{qd} & R_{qq} & R_{q0} \\ R_{0d} & R_{0q} & R_{00} \end{bmatrix}
\end{aligned} \tag{B.7}$$

Assume $R_a=R_b=R_c=R_s$

$$\begin{aligned}
R_{dd} &= \frac{2}{3} \left[R_a \cos^2(\theta_r) + R_b \cos^2\left(\theta_r - \frac{2\pi}{3}\right) + R_c \cos^2\left(\theta_r - \frac{4\pi}{3}\right) \right] = R_s \\
&= \frac{2}{3} \left[R_a \frac{1}{2} (1 + \cos(2\theta_r)) + R_b \frac{1}{2} \left(1 + \cos\left(2\left(\theta_r - \frac{2\pi}{3}\right)\right)\right) + R_c \frac{1}{2} \left(1 + \cos\left(2\left(\theta_r - \frac{4\pi}{3}\right)\right)\right) \right] \\
&= \frac{2}{3} \left[R_a \frac{1}{2} (1 + \cos(2\theta_r)) + R_b \frac{1}{2} \left(1 + \cos\left(2\theta_r - \frac{4\pi}{3}\right)\right) + R_c \frac{1}{2} \left(1 + \cos\left(2\theta_r - \frac{8\pi}{3}\right)\right) \right] \\
&= \frac{2}{3} \left[\begin{aligned} &R_a \frac{1}{2} (1 + \cos(2\theta_r)) + R_b \frac{1}{2} \left(1 + \cos(2\theta_r) \cos\left(\frac{4\pi}{3}\right) + \sin(2\theta_r) \sin\left(\frac{4\pi}{3}\right)\right) \\ &+ R_c \frac{1}{2} \left(1 + \cos(2\theta_r) \cos\left(\frac{8\pi}{3}\right) + \sin(2\theta_r) \sin\left(\frac{8\pi}{3}\right)\right) \end{aligned} \right] \\
&= \frac{2}{3} \left[\begin{aligned} &R_a \frac{1}{2} (1 + \cos(2\theta_r)) + R_b \frac{1}{2} \left(1 - \frac{1}{2} \cos(2\theta_r) - \frac{\sqrt{3}}{2} \sin(2\theta_r)\right) \\ &+ R_c \frac{1}{2} \left(1 - \frac{1}{2} \cos(2\theta_r) + \frac{\sqrt{3}}{2} \sin(2\theta_r)\right) \end{aligned} \right] \\
&= \frac{2}{3} \left[\frac{R_a + R_b + R_c}{2} + \left(\frac{2R_a - R_b - R_c}{6}\right) \cos(2\theta_r) - \left(\frac{\sqrt{3}(R_b - R_c)}{6}\right) \sin(2\theta_r) \right] \\
&= \left[\frac{R_a + R_b + R_c}{3} + \left(\frac{2R_a - R_b - R_c}{2}\right) \cos(2\theta_r) - \left(\frac{\sqrt{3}(R_b - R_c)}{6}\right) \sin(2\theta_r) \right] \\
R_{dq} &= \frac{2}{3} \underbrace{\left[R_a \cos(\theta_r) \sin(\theta_r) + R_b \cos\left(\theta_r - \frac{2\pi}{3}\right) \sin\left(\theta_r - \frac{2\pi}{3}\right) + R_c \cos\left(\theta_r - \frac{4\pi}{3}\right) \sin\left(\theta_r - \frac{4\pi}{3}\right) \right]}_{=0} = 0 \\
R_{d0} &= \frac{2}{3} \underbrace{\left[R_a \cos(\theta_r) + R_b \cos\left(\theta_r - \frac{2\pi}{3}\right) + R_c \cos\left(\theta_r - \frac{4\pi}{3}\right) \right]}_{=0} = 0 \\
R_{qd} &= \frac{2}{3} \underbrace{\left[R_a \sin(\theta_r) \cos(\theta_r) + R_b \sin\left(\theta_r - \frac{2\pi}{3}\right) \cos\left(\theta_r - \frac{2\pi}{3}\right) + R_c \sin\left(\theta_r - \frac{4\pi}{3}\right) \cos\left(\theta_r - \frac{4\pi}{3}\right) \right]}_{=0} = 0 \\
R_{qq} &= \frac{2}{3} \underbrace{\left[R_a \sin^2(\theta_r) + R_b \sin^2\left(\theta_r - \frac{2\pi}{3}\right) + R_c \sin^2\left(\theta_r - \frac{4\pi}{3}\right) \right]}_{\frac{3}{2}} = R_s \\
R_{q0} &= \frac{2}{3} \underbrace{\left[R_a \sin(\theta_r) + R_b \sin\left(\theta_r - \frac{2\pi}{3}\right) + R_c \sin\left(\theta_r - \frac{4\pi}{3}\right) \right]}_{=0} = 0 \\
R_{0d} &= \frac{2}{3} \left[\frac{1}{2} R_a \cos(\theta_r) + \frac{1}{2} R_b \cos\left(\theta_r - \frac{2\pi}{3}\right) + \frac{1}{2} R_c \cos\left(\theta_r - \frac{4\pi}{3}\right) \right] = 0 \\
R_{0q} &= \frac{2}{3} \left[\frac{1}{2} R_a \sin(\theta_r) + \frac{1}{2} R_b \sin\left(\theta_r - \frac{2\pi}{3}\right) + \frac{1}{2} R_c \sin\left(\theta_r - \frac{4\pi}{3}\right) \right] = 0 \\
R_{00} &= \frac{2}{3} \left[\frac{1}{2} R_a + \frac{1}{2} R_b + \frac{1}{2} R_c \right] = R_s
\end{aligned}$$

$$R_{dq0+} = \begin{bmatrix} R_d & 0 & 0 \\ 0 & R_q & 0 \\ 0 & 0 & R_0 \end{bmatrix} = \begin{bmatrix} R_s & 0 & 0 \\ 0 & R_s & 0 \\ 0 & 0 & R_s \end{bmatrix} \quad (\text{B.7a})$$

$$R_{dq0_asy} = \begin{bmatrix} \cos(\theta_r) & -\sin(\theta_r) & 0 \\ \sin(\theta_r) & \cos(\theta_r) & 0 \\ 0 & 0 & 1 \end{bmatrix} \underbrace{\begin{bmatrix} \frac{2}{3}\Delta R_a & 0 & \frac{2}{3}\Delta R_a \\ 0 & 0 & 0 \\ \frac{1}{3}\Delta R_a & 0 & 0 \end{bmatrix}}_{R_{\alpha\beta 0_asy}} \begin{bmatrix} \cos(\theta_r) & \sin(\theta_r) & 0 \\ -\sin(\theta_r) & \cos(\theta_r) & 0 \\ 0 & 0 & 1 \end{bmatrix} \quad (\text{B.8})$$

$$R_{dq0_asy} = \begin{bmatrix} \frac{2}{3}\Delta R_a \cos^2(\theta_r) & \frac{2}{3}\Delta R_a \cos(\theta_r)\sin(\theta_r) & \frac{2}{3}\Delta R_a \cos(\theta_r) \\ \frac{2}{3}\Delta R_a \sin(\theta_r)\cos(\theta_r) & \frac{2}{3}\Delta R_a \sin^2(\theta_r) & \frac{2}{3}\Delta R_a \sin(\theta_r) \\ \frac{1}{3}\Delta R_a \cos(\theta_r) & \frac{1}{3}\Delta R_a \sin(\theta_r) & 0 \end{bmatrix} \quad (\text{B.8a})$$

$$= \frac{2}{3}\Delta R_a \underbrace{\begin{bmatrix} \cos^2(\theta_r) & \cos(\theta_r)\sin(\theta_r) & \frac{1}{2}\cos(\theta_r) \\ \sin(\theta_r)\cos(\theta_r) & \sin^2(\theta_r) & \frac{1}{2}\sin(\theta_r) \\ \frac{1}{2}\cos(\theta_r) & \frac{1}{2}\sin(\theta_r) & 0 \end{bmatrix}}_{R_{dq0_asy}}$$

- Symmetrical and asymmetric inductances' equations

$$L_{dq0_sym} = \begin{bmatrix} \cos(\theta_r) & -\sin(\theta_r) & 0 \\ \sin(\theta_r) & \cos(\theta_r) & 0 \\ 0 & 0 & 1 \end{bmatrix} \begin{bmatrix} (L-M) & 0 & 0 \\ 0 & (L-M) & 0 \\ 0 & 0 & (L-2M) \end{bmatrix} \begin{bmatrix} \cos(\theta_r) & \sin(\theta_r) & 0 \\ -\sin(\theta_r) & \cos(\theta_r) & 0 \\ 0 & 0 & 1 \end{bmatrix}$$

$$= \begin{bmatrix} (L-M)\cos(\theta_r) & -(L-M)\sin(\theta_r) & 0 \\ (L-M)\sin(\theta_r) & (L-M)\cos(\theta_r) & 0 \\ 0 & 0 & (L+2M) \end{bmatrix} \begin{bmatrix} \cos(\theta_r) & \sin(\theta_r) & 0 \\ -\sin(\theta_r) & \cos(\theta_r) & 0 \\ 0 & 0 & 1 \end{bmatrix} \quad (\text{B.9})$$

$$L_{dd} = (L-M)\cos^2(\theta_r) + (L-M)\sin^2(\theta_r) = (L-M)[\cos^2(\theta_r) + \sin^2(\theta_r)] = (L-M)$$

$$L_{dq} = (L-M)\cos(\theta_r)\sin(\theta_r) - (L-M)\cos(\theta_r)\sin(\theta_r) = 0$$

$$L_{qd} = (L-M)\cos(\theta_r)\sin(\theta_r) - (L-M)\cos(\theta_r)\sin(\theta_r) = 0$$

$$L_{qq} = (L-M)$$

(B.9a)

$$L_{dq0_sym}(\theta_r) = \begin{bmatrix} \cos(\theta_r) & -\sin(\theta_r) & 0 \\ \sin(\theta_r) & \cos(\theta_r) & 0 \\ 0 & 0 & 1 \end{bmatrix} \begin{bmatrix} (\frac{1}{2}L_2 + M_2)\cos(2\theta_r) & (\frac{1}{2}L_2 + M_2)\sin(2\theta_r) & - \\ (\frac{1}{2}L_2 + M_2)\sin(2\theta_r) & -(\frac{1}{2}L_2 + M_2)\cos(2\theta_r) & - \\ - & - & - \end{bmatrix} \begin{bmatrix} \cos(\theta_r) & \sin(\theta_r) & 0 \\ -\sin(\theta_r) & \cos(\theta_r) & 0 \\ 0 & 0 & 1 \end{bmatrix} \quad (\text{B.9b})$$

$$L_{dd}(\theta_r) = \begin{bmatrix} [(\frac{1}{2}L_2 + M_2)\cos(2\theta_r)]\cos^2(\theta_e) + [(\frac{1}{2}L_2 + M_2)\sin(2\theta_r)]\sin(\theta_e)\cos(\theta_e) \\ -[(\frac{1}{2}L_2 + M_2)\sin(2\theta_r)]\cos(\theta_e)\sin(\theta_e) - [(\frac{1}{2}L_2 + M_2)\cos(2\theta_r)]\sin^2(\theta_e) \end{bmatrix}$$

$$L_{dd}(\theta_r) = \begin{bmatrix} [(\frac{1}{2}L_2 + M_2)\cos(2\theta_r)]\cos(2\theta_e) - [(\frac{1}{2}L_2 + M_2)\sin(2\theta_r)]\sin(2\theta_e) \end{bmatrix}$$

$$L_{dd}(\theta_r) = -(\frac{1}{2}L_2 + M_2)$$

$$L_{dq}(\theta_r) = 0$$

$$L_{qd}(\theta_r) = 0$$

$$L_{qq}(\theta_r) = \begin{bmatrix} [(\frac{1}{2}L_2 + M_2)\cos(2\theta_r)]\sin^2(\theta_e) - [(\frac{1}{2}L_2 + M_2)\sin(2\theta_r)]\cos(\theta_e)\sin(\theta_e) \\ +[(\frac{1}{2}L_2 + M_2)\sin(2\theta_r)]\sin(\theta_e)\cos(\theta_e) + [(\frac{1}{2}L_2 + M_2)\cos(2\theta_r)]\cos^2(\theta_e) \end{bmatrix}$$

$$L_{qq}(\theta_r) = \begin{bmatrix} [(\frac{1}{2}L_2 + M_2)\cos(2\theta_r)]\sin^2(\theta_e) + [(\frac{1}{2}L_2 + M_2)\cos(2\theta_r)]\cos^2(\theta_e) \end{bmatrix}$$

$$L_{qq}(\theta_r) = (\frac{1}{2}L_2 + M_2)$$

$$L_{dq0_sym} = \begin{bmatrix} (L-M) & 0 & 0 \\ 0 & (L-M) & 0 \\ 0 & 0 & 0 \end{bmatrix} + \begin{bmatrix} -(\frac{1}{2}L_2 + M_2) & 0 & - \\ 0 & (\frac{1}{2}L_2 + M_2) & - \\ - & - & - \end{bmatrix} \quad (\text{B.9c})$$

$$L_{dq0_asy} = \begin{bmatrix} \cos(\theta_r) & -\sin(\theta_r) & 0 \\ \sin(\theta_r) & \cos(\theta_r) & 0 \\ 0 & 0 & 1 \end{bmatrix} \underbrace{\begin{bmatrix} [(\frac{2}{3}\Delta^2 + \frac{4}{3}\Delta)L - \frac{4}{3}\Delta M] & 0 & - \\ 0 & 0 & - \\ - & - & - \end{bmatrix}}_{L_{\alpha\beta 0-}} \begin{bmatrix} \cos(\theta_r) & \sin(\theta_r) & 0 \\ -\sin(\theta_r) & \cos(\theta_r) & 0 \\ 0 & 0 & 1 \end{bmatrix} \quad (\text{B.10})$$

$$L_{dq0_asy} = \begin{bmatrix} [(\frac{2}{3}\Delta^2 + \frac{4}{3}\Delta)L - \frac{4}{3}\Delta M]\cos(\theta_r) & 0 & - \\ [(\frac{2}{3}\Delta^2 + \frac{4}{3}\Delta)L - \frac{4}{3}\Delta M]\sin(\theta_r) & 0 & - \\ - & - & - \end{bmatrix} \cdot \begin{bmatrix} \cos(\theta_r) & \sin(\theta_r) & 0 \\ -\sin(\theta_r) & \cos(\theta_r) & 0 \\ 0 & 0 & 1 \end{bmatrix} \quad (\text{B.10a})$$

$$\begin{aligned} L_{dd_asy} &= [(\frac{2}{3}\Delta^2 + \frac{4}{3}\Delta)L - \frac{4}{3}\Delta M]\cos^2(\theta_r) = [(\frac{1}{3}\Delta^2 + \frac{2}{3}\Delta)L - \frac{2}{3}\Delta M](1 + \cos(2\theta_r)) \\ L_{dq_asy} &= [(\frac{2}{3}\Delta^2 + \frac{4}{3}\Delta)L - \frac{4}{3}\Delta M]\cos(\theta_r)\sin(\theta_r) = -[(\frac{1}{3}\Delta^2 + \frac{2}{3}\Delta)L - \frac{2}{3}\Delta M]\sin(2\theta_r) \\ L_{qd_asy} &= [(\frac{2}{3}\Delta^2 + \frac{4}{3}\Delta)L - \frac{4}{3}\Delta M]\sin(\theta_r)\cos(\theta_r) = -[(\frac{1}{3}\Delta^2 + \frac{2}{3}\Delta)L - \frac{2}{3}\Delta M]\sin(2\theta_r) \\ L_{qq_asy} &= [(\frac{2}{3}\Delta^2 + \frac{4}{3}\Delta)L - \frac{4}{3}\Delta M]\sin^2(\theta_r) = [(\frac{1}{3}\Delta^2 + \frac{2}{3}\Delta)L - \frac{2}{3}\Delta M](1 - \cos(2\theta_r)) \end{aligned} \quad (\text{B.10b})$$

$$L_{dq02_asy}(\theta_r) = \begin{bmatrix} \cos(\theta_r) & -\sin(\theta_r) & 0 \\ \sin(\theta_r) & \cos(\theta_r) & 0 \\ 0 & 0 & 1 \end{bmatrix} \begin{bmatrix} [(\frac{2}{3}\Delta^2 + \frac{4}{3}\Delta)L_2 + (\frac{2}{3}\Delta)M_2]\cos(2\theta_r) & (\Delta M_2)\sin(2\theta_r) & - \\ (\Delta M_2)\sin(2\theta_r) & 0 & - \\ - & - & - \end{bmatrix}$$

$$\begin{bmatrix} \cos(\theta_r) & \sin(\theta_r) & 0 \\ -\sin(\theta_r) & \cos(\theta_r) & 0 \\ 0 & 0 & 1 \end{bmatrix}$$

$$L_{dq02_asy}(\theta_r) = \begin{bmatrix} L_{d_asy}(\theta_r) & M_{dq_asy}(\theta_r) & 0 \\ M_{qd_asy}(\theta_r) & L_{q_asy}(\theta_r) & 0 \\ 0 & 0 & 1 \end{bmatrix}$$

(B.10c)

$$L_{dq0_asy} = \begin{bmatrix} [(\frac{2}{3}\Delta^2 + \frac{4}{3}\Delta)L - \frac{4}{3}\Delta M]\cos^2(\theta_r) & [(\frac{2}{3}\Delta^2 + \frac{4}{3}\Delta)L - \frac{4}{3}\Delta M]\cos(\theta_r)\sin(\theta_r) & - \\ [(\frac{2}{3}\Delta^2 + \frac{4}{3}\Delta)L - \frac{4}{3}\Delta M]\cos(\theta_r)\sin(\theta_r) & [(\frac{2}{3}\Delta^2 + \frac{4}{3}\Delta)L - \frac{4}{3}\Delta M]\sin^2(\theta_r) & - \\ - & - & - \end{bmatrix}$$

$$+ \begin{bmatrix} \Delta L_{d2-}(\theta_r) & \Delta M_{dq2-}(\theta_r) & - \\ \Delta M_{qd2-}(\theta_r) & \Delta L_{q2-}(\theta_r) & - \\ - & - & - \end{bmatrix}$$

(B.10d)

B.3 Back EMF

- Representation in $\alpha\beta 0$ reference frame

$$\begin{bmatrix} \psi_{r\alpha} \\ \psi_{r\beta} \\ \psi_{r0} \end{bmatrix} = \frac{2}{3} \begin{bmatrix} 1 & -\frac{1}{2} & -\frac{1}{2} \\ 0 & \frac{\sqrt{3}}{2} & -\frac{\sqrt{3}}{2} \\ \frac{1}{2} & \frac{1}{2} & \frac{1}{2} \end{bmatrix} \begin{bmatrix} (1+\Delta)\psi_{PM} \cos(\theta_r) \\ \psi_{PM} \cos(\theta_r - \frac{2\pi}{3}) \\ \psi_{PM} \cos(\theta_r - \frac{4\pi}{3}) \end{bmatrix} \quad (\text{B.11})$$

$$\begin{aligned} \psi_{r\alpha} &= \frac{2}{3} \left[(1+\Delta)\psi_{PM} \cos(\theta_r) - \frac{1}{2}\psi_{PM} \cos(\theta_r - \frac{2\pi}{3}) - \frac{1}{2}\psi_{PM} \cos(\theta_r - \frac{4\pi}{3}) \right] \\ &= \frac{2}{3} \begin{bmatrix} (1+\Delta)\psi_{PM} \cos(\theta_r) - \frac{1}{2}\psi_{PM} (-\frac{1}{2}\cos(\theta_r) + \frac{\sqrt{3}}{2}\sin(\theta_r)) \\ -\frac{1}{2}\psi_{PM} (-\frac{1}{2}\cos(\theta_r) - \frac{\sqrt{3}}{2}\sin(\theta_r)) \end{bmatrix} \\ &= \underbrace{\psi_{PM} \cos(\theta_r)}_{\psi_{r\alpha_sym}} + \frac{2}{3} \underbrace{\Delta\psi_{PM} \cos(\theta_r)}_{\psi_{r\alpha_asy}} \end{aligned}$$

$$\begin{aligned} \psi_{r\beta} &= \frac{2}{3} \left[\frac{\sqrt{3}}{2}\psi_{PM} \cos(-\theta_e - \frac{2\pi}{3}) - \frac{\sqrt{3}}{2}\psi_{PM} \cos(-\theta_e - \frac{2\pi}{3}) \right] \\ &= \frac{2}{3} \left[\frac{\sqrt{3}}{2}\psi_{PM} (-\frac{1}{2}\cos(\theta_r) + \frac{\sqrt{3}}{2}\sin(\theta_r)) - \frac{\sqrt{3}}{2}\psi_{PM} (-\frac{1}{2}\cos(\theta_r) - \frac{\sqrt{3}}{2}\sin(\theta_r)) \right] \\ &= \underbrace{\psi_{PM} \sin(\theta_r)}_{\psi_{r\beta_sym}} \end{aligned} \quad (\text{B.11a})$$

- Representation in $dq0$ reference frame

$$\begin{bmatrix} \psi_{rd} \\ \psi_{rq} \\ \psi_{r0} \end{bmatrix} = \frac{2}{3} \begin{bmatrix} \cos(\theta_e) & \cos(\theta_e - \frac{2\pi}{3}) & \cos(\theta_e - \frac{4\pi}{3}) \\ \sin(\theta_e) & \sin(\theta_e - \frac{2\pi}{3}) & \sin(\theta_e - \frac{4\pi}{3}) \\ \frac{1}{2} & \frac{1}{2} & \frac{1}{2} \end{bmatrix} \begin{bmatrix} (1+\Delta)\psi_{PM} \cos(\theta_e) \\ \psi_{PM} \cos(\theta_e - \frac{2\pi}{3}) \\ \psi_{PM} \cos(\theta_e - \frac{4\pi}{3}) \end{bmatrix} =$$

$$\psi_{rd} = \frac{2}{3} \underbrace{[(1+\Delta)F_a \cos^2(\theta_r) + F_b \cos^2(\theta_r - \frac{2\pi}{3}) + F_c \cos^2(\theta_r - \frac{4\pi}{3})]}_{\frac{3}{2}} = \underbrace{\psi_{PM}}_{\psi_{rd_sym}} + \underbrace{\Delta\psi_{PM}}_{\psi_{rd_asy}}$$

$$\psi_{rq} = \frac{2}{3} \underbrace{[F_a \cos(\theta_r) \cdot \sin(\theta_r) + F_b \cos(\theta_r - \frac{2\pi}{3}) \cdot \sin(\theta_r - \frac{2\pi}{3}) + F_c \cos(\theta_r - \frac{4\pi}{3}) \sin(\theta_r - \frac{4\pi}{3})]}_{=0} = 0 \quad (\text{B.10})$$

APPENDIX C Schematic Diagram of the Inverter Board



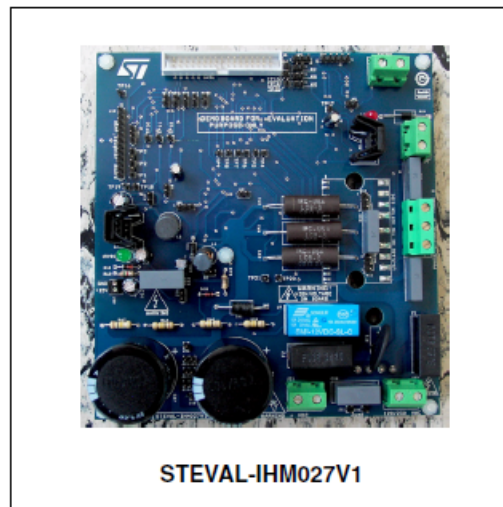
STEVAL-IHM027V1

Power board with MC connector based on the STGIPS10K60A
10 A, 600 V intelligent power module

Data brief

Features

- Minimum input voltage: 125 VDC or 90 VAC
- Maximum input voltage: 350 VDC or 220 VAC
- Capable of using external +15 V supply voltage
- Maximum output power for motor: 1000 W
- Regenerative brake control feature
- Input inrush limitation with bypassing relay
- +15 V auxiliary power supply based on buck converter with VIPer16
- Fully-populated board with test points
- Motor control connector for interfacing with STM3210B-EVAL board and other ST motor control-dedicated kits
- Tachometer and Hall/encoder inputs
- Compatible with BEMF daughterboard for sensor-less six-step control of BLDC motors
- RoHS compliant



Description

The STEVAL-IHM027V1 is a 1 kW, 3-phase motor control demonstration board featuring the STGIPS10K60A 600 V, 10 A IGBT intelligent power module (IPM) from STMicroelectronics.

The system is an AC/DC 3-phase inverter for driving an induction motor or PMSM motors up to 1000 W. The purpose of the application is to demonstrate the performance of the STGIPS10K60A IPM, housed in a 25-lead, small dual inline package.

The STEVAL-IHM027V1 demonstration board is designed to be compatible with single-phase AC supply from 90 to 220 V, or DC supply from 125 to 350 V.

Figure 1. STEVAL-IHM027V1 circuit schematics (1 of 1)

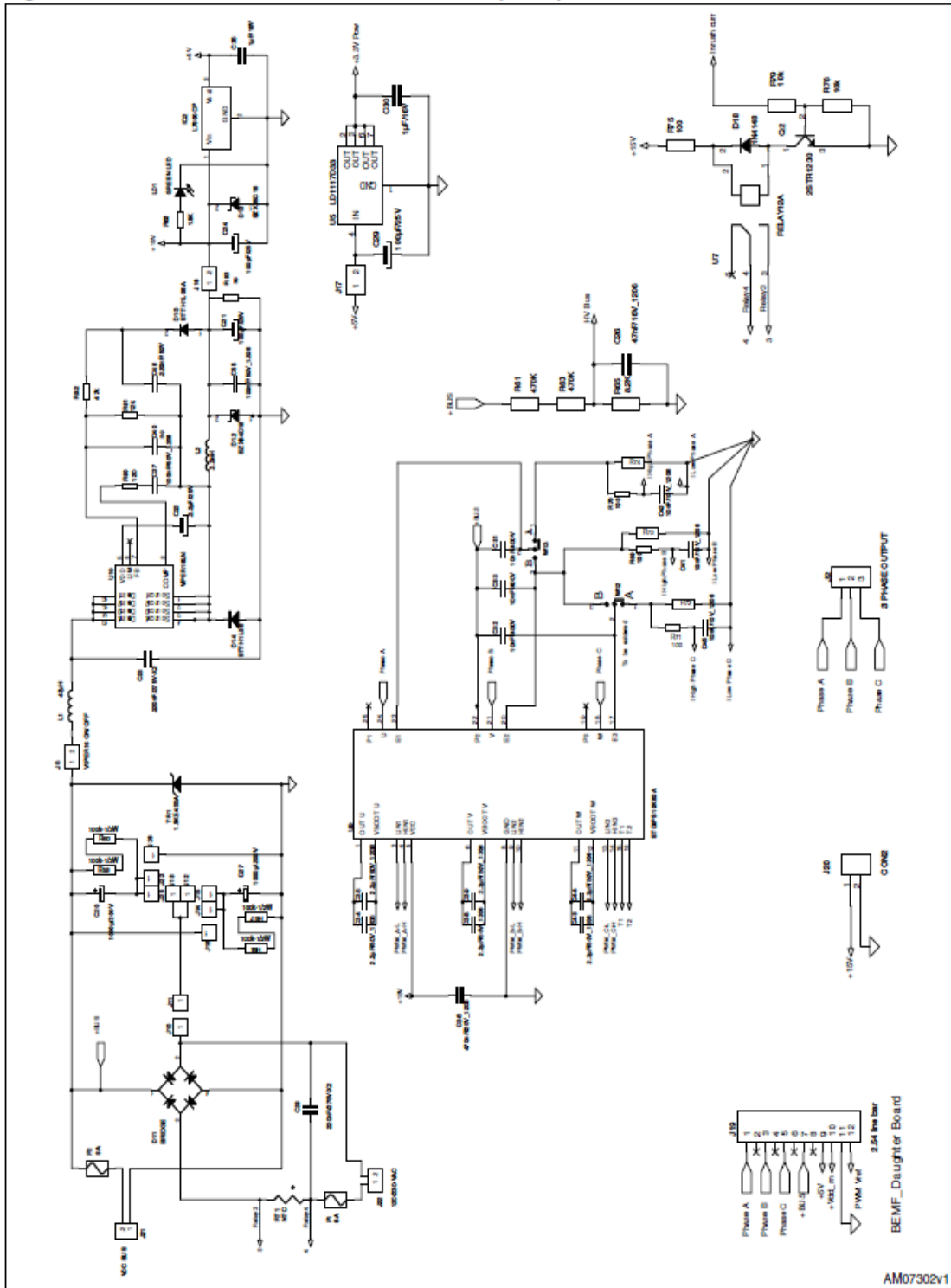


Figure 2. STEVAL-IHM027V1 circuit schematics (2 of 2)

